eXPRESS Polymer Letters Vol.5, No.12 (2011) 1027
Available online at www.expresspolymlett.com
DOI: 10.3144/expresspolymlett.2011.100

Editorial corner – a personal view
Smart polymer systems: a journey from imagination to applications

G. C. Psarras[*]

Department of Materials Science, University of Patras, Patras 26504, Hellas (Greece)

Engineering materials are chosen for a given application mainly via their mechanical and physical properties, which constitute their behaviour at service. The term smart materials, refers to systems which are able to tune their behaviour responding to an external or internal stimulus. Certain properties of these systems can be varied in a controllable way, such as stiffness, shape, damping capacity, natural vibration frequency, polarization, conductivity, energy storing efficiency etc. Smart structures are usually material systems incorporating functional constituents that are able to perform the operations of sensing, actuation and control. The smart behaviour of the whole system is induced by the large changes in amplitude of specific properties of the functional constituents, responding in real time to an imposed stimulus. Typical examples of smart systems' components are: piezo/ferroelectrics, electro/magnetostrictive materials, electro/magnetorheological fluids, thrermoresponsive materials, shape memory materials, electrochromic materials, nanodielectrics and others. Polymers and fibre reinforced polymers are considered as suitable candidates for providing the requisite structure in which functional parts could be embedded. Initial efforts carried out more than 20 years ago met criticism. Polymer composites incorporating shape memory alloys in the form of ribbons or wires represent a characteristic example, in which the dynamic response of the system as well as its shape can be controlled, giving new frontiers in the automotive and aerospace industry. Shape memory alloys and polymer gels exhibit biomechanical and biomedical applications in developing artificial muscles and devices for active control of in-vivo drug-delivery. Piezopolymers are used as infrared sensors and smart skins in comfort control systems. On the other hand the distribution of dielectric inorganic nanoparticles within a polymer matrix offers new possibilities in energy storing devices. This type of materials is tested for power systems in applications such as mobile electronic devices and hybrid electric vehicles. Further applications of polymer matrix-inorganic particles nanocomposites include passive protection, acoustic emission sensors and self-current regulators. Since the driving force for the evolution of new materials is to fulfill the technological requirements of the continuously increasing social demands, and the methodology of developing smart materials follows bio-mimetic criteria, the field of smart polymer systems appears to be wide open and very promising.

Prof. Dr. Georgios C. Psarras
Member of International Advisory Board

[*]Corresponding author, e-mail: G.C.Psarras@upatras.gr

eXPRESS Polymer Letters Vol.5, No.12 (2011) 1028–1040
Available online at www.expresspolymlett.com
DOI: 10.3144/expresspolymlett.2011.101

The influence of Ag^{+}, Zn^{2+} and Cu^{2+} exchanged zeolite on antimicrobial and long term in vitro stability of medical grade polyether polyurethane

P. Kaali[1,2], M. M. Pérez-Madrigal[3], E. Strömberg[1], R. E. Aune[4,5], Gy. Czél[2], S. Karlsson[1,6]*

[1]Deptartment of Fibre and Polymer Technology, School of Chemical Science and Engineering, Royal Institute of Technology (KTH), SE-100 44 Stockholm, Sweden
[2]Department of Polymer Engineering, University of Miskolc, HU-3515 Miskolc, Hungary
[3]Department of Chemical Engineering, Technical University of Catalonia, Av. Diagonal 647, E-08028, Barcelona, Spain
[4]Department of Material Science and Engineering, School of Industrial Engineering and Management, Royal Institute of Technology (KTH), SE-100 44 Stockholm, Sweden
[5]Department of Material Science and Engineering, Norwegian University of Science and Technology (NTNU), NO-7491 Trondheim, Norway
[6]Presently, Vice-Chancellor of Skövde University, SE-541 28 Skövde, Sweden

Received 28 March 2011; accepted in revised form 8 June 2011

Abstract. This study aims to investigate the limitations and applicability of different ion exchanged zeolites as antimicrobial additive in thermoplastic polyether type polyurethanes. These composites were designed to improve the health quality of hospitalized patients by expressing both biocompatibility and relevant antimicrobial activity. The zeolites were exchanged with silver, copper and zinc ions and single, binary and ternary ion-exchanged zeolite-polyurethane composites were prepared. The antimicrobial activity and the resistance of the composites against the human environment play vital role in the applicability of the materials as a medical device therefore these properties were investigated. The antimicrobial test were performed on Methicillin-resistant *Staphylococcus aureus*, *Pseudomonas aeruginosa* and *Candida tropicalis*. The tests showed that the efficiency of the silver ions is superior to the other single ionic systems. Besides, the binary and ternary ion-exchanged samples had similar antimicrobial efficiency regardless the type of the ions in the zeolite.
The biocompatibility tests were carried out in-vitro in artificial body fluids for a period of 12 weeks. As a result of the in-vitro test, degradation of the composites were observed and the structural changes of the materials were detected and described by Scanning Electron Microscopy, Contact Angle measurements and Attenuated Total Reflection Fourier Transform Infrared Spectroscopy.

Keywords: *biocomposites, body fluid, ion-exchanged zeolite, antibacterial, in-vitro test*

1. Introduction

Polyether polyurethane (PU) is a biocompatible material that is preferably used in a variety of medical applications [1–3], e.g. as raw material for central venous catheters tracheostomy tubes and other medical devices. Although these polymers are biocompatible materials, device associated side effect often occurs during the clinical use of the materials that can be inflammation, infection, biofilm formation and growth. This initiates the degradation of the material, e.g. previous studies have proven that the degradation of PU catheters is caused by either oxidation or hydrolysis [4–6]. The bacterial activity is responsible for the biofilm formation and growth

*Corresponding author, e-mail: sigbritt@kth.se

and subsequent degradation of the polymeric material inside the human body. Once the biofilm has formed on the surface of the material it is difficult, or sometimes impossible, to remove it either by washing or antibiotic treatment [7, 8]. There are numerous solutions that have been presented in the literature in order to enhance the antimicrobial properties of polymeric materials e.g. antibiotics or silver containing coatings and composites [9–13]. Compared to some antibiotics, nano-silver coatings have shown superior antimicrobial properties. The antimicrobial activity of silver is based on the release of silver ions which is an ion-exchange process [14, 15]. Some studies have confirmed that the main drawback of silver is that during long term use if the released ions reach a certain concentration, silver could cause toxicity in both human and animal cells [16, 17]. Impregnation of silver ions into the surface is a safer way to ensure antibacterial properties of the material since the silver concentration is lower in this case, and the release is governed by the diffusion of the ion from the top surface layers of the material. For this application silver-sulfadiazine or other silver compounds are usually used [16–18]. Clinical studies have, however, proved that the antibacterial activity of silver-sulfadiazine impregnated catheters decreased rapidly. In addition, impregnated central venous catheters did not show a significant decrease in the number of infections compared to un-treated ones [18–20]. The aim of the antibacterial materials in clinical use is to decrease the number of infections, and thereby to improve the health of the patients, consequently reducing the healthcare costs. In addition, the production cost of these materials is almost twice that of the un-coated materials and the efficiency is questionable. Hence, clinical papers recommend the use of these materials not instead of, but in complement to un-coated materials [18–20].

It has been reported that silver ion exchanged zeolites have good antibacterial activity and therefore have a potential in the medical field to enhance antimicrobial properties of polymers. [21–23]. Since zeolite is a natural mineral, non-toxic, non-carcinogenic and has a high importance as food supplement and medical treatment agent for both humans and animals, it is completely safe to be used in medical devices [24, 25].

The mechanism of silver loaded zeolite's antimicrobial effect is similar to silver coatings and based on an ion exchange reaction. If moisture or liquid film interacts with the surface of the material, ion-exchange initiates where silver ions are exchanged to Na or other cations that can be found in the environment. The released silver ions attach to the bacteria by forming chelate complexes with the deoxyribonucleic acid (DNA) and block the transport processes in the cell [14, 15]. The applications of zeolite as filler in polymeric materials were previously reported in literature and proved that the antibacterial activity of these polymers was enhanced [26, 27]. Furthermore the effect of zeolite content on physical and thermal properties of the polymer was also examined [26, 27]. By increasing the silver-zeolite content in the polymer an increased antimicrobial activity was observed (due to the higher silver ion concentration) [22, 28] but, depending on the application the zeolite content may influence physical, thermal and/or chemical properties.

There are two main reasons to exchange silver as filler in any kind of antimicrobial agent or composite. The first is the current European Union (EU) regulations that aim to ban silver products from the medical industry due to the increased risk to toxicity, while the second is based on economical issues due to the high price of silver products.

The current study aims to investigate the potential of other metallic ions containing zeolites as antimicrobial agents that may replace the silver. This paper presents the preparation and manufacture of PU filled with silver and alternatively copper, zinc and multi-ion exchanged zeolite in order to determine whether the combination of these ions can lead to the elimination of silver. The influence of the presence of different ions in the zeolite on the antimicrobial activity of polyurethane composites was investigated. Furthermore, as a key requirement of the invasive medical applications, *in-vitro* tests were performed in two artificial body fluids in order to monitor the long-term stability of the materials, and to determine how the degradation was influenced by the different ions and the zeolite content. Contact angle measurements, Fourier-transform infrared spectroscopy (FTIR) and scanning electron microscopy (SEM) were used to monitor the changes in surface and chemical properties. In

addition, swelling and ion release measurements were performed to determine diffusion coefficients and the mechanism of zeolite diffusion from the bulk to the surface.

2. Experimental

2.1. Materials

BASF Elastollan 1164D50 polyether type thermoplastic polyurethane (PU) was supplied by TRACOE medical GmbH (Frankfurt, Germany). A type zeolite (ZEOMIC AJ10D) was purchased from Sinanen Zeomic Co., Ltd. (Tokyo, Japan). The particles size was typically 2.5 μm. Silve-nitrate (purum p.a., crystallized, ≥99.0%), zinc nitrate hexahydrate (purum p.a., crystallized, ≥99.0%), copper nitrate trihydrate (purum p.a., 98.0–103%) sodium sulphate (purum, anhydrous, ≥99%), magnesium chloride (purum, anhydrous, ≥98.0%), sodium chloride (purum p.a., ≥99.5%), sodium hydroxide (purum p.a., ≥97.0%), sodium phosphate dibasic (purum p.a., anhydrous, ≥98.0%), potassium chloride (puriss. p.a., ≥99.5%) and calcium chloride dihydrate (purum p.a., 99–103%) were purchased from Fluka (Stockholm, Sweden). Sodium acetate (puriss. ≥99.0%, anhydrous), sodium bicarbonate (powder, ≥99.5%), citric acid (anhydrous, ≥99.5%), sodium citrate dihydrate (puriss. ≥99%), glycine (puriss. ≥99%), sodium L-tartrate dibasic dihydrate (ACS reagent, ≥99%) sodium L-lactate (~98%), and sodium pyruvate (SigmaUltra, ≥99%) were purchased from Sigma Aldrich (Stockholm, Sweden). Methicillin-resistant *Staphylococcus aureus* (MRSA) ATCC 43300, *Pseudomonas aeruginosa* ATCC 27853, *Candida tropicalis* ATCC 90874 were supplied by the Hungarian National Public Health and Medical Officer Service, Miskolc, Hungary.

2.2. Sample preparation

Single, binary and ternary ionic zeolites were prepared with silver, copper, zinc and the variation of these ions. In order to make the antimicrobial effectiveness of the different ions comparable, similar ion concentrations needed to be obtained in the zeolite structure. The ion absorption reactions were performed according to the following protocol: 1 g zeolite powder was added to 40 ml metallic nitrate solution. The reactions took place at room temperature for 24 hours under constant stirring then the samples were washed 5 times with distilled water to remove the excess nitrate. This was followed by drying at 105°C. In case of single ionic systems 0.025 M silver-, 0.05 M zinc- and 0.1 M copper-nitrate was used in order to achieve fairly equal concentrations of each ion in the zeolite structure. For binary and ternary systems the variations of the different metallic solutions were mixed, however the concentration of each ion in the solution was kept at the same value as it was for the single ionic systems. The final ion concentration in the zeolite samples is presented in Table 1. The EDX results confirmed that similar ion concentration was reached in the binary and ternary ion exchanged zeolites by the applied solution concentrations. Altogether seven different samples were prepared: zeolites filled with Ag, Cu, Zn ions and the combination of these ions (Ag-Zn, Ag-Cu, Zn-Cu, Ag-Zn-Cu).

Table 1. Ion content of the different zeolite samples

Sample/Ion	Ag	Cu	Zn
	[wt%]		
Ag	13.21±2.13		
Cu		9.25±0.32	
Zn			18.38±2.26
AgCu	12.60±1.30	10.29±0.69	
AgZn	15.54±1.51		13.37±0.88
CuZn		8.43±0.22	7.39±0.21
AgCuZn	11.94±0.38	9.30±0.28	5.23±0.11

The second step was the incorporation of the zeolite samples into the PU. 1% of zeolite was mixed with PU pellets in a Haake Polylab System equipped with a Rheomix 600 mixer (Thermo Fisher Scientific Inc., Karlsruhe, Germany). The mixing temperature was 210°C at 100 rpm and the duration of constant mixing was 10 minutes. Besides ion filled zeolite, 1–5% unfilled zeolite was also mixed in PU in order to monitor the influence of the zeolite content on the polymer's stability. After the composites were prepared, zeolite-containing PUs were ground into pellets and injection moulded into flat 100 × 100 × 1.5 mm plate with a Krauss Maffei 50-390/C1 type injection molding machine (KraussMaffei Technologie GmbH, München, Germany). Pure PU samples were also prepared and used as a reference sample for the experiments.

2.3. Antimicrobial test

The antimicrobial effect of zeolite-PU composites was determined for two bacterial strains (Methicillin-resistant *Staphylococcus aureus* (MRSA)

ATCC 43300, *Pseudomonas aeruginosa* ATCC 27853) and one mold (*Candida tropicalis* ATCC 90874) according to the ISO 22196 standard. Cell suspensions were prepared from each strain with a cell concentration of $5 \cdot 10^5$ CFU/mL. Then the suspension was inoculated onto the surface of the composite samples and the cells were allowed to grow on the surface for 24 h at 37°C and 98% relative humidity. The dimension of the test pieces was 50 × 50 mm. After the exposure the suspension was washed from the surface and mixed with agar that was deposited on petri dishes. This mixture was let to get solidified an were placed into growing ovens at 37°C. After 24–48 hours the number of the grown colonies in the agar plate was counted.

2.4. *In-vitro* degradation test

Two synthetic body fluids were chosen to simulate different in vivo conditions. Both fluids have been identified to cause degradation of plastic implant materials [29, 30]. Artificial Lysosomal Fluid (ALF) simulates the immunological reaction of the body while the Gamble's solution is similar to the interstitial fluid of the deep lung. The chemical composition of the two test media was previously described [30].

The pure PU and zeolite-PU composites were placed into acid-cleaned (1% HNO_3 for 24 h) glass vessels which were filled with 10 ml of either ALF or Gamble's solution, and thoroughly sealed with Parafilm. Subsequently, the samples were placed in an incubator and stored under static and dark conditions at 37°C during 84 days. Samples were withdrawn from the solution on a weekly basis, and analyzed by scanning electron microscopy (SEM), contact angle (CA) measurements and FTIR spectroscopy. Since the different ions in the zeolite structure may be reduced to oxides (especially silver) on contact with water and cause discoloration of the samples, the colour change was also monitored throughout the whole experiment.

2.5. Diffusion and swelling

During the in-vitro ageing of the materials in ALF and Gambles solution, the liquid uptake of the samples was determined on short and long term. Sampling was performed after 1, 2, 3, 4, 5, 6, 8, 12, 24, 32, 48, 60, 72, 96, 120 and 144 hours in the short term test, while weekly sampling was done during the long term test that lasted 12 weeks. The liquid uptake was determined by weight measurement and calculated by Equation (1).

$$WA\,[\%] = \frac{m_v - m_k}{m_k} \cdot 100 \tag{1}$$

where WA [%] is the absorbed liquid uptake in weight percentage, m_k is the initial weight and m_v is the weight after sampling of the samples.

The diffusion coefficients were calculated from the fluid absorption curves. These curve had two sections that can be clearly distinguished (Figure 1). The first section follows a Fickian characteristic ($\sqrt{h} \leq 7$), where the amount of the absorbed liquid increases linearly as a function of exposure time. The second section is parallel to the X axis, which means that the amount of the liquid remains constant in the composite and indicates the saturation of the material.

This second section is the saturation level, which is marked by M_∞ in the literature. The time that is necessary for the saturation is t_s. This was determined at 95% saturation and the diffusion coefficients of the liquid into the polymer phase was calculated by Fick's second law (Equation (2)) from the linear section of the normalized absorption curves (Figure 1):

$$\frac{M_t}{M_\infty} = \frac{4}{L} \cdot \left(\frac{D}{\pi}\right)^{0.5} \cdot t^{0.5} \tag{2}$$

where M_t is the absorbed liquid amount at a certain time, M_∞ is the maximum absorbable liquid amount, L is the sample thickness and t is the time.

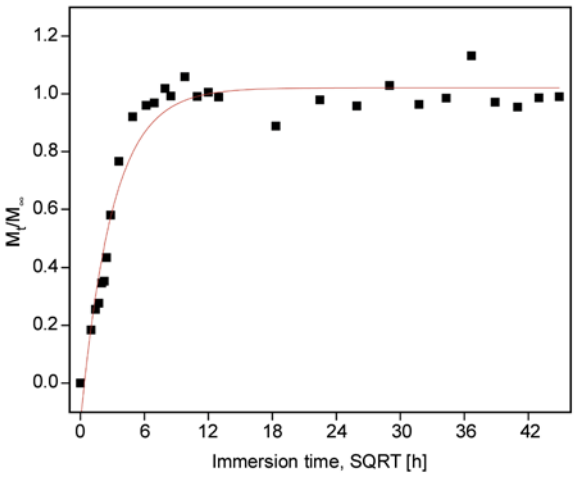

Figure 1. The method to determine the diffusion coefficient from the absorption plot

2.6. Contact angle measurements

The contact angle measurements were performed on a CAM 200 instrument from KSV Instruments Ltd. (Helsinki, Finland). MilliQ grade water from a Synergy 185UV Ultrapure water system (18.2 MΩ·cm, Millipore AB, Solna, Sweden) was used. The contact angle was measured on a reference and all exposed samples, the average value of three pieces cut from the same sample was calculated. Five 3 µl droplets were analyzed on each piece, i.e. a total number of 15 droplets, and ten images were taken for each droplet at 100 frames/s.

2.7. Attenuated Total Reflection Fourier Transform Infrared Spectroscopy (ATR-FTIR)

The sample surfaces were analysed using a Spectrum 2000 FTIR spectrometer from Perkin Elmer (Wellesley, MA, USA) equipped with a Golden Gate single-reflection accessory for Attenuated Total Reflection (ATR). Triplets of the samples were analysed, 16 scans per piece between 4000 and 600 cm^{-1} at intervals of 1 cm^{-1} with a resolution of 4 cm^{-1}. All the spectra were normalized to 1.5 cm^{-1} and average results are presented.

2.8. Scanning electron microscopy (SEM)

SEM micrographs from each sampling area at the different exposure times were taken with a Hitachi S-4800 Ultra-High Resolution Field Emission Scanning Electron Microscope (FE-SEM) (Hitachi High Technologies Europe GmBH, Krefeld, Germany) at various magnifications. The samples were coated with gold/palladium.

3. Results and discussion

3.1. Antimicrobial activity

The results of the antimicrobial test are presented in Figure 2. The reference sample was the pure PU that did not contain any zeolite particles. It was observed that this sample had no antimicrobial effect, all of the microorganisms started to grow intensively on the surface. After 24 hours exposure the number of viable cells increased approximately one order of magnitude for MRSA and *Candida tropicalis* while for *Pseudomonas aeruginosa* this value was two times higher than the initial cell concentration ($5 \cdot 10^5$ CFU/ml). In addition, the number of viable MRSA cells also increased slightly on the

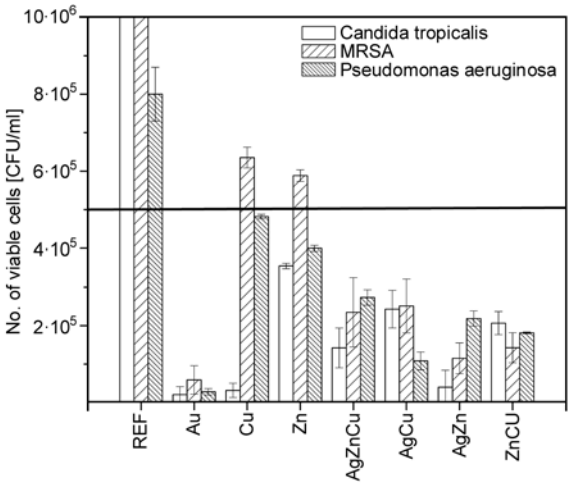

Figure 2. The number of viable cells on the surface of the different ion-filled samples after 24 hours exposure

surface of samples that contained only copper or zinc zeolite. In contrast these samples showed antimicrobial or growth inhibition effect against *Ps. aeruginosa* and *C. trop*. Both copper and zinc containing samples decreased the number of viable cells for *Ps. aeruginosa* slightly, while copper decreased the number of *Candida tropicalis* cells significantly. Microorganisms have different tolerance against antibiotics and antimicrobial material. This good activity of the copper could be explained by the low resistance of *C. tropicalis*. Binary and ternary ionic zeolite samples showed similar antimicrobial activity against all three microorganisms. This is due to the ion distribution of in the zeolite. It was determined during previous experiments that in binary and ternary zeolite systems the different ions may block each others` way and therefore highly influence each others` release. Since silver was superior to all of the other samples. It can be assumed that in silver containing multi-ionic systems the silver ion could be the responsible for the increased antimicrobial activity compared to single ionic copper and zinc zeolite. Although, these two ions did not express significant antimicrobial activity, the binary zinc-copper system decreased the number of viable cells with the same magnitude as the silver containing multi-ionic systems. This increased efficiency could be due to joint activity of copper and zinc. It can be assumed that each of these ions initiate different toxic mechanism within the cell, therefore the duplex system can be more harmful for the cells than single ones.

3.2. Diffusion and swelling

The mechanism of the antimicrobial effect of zeolite-PU composites is based on the diffusion of the ions from the bulk to the surface where they interact with microbial cells. Water uptake is a key factor since it can influence the diffusion of the zeolite and ions in a positive way. Besides, the type of the ion may also influence the diffusion rate of zeolite, which is based on the ion activity. Since zeolites are known to be hygroscopic materials, the zeolite content in the composites may result in an increased water uptake. Figure 3 presents the water uptake of zeolite-PU composites with increasing zeolite content as a function of exposure time in ALF and Gamble's solution.

It can be determined from the water uptake plots that the increasing zeolite content has influence on the rate of the water absorption and slightly increased the amount of total absorbed solution. During the short-term experiment all the composites became saturated with the aging solutions. The rate of absorption of ALF and Gamble solution did not increase at 1 to 3% zeolite content, while at 4 to 5% the rate increased for both ageing solutions.

The calculated diffusion coefficients and maximum absorption values are presented in Table 2. The absorption plots and the measured values show that with the increasing zeolite content the absorption slightly increased in ALF-solution while it did not change in Gamble's solution. Based on this it can be assumed that besides temperature, molecular structure and sample thickness, the diffusing liquid also influences the absorption. The diffusion coefficients show increasing tendency as a function of zeolite content. This is also obvious from Figure 2 since the time that is needed for the saturation decreased as a function of zeolite content. The diffusion coefficients were compared with the literature data and showed a good match.

Table 2. The maximum solution absorption capacity and diffusion coefficients of the PU-zeolite samples in ALF and Gamble's solution

Zeolite content [wt%]	ALF		Gamble	
	WA [%]	D [m^2/s]	WA [%]	D [m^2/s]
0	2.21	$4.01 \cdot 10^{12}$	2.23	$4.31 \cdot 10^{12}$
1	2.28	$3.71 \cdot 10^{12}$	2.21	$4.10 \cdot 10^{12}$
2	2.36	$3.61 \cdot 10^{12}$	2.54	$3.92 \cdot 10^{12}$
3	2.33	$3.51 \cdot 10^{12}$	2.5	$2.82 \cdot 10^{12}$
4	2.41	$3.46 \cdot 10^{12}$	2.53	$2.72 \cdot 10^{12}$
5	2.45	$1.25 \cdot 10^{11}$	2.53	$2.26 \cdot 10^{11}$

3.3. SEM study

Different surface changes were observed during the in vitro degradation of PU composite samples in artificial ageing solutions. Pure PU samples showed surface changes as a function of time in both ALF and Gamble solution (Figure 4). As a result, the surface roughness increased and smaller degradation signs (cracks, holes) appeared on the surface. Some of these changes can originate from manufacturing and preparation of the samples. In addition, high amount of salt residues were also found on the surface of Gamble aged samples.

On the surface of zeolite-PU composites obvious degradation signs were identified (Figure 5). An increasing amount of small holes were observed as a function of time and zeolite content on the surface of ALF exposed samples. These holes started to appear after 1 month and their formation increased intensively during the whole exposure. Since the

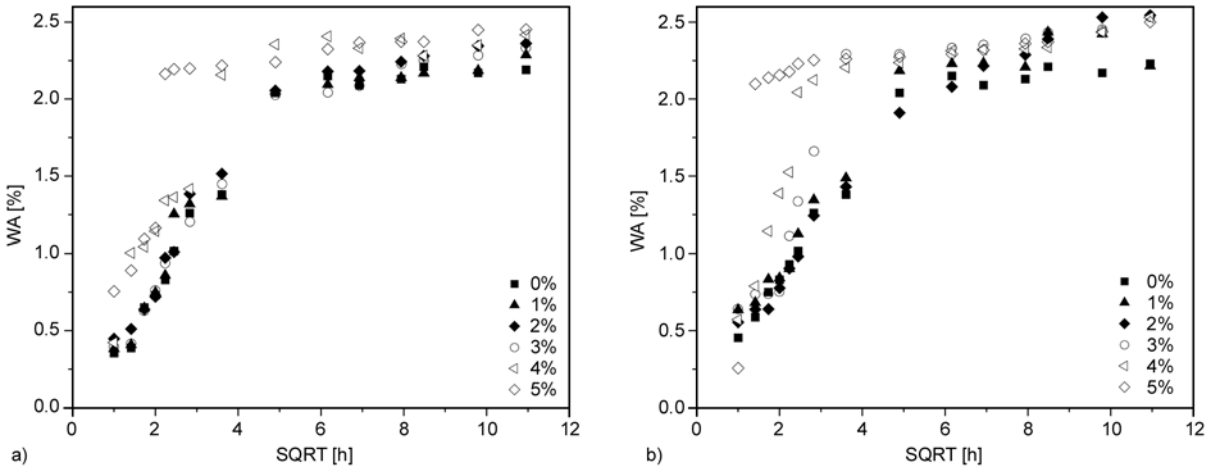

Figure 3. The water uptake of PU-zeolite samples as a function of immersion time in ALF (a) and Gamble's (b) solution

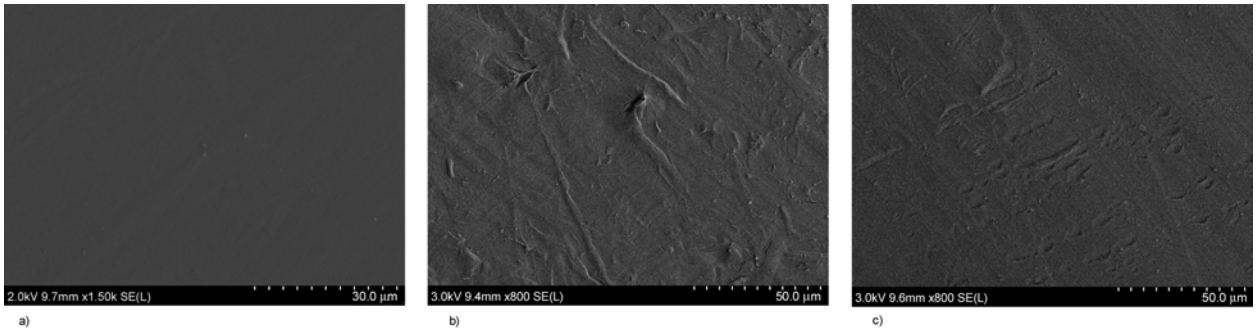

Figure 4. SEM micrographs of the surface of unaged pure PU (a) and aged in ALF (b) and Gamble's (c) solution pure PU samples for 3 months

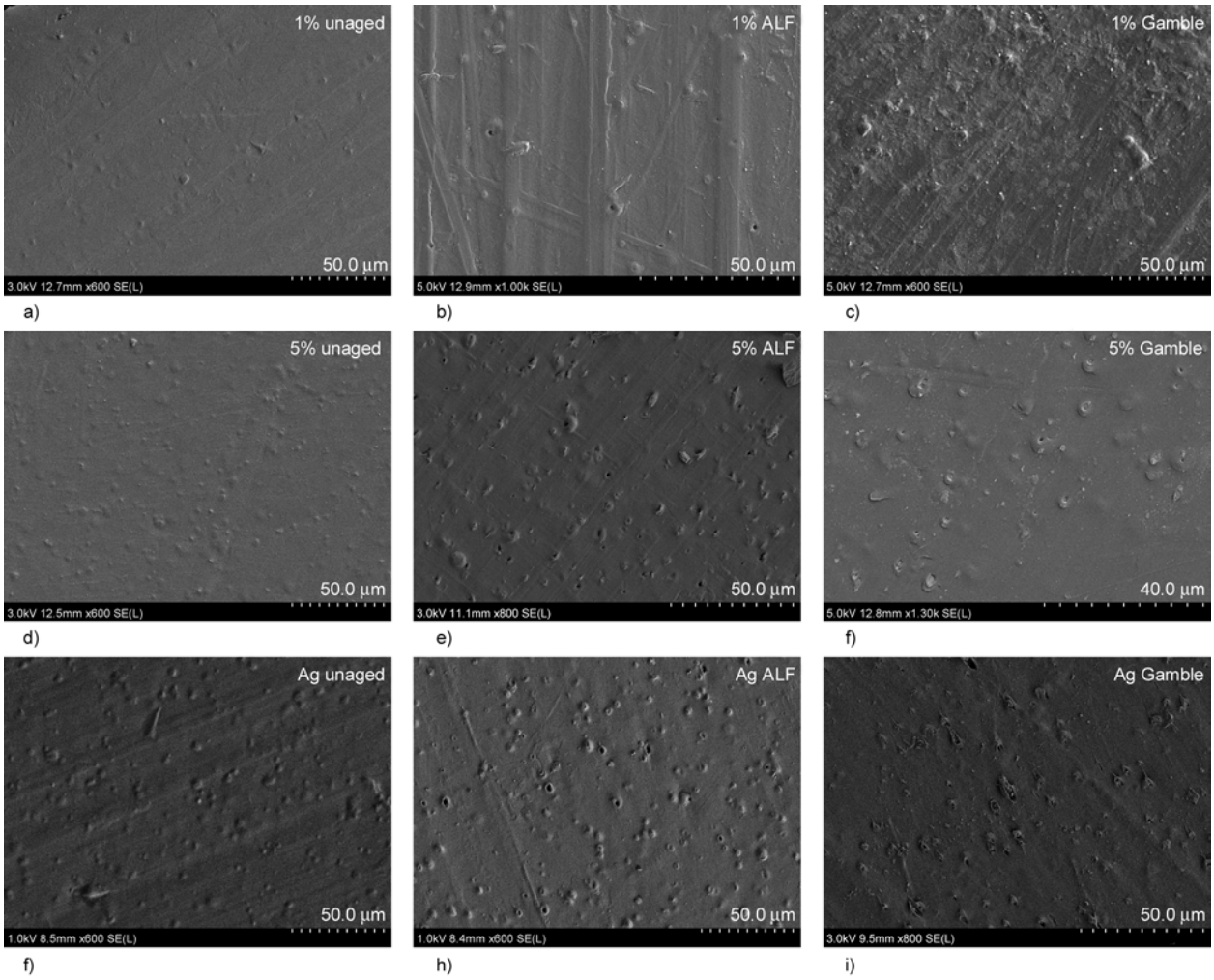

Figure 5. SEM micrographs of the surface of unaged, ALF and Gamble exposed 1% (a, b, c), 5% zeolite-PU (d, e, f) and silver filled zeolite-PU (g, h, i)

dimension of the holes is between 2–4 microns, it is probable that zeolite particles diffused out of the materials by leaving such a cavity behind. The highest amount of cavities was found on the surface of samples that contained Ag ions and 5% zeolite.

This can be explained with the high ion-exchange activity of silver in zeolites since it is known that silver exchanges easily with other ions in the environment. Therefore besides the concentration gradient, the high activity of silver may increased the diffusion of zeolite to the surface. This surface alteration was seen on non-silver containing composites and also on the surface of zeolite-PU composites that were not filled with any ions. This indicates that apart from the activity of the ion, the zeolite itself is capable to diffuse to the surface of the polymer and

migrate out in order to form equilibrium between the bulk and the environment.

In case of Gamble aged samples the previously mentioned cavities were found irregularly on the surface of different samples. Their shape differed from each other. In addition, high amount of salt remained on the surface after cleaning. The reason for this could be that the different salts from the Gamble solution interacted with the surface of the polymer and bonded to the surface structure or reacted with the ions of the zeolite on the surface and stuck there afterwards. This salt layer can highly influence the ion and zeolite release and the hyrophobicity of the composites.

3.4. *In-vitro* biocompatibility test

Contact angle measurements were performed on multi-ionic systems and on composites with increasing zeolite content. Figure 6 represents the contact angle change of the pure PU as the reference and ion-exchanged zeolite-PU samples as a function of exposure time in ALF (Figure 6a) and Gamble's solution (Figure 6b).

The contact angle of pure-PU slightly increased in the beginning and after 2 weeks it remained constant and did not change during the aging process in any of the solutions. This phenomenon is believed to be caused due to the interaction between the polymer surface and the aging solution and as a result hydrophobic groups formed on the surface.

Initially the contact angle of these materials started to increase similarly to the pure PU and reached a maximum value after 4–6 weeks. Then it started to decrease moderately and after 12 weeks exposure the contact angle of the samples aged in ALF solution decreased back to the initial contact angle or to a slightly lower value. This change in hydrophobicity was similar in case of the most ions; however the contact angle change of Cu containing sample showed similar characteristic to the pure PU. After it reached a maximum value, it remained constant through the whole duration of the experiment. In Gamble's solution similar change was observed, but after the contact angle reached the maximum value, a more intense decrease was seen and after 12 weeks the contact angle value of all samples became lower than the initial. By comparing the results of the different ions, the Zn and multi-ionic system Ag-Zn-Cu decreased the most, the contact angle of the surface became lower than 90° which is the value where a hydrophobic surface becomes hydrophilic. Based on the results it can be assumed that the change in contact angle as a function of exposure time was ion dependant.

In Figure 7, the contact angle change of samples with increasing zeolite content is presented as a function of exposure time. These samples didn't contain any ions. Few weeks after the immersion, the contact angle started to increase. This was seen before in case of multi-ionic samples. It reached a maximum value around 4–6 weeks and started to decrease intensively. Compared to the ion-filled zeolite-PU samples, the change of contact angle during the exposure was bigger in these samples that did not contain any ions. The different ions may influence the zeolites hygroscopic behaviour and water absorption as well. This contact angle decrease was slightly influenced by the zeolite content, and

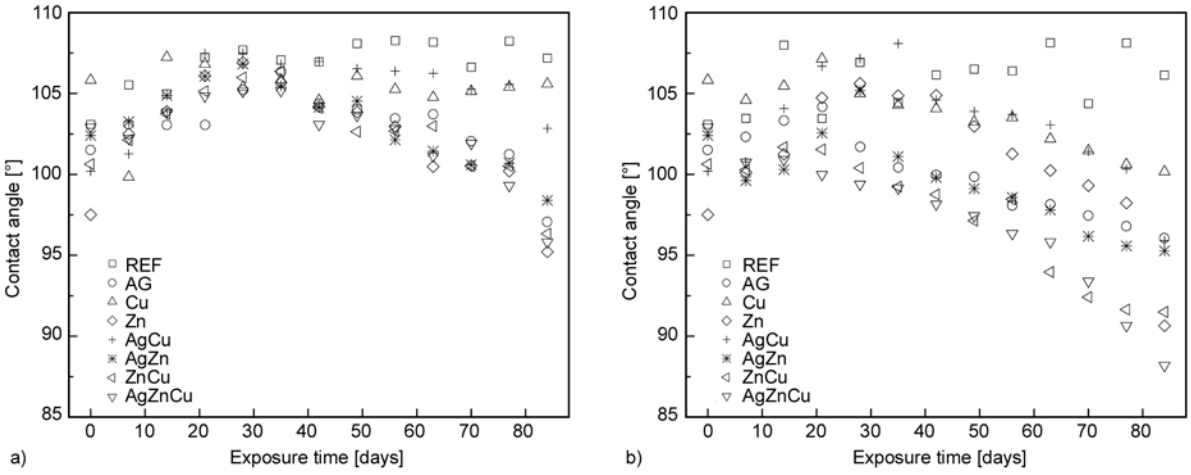

Figure 6. The contact angle change of different ionic PU-zeolite samples as a function of exposure time in ALF (a) and Gamble's solution (b)

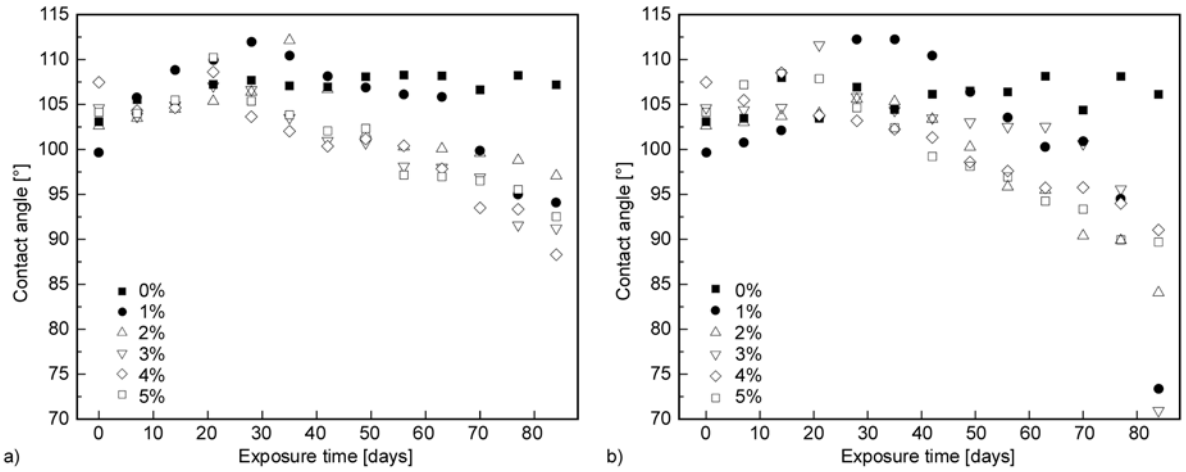

Figure 7. The contact angle change of PU-zeolite samples with increasing zeolite content as a function of exposure time in ALF (a) and Gamble's solution (b)

after 8 weeks exposure these values became lower than the initial and decreased significantly in the last period of the experiment. The contact angle of the samples decreased to slightly lower than 90° in ALF solution, which was observed in multi-ionic systems as well. In Gamble's solution the contact angle change was similar to ALF solution, however in the last weeks of the exposure the contact angle dropped significantly and decreased to 70–80 degrees in some cases.

PU absorbs moisture and zeolite is highly hygroscopic, it was shown that the water absorption of the zeolite-PU composites is increasing with the increased zeolite content. This water uptake is a reasonable explanation for the significant decrease in the contact angle, since more aging solution can reach the bulk and initiate degradation processes. However, for the initial contact angle increase, a change in the chemical structure of the surface can be a good explanation. In order to describe this phenomenon, FTIR analysis was performed on the samples weekly during the aging experiment. In Figure 8 the region of N-H (3445 cm^{-1}) and CH_2 (2854, 2933 cm^{-1}) stretching is presented. Up to 4–6 weeks of exposure the area of CH_2 increased in case of most of the samples and decreased afterwards. The most significant increase of CH_2 was observed on the FTIR spectrum of pure-PU. In addition the area of CH_2 for this sample remained constant after the initial increase. This region of CH_2 represents the bonds of polyether and cyclohexane and the increase indicates the formation of these compounds. It is known that cyclic alkanes are hydrophobic. This may be the reason for the initial contact angle increase in the samples. The formation of these compounds started right after one-week exposure and reached a maximum level within a few weeks. This observation matches well with the contact angle results of zeolite-PU samples, where the maximum value was also reached in 4 weeks and then a decreasing tendency was observed.

In addition, the peak at 1360 cm^{-1}, which corresponds to the wagging of CH_2 increased until 8 weeks and then started to decrease (Figure 9). After 10 weeks exposure the characteristic of the peak changed and started to form two different peaks. Besides CH_2, the formation of –OH groups was also detected in the region 3400–3600 cm^{-1}. In ALF solution this peak started to form after one week and increased slightly as a function time. The formation of –OH groups is a consequence of the water uptake and indicates oxidative degradation of the soft segment. The bond scission in the soft segment occurs on the methylene of the ether group by the formation of hydro-peroxide (3388 cm^{-1}) [3]. In Gamble solution apart from the pure PU the –OH peak broadened and formed an overlap with the N-H region after four weeks exposure. It is confirmed by the literature that the N-H region overlaps with the region of the –OH groups [2, 4, 31, 32]. This alteration of the FTIR spectrum indicates oxidative degradation and the formation of new hydrogen bonds [3, 5, 33]. During the oxidative degradation of the hard segment bond scission takes place on the urethane linkage, which indicates the broadening of the N-H region and is due to the formation of primary amines. In addition, since the carbonyl groups are attached to the N-H group by hydrogen bonds in the

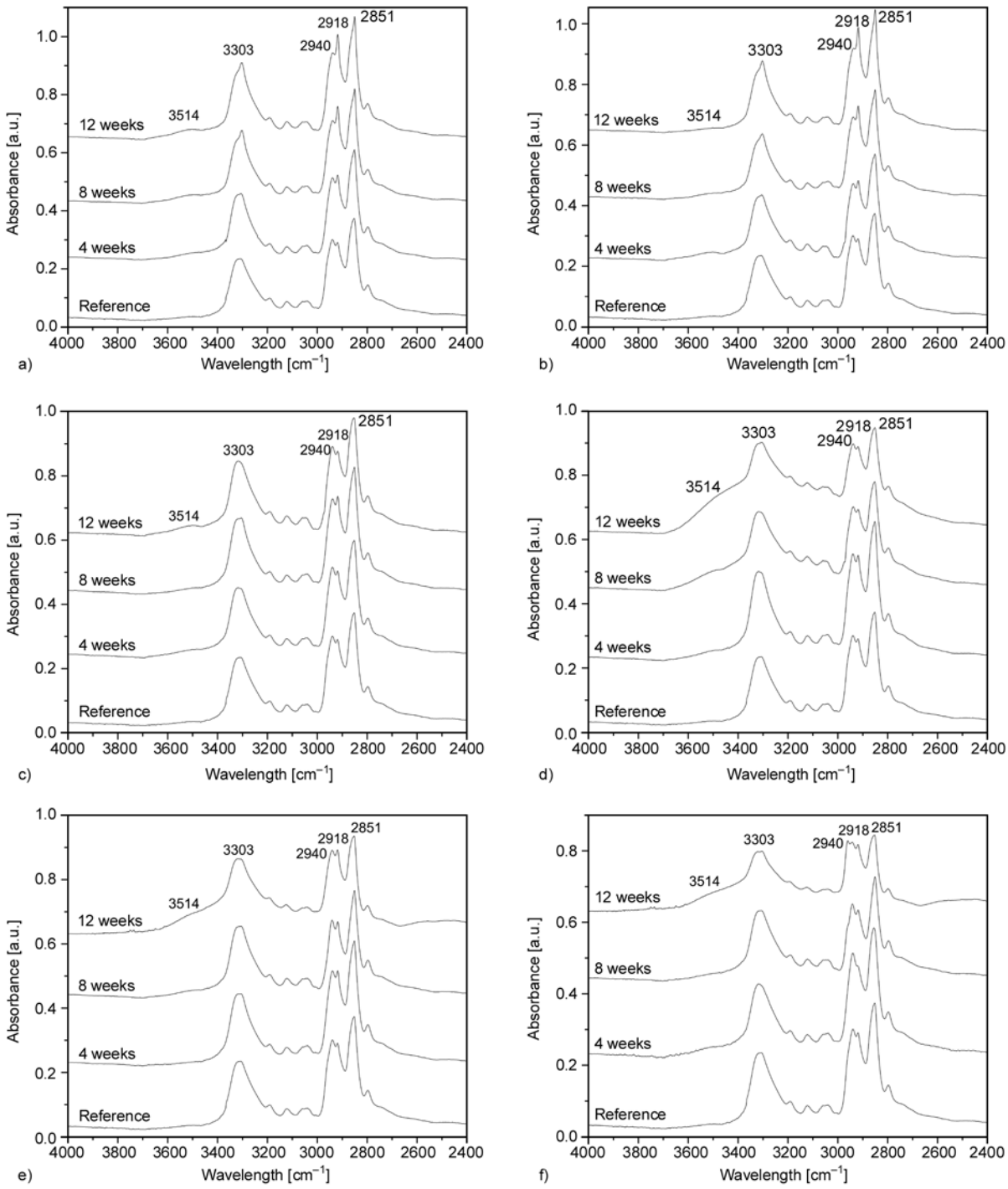

Figure 8. The FTIR spectrum of the N–H and CH_2 (4000–2400 cm^{-1}) region of pure PU (a–b), 1% (c–d) and 5% zeolite-PU (e–f) in ALF (a, c, e) and Gamble's solution (b, d, f)

polymers hard segment, the formed shoulder between the N-H and –OH group can also correspond to the increase of this bond. Since the N-H groups overlap with the –OH, the formation of hydrogen bonds can only be monitored by the carbonyl ratios.

The degradation of the hard segment was confirmed by the formation of a new small peak at 1637 cm^{-1} after 1 week exposure. This peak slightly increased as a function of exposure time. The peak is assigned to the free aromatic amine and correlated to the degradation of the hard segment [34]. Besides, in case of zeolite content higher than 3% in Gamble's solution the C–O–C asymmetric stretching of polyether (1103 and 1070 cm^{-1}), urethane (1017 cm^{-1}) and the asymmetric ring stretching of the cyclohexane increased significantly [3]. This gives evi-

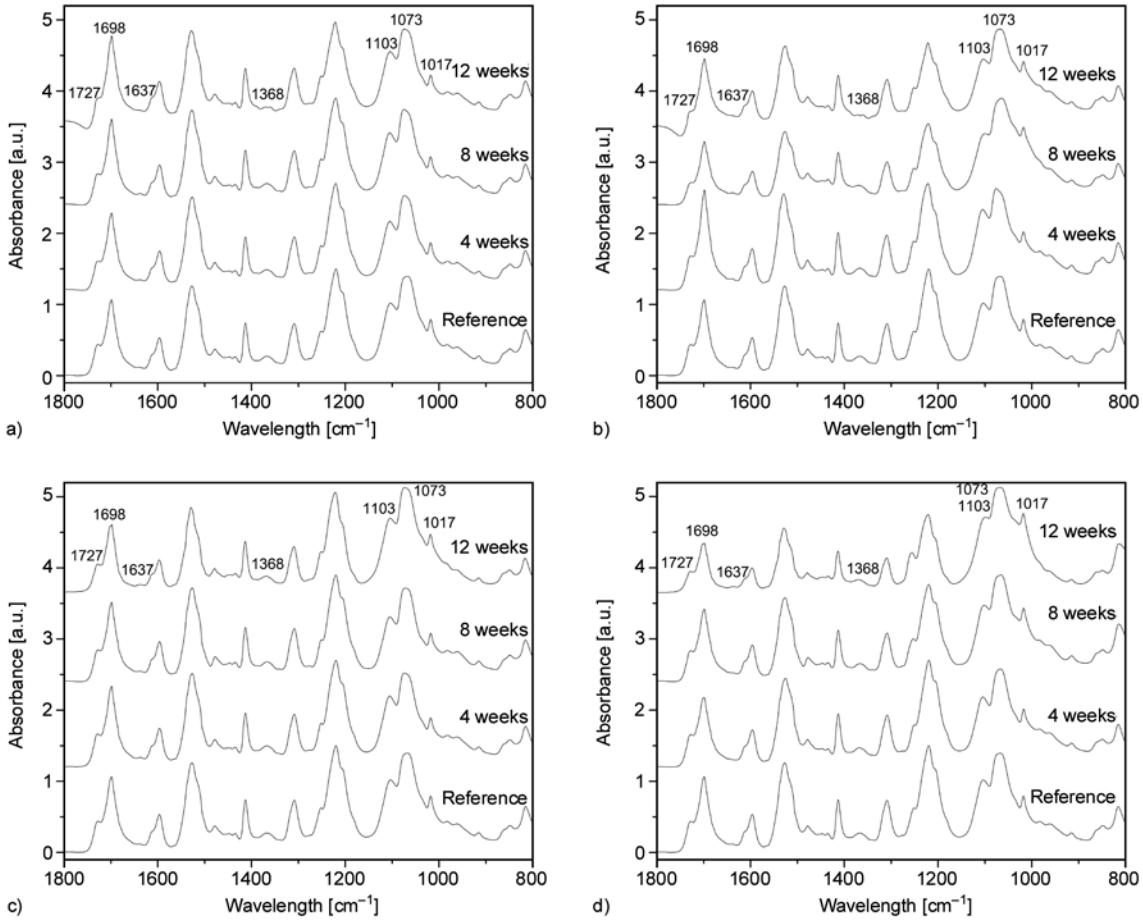

Figure 9. The FTIR spectrum of 1% (a–b) and 5% zeolite-PU (c–d) in ALF (a, c,) and Gamble's solution (b, d) in the region 1800–800 cm^{-1}

dence that oxidative degradation and bond scissions occurred in both the hard and soft segment with increased functionality of ether and aromatic groups. In general the intensity of this change in the chemical structure was the same for pure PU and zeolite-PU up to 3% zeolite. Above this amount more intense alteration of the FTIR spectrum was observed [4]. This is due to the increased solution uptake of the composites, which results an increased degradation rate. It was observed that the different ageing solutions caused the same type of degradation of the composites.

4. Conclusions

It can be concluded that the increasing zeolite content in the polymer resulted an increased water uptake and diffusion coefficient. This may influence the diffusion of the zeolite and the different ions within the polymer matrix. The antimicrobial tests showed that the efficiency of the silver ions is superior to the other single ionic systems. The binary and ternary ion-exchanged samples had similar antimicrobial efficiency. This is due to the ion release and the ion distribution in zeolite. In these systems the different ions may block each others` way that influences the ion release and therefore the antimicrobial properties.

During the ageing of the polymer composites, significant surface changes were observed. The surface of the samples became rough and small holes were detected. These holes were formed due to the zeolite that diffused out of the matrix.

Besides topography, changes in the contact angle first showed increasing tendency up to a couple of weeks and then decreased. This change is thought to be due to the degradation and the complex chemical changes in the structure. The FTIR results confirmed that chemical changes occurred in the materials during exposure to both ALF and Gamble's solutions. It was confirmed that oxidative degradation of the hard and soft segment of PU occurred during the in vitro exposure. In addition the forma-

tion of hydrogen linkages and small amount of cross-linking was also observed as a result of the degradation. The zeolite content has shown to have an influence on the degradation in case of both aging solutions. This can be linked to the increased solution uptake of the composites.

Acknowledgements

The authors acknowledge the Hungarian National Public Health and Medical Officer Service for providing microorganism strains, laboratory and the necessary equipment. For supplying the medical grade polyether polyurethane and valuable discussion on the direction of the current study, Dr. Ralf Schnell and Tracoe medical GmbH is acknowledged. The financial support given by VR and KTH to Peter Kaali is also gratefully acknowledged.

References

[1] Akmal N., Usmani A. M.: An overview of medical polymers and diagnostic reagents. Polymers in Sensors. ACS Symposium Series, **690**, 2–23 (1998).
DOI: 10.1021/bk-1998-0690.ch001

[2] Frautschi J. R., Chinn J. A., Phillips R. E., Zhao Q. H., Anderson J. M., Joshi R., Levy R. J.: Degradation of polyurethanes in vitro and in vitro: Comparison of different models. Colloids and Surfaces B: Biointerfaces, **1**, 305–313 (1993).
DOI: 10.1016/0927-7765(93)80005-J

[3] Guignot C., Betz N., Legendre B., Le Moel A., Yagoubi N.: Degradation of segmented poly(etherurethane) Tecoflex® induced by electron beam irradiation: Characterization and evaluation. Nuclear Instruments and Methods in Physics Research Section B: Beam Interactions with Materials and Atoms, **185**, 100–107 (2001).
DOI: 10.1016/S0168-583X(01)00850-3

[4] Ravat B., Grivet M., Grohens Y., Chambaudet A.: Electron irradiation of polyesterurethane: Study of chemical and structural modifications using FTIR, UV spectroscopy and GPC. Radiation Measurements, **34**, 31–36 (2001).
DOI: 10.1016/S1350-4487(01)00116-0

[5] Sarkar D., Lopina S. T.: Oxidative and enzymatic degradations of L-tyrosine based polyurethanes. Polymer Degradation and Stability, **92**, 1994–2004 (2007).
DOI: 10.1016/j.polymdegradstab.2007.08.003

[6] Skaja A., Fernando D., Croll S.: Mechanical property changes and degradation during accelerated weathering of polyester-urethane coatings. Journal of Coatings Technology and Research, **3**, 41–51 (2006).
DOI: 10.1007/s11998-006-0004-7

[7] O'Toole G., Kaplan H. B., Kolter R.: Biofilm formation as microbial development. Annual Review of Microbiology, **54**, 49–79 (2000).
DOI: 10.1146/annurev.micro.54.1.49

[8] Denyer S. P., Hanlon G. W., Davies M. C.: Mechanisms of microbial adherence. in 'Microbial biofilms: Formation and control' (eds.: Denyer S. P., Gorman S. P., Sussman M.) Blackwell Scientific Publications, Cambridge, 13–27 (1993).

[9] Dowling D. P., Betts A. J., Pope C., McConnell M. L., Eloy R., Arnaud M. N.: Anti-bacterial silver coatings exhibiting enhanced activity through the addition of platinum. Surface and Coatings Technology, **163–164**, 637–640 (2003).
DOI: 10.1016/S0257-8972(02)00689-8

[10] Fang M., Chen J-H., Xu X-L., Yang P-H., Hildebrand H. F.: Antibacterial activities of inorganic agents on six bacteria associated with oral infections by two susceptibility tests. International Journal of Antimicrobial Agents, **27**, 513–517 (2006).
DOI: 10.1016/j.ijantimicag.2006.01.008

[11] Furno F., Morley K. S., Wong B., Sharp B. L., Arnold P. L., Howdle S. M., Bayston R., Brown P. D., Winship P. D., Reid H. J.: Silver nanoparticles and polymeric medical devices: A new approach to prevention of infection? Journal of Antimicrobial Chemotherapy, **54**, 1019–1024 (2004).
DOI: 10.1093/jac/dkh478

[12] Hanna H. A., Raad I. I., Hackett B., Wallace S. K., Price K. J., Coyle D. E., Parmley C. L.: Antibiotic-impregnated catheters associated with significant decrease in nosocomial and multidrug-resistant bacteremias in critically ill patients. Chest, **124**, 1030–1038 (2003).
DOI: 10.1378/chest.124.3.1030

[13] Jain P., Pradeep T.: Potential of silver nanoparticle-coated polyurethane foam as an antibacterial water filter. Biotechnology and Bioengineering, **90**, 59–63 (2005).
DOI: 10.1002/bit.20368

[14] Clement J. L., Jarrett P. S.: Antibacterial silver. Metal-Based Drugs, **1**, 467–482 (1994).

[15] Schierholz J. M., Lucas L. J., Rump A., Pulverer G.: Efficacy of silver-coated medical devices. Journal of Hospital Infection, **40**, 257–262 (1998).
DOI: 10.1016/S0195-6701(98)90301-2

[16] Böswald M., Mende K., Bernschneider W., Bonakdar S., Ruder H., Kissler H., Sieber E., Guggenbichler J-P.: Biocompatibility testing of a new silver-impregnated catheter in vivo. Infection, Supplement, **27**, S38–S42 (1999).
DOI: 10.1007/BF02561616

[17] Paterson D. L., Bach A., Maury E., Offenstadt G., Yasukawa T., Fujita Y., Sari A., Darouiche R. O., Raad I. I.: Antimicrobial-impregnated central venous catheters. The New England Journal of Medicine, **340**, 1761–1762 (1999).
DOI: 10.1056/nejm199906033402212

[18] Crabtree J. H., Burchette R. J., Siddiqi R. A., Huen I. T., Hadnott L. T., Fishman A.: The efficacy of silver-ion implanted catheters in reducing peritoneal dialysis-related infections. Peritoneal Dialysis International, **23**, 368–374 (2003).

[19] Furno F., Morley K. S., Wong B., Sharp B. L., Arnold P. L., Howdle S. M., Bayston R., Brown P. D., Winship P. D., Reid H. J.: Silver nanoparticles and polymeric medical devices: A new approach to prevention of infection? Journal of Antimicrobial Chemotheraphy, **54**, 1019–1024 (2004).
DOI: 10.1093/jac/dkh478

[20] Walder B., Pittet D., Tramèr M.: Prevention of bloodstream infections with central venous catheters treated with anti-infective agents depends on catheter type and insertion time: Evidence from a meta-analysis. Infection Control and Hospital Epidemiology, **23**, 748–756 (2002).
DOI: 10.1086/502005

[21] Zhang Y., Zhong S., Zhang M., Lin Y.: Antibacterial activity of silver-loaded zeolite A prepared by a fast microwave-loading method. Journal of Materials Science, **44**, 457–462 (2009).
DOI: 10.1007/s10853-008-3129-5

[22] Kawahara K., Tsuruda K., Morishita M., Uchida M.: Antibacterial effect of silver-zeolite on oral bacteria under anaerobic conditions. Dental Materials, **16**, 452–455 (2000).
DOI: 10.1016/S0109-5641(00)00050-6

[23] Inoue Y., Hoshino M., Takahashi H., Noguchi T., Murata T., Kanzaki Y., Hamashima H., Sasatsu M.: Bactericidal activity of Ag–zeolite mediated by reactive oxygen species under aerated conditions. Journal of Inorganic Biochemistry, **92**, 37–42 (2002).
DOI: 10.1016/S0162-0134(02)00489-0

[24] Goldman M., Gronsky R., Long G. G., Pruitt L.: The effects of hydrogen peroxide and sterilization on the structure of ultra high molecular weight polyethylene. Polymer Degradation and Stability, **62**, 97–104 (1998).
DOI: 10.1016/S0141-3910(97)00265-6

[25] Bracco P., Brunella V., Luda M. P., Brach del Prever E. M., Zanetti M., Costa L.: Oxidation behaviour in prosthetic UHMWPE components sterilised with high-energy radiation in the presence of oxygen. Polymer Degradation and Stability, **91**, 3057–3064 (2006).
DOI: 10.1016/j.polymdegradstab.2006.08.002

[26] Pehlivan H., Balköse D., Ülkü S., Tihminlioğlu F.: Characterization of pure and silver exchanged natural zeolite filled polypropylene composite films. Composites Science and Technology, **65**, 2049–2058 (2005).
DOI: 10.1016/j.compscitech.2005.04.011

[27] Kamışoğlu K., Aksoy E. A., Akata B., Hasirci N., Baç N.: Preparation and characterization of antibacterial zeolite–polyurethane composites. Journal of Applied Polymer Science, **110**, 2854–2861 (2008).
DOI: 10.1002/app.28838

[28] Haugen H. J., Brunner M., Pellkofer F., Aigner J., Will J., Wintermantel E.: Effect of different γ-irradiation doses on cytotoxicity and material properties of porous polyether-urethane polymer. Journal of Biomedical Materials Research Part B: Applied Biomaterials, **80**, 415–423 (2007).
DOI: 10.1002/jbm.b.30612

[29] Herting G., Odnevall Wallinder I., Leygraf C.: Metal release from various grades of stainless steel exposed to synthetic body fluids. Corrosion Science, **49**, 103–111 (2007).
DOI: 10.1016/j.corsci.2006.05.008

[30] Midander K., Odnevall Wallinder I., Leygraf C.: In vitro studies of copper release from powder particles in synthetic biological media. Environmental Pollution, **145**, 51–59 (2007).
DOI: 10.1016/j.envpol.2006.03.041

[31] Rehman I., Andrews E. H., Smith R.: In vitro degradation of poly(ester-urethanes) for biomedical applications. Journal of Materials Science: Materials in Medicine, **7**, 17–20 (1996).
DOI: 10.1007/BF00121184

[32] McCarthy S. J., Meijs G. F., Mitchell N., Gunatillake P. A., Heath G., Brandwood A., Schindhelm K.: *In-vivo* degradation of polyurethanes: Transmission-FTIR microscopic characterization of polyurethanes sectioned by cryomicrotomy. Biomaterials, **18**, 1387–1409 (1997).
DOI: 10.1016/S0142-9612(97)00083-5

[33] Santerre J. P., Labow R. S., Adams G. A.: Enzyme-biomaterial interactions: Effect of biosystems on degradation of polyurethanes. Journal of Biomedical Materials Research, **27**, 97–109 (1993).
DOI: 10.1002/jbm.820270113

[34] Gilding D. K., Reed A. M., Baskett S. A.: Ethylene oxide sterilization: Effect of polymer structure and sterilization conditions on residue levels. Biomaterials, **1**, 145–148 (1980).

eXPRESS Polymer Letters Vol.5, No.12 (2011) 1041–1049
Available online at www.expresspolymlett.com
DOI: 10.3144/expresspolymlett.2011.102

Microstructure and magneto-dielectric properties of the chitosan/gelatin-YIG biocomposites

E. J. J. Mallmann[1], J. C. Góes[2], S. D. Figueiró[2], N. M. P. S. Ricardo[3], J. C. Denardin[4], A. S. B. Sombra[2], F. J. N. Maia[3], S. E. Mazzeto[3], P. B. A. Fechine[1]*

[1]Grupo de Química de Materiais Avançados (GQMAT)- Departamento de Química Analítica e Físico-Química, Universidade Federal do Ceará – UFC, Campus do Pici, CP 12100, CEP 60451-970 Fortaleza – CE, Brazil
[2]Laboratório de Telecomunicações e Ciência e Engenharia dos Materiais -(LOCEM) - Departamento de Física, Universidade Federal do Ceará – UFC, Campus do Pici, CP 12100, CEP 60451-970 Fortaleza – CE, Brazil
[3]Laboratório de Produtos e Tecnologia em Processos (LPT), Departamento de Química Orgânica e Inorgânica, Universidade Federal do Ceará – UFC, Campus do Pici, CP 12100, CEP 60451-970 Fortaleza - CE, Brazil
[4]Departamento de Física, Universidad de Santiago de Chile, USACH, Av. Ecuador 3493, Santiago, Chile

Received 24 March 2011; accepted in revised form 16 June 2011

Abstract. This work is devoted to the preparation of yttrium iron garnet (YIG) ferrimagnetic biocomposites based in biodegradable chitosan and gelatin. The aim was to produce composite films containing controlled amounts of YIG to obtain a new biological material with magneto-dielectric features. Structural characterization of the biocomposites was made by scanning electron microscopy, X-ray diffraction, infrared absorption spectroscopy and thermal analysis, while the dielectric and magnetic properties were obtained from dielectric spectroscopy and magnetic hysteresis loops, respectively. The versatility of the films obtained makes them possible candidates for use as biomaterials or electronic device.

Keywords: *biocomposites, chitosan, gelatin, yttrium iron garne*

1. Introduction

There are a lot of researches about association of the magnetic ceramics with biological material. Kim *et al.* [1] have obtained microspheres of Fe_3O_4 encapsulated with chitosan as a MRI image contrast, while Jain *et al.* [2] obtained magnetic nanoparticles coated with Oleic-Pluronic for sustained delivery of cancer agents. Matsumine *et al.* [3] have developed a novel hyperthermic treatment modality using magnetic materials (calcium phosphate cement containing Fe_3O_4) for metastatic bone tumors. In this sense, biological molecules are important to begin the magnetic component in a bio-inert composite.

Chitosan is obtained from partial deacetylation of chitin. It is a very interesting polysaccharide which can be widely chemically modified on its amino and hydroxyl groups. It is promising in plastic products in the medical and food fields, due to the fact that it is a biodegradable, versatile and biocompatible polymer. The use of chitosan and its association to other materials to obtain biocomposites is widely shown in literature [4–8]. On the other hand, gelatin is a protein extracted from collagen. It is water soluble, also biodegradable and extremely biocompatible. Chitosan-gelatin blends are very interesting polymers, since a mixture of both does not result in a loss of their individual properties [9–13].

Yttrium iron garnet (YIG – $Y_3Fe_5O_{12}$) is a ferrimagnetic particle that belongs to a family of complex oxides, the garnet. They are part of a family of materials that exhibit characteristic magnetic behavior. Their magnetic properties depend on the composi-

*Corresponding author, e-mail: fechine@ufc.br

tion (presence of magnetic ions), the crystal structure (the three-dimensional geometric arrangement of the ions) and temperature. These oxides have unique magnetic properties, magneto-optical, thermal, electrical and mechanical as well as ferrimagnetism, excellent resistance to radiation damage, high thermal conductivity, high electrical resistivity, controllable saturation magnetization and moderate thermal expansion coefficient [14–16].

Results about properties of the collagen/YIG biocomposite films were presented in previous studies [17]. In this work, a novel magnetic biocomposite with magneto-dielectric properties was obtained from chitosan and gelatin as polymeric matrix, cross-linked with glutaraldehyde and YIG as ferrimagnetic phase. Thus, the polymeric matrix was changed and the experimental procedures were improved to obtain a better quality of the biocomposites. These changes increased the YIG homogenate in biological matrix and modified the magnetic-dielectric behavior. The structural, dielectric and magnetic properties were investigated to characterize the material, applying techniques such as infrared spectroscopy, X-ray diffraction, scanning electron microscopy, thermogravimetric analysis, differential scanning calorimetry, dielectric and magnetic measurements.

2. Material and methods

2.1. Ferrimagnetic particle

The preparation of the ferrimagnetic particles was made reacting iron and yttrium oxides, where stoichiometric amount of Y_2O_3 (99.99%, Aldrich) and Fe_2O_3 (99.00%, Sigma-Aldrich, St. Louis, MO, USA) were used in the YIG preparation. The material was grounded on a Fritsch Pulverisette 6 (Fristsch GmbH, Idar-Oberstein, Germany) planetary mill in sealed stainless steel vials (221.69 cm^3) and balls (ø10 mm) under air in weight ratio 1/9 (wt. of mixture powder/wt. of balls). Mechanical alloying was performed for 1 h of milling with 370 rpm. After this, the powder was submitted to calcination in air at 1150°C for 5 h. The reaction occurring during calcination can be summarized as per Equation (1):

$$3Y_2O_{3(s)} + 5Fe_2O_{3(s)} \rightarrow 2Y_3Fe_5O_{12(s)}\ (YIG) \qquad (1)$$

2.2. Chitosan and gelatin solutions

Chitosan (PADETEC Fortaleza-Ceará-Brazil, DD = 80%) and gelatin (99.00%, VETEC, Xerém – Duque de Caxias – RJ) were dissolved into a 2% v/v acetic acid solution and centrifuged for 30 min at 900 rpm until complete dissolution to obtain a 2% w/v solution of each one. Both solutions were mixed in a 1:1 proportion and centrifuged for 15 min at 5000 rpm to obtain the chitosan-gelatin solution.

2.3. Preparation of chitosan-gelatin-YIG films

The YIG powder was dispersed in 50 ml of chitosan-gelatin solution using a glass rod. The amount of YIG used was 250 mg and 500 mg, respectively. A total of ten samples were prepared, where eight of those were cross-linked by 0.1% and 0.025% v/v glutaraldehyde (VETEC). The homogeneous emulsions were formatted into an acrylic mould and dried into a refrigerator. The samples were labeled as F, $FG_{0.1}$, $FG_{0.025}$, FY_{25}, $FG_{0.1}Y_{25}$, $FG_{0.025}Y_{25}$, FY_{50}, $FG_{0.1}Y_{50}$ and $FG_{0.025}Y_{50}$, where FG_aY_b can be read as F = film, G = glutaraldehyde, Y = YIG and a = glutaraldehyde concentration [%] and b = YIG weight used during the preparation (250 and 500 mg), as shown in Table 1. The effective YIG concentration on each composite was obtained by the relation between the residual and initial weight. The film thickness was measured using a Micrometer (Model 549E, Testing Machines Inc, Mineola, LI, NY). The thickness measurements were taken at ten different points along the gauge length of each specimen and the meaningful values were taken.

Table 1. Composition and nomenclature of the samples

%G	V_G mL]	W_G [mg]	F/G	Sample	
				$YIG_{(500\ mg)}$	$YIG_{(250\ mg)}$
0.0	–	–	0	FY_{50}	FY_{25}
0.1	0.20	50	20:1	$FG_{0.1}Y_{50}$	$FG_{0.1}Y_{25}$
0.075	0.15	37.5	26.6:1	$FG_{0.075}Y_{50}$	$FG_{0.075}Y_{25}$
0.050	0.10	25	40:1	$FG_{0.050}Y_{50}$	$FG_{0.050}Y_{25}$
0.025	0.05	12.5	80:1	$FG_{0.025}Y_{50}$	$FG_{0.025}Y_{25}$

G = glutaraldehyde; V_G = glutaraldehyde volume; W_G = glutaraldehyde weight; F = chitosan-gelatin 1:1 film; F/G = ratio of film/glutaraldehyde weight; Y = YIG

2.4. Scanning electron microscopy

Micrographs of magnetic biocomposites were obtained by scanning electron microscope (SEM) (Vega XMU/Tescan, Bruker (Billerica, MA, USA)),

operating with bunches of primary electrons ranging from 12 to 30 keV of 5.0 mm × 5.0 mm square samples. The samples were covered with a 90 nm gold powder layer.

2.5. X-ray diffraction

A Rigaku (Tokyo, Japan) X-ray powder diffractometer operating on 40 kV/30 mA with a Cu-$K_{\alpha I}$ tube (λ = 1.54056 Å) was used to obtain the X-ray diffraction pattern of the ferrimagnetic biocomposites. The diffraction patterns were carried out using Bragg-Brentano geometry in continuous mode with speed of 0.5°/min and step size of 0.02° (2θ) in the angular range 20–60° (2θ).

2.6. FT-IR spectroscopy

Infrared (IR) spectra were recorded using a VERTEX 70 (BRUKER, Billerica, MA, USA) spectrophotometer. The samples were prepared be freezing at liquid nitrogen and mixing with KBr pastilles. The region analyzed was between 400–1800 cm^{-1}.

2.7. Thermogravimetric analysis

Thermogravimetric analyses (TGA) were performed using a Mettler Toledo (Zürich, Switzerland) TGA/SDTA851^e, equipped with a micro-balance. The rate was 10ºC/min (50 ml/min flow) in a dynamic N_2 atmosphere. Each sample was sealed in an aluminum pan and heated from 25 to 900ºC temperatures.

2.8. Differential scanning calorimetry

Differential scanning calorimetry was carried out using NETZSCH (Selb, Germany) DSC 204 F1Phoenix® equipment. Accurately weighed 5 mg dried material was placed in an aluminum cup and hermetically sealed. An empty cup was used as reference. Samples were analyzed under continuous flow of dry nitrogen gas at a heating rate of 10°C·min^{-1} from 25 to about 300°C.

2.9. Dielectric and magnetic measurements

Dielectric measurements: real (ε'_r) parts of relative permittivity and loss tangent ($\tan\delta = \varepsilon''_r/\varepsilon'_r$) were performed using an Agilent (Santa Clara, CA, USA) 4991A RF impedance material analyzer. It covered the region of 10 MHz–1GHz at room temperature (300 K). The magnetization measurements were performed at room temperature with a magnetometer VSM (vibrating sample magnetometer) previously calibrated with Ni wire. The magnitude of magnetization was given in emu/g.

3. Results and discussion

The SEM was performed to investigate the interaction between the polymeric matrix and the ceramic. The samples FY_{25}, $FG_{0.1}Y_{25}$, FY_{50} and $FG_{0.1}Y_{50}$ were chosen to represent the behavior of all the system and they are shown in Figures 1a and b, and Figures 2a and b, respectively. The amount of YIG present in series prepared with 500 mg of YIG is higher than the 250 mg ones, as revealed in Figures 1a and 2a, and as shown in thermogravimetric analysis. It is possible to observe that the polymeric matrix in 250 mg series is larger, and the grains are deeply encapsulated on it, while in 500 mg series the amount of YIG particles is outside the membrane. When the blend received the glutaraldehyde treatment, the YIG particles were encapsulated by polymeric matrix, and YIG was found only in cer-

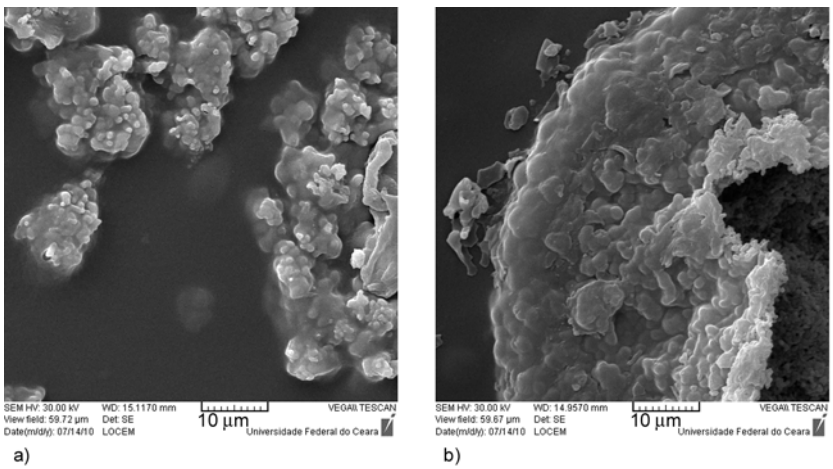

Figure 1. Scanning electron photomicrograph of FY_{25} (a) and $FG_{0.1}Y_{25}$ (b) at 2500×

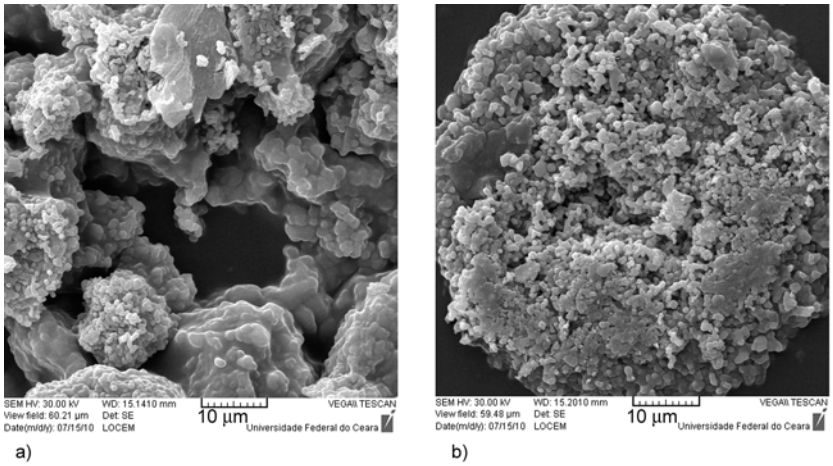

Figure 2. Scanning electron photomicrograph of FY_{50} (a) and $FG_{0.1}Y_{50}$ (b) at 2500×

tain places, causing an extrusion within the composite, as shown in Figures 1b and 2b.

Figure 3 shows the XRD patterns of the samples F (only chitosan and gelatin), FY_{25}, FY_{50} and YIG. The crystalline phase obtained from the YIG powder was identified by comparing the diffractograms from the ICDD database (ICDD/PDF–70-0953), see Figure 3. One can observe in F sample an amorphous phase characteristic to the matrix polymer and this pattern follows those observed in the literature [18–22]. This behavior is present in all composites, see FY_{25} and FY_{50} (Figure 3). The broad peak in composites at $2\theta = 32.2°$ happened due to the association of the chitosan-gelatin with YIG particles. When we observe the composites containing YIG, some peaks appears to be dislocated, according to Figure 3. The peak of YIG crystal at $2\theta = 28.9°$ is increased when compared to others. While some peaks appear enlarged due to the alignment of their plane with the polymer, others showed an attenuation of their intensity due to a non-alignment plane with the organic phase that scatters X-rays, where the crystalline phase had reduced the intensity of its peak. The peaks in $2\theta = 28.9$, 45.16 and 51.12° were shifted when observed in the composite. These displacements are due to the fact that the sample is not completely flat and there was the influence of conformation on the incidence of X-rays in the region between $2\theta = 28.9$ and 51.12.

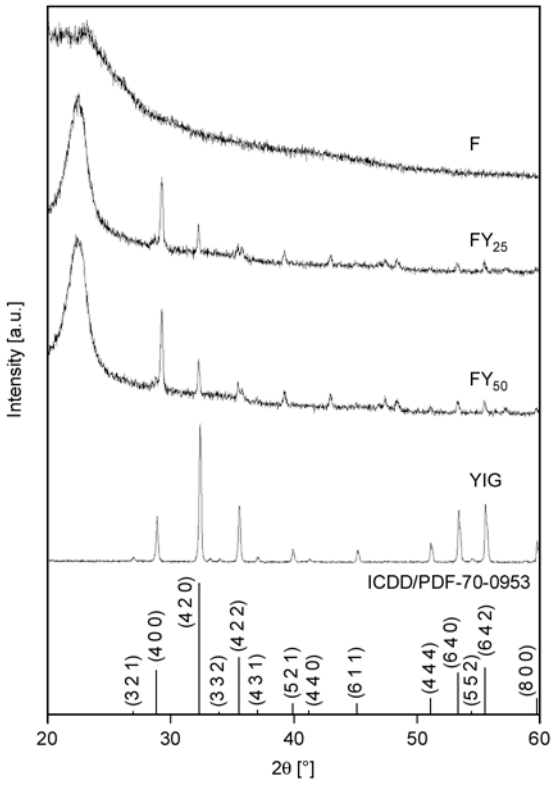

Figure 3. XRPD patterns of the ferrimagnetic phase (YIG), F and their composites (FY_{25} and FY_{50})

The IR spectrum of the F, $FG_{0.1}$ and FY_{50} samples are illustrated in Figure 4. One can observe an absorption band in the region of 1641–1630 cm^{-1}, characteristic of the stretching of the C=O group of acetamide of chitosan, which characterizes its partial deacetylation. It is likely that the band on the imine bond (C=N), formed from the cross-linking with glutaraldehyde, is superimposed on the C=O group of chitosan acetamide, since both absorb in the same region of the infrared spectrum. The band shown at 1544–1537 cm^{-1} refers to the C–N bond (amide II), whereas in 1238 cm^{-1} there is a characteristic absorption band of the C–N bond of amide III. Both bands are referred to peptide bonds of gelatin. The absorption band at 1400 cm^{-1} existing features the C–N bond of proline, amino acid of gelatin. In

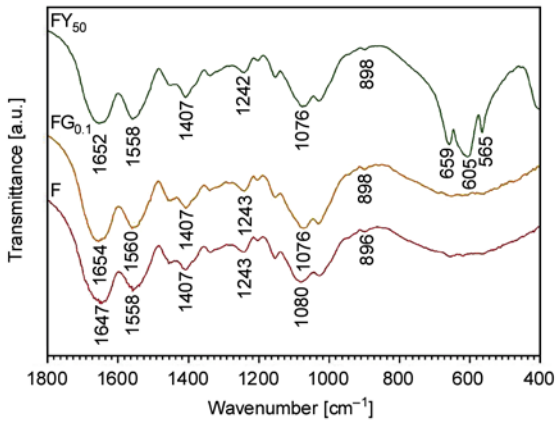

Figure 4. Infrared spectroscopy of the F, $FG_{0.1}$ and FY_{50} composites

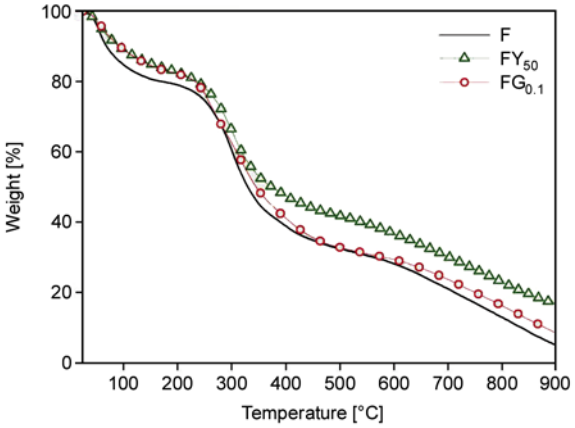

Figure 5. Thermogravimetric analysis of F, $FG_{0.1}$ and FY_{50} composites

1072–1062 cm^{-1} there is an absorption band which is typical of stretch of the connecting piranosydic rings of chitosan (C–O–C). The region of 1200–800 cm^{-1} shows characteristic absorption bands of saccharides structures. The YIG is characterized by absorption bands exist at 565, 605 and 659 cm^{-1}. These bands are assigned to Fe–O bonds. The bands obtained in the analysis were conferred with the literature data [23–27] and are shown in Table 2.

Table 2. Infrared wavenumbers and assignments

Sample	Wavenumbers [cm^{-1}]	Assignments
F	1647	υ (–C=O)
	1558	υ (–NHC=O)
	1407	υ (–C–N)
	1243	υ ($–NH_2$)
	1080	.υ (–C-OH)
	896	σ (–CH)
$FG_{0.1}$	1654	υ (–C=O)
	1560	υ (–NHC=O)
	1407	υ (–C–N)
	1243	υ ($–NH_2$)
	1076	.υ (–C–OH)
	898	σ (–CH)
FY_{25}	1652	υ (–C=O)
	1558	υ (–NHC=O)
	1407	υ (–C–N)
	1242	υ ($–NH_2$)
	1076	.υ (–C–OH)
	898	σ (–CH)
	659	υ (Fe–O)
	605	υ (Fe–O)
	565	υ (Fe–O)

The thermogravimetric analysis was performed to obtain the degradation profile of samples as well as to identify the mass of residual YIG and help to explain the dielectric and magnetic results. Figure 5 shows the degradation curves while Table 3 illustrates the events of degradation for the samples. The mass of each sample was fixed in 5.00 mg. Three samples were chosen: the composite without YIG and glutaraldehyde (F), the one without YIG and cross-linked with glutaraldehyde 0.1% ($FG_{0.1}$) and the sample containing 500 mg of YIG. Samples cross-linked with 0.1% glutaraldehyde had more waste (0.429 mg) compared to non cross-linked that left 0.254 mg, as well as those containing a greater mass of YIG on its constitution also left a larger residual mass according to the values shown in Table 3. The higher residue in FY_{50}, 0.843 mg is attributed to the presence of ceramic in the composite, which is more resistant to the thermal treatment than other films, according the Table 3, where the events of degradation show the higher intervals, 25–181°C as first event and started at 247°C on second event. Comparing the two samples without YIG, the sample cross-linked with glutaraldehyde left more residues than F sample, because of the larger

Table 3. Samples degradation events

Sample	1st event			2nd event		M^R	M
	M^I	T^G	W^L	T^G	W^L		
F	5.0	25–177	20.23	201–452	43.76	5.08	0.254
$FG_{0.1}$	5.0	25–173	16.80	201–472	48.21	8.58	0.429
FY_{50}	5.0	25–181	16.49	247–497	36.04	16.87	0.843

M^I – initial mass [mg)], W^L – weight loss [%], T^G – event temperature gap [°C], M^R – mass residues [%] and M – mass residues [mg]

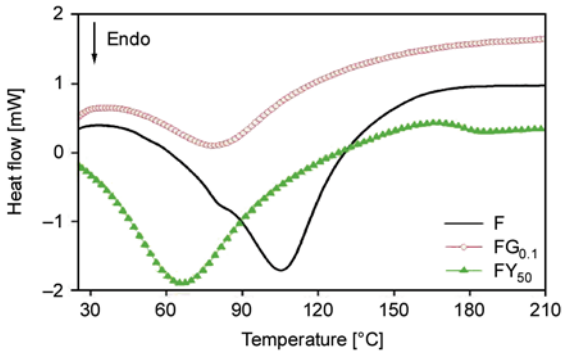

Figure 6. Differential scanning calorimetry of F, $FG_{0.1}$ and FY_{50} composites

chains formed by incorporation of the aldehyde into the gelatin-chitosan composite.

The DSC scans in Figure 6 show that polymeric matrix of all samples is characterized by an endothermic peak. It is due to the denaturation process of gelatin and chitosan molecules and it is hydration dependant. For chitosan-gelatin film, the denaturation temperature is 105.4°C. When it is crosslinked with glutaraldehyde, $FG_{0.1}$, the temperature decreases to 78.5°C, but the lower denaturation temperature is observed at 65.01°C, in the FY_{50} sample. These results show that YIG addition decreases considerably the thermal stability of the polymeric matrix, while $FG_{0.1}$ shows a slight decrease, comparing to the F sample. These results may be related to the shrinkage of the chitosan-gelatin matrix that is observed macroscopically.

The obtained data from dielectric spectroscopy are shown in Figure 7. The values of ε'_r decreased with the increase of frequency. Table 4 illustrates dielectric properties at 10, 100 and 1000 MHz frequencies. The sample $FG_{0.1}$ showed the higher ε'_r values, while $FG_{0.025}Y_{50}$ the lower. The samples without YIG had shown the higher ε'_r values, which are higher values than polymeric compounds in literature [28–31]. According to Fechine *et al.* [32], YIG has ε'_r near to 7.6 at 10, 100 and 1000 MHz, with a tanδ of 0.0602,

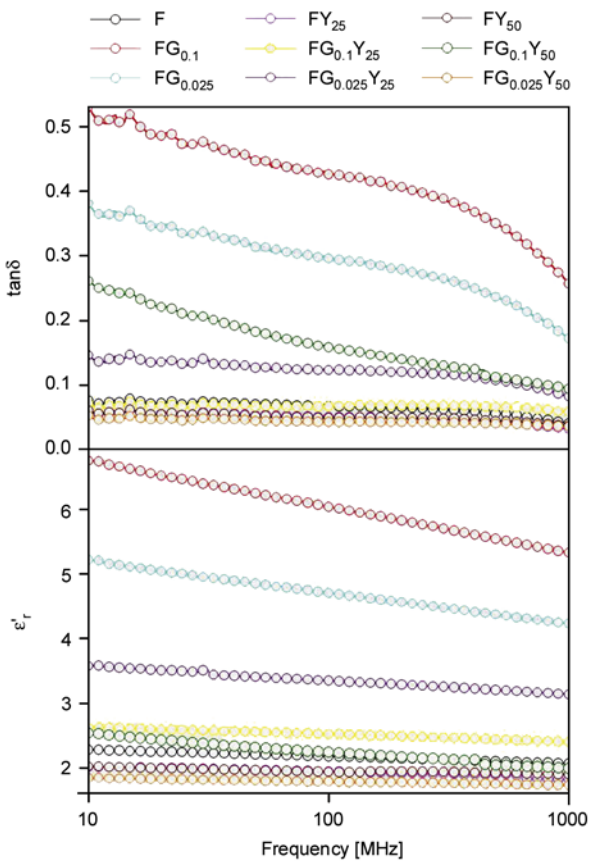

Figure 7. Dielectric spectroscopy measurements

0.0132 and 0.0032, respectively. The addition of YIG to polymeric matrix has not resulted in a composite with higher values to ε'_r, however the decrease of tanδ is observed. It was not detected dielectric relaxation process in this frequency range for dielectric (ε'_r and tanδ) measurements. Thus, these biocomposites have a moderate dielectric stability in the analyzed range frequency. The YIG stability along the frequency analyzed is a characteristic that may be incorporated to the composites. The literature data report cases of increase [33] and decrease [18] of the ε'_r, depending on the cross-linker agent and the polymeric material employed. This happens due to density, that is dependent on the material

Table 4. Films thickness, permittivity dielectric and loss tangent values of the biocomposites

Sample	Thickness [μm]	10 MHz		100 MHz		1 GHz	
		ε'_r	tan δ	ε'_r	tan δ	ε'_r	tan δ
F	139	2.273	0.075	2.174	0.067	2.066	0.041
$FG_{0.1}$	184	6.748	0.525	6.029	0.385	5.319	0.255
$FG_{0.025}$	173	5.207	0.378	4.696	0.295	4.224	0.171
FY_{25}	155	2.011	0.059	1.944	0.051	1.821	0.032
$FG_{0.1}Y_{25}$	214	2.621	0.070	2.520	0.067	2.397	0.058
$FG_{0.025}Y_{25}$	193	3.572	0.143	3.344	0.123	3.131	0.082
FY_{50}	179	2.025	0.060	1.936	0.049	1.894	0.037
$FG_{0.1}Y_{50}$	163	2.531	0.259	2.236	0.158	1.992	0.094
$FG_{0.025}Y_{50}$	193	1.848	0.051	1.783	0.042	1.726	0.036

porosity, i.e., when material has a large number of vacancies, the ε'_r decreases to minor values due to air amount in the composite. The cross-linking changes the charges' movement on the dielectric material, promoting the formation of new covalent bonds, hydrogen bonds and Van der Waals interactions [33]. It can be observed in the sample F that, when crosslinked with glutaraldehyde 0.1%, the value of dielectric constant increases. This shows that the dielectric is also an intrinsic behavior of the material, depending on the distribution of charges and electronic density.

The curves of Figures 8a and 8b show the profile of magnetization (M) as a function of applied magnetic field (H). Fechine *et al.* identified that the subnets of the shells can be represented by $\{\vec{R}_3\}[\vec{Fe}_2](\overleftarrow{Fe}_3)$ where {}, [] and () indicate occupation dodecahedral, octahedral and tetrahedral, respectively [32]. Arrows show the relative orientations of magnetic moments. Most interaction is $[\vec{Fe}_2](\overleftarrow{Fe}_3)$, since the rare earth cations are large and very weakly engaged with the subnets of iron. The profile of magnetization shown in Figures 8a and b suggest the obtaining of a soft ferrimagnetic composite, because the samples are very sensitive to an external magnetic field and reached their saturation magnetization (M_S) with application of relatively small magnetic fields. The hysteresis can be caused by some of these phenomena [34]: interactions between the fields, anisotropy, strength of internal friction caused by the interstices, dislocations, impurities etc. Rajendran *et al.* [35], studying the effects of the magnetic properties of YIG as a function of particle size, observed that samples with approximately 25 nm still show magnetic saturation. However, they reported that below this value, the YIG can increase their magnetization with increasing field, without any magnetic hysteresis appearing, being a typical case of superparamagnetic behavior. Table 5 contains the hysteresis data for the samples, where remanent magnetization (M_r) and coercive field (H_c) were obtained from in-set figures in Figures 8a and b. It is possible to observe a small hysteresis in these samples due them being soft ferrimagnetic. The general behavior of the obtained composite is similar to a collagen-YIG composite, according to Figueiró *et al.* [17].

It was added 250 mg (FY_{25}, $FG_{0.025}Y_{25}$ and $FG_{0.1}Y_{25}$) and 500 mg (FY_{50}, $FG_{0.025}Y_{50}$ and $FG_{0.1}Y_{50}$) of the YIG in the samples. However, the magnetic properties obtained for each group were slightly different due to the composition of the material. For example, FY_{50} presented high value of M_S than FY_{25} due to YIG amount in the composition. When the glutaraldehyde quantity added is analyzed, one can observe that $FG_{0.1}Y_{25}$ and $FG_{0.025}Y_{50}$ have the major values. In this case, there is an ideal composition of biopolymers (chitosan and gelatin) and glutaralde-

Table 5. Properties obtained from hysteresis data

	FY_{25}	$FG_{0.025}Y_{25}$	$FG_{0.1}Y_{25}$	FY_{50}	$FG_{0.025}Y_{50}$	$FG_{0.1}Y_{50}$
H_c [Oe]	14	15	14	16	14	14
M_r [emu/g]	0.17	0.27	0.21	0.46	0.32	0.21
M_s [emu/g]	2.63	2.39	3.18	5.53	4.73	3.18

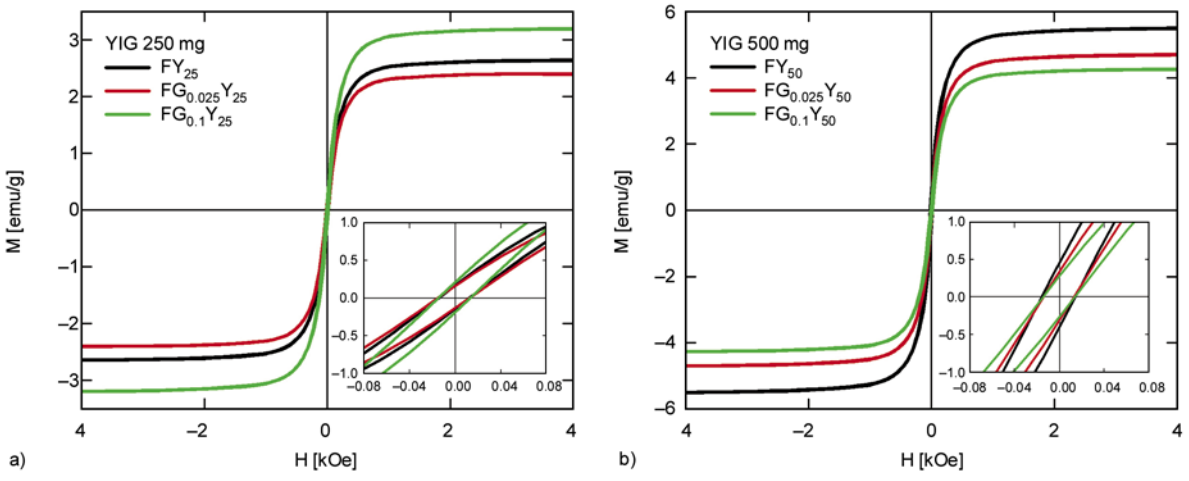

Figure 8. Magnetic measurements of (a) 250 mg-YIG series and (b) 500 mg-YIG series

hyde to attach YIG to the film to obtain higher M_S. Thus, the magnetic-dielectric properties of these biocomposites are modified as a function of the quantity of each component in the system due to interactions between biopolymers, crosslinking agent and magnetic ferrite.

4. Conclusions

The results of this study suggest that a ferrimagnetic garnet and polymeric fiber (chitosan and gelatin) can be used to obtain a well distributed composite, where YIG particles were densely found into the polymeric matrix. This composite shows variable magnetic properties and values of dielectric constant according its constitution. These new biocomposites may be employed as a versatile material, due to its biocompatibility, flexibility, biodegradability and magnetic features.

Acknowledgements

Thanks to X-Ray Laboratory (Department of Physics – UFC). Núcleo Milenio Magnetismo Básico y Aplicado and Proyecto BASAL FB0807 (Chilean agencies). This work was supported by **CAPES**, **Funcap** and **CNPq** (Brazilian agencies).

References

[1] Kim E. H., Ahn Y., Lee H. S.: Biomedical applications of superparamagnetic iron oxide nanoparticles encapsulated within chitosan. Journal of Alloys and Compounds, **434–435**, 633–636 (2007).
DOI: 10.1016/j.jallcom.2006.08.311

[2] Jain T. K., Morales M. A., Sahoo S. K., Leslie-Pelecky D. L., Labhasetwar V.: Iron oxide nanoparticles for sustained delivery of anticancer agents. Molecular Pharmaceutics, **2**, 194–205 (2005).
DOI: 10.1021/mp0500014

[3] Matsumine A., Kusuzaki K., Matsubara T., Shintani K., Satonaka H., Wakabayashi T., Miyazaki S., Morita K., Takegami K., Uchida A.: Novel hyperthermia for metastatic bone tumors with magnetic materials by generating an alternating electromagnetic field. Clinical and Experimental Metastasis, **24**, 191–200 (2007).
DOI: 10.1007/s10585-007-9068-8

[4] El Badawy M.: Chemical modification of chitosan: Synthesis and biological activity of new heterocyclic chitosan derivatives. Polymer International, **57**, 254–261 (2008).
DOI: 10.1002/pi.2333

[5] Chan P., Kurisawa M., Chung J. E., Yang Y-Y.: Synthesis and characterization of chitosan-*g*-poly(ethylene glycol)-folate as a non-viral carrier for tumor-targeted gene delivery. Biomaterials, **28**, 540–549 (2007).
DOI: 10.1016/j.biomaterials.2006.08.046

[6] Chen R-N., Wang G-M., Chen C-H., Ho H-O., Sheu M-T.: Development of *N*,*O*-(carboxymethyl)chitosan/collagen matrixes as a wound dressing. Biomacromolecules, **7**, 1058–1064 (2006).
DOI: 10.1021/bm050754b

[7] Eweis M., Elkholy S. S., Elsabee M. Z.: Antifungal efficacy of chitosan and its thiourea derivatives upon the growth of some sugar-beet pathogens. International Journal of Biological Macromolecules, **38**, 1–8 (2006).
DOI: 10.1016/j.ijbiomac.2005.12.009

[8] Ding P., Huang K-L., Li G-Y., Liu Y-F.: Preparation and properties of modified chitosan as potential matrix materials for drug sustained-release beads. International Journal of Biological Macromolecules, **41**, 125–131 (2007).
DOI: 10.1016/j.ijbiomac.2006.12.008

[9] Asghar A., Henrickson R. L.: Chemical, biochemical, functional, and nutritional characteristics of collagen in food systems. Advances in Food Research, **28**, 231–372 (1982).
DOI: 10.1016/S0065-2628(08)60113-5

[10] Farrugia C. A., Farrugia I. V., Groves M. J.: Comparison of the molecular weight distribution of gelatin fractions by size-exclusion chromatography and light scattering. Pharmacy and Pharmacology Communications, **4**, 559–562 (1998).
DOI: 10.1111/j.2042-7158.1998.tb00675.x

[11] Saddler J. M., Horsey P. J.: The new generation gelatins: A review of their history, manufacture and properties. Anaesthesia, **42**, 998–1004 (1987).
DOI: 10.1111/j.1365-2044.1987.tb05376.x

[12] Courts A.: The N-terminal amino acid residues of gelatin: 2. Thermal degradation. Biochemistry Journal, **58**, 74–79 (1954).

[13] Sakai Y., Yamato R., Onuma M., Kikuta T., Watanabe M., Nakayama T.: Non-antigenic and low allergenic gelatin produced by specific digestion with an enzyme-coupled matrix. Biological and Pharmaceutical Bulletin, **21**, 330–334 (1998).

[14] Vajargah S. H., Hosseini H. R. M., Nemati Z. A.: Preparation and characterization of yttrium iron garnet (YIG) nanocrystalline powders by auto-combustion of nitrate-citrate gel. Journal of Alloys and Compounds, **430**, 339–343 (2007).
DOI: 10.1016/j.jallcom.2006.05.023

[15] Garskaite E., Gibson K., Leleckaite A., Glaser J., Niznansky D., Kareiva A., Meyer H-J.: On the synthesis and characterization of iron-containing garnets ($Y_3Fe_5O_{12}$, YIG and $Fe_3Al_5O_{12}$, IAG). Chemical Physics, **323**, 204–210 (2006).
DOI: 10.1016/j.chemphys.2005.08.055

[16] Yang Q., Zhang H., Liu Y., Wen Q., Jia L.: The magnetic and dielectric properties of microwave sintered yttrium iron garnet (YIG). Materials Letters, **62**, 2647–2650 (2008).
DOI: 10.1016/j.matlet.2008.01.040

[17] Figueiro S. D., Mallmann E. J. J., Góes J. C., Ricardo N. M. P. S., Denardin J. C., Sombra A. S. B., Fechine P. B. A.: New ferrimagnetic biocomposite film based in collagen and yttrium iron garnet. Express Polymer Letters, **4**, 790–797 (2010).
DOI: 10.3144/expresspolymlett.2010.95

[18] Figueiró S. D., Góes J. C., Moreira R. A., Sombra A. S. B.: On the physico-chemical and dielectric properties of glutaraldehyde crosslinked galactomannan–collagen films. Carbohydrate Polymers, **56**, 313–320 (2004).
DOI: 10.1016/j.carbpol.2004.01.011

[19] Beppu M. M., Vieira R. S., Aimoli C. G., Santana C. C.: Crosslinking of chitosan membranes using glutaraldehyde: Effect on ion permeability and water absorption. Journal of Membrane Science, **301**, 126–130 (2007).
DOI: 10.1016/j.memsci.2007.06.015

[20] Cheng M., Deng J., Yang F., Gong Y., Zhao N., Zhang X.: Study on physical properties and nerve cell affinity of composite films from chitosan and gelatin solutions. Biomaterials, **24**, 2871–2880 (2003).
DOI: 10.1016/S0142-9612(03)00117-0

[21] Sarhan A. A., Monier M., Ayad D. M., Badawy D. S.: Evaluation of the potential of polymeric carriers based on chitosan-*grafted*-polyacrylonitrile in the formulation of drug delivery systems. Journal of Applied Polymer Science, **118**, 1837–1845 (2010).
DOI: 10.1002/app.32522

[22] Monteiro O. A. C., Airoldi C.: Some studies of crosslinking chitosan–glutaraldehyde interaction in a homogeneous system. International Journal of Biological Macromolecules, **26**, 119–128 (1999).
DOI: 10.1016/S0141-8130(99)00068-9

[23] Kasaai M. R.: A review of several reported procedures to determine the degree of *N*-acetylation for chitin and chitosan using infrared spectroscopy. Carbohydrate Polymers, **71**, 497–508 (2008).
DOI: 10.1016/j.carbpol.2007.07.009

[24] Ganji F., Abdekhodaie M. J.: Chitosan–g-PLGA copolymer as a thermosensitive membrane. Carbohydrate Polymers, **80**, 740–746 (2010).
DOI: 10.1016/j.carbpol.2009.12.021

[25] Peng H., Xiong H., Li J., Xie M., Liu Y., Bai C., Chen L.: Vanillin cross-linked chitosan microspheres for controlled release of resveratrol. Food Chemistry, **121**, 23–28 (2010).
DOI: 10.1016/j.foodchem.2009.11.085

[26] Tsai H-S., Wang Y-Z.: Properties of hydrophilic chitosan network membranes by introducing binary crosslink agents. Polymer Bulletin, **60**, 103–113 (2008).
DOI: 10.1007/s00289-007-0846-x

[27] Fechine P. B. A., Silva E. N., de Menezes A. S., Derov J., Stewart J. W., Drehman A. J., Vasconcelos I. F., Ayala A. P., Cardoso L. P., Sombra A. S. B.: Synthesis, structure and vibrational properties of $GdIG_X$:YIG_{1-X} ferrimagnetic ceramic composite. Journal of Physics and Chemistry of Solids, **70**, 202–209 (2009).
DOI: 10.1016/j.jpcs.2008.10.008

[28] Ni N., Zhao K.: Dielectric analysis of chitosan gel beads suspensions: Influence of low crosslinking agent concentration on the dielectric behavior. Journal of Colloid and Interface Science, **312**, 256–264 (2007).
DOI: 10.1016/j.jcis.2007.03.073

[29] Maier G.: Low dielectric constant polymers for microelectronics. Progress in Polymer Science, **26**, 3–65 (2001).
DOI: 10.1016/S0079-6700(00)00043-5

[30] Popielarz R., Chiang C.: Polymer composites with the dielectric constant comparable to that of barium titanate ceramics. Materials Science and Engineering B, **139**, 48–54 (2007).
DOI: 10.1016/j.mseb.2007.01.035

[31] Kobayashi Y., Tanase T., Tabata T., Miwa T., Konno M.: Fabrication and dielectric properties of the $BaTiO_3$–polymer nano-composite thin films. Journal of the European Ceramic Society, **28**, 117–122 (2008).
DOI: 10.1016/j.jeurceramsoc.2007.05.007

[32] Fechine P. B. A., Pereira F. M. M., Santos M. R. P., Filho F. P., de Menezes A. S., de Oliveira R. S., Góes J. C., Cardoso L. P., Sombra A. S. B.: Microstructure and magneto-dielectric properties of ferrimagnetic composite $GdIG_X$:YIG_{1-X} at radio and microwave frequencies. Journal of Physics and Chemistry of Solids, **70**, 804–810 (2009).
DOI: 10.1016/j.jpcs.2009.03.009

[33] Marzec E., Pietrucha K.: The effect of different methods of cross-linking of collagen on its dielectric properties. Biophysical Chemistry, **132**, 89–96 (2008).
DOI: 10.1016/j.bpc.2007.10.012

[34] Valenzuela R.: Magnetic Ceramics. Cambridge University Press, New York (1994).

[35] Rajendran M., Deka S., Joy P. A., Bhattacharya A. K.: Size-dependent magnetic properties of nanocrystalline yttrium iron garnet powders. Journal of Magnetism and Magnetic Materials, **301**, 212–219 (2006).
DOI: 10.1016/j.jmmm.2005.06.027

eXPRESS Polymer Letters Vol.5, No.12 (2011) 1050–1061
Available online at www.expresspolymlett.com
DOI: 10.3144/expresspolymlett.2011.103

The effect of a synthetic double layer hydroxide on the rate of II→I phase transformation of poly(1-butene)

C. Marega[1], V. Causin[1], R. Neppalli[1], R. Saini[1], G. Ferrara[2], A. Marigo[1]*

[1]Dipartimento di Scienze Chimiche, Università di Padova, and INSTM Research Unit, via Marzolo 1, 35131 Padova, Italy
[2]LyondellBasell Poliolefine Italia SpA – Centro Ricerche 'Giulio Natta', P.le Donegani 12, 44100 Ferrara, Italy

Received 14 April 2011; accepted in revised form 16 June 2011

Abstract. Perkalite is an unusual clay in the domain of polymer-based nanocomposites. In this paper, the use of perkalite as a filler for poly(1-butene) was investigated. Particular attention was posed on the study of the effect of this particular kind of clay on the rate of II→I phase transition of the matrix. Wide angle X-ray diffraction (WAXD), small angle X-ray scattering (SAXS), transmission electron microscopy (TEM) and differential scanning calorimetry (DSC) were used to determine the structure and morphology of the samples, the degree of dispersion of the filler and to follow the kinetics of the phase transition of poly(1-butene). Mechanical properties were moreover measured. Perkalite was found to increase the rate of II→I phase transition with respect to the neat matrix, because it affected the free energy of the crystalline phase, by decreasing the perfection of the crystals. Rather than the disruption of the regular ordering at a crystalline cell level, the effect on the lamellar morphology seems to be preponderant. The fragility of perkalite layers and the substantial reduction of the tactoids did not allow to influence the entropic factor to the phase diagram of poly(1-butene), because the filler was not able to locally increase the pressure on the nascent crystalline domains. Perkalite was therefore not able to achieve a direct formation of the phase I of poly(1-butene) directly from the melt.
The reduction of the size of perkalite tactoids confirmed that poly(1-butene) is very efficient in homogeneously dispersing the filler, thereby justifying the use of the materials produced in the present study as viable masterbatches for the production of polyolefin-based nanocomposites.

Keywords: *nanocomposites, poly(1-butene), perkalite*

1. Introduction

Ever since its discovery in 1954, isotactic poly(1-butene) (PB) was recognized for its remarkable properties. PB has superior toughness, tear strength, flexibility and creep with respect to other polyolefins, and it also displays a better resistance to stress cracking, to impact, to abrasion and to high temperature. An important drawback affecting the direct commercial exploitation of this polymer is related to the complex relationship between the kinetics and thermodynamics of its polymorphism. When PB is crystallized from the melt, it preferentially crystallizes according to the tetragonal phase II, which on the other hand is metastable at room temperature, and it spontaneously converts to the hexagonal phase I, with a concurrent loss of dimensional stability of molded items. This transition requires several days to be completed [1, 2]. The thermodynamically favored phase I has moreover improved physical-mechanical properties with respect to phase II [1, 3, 4], so acceleration of the II→I phase transition is key for the commercial development of PB. In previous works, it was shown that addition of montmorillonite clay could be exploited to increase the rate of this transition [3–7]. Coupling the role of clay with the effect of the insertion of ethylene

*Corresponding author, e-mail: valerio.causin@unipd.it

comonomeric units in the PB chains, crystallization from the melt directly into phase I was reported for the first time [7].

Layered silicates have been traditionally chosen as nanofillers due to their wide availability and relatively low cost. Most of the research in this field has been centered on smectite-type materials, such as montmorillonite or hectorite, which are commonly found in nature, but they can not be easily synthesized. On the contrary, layered double hydroxides (LDH) have been much less employed as nanofillers. The formula of LDH can be generalized as $|M^{2+}_{x}M^{3+}_{1-x}(OH)_2|_{intra}|A^{m-}_{x/m}\cdot nH_2O|_{inter}$, where M^{2+} and M^{3+} are metal cations, *A* are the anions and *intra* and *inter* designate the intralayer domain and the interlayer space, respectively. The structure of LDH derives from brucite, i.e. $Mg(OH)_2$, with layers obtained by isomorphous substitution of divalent cations. The replacement of Mg^{2+} by M^{3+} ions generates a net positive charge that is balanced by incorporation of anions in interlayer space. Differently from smectite-type clays, LDH are much more prone to be synthesized. LDH have high charge density and a high content of interlayer anions and water molecules, resulting in strong electrostatic interactions between the sheets and strong hydrophilic properties. As a consequence, LDH layers are very tightly stacked and are quite difficult to exfoliate [8–12].

Never LDHs were applied for the preparation of PB-based nanocomposites, although these fillers showed a big potential. Perkalite is especially interesting due to the advantage of being compliant with the European Union regulations for materials coming into contact with foodstuffs [12].

In the cited work on PB-based nanocomposites, an interesting affinity of PB with clay emerged. Differently from what normally happens with polypropylene or polyethylene, a rather extensive reduction of clay tactoid size could be achieved in PB [4–7]. This feature and the compatibility of PB with polypropylene open a potential for PB as a highly performing vector to include clay within a polypropylene matrix. The classical approach to pursue this objective is the use of maleated polypropylene as a compatibilizer [13]. Despite the big amount of research carried out on this subject, the recent literature shows just very marginal improvements with respect to previous results [14]: a change in perspective is necessary in the preparation techniques of these materials. The use of masterbatches based on a highly performing material such as PB to introduce clay into an otherwise recalcitrant matrix such as polypropylene can be an example of such novel approach.

In this work, the preparation and the characterization of a series of clay-PB nanocomposites are reported. Such materials will be used as masterbatches to be subsequently included into polypropylene matrices [15].

In this paper, focus will be posed on the characteristics and properties of the materials, in order to evaluate their physical mechanical performance and also to investigate the effect of clay on the rate of II→I phase transition.

The structure, morphology and phase transition of the materials were studied by wide-angle X-ray diffraction (WAXD), small-angle X-ray scattering (SAXS), differential scanning calorimetry (DSC) and transmission electron microscopy (TEM).

2. Experimental

2.1. Materials and sample preparation

The samples were prepared using PB0300M, a commercial isotactic poly(1-butene) produced by LyondellBasell Polyolefins (Ferrara, Italy) ($\overline{M}_w$ = 284 196 g/mol, $\overline{M}_w/\overline{M}_n$ = 3.6, density = 0.915 g/cm^3). The melt flow rate of this matrix was 4 g/10 min (190°C, 2.16 kg according to ASTM D-1238) and 70 g/10 min (190°C, 10 kg according to ASTM D-1238).

As compatibilizer, Polybond 3200 (Chemtura, Middlebury, CT, USA), a maleated PP (MFR = 115 g/10 min ASTM D-1238 at 190°C and 2.16 kg, 1% w/w maleic anhydride, density = 0.91 g/cm^3) was used. Perkalite is a synthetic hydrotalcite clay, treated with anionic surfactants (Akzo Nobel Polymer Chemicals, Deventer, The Netherlands). In particular the Perkalite F100 grade was employed, where the anion surfactants are hydrogenated fatty acids.

The components were mixed in a reciprocating single screw extruder, Buss MDK 70 (Pratteln, Switzerland). The extrusion average temperature was 180°C, the residence time was 80 s. The profile of the employed screw was obtained by that normally used with talc by the elimination of restriction rings to optimize distributive mixing and residence time

Table 1. Formulation of the studied samples

Sample	PB [%]	Compatibilizer [%]	Perkalite [%]
PB0	100	0	0
PB5	90	5	5
PB10	80	10	10
PB15	70	15	15
PB20	60	20	20
PB5NoC	95	0	5
PB10NoC	90	0	10

[13]. Table 1 summarizes the formulation of the samples employed. To rule out the effect of processing, also the matrix polymer alone was subjected to extrusion at the same conditions of the composites. For the subsequent WAXD, SAXS, DSC and PLOM analyses and for the study of the II→I transition, test specimens were prepared from both the matrix and the composites by melting aliquots of the samples between two aluminum plates in a press at 170°C for 10 min, in order to cancel any previous thermal history, and then quenching the specimens to room temperature by immersion in ice. Specimens 1 mm thick were so obtained. Tests were also made by slowly cooling, at 10°C/min, the samples from the melt, but the results did not change with respect to the quenched ones. Samples for mechanical testing were prepared by injection molding, as described in paragraph 2.7.

2.2. Wide angle X-ray diffraction

WAXD patterns were recorded in the diffraction angular range 1.5–40° 2θ by a Philips X'Pert PRO (Almelo, The Netherlands) diffractometer, working in the reflection geometry and equipped with a graphite monochromator on the diffracted beam (CuK_α radiation). Transmission patterns were also recorded in the diffraction range 5–40° 2θ by a diffractometer GD 2000 (Ital Structures, Riva del Garda, Italy) working in a Seeman-Bohlin geometry and with a quartz crystal monochromator on the primary beam ($CuK_{\alpha 1}$ radiation). Results were the same either in the transmission and reflection mode, so it was concluded that no difference in structure and morphology existed in the samples between the bulk and the surface. The data presented in this paper were gathered in the reflection geometry. The application of the least-squares fit procedure elaborated by Hindeleh and Johnson [16] gave the degree of crystallinity by weight. The estimate of the degree of crystallinity was made after completion of the II→I phase transition, in order to rule out the effect of polymorphism and of the post crystallization, during which part of the amorphous polymer crystallizes in phase I [17, 18]. The phase transition II→I was followed observing the WAXD patterns and estimating, as a function of time, the ratio A_t/A_0, where A_t represents the area under the peak at 11.9° 2θ, i.e. the (200) reflection of phase II, at time t, and A_0 is the area of the same peak just after crystallization from the melt. Right after quenching from the melt, the samples were immediately mounted in the diffractometer, so the WAXD data at $t = 0$ relative to the reflections above were acquired in 10 minutes.

2.3. Small angle X-ray scattering

The SAXS patterns of the samples were recorded by a MBraun (Graz, Austria) system, using a CuK_α radiation from a Philips PW 1830 X-ray generator. The data were collected by a position sensitive detector and were successively corrected for blank scattering, desmeared and Lorentz-corrected.

A fitting method of SAXS patterns was developed on the basis of a theoretical model [19–23] referring to the Hosemann model [24], that assumes the presence of lamellar stacks having an infinite side dimension. This assumption takes into account a monodimensional electron density change along the normal direction to the lamellae.

2.4. Transmission electron microscopy

TEM analyses were performed by a Philips CM 120 (Eindhoven, The Netherlands). Samples were stained by RuO_4 and cryomicrotomed. Sections about 100 nm thick were obtained and analyzed.

2.5. Polarized light optical microscopy

The spherulitic morphology of the samples was studied with a Leica DM400M (Wetzlar, Germany) polarized light microscope. The samples were placed between a glass slide and a cover slip and were kept at 170°C for 10 min, to ensure uniform melting and to delete their thermal history. The slide was then transferred to a Mettler FP82HT (Columbus, OH, USA) hot stage set at 95°C. Photomicrographs were taken between cross-polarizers with a Leica DFC280 (Wetzlar, Germany) digital camera.

2.6. Differential scanning calorimetry

All the measurements were carried out with a TA Instruments mod. 2920 (New Castle, DE, USA) calorimeter operating under N_2 atmosphere. Polymer samples weighing about 5 mg closed in aluminum pans were used throughout the experiments. Indium of high purity was used for calibrating the DSC temperature and enthalpy scales. In order to determine the samples' crystallization temperature (T_c), their thermal history was cancelled by a 5 min long isotherm at 170°C, subsequently the samples were cooled down to room temperature at 10°C/min. T_c was the temperature corresponding to the maximum in the exothermic peak.

2.7. Physical mechanical properties

The specimens for mechanical testing were prepared by injection molding in accordance with ISO 294, treated for 10 minutes in autoclave at 2000 bars and conditioned for 40 h at 23±2°C and 50±5% relative humidity following ISO 291. All the samples were prepared with the same processing parameters to allow a proper comparison, because the preparation step affects the resulting properties. All the mechanical tests were performed after completion of the II→I phase transition. The flexural and elongational properties were determined in accordance with ISO 178 using a Model 4301 instrument (Instron, Norwood, MA, USA) on injection moulded specimens, prepared following ISO 294-1 (length = 80±2 mm, width = 10±0.2 mm and thickness = 4.0±0.2 mm).

Impact strength was measured with a 6545 pendulum-type hammer (Ceast, Pianezza, Italy) striking a notched specimen with a 0.05 mm notch (ISO 180).

3. Results

Table 1 summarizes the composition of the considered samples. The formulation of the specimens allowed also to study the effect of compatibilization, because 4 of the composite samples were compatibilized with an amount of polypropylene grafted with maleic anhydride (PP-g-MA) (1% w/w) equal to that of perkalite, whereas two of the composites did not contain any compatibilizer. The polymeric matrix will be designated in the rest of this paper as PB0. One of the aims was in fact to investigate if these different formulations could attain different composite morphologies and dispersions of the filler in the matrix, therefore studying its effect on the polymer semicrystalline framework and on the rate of phase transformation. The morphology of the composite was in fact shown to be key for the property improvement, for the stability of the metastable phase and also for the acceleration of the rate of the II→I transition [4–7].

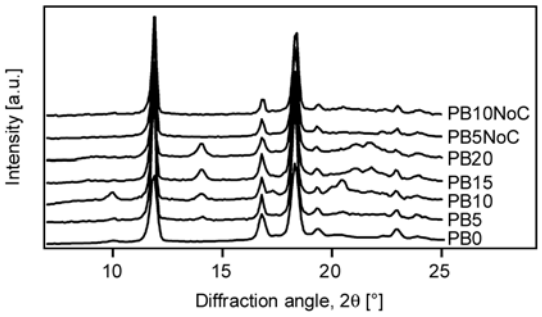

Figure 1. WAXD patterns of the samples at $t = 0$

WAXD was used to follow the phase transition, acquiring diffractograms at different times after cooling from the melt. Figure 1 shows the WAXD patterns at $t = 0$, i.e. immediately after quenching from the melt, of the considered samples. The reflections relative to the tetragonal phase II are three main peaks at 11.9, 16.9 and 18.4° 2θ, due to the (200), (220) and (301) planes. The hexagonal phase I is characterized by four signals at 9.9, 17.3, 20.2 and 20.5° 2θ, originated by the (110), (300), (220) and (211) planes [25].

Mixed I/II polymorphism is displayed just by sample PB10, and to a lesser extent by PB5 and PB0. In these samples, a small amount of phase I is present since time 0, as especially evidenced by the small (110) peak visible at 9.9° 2θ. It has already been noted that in PB-based nanocomposites filled with layered silicates, some phase I can coexist with phase II right after cooling from the melt. This is due to the appearance of a defective population of phase II crystals, which very rapidly transforms into phase I [7, 25, 26]. All the other samples showed, right after melting, 100% phase II.

In Figure 1, an increasing peak located at 14.1° 2θ is evident in the samples containing the largest amounts of clay. This is ascribable to the increasing quantity of PP-MA compatibilizer, and corresponds to the (110) peak of the α phase of polypropylene. The presence of this compatibilizer should therefore be

taken into account as a material seriously capable to influence the structure, material and properties of the composites.

Figure 2a shows an example, for sample PB10, of the evolution of the WAXD patterns as a function of time. Analyzing these diffractograms, it was possible to follow and quantify the kinetics of phase transformation in the studied samples. Figure 2b shows for example the rate of disappearance of phase II as a function of time, extracted from the data in Figure 2a. For the quantification of the kinetics of the II→I phase transition, the disappearance of phase II, rather than the increase in phase I, was followed because it is known that, together with the phase transition, a post-crystallization phenomenon takes place, during which part of the amorphous polymer crystallizes in phase I [17, 18, 25, 27]. The calculations were also done considering the amount of phase II as a ratio of the sum of the peaks of phases I and II [25], obtaining analogous results because the initial amount of phase I was almost always negligible. Table 2 shows the trend of the degree of crystallinity measured on the samples before and after the phase transition, and Figure 3 shows the evolution of crystallinity as a function of time for sample PB5. A clear increase in the crystallinity can be observed, confirming that a post-crystallization process indeed happens. An increase in crystallinity occurs with aging time, reaching a plateau around 70 h.

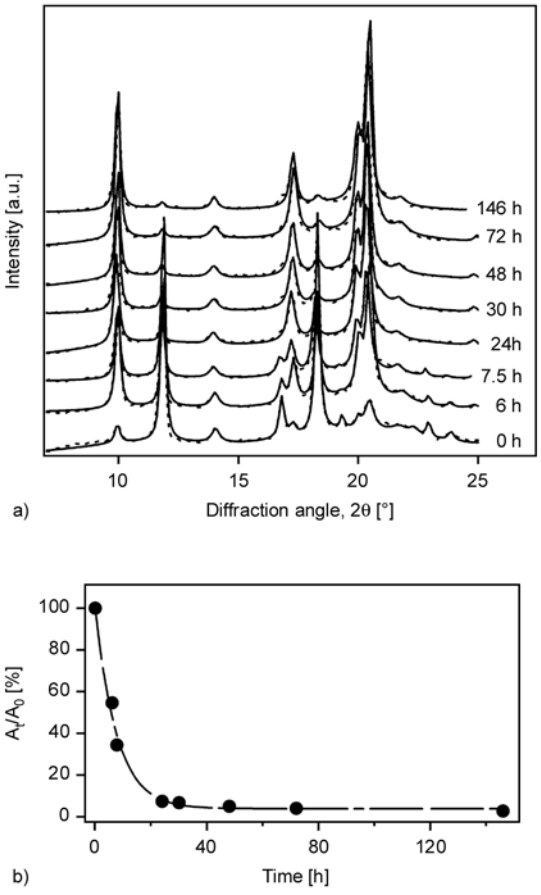

Figure 2. a) WAXD patterns of sample PB10 at different aging times, experimental patterns are shown by dotted lines, the fitting functions are shown by solid lines; b) Percent change, as a function of time, of the (200) peak area. The line indicates the exponential fitting function used to determine the half time of transformation.

Table 2. Crystallinity, evaluated by WAXD, φ_{WAXD}, of the studied samples at time 0 and after 5 days

Sample	φ_{WAXD} at time 0 [%]	φ_{WAXD} after 120 h [%]
PB0	66	76
PB5	53	63
PB10	50	57
PB15	49	59
PB20	43	55
PB5NoC	49	60
PB10NoC	45	63

On the basis of diagrams such as those displayed in Figure 2b, the half time of II→I phase transition, $t_{1/2}$, could be assessed. The experimental points were fitted with an exponential function (also displayed in Figure 2b). The analytical function so obtained was used to calculate $t_{1/2}$, i.e the time needed to reduce by 50% the initial phase II content. Table 3 shows the $t_{1/2}$ for the studied samples. For comparison purposes, in this same table the $t_{1/2}$ for a composite based on the same PB matrix containing 5% montmorillonite clay and 7% compatibilizer is also shown (this sample is labeled PB5M in Table 3 and further details on this sample can be found in Ref. 6). This sample is a suitable benchmark for assessing the role of perkalite, because it displayed a morphology of clay dispersion very similar to the one detected in the samples described

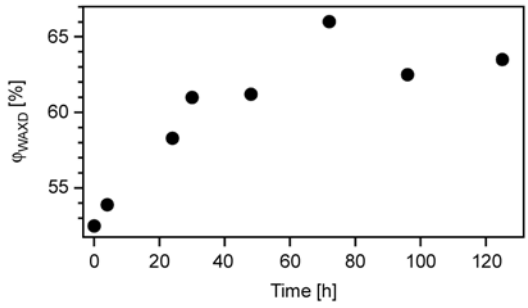

Figure 3. Evolution as a function of time of the crystallinity, evaluated by WAXD, for sample PB5

Table 3. Half time of the II→I phase transformation and residual phase II remaining after 5 days

Sample	$t_{1/2}$ [h]	Residual phase II
PB0	13.5	6%
PB5	5.8	5%
PB10	5.7	4%
PB15	16.6	7%
PB20	16.7	9%
PB5NoC	16.5	11%
PB10NoC	15.5	11%
PB5M	2.2	3%

in this work: a reduction in tactoid size, with some degree of intercalation [6].

Two groups of samples can be identified. The composites containing the lesser amount of perkalite, PB5 and PB10, displayed a sharp increase in the rate of phase transition, with a much reduced $t_{1/2}$ with respect to that of pristine PB. It is also worth noting that some residual phase II remained after 5 days, indicating that the phase transformation does not go to completion. The lowest amounts of residual phase II was observed in samples PB5 and PB10, i.e. those with the fastest II→I phase transition.

As will be better detailed in the discussion section of this paper, in order to better interpret the reasons of these increases in the rate of phase transformation, it is necessary to thoroughly characterize the structure and morphology of the composites.

The effect of clay on the regular arrangement of the semicrystalline framework can be assessed by the trend of the degrees of crystallinity in Table 2. A decrease in φ_{WAXD} can be observed before and after the phase transformation. The detrimental effect of clay on the regularity of the crystalline cell is well known [3, 28–30]. The disruptive effect of clay was not limited to the crystalline cell, but it extended also to the lamellar morphology, as evidenced by SAXS data. Figure 4 shows the SAXS patterns obtained for the considered samples. The neat PB matrix shows a quite defined peak whereas, with an

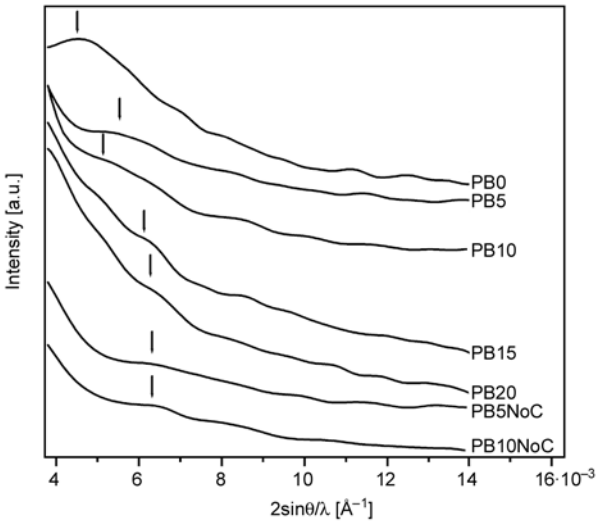

Figure 4. SAXS patterns of the considered samples in the polymer lamellar periodicity region. The arrows indicate the position of the peak maximum.

increasing perkalite content, such peak becomes weaker and shifts progressively towards wider angles. The experimental traces due to the matrix and to the composite samples were fitted according to a method [19, 20, 24] which was shown [23] to reliably determine the thicknesses and distributions of the crystalline and amorphous layers, the long period and the crystallinity, along with their distribution, associated to lamellar stacks. The results are shown in Table 4. The patterns relative to samples PB15 and PB20 had signals so weak that they could not be fitted. The data in Table 4 confirm the shift of the long period that could be qualitatively detected on the SAXS traces. It is interesting to note that the samples with the lowest degree of crystallinity as measured by SAXS were PB5 and PB10, i.e. those with the fastest phase transition. Comparing the data in Tables 2 and 4, it can be seen that the crystallinities assessed by SAXS have larger values relative to those estimated by WAXD. This divergence can be explained considering the difference between the two techniques. SAXS is only sensitive to the crystalline regions organized in lamellar stacks,

Table 4. Morphological parameters of the lamellar stacks obtained by SAXS analysis of the samples. The thickness of the crystalline (C) and amorphous layer (A), the long period (D), and the crystallinity (φ_{SAXS}), along with their relative distributions ($\sigma_c/C = \sigma_A/_A$, $\sigma_D/_D$), and number of lamellae (N) are shown

Sample	C [Å]	σ_C/C	A [Å]	σ_A/A	D [Å]	σ_D/D	Φ_{SAXS} [%]	N
PB0	181	0.43	59	0.43	240	0.34	76	5
PB5	122	0.42	52	0.42	174	0.32	70	2
PB10	133	0.49	61	0.49	194	0.37	68	3
PB05NoC	110	0.26	42	0.26	152	0.20	72	3
PB10NoC	111	0.31	41	0.31	152	0.24	73	3

whereas WAXD allows the detection of all the regions contributing to the semicrystalline framework, including the amorphous phase located between the lamellar stacks. Therefore WAXD crystallinity is lower because the contribution of crystalline domains is 'diluted' by the interstack amorphous parts.

It is also striking that all the samples, including PB0, have an extremely low average number of lamellae per stack, which decreases with increasing perkalite content.

A further observation that can be made on the data in Table 4 is that the distribution of the thicknesses of the crystalline (σ_C/C) and amorphous layers (σ_A/A), and of the long period (σ_D/D) is broadened by an increasing perkalite content, when the compatibilizer is used. On the other hand, in the uncompatibilized composites such distribution is significantly narrower than that of the matrix. Apparently the presence of the compatibilizer poses an obstacle to the regularity of the lamellar stacks and to the homogeneous distribution of the layers which compose the stacks.

WAXD and SAXS were used to evaluate the degree of dispersion of clay in the polymer matrix. Figure 5 and 6 show the results of such analyses. Neat clay displays, both in WAXD and SAXS, a single peak correspondent to a *d*-spacing of 36 Å, which should be attributed to the reflections from the (003) family of crystallographic planes [31]. The d_{003} can be termed the interlayer spacing and includes a contribution from the metal hydroxide layer and the gallery that contains the intercalated anions [31].

It may be seen in Figure 5 that the basal peaks of clay in the composites are not significantly shifted with respect to that of pristine clay. The periodicity

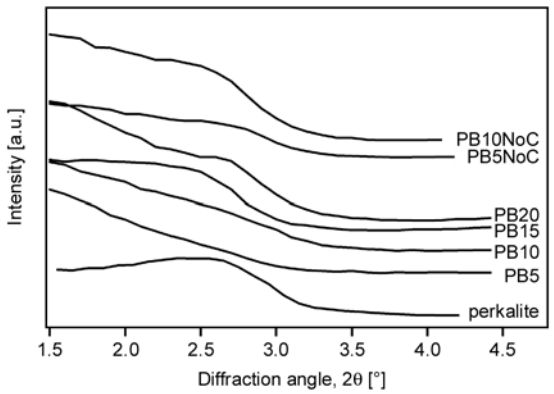

Figure 5. WAXD patterns of the considered samples in the angular region of the basal planes

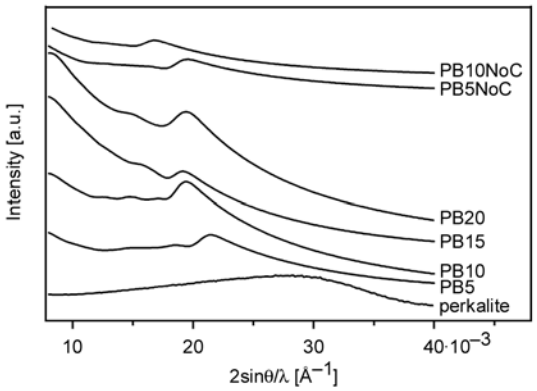

Figure 6. SAXS patterns of the considered samples in the clay periodicity region

values obtained from the position of the basal peaks are quite constant throughout the samples and are all equal to about 35 Å. This is consistent with the presence of a non-intercalated population of tactoids which retains the interlayer spacing of pristine clay.

SAXS allowed to complement this information, investigating a range of interlayer distances beyond the low angle limit of WAXD. In Figure 6 SAXS spectra gathered on the composites are shown, along with the SAXS pattern of neat perkalite. It is known that the width of diffraction peaks is related to the size of the diffracting domains. The basal peaks detected by WAXD were very broad, indicative of rather small non-intercalated tactoids. Such small tactoids did not produce a signal intense enough to be detected by SAXS in an angular position close to the wide-angle limit of SAXS, so the non-intercalated population of tactoids was not visible in the SAXS traces. On the other hand, neat perkalite yielded a detectable SAXS signal located at about 30 $Å^{-1}$ because the pristine filler has very large and very ordered tactoids, which give rise to a rather intense SAXS peak. SAXS evidenced that, along with the non-intercalated tactoid population observed by WAXD, another population was present, which was composed by intercalated tactoids. A clear shift in the SAXS peak is observed for the composites with respect to the neat perkalite, indicating a significant degree of intercalation. A quantitative estimation of the average size of the clay stacks was performed by fitting procedures of the SAXS traces. On the basis of theoretical models which are functions of the morphological features of tactoids, calculated SAXS spectra were generated to reproduce

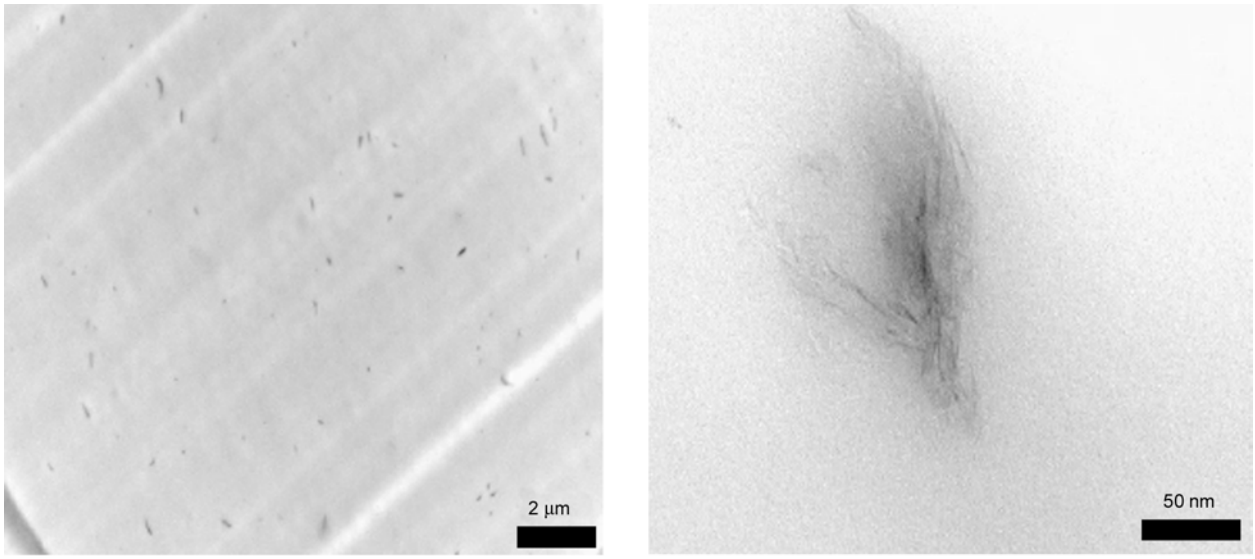

Figure 7. TEM micrograph of sample PB5 at different magnifications

experimental ones, allowing an evaluation of the mean number of layers, their spacing and distribution [22]. The fitting showed that the average number of layers per each intercalated stack was about 5 for all the composites, indicating a significant degree of interaction between polymer and filler. TEM was used to complement and to amend one of the limitations of SAXS, i.e. that SAXS alone is not able to assess the proportion of intercalated tactoids, with respect to the total amount of clay. TEM confirmed that clay is not exfoliated. However, low and high magnification TEM micrographs showed that the size of tactoids is very small, coherently with SAXS data (Figure 7). It has been argued that this latter situation, i.e. reduction of the size of tactoids to just two or three layers, can be considered practically equivalent to exfoliation, as far as properties are concerned [6, 30, 32–34].

The nucleation behavior of perkalite was also studied, by DSC and PLOM. Figure 8 displays two exemplary micrographs of samples PB0 and PB5 which show that the size of spherulites after 10 minutes of isothermal crystallization at 95°C was much larger in the neat matrix, than in the composites. This is due to the nucleating ability of perkalite, which was confirmed by the increase in the non-isothermal crystallization temperature measured by DSC. In fact, in the cooling ramp from the melting tempera-

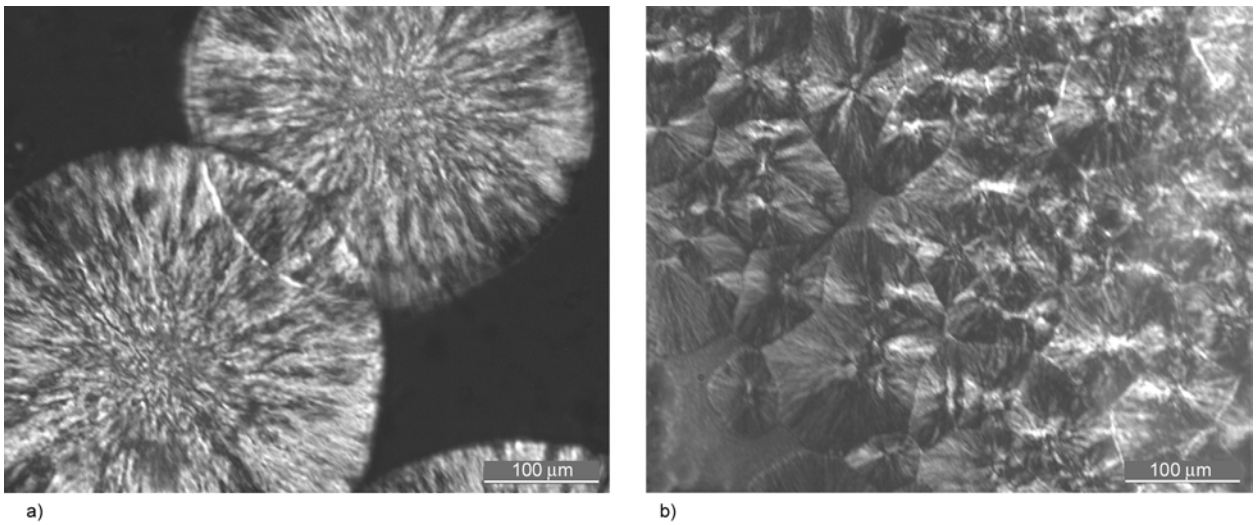

Figure 8. PLOM micrographs of the spherulites obtained after 10 minutes of isothermal crystallization at 95°C for samples a) PB0 and b) PB5

ture to room temperature, the position of the crystallization peak shifted from 76°C of PB0 to 88°C of the composites.

The physical mechanical properties were extremely similar to those measured on analogous montmorillonite-containing samples (Table 5) [6]. With increasing perkalite content, an increase in modulus was observed, up to an improvement, in sample PB20, of 81% with respect to the neat matrix. This higher rigidity of the samples, though, was obtained at the expense of ductility, because the impact strength and the elongation at break severely decreased as a function of perkalite content.

4. Discussion

Poly(1-butene) is an interesting polymer for the scientific community and for the industry because it displays very promising physical mechanical properties, at the same time suffering the drawback of a slow phase transition which so far reduced its applicative potential.

The purpose of this paper was to contribute in shedding light on the relationship between the morphology of poly(1-butene)-layered silicate nanocomposites and the rate of II→I phase transition.

In this work, it was seen that the compatibilized composites with a low perkalite content, i.e. samples PB5 and PB10, have a much faster II→I phase transition with respect to the pure PB matrix. Comparing the results obtained in this work with analogous composites prepared by adding montmorillonite clay (Table 3), it can be seen that the half-time of transformation is just 2.2 h with montmorillonite, and 5.7 h for perkalite. The half-time of II→I phase transition of pure PB was 13.5 h. Montmorillonite is therefore more efficient than perkalite in increasing the rate of phase transition.

Previous results indicated that the phase diagram of poly(1-butene) depends on the balance between homogeneity of the system and rate and regularity of crystallization [7]. In cases like this of poly(1-butene), the Ostwald's rule [35] is valid, which states that phase transformations will always proceed through stages of metastable states whenever these exist. In such cases, the crystallization pathway involves the formation of the nuclei in the metastable phase, followed by growth in this phase and eventually by a transition into the stable form [36, 37]. The stability of such metastable state is critically dependent on the relative free energy content of the liquid (melt), metastable (phase II) and stable (phase I) crystal phases. Events that decrease the entropy of the melt (i.e. stiffening of the chains, orientation or formation of mesophases), or that increase the free energy of the crystalline phase (i.e. decrease of crystal perfection or reduction of crystal size) modify the region of existence of the metastable phase [36] and have therefore important consequences on the kinetics of the transformations also, because they influence the size of the critical nuclei [36, 37].

High pressure treatments, that act on the entropy of the melt, are industrially employed to quickly transform PB into phase I. At a molecular level, it has been argued that the stress exerted by the amorphous layers or tie molecules on the crystalline cores accelerates the phase transition [38, 39]. Layered silicates, which are usually preferentially distributed in the amorphous phase within spherulites [40–42], were shown to partly mimic this entropic effect by locally increasing the pressure on the nascent crystalline domains [7]. It was observed that large montmorillonite aggregates were desirable in delivering this effect, because small tactoids are too flexible and they are not able to exert pressure on the macromolecular chains [43–45]. This is confirmed by our results. All the composites had small tactoids, with an average number of layers per tactoid of just 5. Moreover, perkalite layers, as those of other layered double hydroxides, are more fragile in nature than montmorillonite-type clays [46–48], and so they are less able to put pressure on the nascent crystalline domains, and so they increase the rate of II→I phase transition less than bulkier montmorillonite tactoids.

Concurrently with the effect on the entropy of the melt, the filler also affects the free energy of the crystalline phase. Perkalite, like montmorillonite clay, exerts this role by decreasing the perfection of the crystals, as reflected by the above reported decrease in the degree of crystallinity found by WAXD and SAXS, with respect to the neat matrix. Rather than the disruption of the regular ordering at a crystalline cell level, the effect on the lamellar morphology seems to be preponderant. The crystallinity associated to the lamellar stacks, φ_{SAXS}, is lower in samples PB5 and PB10, whereas it increases in PB5NoC and PB10NoC, with a trend that reflects

Table 5. Physical mechanical properties of the considered samples. FEM = flexural modulus, Izod = Izod impact test, StBr = stress at break, ElBr = elongation at break, HDT = heat deflection test

Sample	FEM [MPa]	Izod [kJ/m^2]	Izod 0°C [kJ/m^2]	StBr [MPa]	ElBr [%]	HDT [°C]
PB0	549	6.0	3.4	25	225	110
PB5	600	5.4	2.4	21	100	109
PB10	712	3.2	2.3	21	57	109
PB15	815	2.5	1.4	21	11	106
PB20	995	2.0	1.3	20	3	103
PB5NoC	555	8.8	3.9	25	250	110
PB10NoC	647	6.8	3.1	20	92	109

the II→I phase transition half-times. Moreover, a disturbing effect due to the presence of the compatibilizer was observed, which was reflected by a broadening of the distribution of the thicknesses of the lamellar stacks. This explains why larger amounts of perkalite, i.e. samples PB15 and PB20, and the absence of compatibilizer, i.e. PB5NoC and PB10NoC, proved to be detrimental for the rate of phase transition: the $t_{1/2}$ was comparable to that for the neat PB matrix. Thus, although a blank poly(1-butene)/compatibilizer sample with no clay was not prepared and analyzed in this work, on the basis of our data we could infer that the compatibilizer does not favor an increase of the rate of II→I phase transition, confirming what was already reported elsewhere in the case of montmorillonite-based composites [7]. This large effect of the crystallinity at a lamellar level is also in agreement and contributes to explain previously reported results, according to which the nucleation centers of the II→I phase transition are located in the lamellar distortion points [17, 49], i.e. larger inhomogeneity in the lamellar structure brings about the earlier appearance of phase I domains.

5. Conclusion

Nanocomposite samples were prepared by adding perkalite to a matrix of poly(1-butene), in order to study the effect of this particular kind of clay on the rate of II→I phase transition of the matrix. Perkalite was found to increase the rate of II→I phase transition with respect to the neat matrix, albeit less dramatically than montmorillonite. The fragility of perkalite layers and the substantial reduction of the tactoids did not allow to influence the entropic factor to the phase diagram of poly(1-butene), because the filler was not able to locally increase the pressure on the nascent crystalline domains.

The reduction of the size of perkalite tactoids confirmed that poly(1-butene) is very efficient in homogeneously dispersing the filler, thereby justifying the use of the materials produced in the present study as viable masterbatches for the production of polyolefin-based nanocomposites. Therefore, a further development of this work, which will be more completely discussed in a further article, will be to exploit the good propensity of poly(1-butene) in dispersing layered fillers more efficiently than other polyolefins, and to use these materials as masterbatches for the preparation of polymer nanocomposites with a polypropylene matrix.

Acknowledgements

Ramesh Neppalli is grateful to Fondazione Cassa di Risparmio di Padova e Rovigo for the support of his PhD grant.

References

[1] Azzurri F., Flores A., Alfonso G. C., Baltá Calleja F. J.: Polymorphism of isotactic poly(1-butene) as revealed by microindentation hardness. 1. Kinetics of the transformation. Macromolecules, **35**, 9069–9073 (2002). DOI: 10.1021/ma021005e

[2] Kaszonyiova M., Rybnikar F., Geil P. H.: Crystallization and transformation of polybutene-1. Journal of Macromolecular Science Part B: Physics, **43**, 1095–1114 (2004). DOI: 10.1081/MB-200033322

[3] Wanjale S. D., Jog J. P.: Poly (1-butene)/clay nanocomposites: A crystallization study. Journal of Macromolecular Science Part B: Physics, **42**, 1141–1152 (2003). DOI: 10.1081/MB-120024810

[4] Wanjale S. D., Jog J. P.: Poly(1-butene)/clay nanocomposites: Preparation and properties. Journal of Polymer Science Part B: Polymer Physics, **41**, 1014–1021 (2003). DOI: 10.1002/polb.10418

[5] Nathani H., Dasari A., Misra R. D. K.: On the reduced susceptibility to stress whitening behavior of melt intercalated polybutene–clay nanocomposites during tensile straining. Acta Materialia, **52**, 3217–3227 (2004). DOI: 10.1016/j.actamat.2004.03.021

[6] Causin V., Marega C., Marigo A., Ferrara G., Idiyatullina G., Fantinel F.: Morphology, structure and properties of a poly(1-butene)/montmorillonite nanocomposite. Polymer, **47**, 4773–4780 (2006). DOI: 10.1016/j.polymer.2006.04.035

[7] Marega C., Causin C., Marigo A., Saini R., Ferrara G.: Crystallization of a (1-butene)-ethylene copolymer in phase I directly from the melt in nanocomposites with montmorillonite. Journal of Nanoscience and Nanotechnology, **10**, 3078–3084 (2010). DOI: 10.1166/jnn.2010.2184

[8] Leroux F.: Organo-modified anionic clays into polymer compared to smectite-type nanofiller: Potential applications of the nanocomposites. Journal of Nanoscience and Nanotechnology, **6**, 303–315 (2006). DOI: 10.1166/jnn.2006.003

[9] Chen W., Qu B. J.: Structural characteristics and thermal properties of PE-g-MA/MgAl-LDH exfoliation nanocomposites synthesized by solution intercalation. Chemistry of Materials, **15**, 3208–3213 (2003). DOI: 10.1021/cm030044h

[10] Li B., Hu Y., Zhang R., Chen Z., Fan W. C.: Preparation of the poly(vinyl alcohol)/layered double hydroxide nanocomposite. Materials Research Bulletin, **38**, 1567–1572 (2003). DOI: 10.1016/S0025-5408(03)00203-4

[11] Wang G-A., Wang C-C., Chen C-Y.: The disorderly exfoliated LDHs/PMMA nanocomposite synthesized by in situ bulk polymerization. Polymer, **46**, 5065–5074 (2005). DOI: 10.1016/j.polymer.2005.04.054

[12] Marega C., Causin V., Marigo A., Ferrara G., Tonnaer H.: Perkalite as an innovative filler for isotactic polypropylene-based nanocomposites. Journal of Nanoscience and Nanotechnology, **9**, 2704–2714 (2009). DOI: 10.1166/jnn.2009.dk01

[13] Benetti E. M., Causin V., Marega C., Marigo A., Ferrara G., Ferraro A., Consalvi M., Fantinel F.: Morphological and structural characterization of polypropylene based nanocomposites. Polymer, **46**, 8275–8285 (2005). DOI: 10.1016/j.polymer.2005.06.056

[14] Ciardelli F., Coiai S., Passaglia E., Pucci A., Ruggeri G.: Nanocomposites based on polyolefins and functional thermoplastic materials. Polymer International, **57**, 805–836 (2008). DOI: 10.1002/pi.2415

[15] Broekaert C., Peeterbroeck S., Benali S., Monteverde F., Bonnaud L., Alexandre M., Dubois P.: Chlorinated polyethylene/layered silicate nanocomposites: Poly(ε-caprolactone)-based 'masterbatch' approach. European Polymer Journal, **43**, 4160-4168 (2007). DOI: 10.1016/j.eurpolymj.2007.08.003

[16] Hindeleh A. M., Johnson D. J.: The resolution of multipeak data in fibre science. Journal of Physics D: Applied Physics, **4**, 259–263 (1971). DOI: 10.1088/0022-3727/4/2/311

[17] Marigo A., Marega C., Cecchin G., Collina G., Ferrara G.: Phase transition II→I in isotactic poly-1-butene: Wide- and small-angle X-ray scattering measurements. European Polymer Journal, **36**, 131–136 (2000). DOI: 10.1016/S0014-3057(99)00043-9

[18] Zannetti R., Manaresi P., Buzzoni G. C.: Crystallinity and polymorphism of poly-α-butene (in Italian). La Chimica e l'Industria, **43**, 735–740 (1961).

[19] Blundell D. J.: Models for small-angle X-ray scattering from highly dispersed lamellae. Polymer, **19**, 1258–1266 (1978). DOI: 10.1016/0032-3861(78)90302-6

[20] Marega C., Marigo A., Cingano G., Zannetti R., Paganetto G.: Small-angle X-ray scattering from high-density polyethylene: Lamellar thickness distributions. Polymer, **37**, 5549–5557 (1996). DOI: 10.1016/S0032-3861(96)80440-X

[21] Marega C., Marigo A., Causin V.: Small-angle X-ray scattering from polyethylene: Distorted lamellar structures. Journal of Applied Polymer Science, **90**, 2400–2407 (2003). DOI: 10.1002/app.12890

[22] Causin V., Marega C., Marigo A., Ferrara G.: Assessing organo-clay dispersion in polymer layered silicate nanocomposites: A SAXS approach. Polymer, **46**, 9533–9537 (2005). DOI: 10.1016/j.polymer.2005.08.034

[23] Marega C., Causin V., Marigo A.: A SAXS-WAXD study on the mesomorphic-α transition of isotactic polypropylene. Journal of Applied Polymer Science, **109**, 32–37 (2008). DOI: 10.1002/app.28017

[24] Hosemann R., Bagchi S. N.: Direct analysis of diffraction by matter. North Holland, Amsterdam (1962).

[25] Azzurri F., Alfonso G. C., Gómez M. A., Martì M. C., Ellis G., Marco C.: Polymorphic transformation in isotactic 1-butene/ethylene copolymers. Macromolecules, **37**, 3755–3762 (2004). DOI: 10.1021/ma0358327

[26] Azzurri F., Gómez M. A., Alfonso G. C., Ellis G., Marco C.: Time-resolved SAXS/WAXS studies of the polymorphic transformation of 1-butene/ethylene copolymers. Journal of Macromolecular Science Part B: Physics, **43**, 177–189 (2004). DOI: 10.1081/MB-120027757

[27] Asada T., Sasada J., Onogi S.: Rheo-optical studies of high polymers. XXI. The deformation process and crystal transformation in polybutene-1. Polymer Journal, **3**, 350–356 (1972). DOI: 10.1295/polymj.3.350

[28] Ma J., Zhang S., Qi Z., Li G., Hu Y.: Crystallization behaviors of polypropylene/montmorillonite nanocomposites. Journal of Applied Polymer Science, **83**, 1978–1985 (2002).
DOI: 10.1002/app.10127

[29] Hambir S., Bulakh N., Jog J. P.: Polypropylene/clay nanocomposites: Effect of compatibilizer on the thermal, crystallization and dynamic mechanical behavior. Polymer Engineering and Science, **42**, 1800–1807 (2002).
DOI: 10.1002/pen.11072

[30] Causin V., Marega C., Marigo A., Ferrara G., Ferraro A., Selleri R.: Structure-property relationships in isotactic poly(propylene)/ethylene propylene rubber/ montmorllonite nanocomposites. Journal of Nanoscience and Nanotechnology, **8**, 1823–1834 (2008).
DOI: 10.1166/jnn.2008.0031823

[31] Wilson O. C., Olorunyolemi T., Jaworski A., Borum L., Young D., Siriwat A., Dickens E., Oriakhi C., Lerner M.: Surface and interfacial properties of polymer-intercalated layered double hydroxide nanocomposites. Applied Clay Science, **15**, 265–279 (1999).
DOI: 10.1016/S0169-1317(99)00023-X

[32] Mehta S., Mirabella F. M., Rufener K., Bafna A.: Thermoplastic olefin/clay nanocomposites: Morphology and mechanical properties. Journal of Applied Polymer Science, **92**, 928–936 (2004).
DOI: 10.1002/app.13693

[33] Fasulo P. D., Rodgers W. R., Ottaviani R. A., Hunter D. L.: Extrusion processing of TPO nanocomposites. Polymer Engineering and Science, **44**, 1036–1045 (2004).
DOI: 10.1002/pen.20097

[34] Zhang Z., Zhang L., Li Y., Xu H.: New fabricate of styrene–butadiene rubber/montmorillonite nanocomposites by anionic polymerization. Polymer, **46**, 129–136 (2005).
DOI: 10.1016/j.polymer.2004.11.008

[35] Ostwald W.: The formation and changes of solids. Zeitschrift für Physikalische Chemie, **22**, 286–330 (1897).

[36] Keller A., Hikosaka M., Rastogi S., Toda A., Barham P. J., Goldbeck-Wood G.: An approach to the formation and growth of new phases with application to polymer crystallization: Effect of finite size, metastability, and Ostwald's rule of stages. Journal of Materials Science, **29**, 2579–2604 (1994).
DOI: 10.1007/BF00356806

[37] Keller A., Goldbeck-Wood G., Hikosaka M.: Polymer crystallization: Survey and new trends with wider implications for phase transformations. Faraday Discussions, **95**, 109–128 (1993).
DOI: 10.1039/FD9939500109

[38] Weynant E., Haudin J. M., G'Sell C.: Plastic deformation and solid-phase transformation in polybutene-1. Journal of Materials Science, **17**, 1017–1035 (1982).
DOI: 10.1007/BF00543521

[39] Chau K. W., Yang Y. C., Geil P. H.: Tetragonal → twinned hexagonal crystal phase transformation in polybutene-1. Journal of Materials Science, **21**, 3002–3014 (1986).
DOI: 10.1007/BF00553329

[40] Ninomiya N., Nam P. H., Fujimori T., Masuko T.: Distribution of clay particles in the spherulitic texture of poly(L-lactide)/organo-modified montmorillonite hybrids. e-Polymers, no.041 (2004).

[41] Maiti P., Nam P. H., Okamoto M., Kotaka T., Hasegawa N., Usuki A.: The effect of crystallization on the structure and morphology of polypropylene/clay nanocomposites. Polymer Engineering and Science, **42**, 1864–1871 (2002).
DOI: 10.1002/pen.11079

[42] Maiti P., Nam P. H., Okamoto M., Hasegawa N., Usuki A.: Influence of crystallization on intercalation, morphology, and mechanical properties of polypropylene/clay nanocomposites. Macromolecules, **35**, 2042–2049 (2002).
DOI: 10.1021/ma010852z

[43] Schaefer D. W., Justice R. S.: How nano are nanocomposites? Macromolecules, **40**, 8501–8517 (2007).
DOI: 10.1021/ma070356w

[44] Wanjale S. D., Jog J. P.: Crystallization and phase transformation kinetics of poly(1-butene)/MWCNT nanocomposites. Polymer, **47**, 6414–6421 (2006).
DOI: 10.1016/j.polymer.2006.07.011

[45] Yang B. X., Shi J. H., Li X., Pramoda K.P., Goh S.H.: Mechanical reinforcement of poly(1-butene) using polypropylene-grafted multiwalled carbon nanotubes. Journal of Applied Polymer Science, **113**, 1165–1172 (2009).
DOI: 10.1002/app.30056

[46] Chen W., Feng L., Qu B. J.: Preparation of nanocomposites by exfoliation of ZnAl layered double hydroxides in nonpolar LLDPE solution. Chemistry of Materials, **16**, 368–370 (2004).
DOI: 10.1021/cm0303484

[47] Qiu L., Chen W., Qu B.: Structural characterisation and thermal properties of exfoliated polystyrene/ZnAl layered double hydroxide nanocomposites prepared via solution intercalation. Polymer Degradation and Stability, **87**, 433–440 (2005).
DOI: 10.1016/j.polymdegradstab.2004.09.009

[48] Costa F. R., Abdel-Goad M., Wagenknecht U., Heinrich G.: Nanocomposites based on polyethylene and Mg–Al layered double hydroxide. I. Synthesis and characterization. Polymer, **46**, 4447–4453 (2005).
DOI: 10.1016/j.polymer.2005.02.027

[49] Gohil R. M., Miles M. J., Petermann J.: On the molecular mechanism of the crystal transformation (tetragonal-hexagonal) in polybutene-1. Journal of Macromolecular Science Part B: Physics, **21**, 189–201 (1982).
DOI: 10.1080/00222348208204934

eXPRESS Polymer Letters Vol.5, No.12 (2011) 1062–1074
Available online at www.expresspolymlett.com
DOI: 10.3144/expresspolymlett.2011.104

Multiple criteria decision making with life cycle assessment for material selection of composites

A. S. Milani, C. Eskicioglu, K. Robles, K. Bujun, H. Hosseini-Nasab*

School of Engineering, University of British Columbia, Okanagan Campus, Kelowna, BC V1V 1V7, Canada

Received 25 January 2011; accepted in revised form 25 June 2011

Abstract. With the advancement of interdisciplinary approaches in today's modern engineering, current efforts in optimal design of composites include seeking material selection protocols that can (1) simultaneously consider a series of mechanical/electrical/chemical cost criteria over a set of alternative material options, and (2) closely take into account environmental aspects of final products including recycling and end-of-life disposal options. In this paper, in addition to a review of some recent experimental and methodological advances in the above areas, a new application of multiple criteria decision making (MCDM) is presented to deal with decision conflicts often seen among design criteria in composite material selection with the help of life cycle assessment (LCA). To show the application, an illustrative case study on a plastic gear material selection is conducted where the cost, mechanical and thermal properties along with environmental impact criteria are to be satisfied simultaneously. A pure plastic gear is compared to a Polyethylene terephthalate (PET)/aluminum-powder composite alternative. Results suggest that simple MCDM models, including a signal-to-noise measure adapted to MCDM in the same case study, can be used to explore both trade-offs and design break-even points in large decision spaces as the decision maker's perspective over environmental, material performance and cost attributes change during the design process. More advanced topics including the account of material data uncertainties are addressed.

Keywords: *polymer composites, material selection, multiple criteria decision making, life cycle assessment, sensitivity analysis*

1. Introduction

Material selection is crucial in many engineering projects as it can determine the durability, cost, and manufacturability of final products. In addition, due to increasing regulations by government organizations, manufactures are required to minimize environmental impacts of their processes and products. In fact, material selection can be pivotal for environmental concerns as recyclability and/or the end-of-life disposal methods vary from one choice of material to another. In today's integrated design processes (IDP), a systematic selection of the best material for a given application begins with indentifying multiple mechanical/electrical/chemical/thermal properties, environmental impact factors, and life cycle costs of candidate materials (Figure 1). In essence, IDP requires design teams from different disciplines to work together from the project onset to develop solutions that have *multiple benefits*. When multiple criteria from different disciplines are to be satisfied in a material selection problem, however, complexities often rise with regards to criteria conflicts and/or the importance of each criteria/discipline. Also, expert knowledge becomes fundamentally important to define correct indices within each discipline. For example, the leaf spring/beam of a wing spar may be desired to be light and at the same time strong to support a given bending load without deflecting excessively. The beam material selection problem is then considered as an opti-

*Corresponding author, e-mail: abbas.milani@ubc.ca

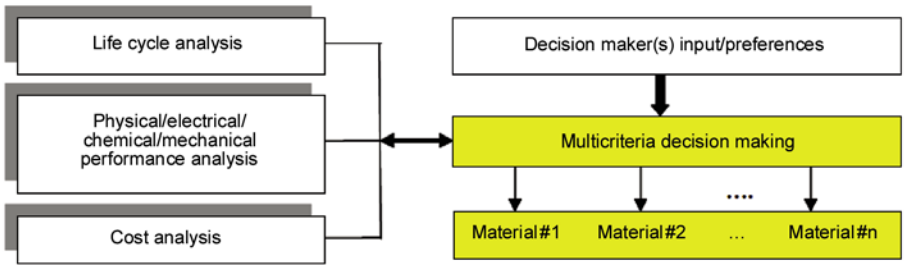

Figure 1. Schematic of material selection in an integrated design process

mization problem where the density, ρ, should be low while the elastic modulus, E, should be high enough to bear the load without exceeding a given maximum allowable deflection. It maybe assumed that the beam's length and width are constant and only its thickness can vary to accommodate the design objectives. The simultaneous formulation of the beam's mass and elastic deflection as a function of the thickness gives a material performance index (i.e., a combination/ratio of the material properties) as $E^{1/3}/\rho$. This index should be maximized during the material selection process; see [1] for more theoretical details. If during decision-making the mechanical design group in the project uses the density and stiffness as individual material properties (and not as a ratio as defined above), less accurate or not application-specific results would be obtained.

A number of recent experimental studies and selection methods have been reported in the literature to highlight the above multi-disciplinary nature of composite material and product selection in IDP's. Among these studies, those with a focus on environmental performance of composites are reviewed in Section 2. Research directions in relation to current efforts in improving the recycling techniques of composites are also addressed (Section 3). Next, an illustrative case study is presented in Section 4 on gear material selection with an emphasis on the application of multiple criteria optimization methods and their appropriateness to explore trade-offs and break-even design points when cost, environmental and mechanical factors are simultaneously taken into account. A new signal-to-noise (S/N) concept in MCDM is also adapted in the same case study. Concluding remarks are included in Section 5.

2. Composite design and material selection with environmental considerations: A review

In recent years, there has been an increasing trend in the use of composite materials primarily in the aerospace and transportation industries. In comparison to traditional materials, composites offer higher strength to weight ratios, non-corrosive properties, dimensional stability and good conformability. To give a few examples, percentage weight of composites has increased from 3% in Airbus A320 to over 20% in A380. Similarly, Boeing uses over 50% of composite materials in its 787 aircraft (for more specific examples of current applications of fiber-reinforced composites in the aircraft industry, see the study [2]). Similarly, composite materials have played key roles in reducing the magnetic, acoustic, hydrodynamic, radar, thermal signatures, as well as increasing payload, top speed, and operation range in marine structures [3].

Next to the above-mentioned superior physical and mechanical properties, recent studies show that composites can increase savings of emissions to the environment, in particular in transport industries, when compared to more traditional structural materials such as aluminum [4]. In air transport, emissions can be more environmentally damaging than those at ground level due to increased interaction of structures with gases at high altitudes. Scelsi *et al.* [4] through a life cycle assessment (LCA) analysis on a set of actual aerospace components showed that commercial fiber-reinforced composites such as GLARE yield substantial reductions in overall environmental impact during the use stage (e.g., 240 000 km of flight distance). This is despite the fact that composites are more energy intensive to manufacture and more difficult to dispose com-

pared to traditional materials such as aluminum. To address the latter gap/difficulty, numerous research groups have launched state-of-the-art projects to develop more environmentally friendly composites such as natural fiber-reinforced polymers.

Holbery and Houston [5] describe applications of natural-fiber-reinforced polymer composites in automotive components. Their work suggested that natural fibers in composites yield high quality composite products while minimizing environmental impacts. Namely, fibers such as flax, hemp, and kenaf were tested and compared to more traditional composites (such as glass fibers) to demonstrate the competence of the natural counterparts. Nonetheless, it was concluded that there still exist challenges to overcome in this field, including moisture stability, fiber-polymer interface compatibility, and consistency of fibers. Mechanical properties and biodegradability of green composites (as linked to environmental factors) have also been studied experimentally by Shibata *et al.* [6]. They scrutinized a set of composite laminates composed of regenerated cellulose (lyocell) fabric and three types of biodegradable polyesters [poly(3-hydroxybutyrate-co-3-hydroxyvarelate) (PHBV), poly(butylene succinate) (PBS), and poly(lactic acid) (PLA)]. The polyester/lyocell composite specimens were made of compression molding and examined for the effect of natural fiber content on their tensile moduli and strengths, as well as Izod impact resistance. In addition, biodegradability of the specimens were compared via a 120 day soil viral test and the order of highest to lowest biodegradable polyester/lyocell composite was found to be: PHBV > PLA > PBS. Regarding mechanical properties, at the same fiber content the order of candidate materials was as follows. Tensile moduli of PLA composites was higher than those of PBS and PHBV composites, whereas PBS composites had higher tensile strength than PHBV and PLA specimens. In view of MCDM, a clear indication of these results is that for each chosen design/ material selection criterion, a different top candidate can be nominated (i.e., the presence of conflicting criteria in choosing a final material).

Netravali *et al*. [7] presented a set of experiments intended to compare the mechanical performance of environmentally friendly (green) composites to common synthetic reinforced plastics. A modified soy protein based matrix was used by creating an 'interpenetrating network like (IPN-like) resin' with mechanical properties comparable to those of commonly used epoxy resin. The IPN-like soy protein-based resin was further reinforced using nano-clay and microfibrillated cellulose. Different fibers including high strength liquid crystalline cellulose, aramid and E-glass fibers in the modified resin were used and the ensuing tensile and flexural strengths of composites were tested. It was demonstrated that the green fiber alternative was very competent. Although the soy-based materials and cellulose were fully biodegradable, challenges such as consistent quality and water resistance remained yet to be overcome for full applications of green composites.

A formal LCA of biofibers as reinforcement in plastic transport pallets has been conducted by Corbiere-Nicollier *et al*. [8]. They performed LCA in order to analyze the possibility of using China's reed (CR) fiber as a replacement for glass fiber (GF). The analysis considered the entire life cycle of the two candidate materials including energy use, efficiency of transportation, and disposal waste phase. A comparison of emissions of pollutants into air, soil and water due the life cycle stages of the two materials was made (Table 1 only shows the emissions to the air as sample results). It was concluded that CR fiber could be an excellent alternative given that its lifetime is greater than the required minimum three years and over this period a notable effect on the reduction of polypropylene content, reduction of energy to create fibers, and improved fuel efficiency in transportation due to the use of lighter material are achieved. The CO_2 emission from GF pallet was 33.1 kg more than CR pallet.

Katz [9] compared the environmental load of fiber-reinforced polymer (FRP) reinforced pavements to that of steel reinforced pavement. The study accounted for the entire life cycle of the pavements, from obtaining the material resources to disposal. The analysis was carried out using the Eco-Indicator 99©: the environmental performance indicator method for LCA and ecodesign. The study divided the life cycle of a given pavement reinforcement candidate to three stages: erection, maintenance, and disposal (Table 2). Three types of carbon FRP's were tested and they all showed a lower environmental burden than the steel alternative in the main-

tenance stage, mainly due to the reduced cement content. However, at the disposal stage, the environmental load of the steel reinforced pavement, as can be seen in Table 2, was found to be lower than that of FRP reinforced pavements (i.e., again an example of a local criteria conflict in choosing the final/optimum material).

Table 1. Comparison of emissions of pollutants into air for glass fiber and China reed pallets [8]

Substance	Unit	GF pallet	CR pallet
Maleic anhydride	[mg]	×	5.88
Benzo[a]pyrene	[μg]	84.1	57.8
Cd	[mg]	32.7	26.8
CO	[g]	74.3	54.6
CO_2	[kg]	73.1	42.0
Cr	[mg]	8.53	4.92
Cu	[mg]	45	28.6
Dimethenamide	[mg]	×	36.9
Glyphosate	[mg]	×	38.7
H_2S	[mg]	80.6	28.3
HCl	[g]	4.48	3.65
HF	[mg]	506	201.0
Hg	[mg]	1.48	0.68
Methane	[g]	150	79.4
Mn	[mg]	36.6	24.3
N_2O	[g]	1.96	2.2
NH_3	[g]	0.123	11.3
Ni	[mg]	142	88.6
NMHC	[g]	497	318
NO_x	[g]	513	349
P	[mg]	5.19	2.27
Particles	[g]	57.5	35.1
Pb	[mg]	195	56.2
Pendimethaline	[mg]	×	34.6
SO_x	[g]	289	163
V	[g]	1.16	0.731
Zn	[mg]	512	375

Life cycle assessment of fiber reinforced composites (FRCs) has been extensively discussed by Umair [10]. After a review of the history of FRCs and a general classification of their constituents, a number of prominent applications of composites has been discussed in construction, aerospace and military, transportation, medical sciences, sports goods, musical instruments, household products, energy production, and marine industries. Subsequently, a possible method to analyze the life cycle of FRCs was developed and exemplified for lightweight materials selection in ship construction. Three candidate superstructures were compared: steel, balsawood core, and Polyvinyl chloride (PVC) foam. The life cycle of each superstructure was divided into manufacturing, maintenance, and scrapping stages for a total service life of 25 years. Considering the global warming, acidification, and abiotic depletion criteria, it was found that at the end-of-life stage of the LCA (Table 3), the steel structure would contribute most negatively to the environment. The production stage of the PVC structure would present the largest environmental impact due to the glass content in the insulation and in the face material.

The Centre for Design at the Royal Melbourne Institute of Technology or RMIT University has provided a technical report [11] on material selection strategies for sustainable product development. Among other examples, the report discussed the need for change in the economic and environmental impacts of the textile and fiber industry and made recommendations for improved resource management. Current textile production methods, for most part, cause resource depletion and excessive water consumption, as well as pollution through toxic

Table 2. Comparison of environmental loads (expressed in Eco-indicator 99 points) of alternative pavements [9]; *n* represents a given number of maintenance activities

Slab type	Erection	Maintenance	Disposal	Total	Relative load [%]
Steel reinforced pavement	179000	*n*·13200	6020	291000	100
FRP reinforced pavement 1	114000	N/A	7680	122000	44
FRP reinforced pavement 2	117000	N/A	7680	124000	45
FRP reinforced pavement 3	134000	N/A	9310	144000	52

Table 3. Comparison of environmental impact data for three ship superstructures with different waste disposal scenarios [10]

Impact categories	Balsa core sandwich super structure			PVC sandwich foam super structure			Steel super structure
	Landfill	Incineration	Recycle	Landfill	Incineration	Recycle	Recycle
Global warming (in kg CO_2 eq.)	0.127	0.127	0.127	0.128	0.128	0.128	0.152
Acidification (in kg SO_2 eq.)	0.000943	0.000943	0.000943	0.000951	0.000951	0.000951	0.00113
Abiotic depletion (in kg Sb eq.)	0.0111	0.0111	0.0111	0.0112	0.0112	0.0112	0.0133

chemicals. The study found that environmental impacts during all phases of fabric production can be reduced with changes in the use of renewable/recyclable crops, increased product life, optimization of water systems and reduced waste production.

Giudice *et al*. [12] described a new method of materials selection in the life-cycle design process by integrating mechanical and environmental performance criteria. Their method utilized a multi-objective analysis technique to show the application of the approach for material selection of a car brake disk. The considered decision parameters were cost, environmental impact, and mechanical performance. The candidate materials were grey cast iron BS 350 and F3K20S Duralcan (aluminum matrix composite). Limiting factors such as mechanical design thresholds, geometry constraints, and feasibility of manufacturing methods for each candidate material were accounted for. Next to formulating environmental impact indices for the problem, an original step was taken in their work to incorporate computer aided design tools (including finite element method/FEM) into the multi-objective decision model, thus avoiding the need for physical experiments in the early stages of decision-making. In fact, the use of FEM models in complex structural material selection problems automatically ensures the use of application-specific criteria values, which otherwise would have to be found through definition of performance indices as described in Section 1. For complex parts with nonlinear material and/or geometries, defining such indices analytically can be a very difficult task.

A multi-criteria decision matrix along with a grey relational solution method was developed by Chan and Tong [13] to choose the best materials for a vacuum cleaner dustbin. The candidate materials were analyzed with respect to their cost, impact on the environment and human health, and disposal methods. A weight (importance factor) was given to each criterion, but the weights could change depending on who makes the analysis (i.e., a subjective weighting method was adapted). Three types of materials were nominated: aluminum alloy (AL), acrylonitrile butadiene styrene (ABS) and polyurethane (PU). For the end-of-life (EOL) disposal stage, four strategies were taken into consideration: remanufacturing/reuse (REM), recycling (REC), incineration with energy recovery (INC), and disposal to landfill (LND). Subsequently, a grey coefficient was calculated and assigned to each combination of material-disposal options (e.g., ABS with recycling). The coefficients (scores) made it possible for the decision-maker to rank the candidates as shown in Table 4. The higher the coefficients, the better the option in relation to the EOL treatment.

Table 4. The EOL grey relational grades for candidate materials of a vacuum cleaner dustbin [13]

Ranking	EOL order pair	Grey relational grade
1	ABS-REC	0.7708
2	AL-REM	0.6920
3	ABS-INC	0.5083
4	ABS-LND	0.5081
5	AL-REC 0	0.4863
6	PU-INC 0	0.3846
7	PU-LND	0.3647

A systematic comparison of LCAs of compression moulded wood-fiber-reinforced polypropylene composite sheets with that of pure polypropylene is discussed by Xu *et al*. [14]. They introduced a new analysis index called 'material service density', which is defined as the volume of material satisfying a specific strength requirement. In contrast, for the cases where the volume of a part is fixed, they used the notion of 'volume functional unit'. Two sets of LCA were conducted on the wood-fiber-reinforced composites with 10, 30, and 50% levels of fiber (mass) contents and the pure polypropylene. It was concluded that when material service density is used as a functional index during decision-making, wood-fiber-reinforced composite demonstrates superior environmental friendliness compared to polypropylene. Authors also discussed that environmental loads of natural fiber reinforced composites can decrease with sufficient evidence when the use phase of the design is focused on. In other words, *it is of utmost importance for material designers to note that the use of natural fibers in composite materials does not automatically make them 'sustainable/ environment friendly' unless the use phases (i.e., transportation) can justify that.* It is the light density of natural fiber reinforced polymer products that makes them very attractive alternatives regarding their environmental impact during the use stage. If the material production phase is taken into account only, which often includes cultivation, pesticides and other types of chemical by-products, the envi-

ronmental standing of natural fiber composites compared to their counterparts made of synthetic fibers and resins is not conclusive. The energy regain obtained during recycling phase of green composites also plays an important role in the LCA analysis.

3. Recycling

While at the design stage, decision-making models are considered as powerful mathematical tools to assess the performance of different existing composite options against more traditional material alternatives, from the reviews presented in Section 2 and related patents such as [15], it is clear that a significant research interest is currently on the development of green composites composed of natural fibers (such as wood, bagasse, rice straw, and pine fibers) and/or biodegradable polymers such as polyglycolic acid (PGA) and cellulosic plastics. Some of the main challenges in this area remains to be the high cost of production, moisture stability problems during storage and utilization, quality consistency in produced composites, and effective coupling agents between fibers and polymer [16, 17]. Further research is needed before these new genre of composites can fully replace current synthetic composite constituents. At the same time, improving recycling techniques of synthetic composites is a key factor to address environmental aspects of using these materials and also landfill use restrictions that are increasingly faced by different composite manufacturers. Recycling technologies for thermoset composites is extensively reviewed in the reference [18]. The major problem with recycling these materials is the existence of cross linked molecules in the polymer. Some reported recycling processes include pyrolysis, use of thermal fluidized bed, and grinding. The LCA and recycling techniques of thermoplastic composites such as PE, PP, PS and PVC, technical challenges along with their economic merits can be found in other studies such as [19, 20]. The most commonly used technique is perhaps mechanical recycling, when compared to chemical, physicochemical or energy recovery recycling. In the mechanical method, plastics from industrial waste undergo sorting, shredding and washing processes to yield plastic flakes, pellets or powder that can be reused in the manufacturing of new products, e.g., via extrusion. It is shown that recycled composites can significantly reduce environmental impact during the materials acquisition and processing phases compared to conventional virgin thermoplastics [20].

Remark: It is worth adding that although over the past decade some of the recycling processes of synthetic composites along with the development of natural composites have proven to yield high amounts of recyclates and save significant environmental loads, there still seems to be a need for more imminent demand in market in order to achieve their cost effectiveness across composite sectors for mass production. The actual case studies such as [21] show that the recycling of composites would not be cost-effective for companies unless there are dramatic changes to recycling policies or cost of petroleum.

4. An illustrative example on gear material selection: A new application of signal-to-noise

This case study is primarily intended to illustrate the application of MCDM by which concerns about multiple conflicting criteria can be formally addressed into an interdisciplinary material selection process. MCDM, also often referred to as multicriteria optimization, is particularly useful for the comparison of a finite set of different alternatives/scenarios against a set of decision criteria [22]. Both qualitative and quantitative values, monotonic and non-monotonic criteria, design tolerances, along with both objective and subjective weighting factors from individual or group of decision makers can be incorporated into such solution methods.

Different types of MCDM models have been already employed in the past decade for material selection problems concerning mechanical properties, cost and manufacturing criteria; see [23] for a state-of-the-art review.

In the early stage of a design, more general methods such as Ashbey's material selection charts can be used to identify a range of possible material solutions/candidates given an application. Alternatively screening methods, such those reviewed in [23], can be applied to shortlist a large pool/table of material candidates. In the simplest form, the screening process may involve defining a minimum/threshold value for each decision criteria. A candidate material is shortlisted only if it passes all

the criteria thresholds. As such, all the screened candidates are considered feasible solutions, yet they should be ranked from top to bottom for a final decision at the end of the design process. For the latter ranking, MCDM methods such as the weighted sum method (WSM), TOPSIS, ELECTRE can be used [24]. No or little effort has been made to formally incorporate the above powerful decision making tools in material selection problems in the presence of LCA criteria. The selection techniques employed in the studies [12] and [13] can be indentified within this category of models.

To exemplify the application of MCDM in the intended case study, let us take two different gear material options along with their cost, thermal and mechanical performances, and environmental impacts. The given material options are pure polyethylene terephthalate (PET) and a composite made of 70% PET (i.e., with the weight fraction μ_{PET} = 0.7) and 30% aluminum powder (μ_{Al} = 0.3). The PET/aluminum powder composite (Figure 2) is an example of the large variety of polymer-matrix/particle filling composites that are widely used in military and civil applications [25]. The material cost, thermal and mechanical properties of each alternative gear option are included in Table 5. Environmental impact of PET-Al gear is assessed by establishing a life cycle shown in Figure 3. Subsequently, using the GaBi 4 software, an LCA analysis was performed based on three stages of life cycle: material production, transportation, and disposal/recycling. In Figure 3, the composite gear manufacturing facility receives PET (70% by weight) and aluminum (30% by weight) as raw materials which weigh a total of 1 lb. Only 50% (0.35 lb) of the total PET (0.70 lb) is new PET while the remaining portion (0.35 lb) is the recycled material according to the recyclable fraction in Table 5. Similarly, only 15% (0.045 lb) of the total aluminum (0.30 lb) is new aluminum as the remaining weight (0.255 lb) is comprised of the recycled material based on 85% recyclable fraction indicated for aluminum. In Figure 3, in addition to manufacturing, two separate disposal options are considered. Upon manufacturing and consumer use, 50% of the non-recyclable portions of the PET (0.175 lb) and aluminum (0.0225 lb), in other words the 'solid waste' generated, are assumed to be incinerated while the remaining waste fractions (50%) are directed to a nearby landfill. Similarly, the LCA analysis was repeated for the pure PET gear option.

The obtained environmental criteria values from LCA are added in Table 5 next to the mechanical and cost criteria. It is assumed that the manufactur-

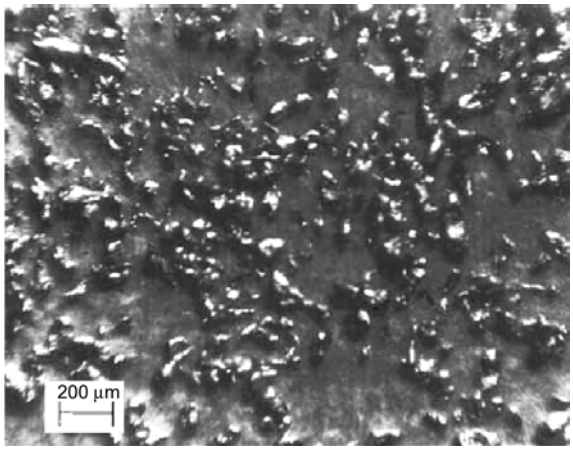

Figure 2. Sample micrograph of aluminum powder in a polymer matrix (Tavman, 1996)

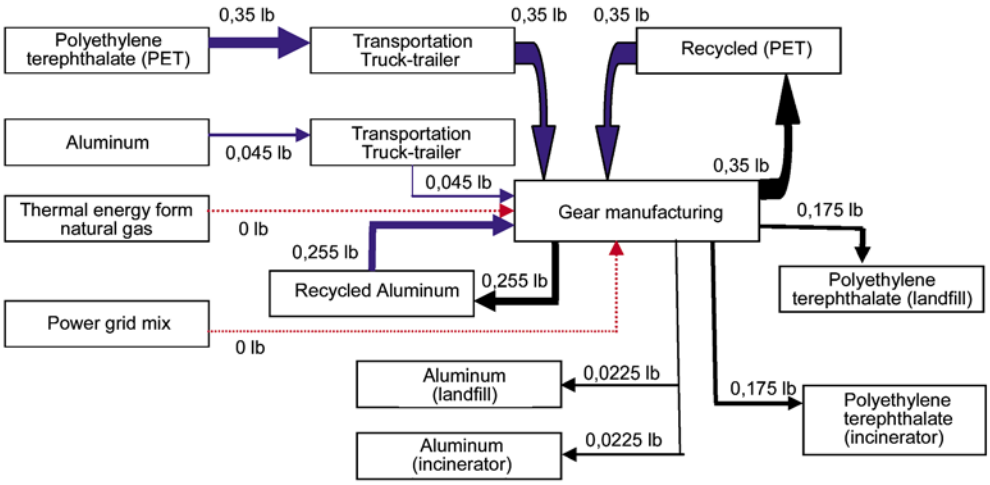

Figure 3. A basic life cycle of the PET-Al composite gear

ing cost and energy of the two material candidates are comparable (at least for a low-scale production). The negative signs in the last column of Table 5 indicate that the corresponding criteria are defined as cost-type (i.e., the lower the better) by the designer. The composite mechanical properties needed to be estimated from the volume fraction of its constituents (i.e., PET and Al). To this end, a simple rule of mixture was used as Equation (1):

$$P_{composite} = v_{Al} \cdot P_{Al} + v_{PET} \cdot P_{PET} \quad (1)$$

where P represents the property to be obtained in relation to the percentage compositions of the constituent materials v_{Al} and v_{PET} are the volume fractions of the composite constituents and can be related to their weight fractions based on Equations (2) and (3) [26]:

$$\mu_{Al} = \frac{\rho_{Al}}{\rho_{composite}} v_{Al} \quad (2)$$

$$\mu_{PET} = \frac{\rho_{PET}}{\rho_{composite}} v_{PET} \quad (3)$$

where $\rho_{composite}$ is the density of the composite and is related to the density of the constituents as Equation (4):

$$\frac{1}{\rho_{composite}} = \frac{\mu_{Al}}{\rho_{Al}} + \frac{\mu_{PET}}{\rho_{PET}} \quad (4)$$

For calculating the effective longitudinal thermal expansion coefficient of the composite, $\alpha_{composite}$,

Table 5. Multi-disciplinary property values of candidate materials in the present case study

Category	Properties	Al (Min)	Al (Max)	PET (Min)	PET (Max)	Al (Ave)	PET gear (Ave)	Composite gear (Ave)	Normalized PET properties	Normalized composite properties	± Factor
Cost	Price [USD/lb]	0.6453	1.046	0.835	0.919	0.846	0.4383*	0.3449**	–1	–0.7868	–
Mechanical-thermal	Density [lb/in^3]	0.0964	0.0986	0.047	0.051	0.098	0.0486	0.0572	–0.8494	–1.0000	–
	Young's modulus [10^6 psi]	10.1	10.44	0.4	0.601	10.27	0.5004	2.2191	0.2255	1.0000	+
	Elastic limit [ksi]	4.134	4.569	8.195	9.036	4.352	8.6155	7.8653	1	0.9129	+
	Tensile strength [ksi]	11.02	12.18	7.005	10.5	11.6	8.7525	9.2535	0.9459	1.0000	+
	Hardness rockwell [R]	24.5	25.5	17	18.7	25	17.85	19.1079	0.9342	1.0000	+
	Endurance limit [ksi]	3.046	3.336	2.802	4.2	3.191	3.501	3.4465	1	0.9844	+
	Fracture toughness [ksi·in$^{1/2}$]	27.3	31.85	4.323	4.778	29.58	4.5505	8.9530	0.5083	1.0000	+
	Thermal conductivity [BTU·ft/h·ft^2·F]	118.4	123.1	0.08	0.087	120.8	0.0835	21.3119	0.0039	1.0000	+
	Thermal expansion [µstrain/F]	12.33	13	63.7	66.3	12.67	65	22.3901	–1	–0.3445	–
	Max service temp [F]	266	392	152.6	188.6	329	170.6	198.4667	0.8596	1.0000	+
Environmental	Production energy [kcal/lb]	20500	22600	8624	9534	21560	9079	12823	–0.7080	–1	–
	CO_2 creation [lb/lb],	9.03	9.98	2.21	2.45	9.505	2.33	4.4825	–0.5198	–1	–
	Recyclable fraction	0.8	0.9	0.45	0.55	0.85	0.5	0.605	0.8264	1	+
	Resources [lb/lb]						247.91	247.93	–0.9999	–1	–
	Emission to air [lb/lb]						240.82	240.75	–1	–0.9997	–
	Emission to fresh water [lb/lb]						0.3375	0.32	–1	–0.9483	–
	Emission to sea water [lb/lb]						0.0101	0.0101	–1	–1	–
	Emission to industrial soil [lb/lb]						0.0001	0.0001	–1	–0.9663	–

*For 1 lb of the PET gear, 50% of the material comes from the recycled fraction, thus the net cost is reduced by 50%.
**For 1 lb of the composite gear, 50% of PET and 85% of Al come from the corresponding recycled fractions, thus the estimated cost is adjusted.

the thermoelastic extremum principle yields [26] (Equation (5)):

$$\alpha_{composite} = \frac{E_{Al}}{E_{composite}}(v_{Al}\cdot\alpha_{Al}) + \\ + \frac{E_{PET}}{E_{composite}}(v_{PET}\cdot\alpha_{PET}) \quad (5)$$

where $E_{AL,\ PET,\ composite}$ denotes, respectively, the Young's modulus of Al, PET and the composite (Table 1). Finally, for the composite environmental factors, a similar rule of mixture as in Equation (1) was employed by using the weight fractions in order to be consistent with the Eco-indicator 99 values.

Next, properties within each category of cost, environmental impact, thermal/mechanical performance are normalized using the two average values in each row (one for PET and one for the composite). The normalization is necessary since different properties are of different units. To this end, each criterion value is divided by the maximum of the two material values. For example, for the elastic limit criterion, the (average) PET value is 8.6155 ksi and the composite value is 7.8653 ksi. The normalized values, respectively, are calculated as 8.6155/8.6155 and 7.8653/8.6155. For cost-type criteria, after the above normalization, the values are multiplied by '–1' as seen in the grey cell (i.e., the final decision matrix) in Table 5.

From the normalized decision matrix, where for all values the higher-the-better, one can notice that each material option is superior to the other under some particular criteria, but lacking under the rest of criteria. To aggregate all the conflicting criteria values into one overall score, the well-known weighted sum method (WSM) was used for each material; $i = 1, 2$ (Equation (6)) [22]:

$$Score_i = \sum \omega_{(cost)}\cdot NP_{j(cost)} \\ + \sum \omega_{(Mechanical\text{-}Thermal)}\cdot NP_{j\ (Mechanical\text{-}Thermal)} + \\ + \sum \omega_{(Environmental)}\cdot NP_{j(Environmental)} \quad (6)$$

where NP_j refer to the normalized values and ω values are the weights of the three categories of criteria for the decision maker/designer. For instance, if environmental impact is a major concern in a project, the weight of all criteria under this category would have higher values than the rest of criteria. In the current example, a set of initial weights was assumed as shown in Table 6. Based on these weights and the equation above, the sub-total and the total score of each material are calculated in Table 7. The overall score of the composite suggests that it should be ranked/preferred over the pure PET option. Also, for both materials, it is clear from the sub-criteria scores that the (negative) environmental load is the highest compared to the mechanical/thermal and cost performance values.

Table 6. Initial weights of different criteria categories based on the designer/decision-maker's viewpoint

	Category		
	Cost	**Mechanical/Thermal**	**Environmental**
Weight	0.25	0.25	0.5

Table 7. Scores for the PET and composite options using the weights in Table 6

Materials / Criteria categories	PET	Composite
Cost	–0.250	–0.196
Mechanical/Thermal	0.907	1.638
Environmental	–2.700	–2.957
WSM total score	–2.043	–1.515

4.1. Sensitivity analysis

After an initial estimation of weights, it is often the case that the designer/decision maker (DM) would be interested to know how the trade-off between criteria categories plays a role on the final material ranking (sensitivity analysis). To this end, it would suffice that the DM simply changes the relative weight values (ω) between the criteria groups and recalculates the scores. Different weight combinations yield different material recommendations as summarized in Figures 4–6. Since here we have three categories of criteria, for better visualization purposes, a mapping from three-dimensional Pareto space to the two-dimensional space has been used by fixing the level of one weight at a time and plotting the effect of the variation of the other two on the material scores. Also note that at each point, the sum of weights (cost, environmental, and mechanical-thermal) is the unity. For instance, in Figure 4a, given the cost weight of 10%, the summation of mechanical-thermal and environmental criteria should be 90%. That means, e.g., for the two points

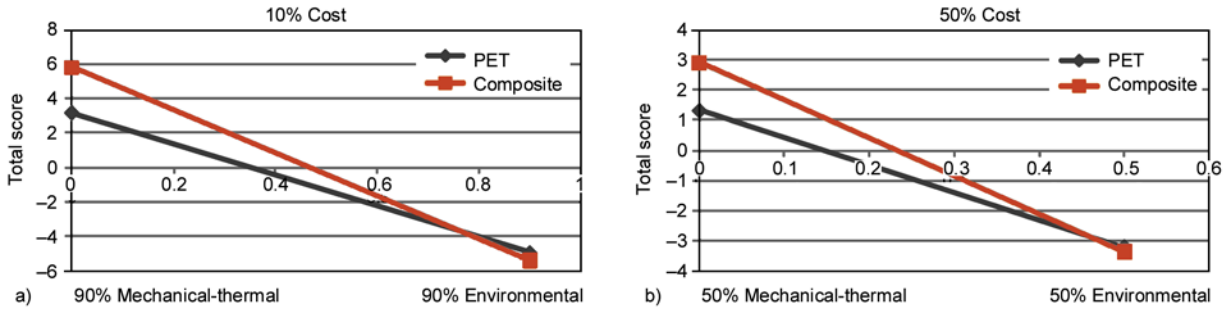

Figure 4. The trade-off between the (thermo) mechanical and environmental criteria at different fixed cost criterion weights

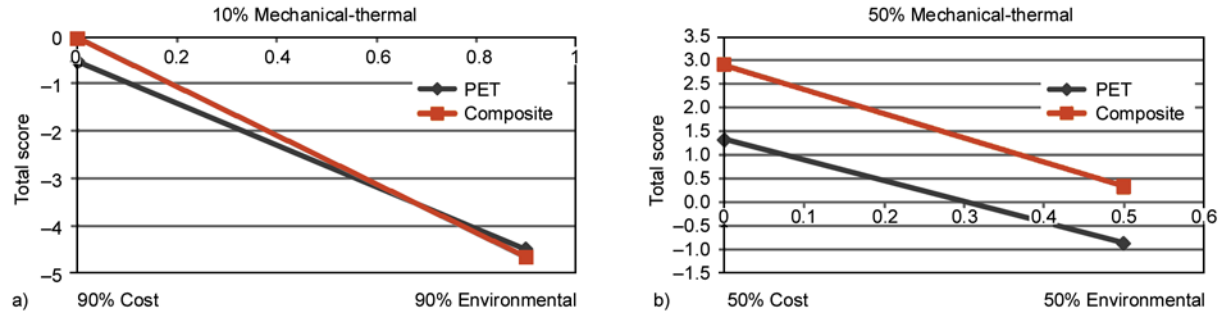

Figure 5. The trade-off between the cost and environmental criteria at different fixed (thermo) mechanical criteria weights

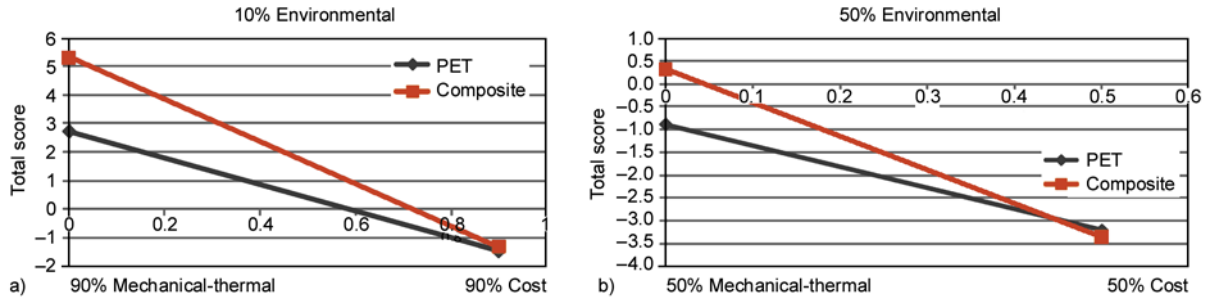

Figure 6. The trade-off between the cost and (thermo) mechanical criteria at different fixed environmental criteria weights

on the left corner of the plot, the mechanical-thermal criteria weight is 90% and the environmental 0%.

From Figure 4b one can conclude that at a high weight of cost (~50%), the composite material outperforms PET regardless of their differences in the mechanical-thermal performance and environmental impact values due to higher recyclability percentage. From Figure 4a, however, one notices that when the cost weight is low (10%), there is a 'break even' point (~15% mechanical-thermal, i.e., 75% environmental) where the ranking of the two material swaps. A similar break-even point can be noticed in Figure 5a regarding the cost and environmental criteria. The indication from this figure along with Table 7 is that a low cost can be achieved at the expense of higher environmental impact and vice versa. For higher mechanical-thermal weights as in Figure 5b, the composite is noticeably preferred over PET. Finally, from Figure 6, it is seen that the composite can outperform the PET alternative with no break-even point for lower environmental weights (up to ~35%).

4.2. A signal-to-noise concept

The WSM method in Equation (6) is perhaps the most common method among MCDM models in practical applications [27]. It is important, however, to understand that this method is compensatory in that the sub-scores of criteria (after normalization and weighting) are added together to find a total score. As such, the decision maker/designer implicitly agrees that a low value of one criterion can be compensated by a high value of another criterion in the final decision-making. This should be true most of the time for the type of applications outlined in

this paper (selection of optimal composite product), but there may be cases where the designer would like to limit this direct compensation among selection criteria by means of their variability. To this end, here we use a new concept based on a signal-to-noise (S/N) ratio for material selection.

The definition of S/N may be based on the inverse of well-known 'coefficient of variation (CV)' in statistics. CV, also known as unitized risk, is a normalized measure of dispersion which is found by dividing the standard deviation of a sample σ to its mean μ. Thus, the S/N score may be defined as μ/σ. To understand this in the MCDM context, let us recall the upper-level decision matrix of Table 7, where sub-criteria within each category (environmental, mechanical/thermal, and cost) have been aggregated, but the designer may hesitate to sum the values between groups of different criteria. To formalize this non-compensatory ranking preference, for each material column in Table 7 one can find the mean μ and divide it by the standard deviation of the column σ. For instance, for PET (Equation (7)):

$$S/N_{(PET)} = \frac{\text{Average}(-0.250, 0.907, -2.700)}{\text{STD}(-0.250, 0.907, -2.700)} = \\ = -0.369 \quad (7)$$

Similarly, for the composite option we find $S/N_{(composite)} = -0.218$. A larger signal to noise ratio should be preferred. In essence this means, one would like to chose a material that on average has a high score (μ) over all criteria but at the same time has a low variation (σ) among different categories of criteria. That is, ideally, the chosen material should be good in all criteria. Given the above scores for the two alternative materials in the present case study, the composite option outperforms the pure plastic material with the S/N non-compensatory approach.

5. Conclusions

In today's integrated design processes for composite products, it is necessary to explore optimal design options by simultaneously analyzing material properties in a multitude of disciplines (mechanical, cost, environmental, etc). Next to the existing selection tools [28], MCDM models can provide the ability to formulate and systematically compare different alternatives against large sets of design criteria, thus giving engineers a versatile tool to tackle complex decision-making tasks. To show an application of a well-known MCDM method (namely the WSM) in a relatively large-scale decision space (with one cost, seven environmental, and eleven mechanical/thermal attributes), an illustrative example was presented in a plastic gear material selection problem. A pure PET gear was compared to a composite PET/aluminum-powder alternative. The results showed a higher total score for the composite. It was also shown that the method can be employed to explore criteria trade-offs and decision break-even points by varying the designer's weights over different criteria categories. Similar MCDM models can be used by other practitioners to mathematically study the benefits gained and losses endured during material development, replacement or selection of new products. In doing so, however, next to basic MCDM models such as WSM, it may be worth investigating the application of more advanced methods that can include uncertainties both in material datasets as well as designers/decision makers' opinions over criteria weights (see, e.g. [29] for an application of ELECTRE III and revised Simos' methods). Advanced MCDM methods under uncertain/incomplete data can be particularly important for the LCA analysis of composites since inventory databases in the commercial LCA packages are still not inclusive and modeling assumptions normally need to be made (as is the case in several reported LCA studies including those reviewed in this article). The notation of compensation and non-compensations may be accounted for during multi-disciplinary material selection problems. An application of a signal-to-noise concept was recommended in the present case study by dividing the average score of each alternative over a dispersion measure showing the non-uniformity of the given material performance over different criteria categories. Finally, it should be pointed out that for more practical, real-world design scenarios, the analysis of material candidates' disposal options as well as their recyclable percentages need to be aligned with waste management codes and regulations of both manufacturers and local authorities. Accordingly, next to the cost of raw material, the inclusion of production and disposal costs can be vital for a successful multiple criteria material selection process.

Acknowledgements

Financial support from the Natural Sciences and Engineering Research Council (NSERC) of Canada as well as the UBC's Work-Learn Program is acknowledged. The authors are also grateful to the anonymous referees for their constructive comments and suggestions.

References

[1] Ashby M.: Materials selection in mechanical design. Butterworth-Heinemann, Burlington (1999).

[2] Soutis C.: Fibre reinforced composites in aircraft construction. Progress in Aerospace Sciences, **41**, 143–151 (2005). DOI: 10.1016/j.paerosci.2005.02.004

[3] Lua J.: Thermal–mechanical cell model for unbalanced plain weave woven fabric composites. Composites Part A: Applied Science and Manufacturing, **38**. 1019–1037 (2007). DOI: 10.1016/j.compositesa.2006.06.023

[4] Scelsi L., Bonner M., Hodzic A., Soutis C., Wilson C., Scaife R., Ridgway K.: Potential emissions savings of lightweight composite aircraft components evaluated through life cycle assessment. Express Polymer Letters, **5**, 209–217 (2011). DOI: 10.3144/expresspolymlett.2011.20

[5] Holbery J., Houston D.: Natural-fiber-reinforced polymer composites in automotive applications. Journal of the Minerals, Metals and Materials Society, **58**, 80–86 (2006). DOI: 10.1007/s11837-006-0234-2

[6] Shibata M., Oyamada S., Kobayashi S., Yaginuma D.: Mechanical properties and biodegradability of green composites based on biodegradable polyesters and lyocell fabric. Journal of Applied Polymer Science, **92**, 3857–3863 (2004). DOI: 10.1002/app.20405

[7] Netravali A. N., Huang X., Mizuta K.: Advanced 'green' composites. Advanced Composite Materials, **16**, 269–282 (2007). DOI: 10.1163/156855107782325230

[8] Corbière-Nicollier T., Gfeller Laban B., Lundquist L., Leterrier Y., Månson J.: Jolliet O.: Life cycle assessment of biofibres replacing glass fibres as reinforcement in plastics. Resources, Conservation and Recycling, **33**, 267–287 (2001). DOI: 10.1016/S0921-3449(01)00089-1

[9] Katz A.: Environmental impact of steel and fiber–reinforced polymer reinforced pavements. Journal of Composites for Construction, **8**, 481–488 (2004). DOI: 10.1061/(ASCE)1090-0268(2004)8:6(481)

[10] Umair S.: Environmental impacts of fiber composite materials. MSc Thesis, Royal Institute of Technology, Stockholm (2006).

[11] Centre for Design at RMIT University: Aiming for sustainable product development. Technical report (2001).

[12] Giudice F., La Rosa G., Risitano A.: Materials selection in the life-cycle design process: A method to integrate mechanical and environmental performances in optimal choice. Materials and Design, **26**, 9–20 (2005). DOI: 10.1016/j.matdes.2004.04.006

[13] Chan J. W. K., Tong T. K. L.: Multi-criteria material selections and end-of-life product strategy: Grey relational analysis approach. Materials and Design, **28**, 1539–1546 (2007). DOI: 10.1016/j.matdes.2006.02.016

[14] Xu X., Jayaraman K., Morin C., Pecqueux N.: Life cycle assessment of wood-fibre-reinforced polypropylene composites. Journal of Materials Processing Technology, **198**, 168–177 (2008). DOI: 10.1016/j.jmatprotec.2007.06.087

[15] Turnlund T. H.: Biodegradable mesh and film stent. U.S. Patent 5766710, USA (1998).

[16] Mohanty A. K., Misra M., Drzal L. T.: Sustainable biocomposites from renewable resources: Opportunities and challenges in the green materials world. Journal of Polymers and the Environment, **10**, 19–26 (2002). DOI: 10.1023/A:1021013921916

[17] Xu Y., Wu Q., Lei Y., Yao F., Zhang Q.: Natural fiber reinforced poly(vinyl chloride) composites: Effect of fiber type and impact modifier. Journal of Polymers and the Environment, **16**, 250–257 (2008). DOI: 10.1007/s10924-008-0113-8

[18] Pickering S. J.: Recycling technologies for thermoset composite materials – Current status. Composites Part A: Applied Science and Manufacturing, **37**, 1206–1215 (2006). DOI: 10.1016/j.compositesa.2005.05.030

[19] Gowayed Y. A., Vaidyanathan R., El-Halwagi M.: Synthesis of composite materials from waste fabrics and plastics. Journal of Elastomers and Plastics, **27**, 78–90 (1995). DOI: 10.1177/009524439502700106

[20] Vidal R., Martínez P., Garraín D.: Life cycle assessment of composite materials made of recycled thermoplastics combined with rice husks and cotton linters. International Journal of Life Cycle Assessment, **14**, 73–82 (2008). DOI: 10.1007/s11367-008-0043-7

[21] Duval D., MacLean H. L.: The role of product information in automotive plastics recycling: A financial and life cycle assessment. Journal of Cleaner Production, **15**, 1158–1168 (2007). DOI: 10.1016/j.jclepro.2006.05.030

[22] Sen P., Yang J-B.: Multiple criteria decision support in engineering design. Springer, New York (1998).

[23] Jahan A., Ismail M. Y., Sapuan S. M., Mustapha F.: Material screening and choosing methods – A review. Materials and Design, **31**, 696–705 (2010).
DOI: 10.1016/j.matdes.2009.08.013

[24] Milani A. S., Shanian A.: Gear material selection with uncertain and incomplete data. Material performance indices and decision aid model. International Journal of Mechanics and Materials in Design, **3**, 209–222 (2006).
DOI: 10.1007/s10999-007-9024-4

[25] Tavman I. H.: Thermal and mechanical properties of aluminum powder-filled high-density polyethylene composites. Journal of Applied Polymer Science, **62**, 2161–2167 (1996).
DOI: 10.1002/(SICI)1097-4628(19961219)62:12<2161::AID-APP19>3.0.CO;2-8

[26] Kaw A. K.: Mechanics of composite materials. CRC Press, Boca Raton (2005).

[27] Triantaphyllou E.: Multi-criteria decision making methods: A comparative study. Kluwer, New York (2000).

[28] Ashby M. F., Bréchet Y. J. M., Cebona D., Salvoc L.: Selection strategies for materials and processes. Materials and Design, **25**, 51–67 (2004).
DOI: 10.1016/S0261-3069(03)00159-6

[29] Shanian A., Milani A. S., Carson C., Abeyaratne R. C.: A new application of ELECTRE III and revised Simos' procedure for group material selection under weighting uncertainty. Knowledge-Based Systems, **21**, 709–720 (2008).
DOI: 10.1016/j.knosys.2008.03.028

eXPRESS Polymer Letters Vol.5, No.12 (2011) 1075–1084
Available online at www.expresspolymlett.com
DOI: 10.3144/expresspolymlett.2011.105

Permeability characterization of stitched carbon fiber preforms by fiber optic sensors

V. Antonucci[1*], *M. Esposito*[1], *M. R. Ricciardi*[1], *M. Raffone*[2], *M. Zarrelli*[1], *M. Giordano*[1]

[1]Institute for Composite and Biomedical Materials (IMCB-CNR), P.le E. Fermi, 1 80055, Portici (NA), Italy
[2]Alenia Aeronautica S.p.A., zona industriale ASI Incoronata, 71100 Foggia, Italy

Received 31 March 2011; accepted in revised form 26 June 2011

Abstract. The in-plane and through thickness permeability of unidirectional stitched carbon fiber preforms have been determined through vacuum infusion tests. The impregnation of various dry preforms with different stitching characteristics has been monitored by fiber optic sensors that have been stitched together with the dry tow to manufacture the dry preform. The experimental infusion times have been fitted by a numerical procedure based on Finite Element (FE) processing simulations. A good agreement between the numerical and experimental infusion times has been found demonstrating the potentiality of the fiber sensor system as suitable tool to evaluate impregnation times and permeability characteristics.

Keywords: *polymer composites, fiber optic sensor, permeability, VARTM*

1. Introduction

Liquid Composite Molding (LCM) processes have become increasingly popular for several industrial fields providing significant reduction of manufacturing costs compared with traditional autoclave processing and hand-lay up. Variations of this process include Resin Transfer Molding (RTM), vacuum-assisted RTM (VARTM), resin film infusion (RFI) and injection-compression RTM (I-CRTM). The common feature to all LCM processes is the impregnation of a dry fiber reinforcement by a thermoset liquid or film resin. The most popular technique is the RTM that consists in injecting a liquid resin in a closed mold containing the dry fiber preform. After the injection is completed, the mold is heated in order to activate the curing process.

Vacuum Assisted Resin Transfer Molding (VARTM) is a variant of the traditional resin transfer molding (RTM) process. VARTM process basically involves: lay up of a fiber preform, vacuum application, injection of a thermoset resin and resin cure. The reinforcement, typically carbon or glass fabric, is placed onto a one-sided rigid mold, on the other side a vacuum bag material replaces the common RTM matched metal tool. The resin is injected through one or more inlet gates, depending on part size and shape. Vacuum is applied through a single or multiple vents in order to remove the air from the fiber preform and to drive the fiber impregnation of the part by resin. A resin distribution medium is often placed onto the reinforcement to promote the resin flow, to eliminate voids and dry spots. This technology offers some advantages over the conventional RTM by saving the costs associated with matched-metal tooling, reducing volatiles emission and involving low injection pressures. Furthermore it provides better results than other production processes for the good repeatability and reliability of the material properties and enabling the production of cored structures in one operation. For these reasons VARTM is seeing increased commercial use for production of large quantities of parts.

*Corresponding author, e-mail: vinanton@unina.it

Currently, the VARTM process is commonly designed and optimized experimentally by trial-and-error approaches. This procedure requires a series of experiments in order to determine the optimal positioning of the resin injection gates and vacuum vents. To overcome critical manufacturing issues (dry zones) and optimize the process, some authors have developed numerical simulations able to model the resin infusion [1–9] during a VARTM process and active flow control methodologies to guarantee a filling uniformity [10, 11].

To predict the resin flow and model accurately the process, key input parameter is the permeability behaviour of the dry reinforcement preforms. Permeability measurements have been treated by numerous authors in the planar directions [12–16]. In addition, several studies deal with the subject of transverse permeability [18–21], that needs to be characterized especially in the case of processes like as VARTM process or the resin film infusion (RFI) [22]. In fact, conversely to RTM, these processes exhibit significant through-the-thickness impregnation gradients [23, 24] that may affect the total fiber impregnation, the filling time and, consequently, the dimensions and mechanical properties of the final composite part. In addition, due to the use of the flexible vacuum bag and, consequently, due to the variation of compaction pressure, the part thickness and local permeability of the fibre preform change during resin injection as function of time and space [25]. Therefore, to achieve a desired thickness in the final part, one should model the coupled fabric compaction and resin flow [26–28].

The most common technique to measure the permeability is to induce an unidirectional flow trough the reinforcement and monitor both the matrix front and the pressure as function of time [29]. Then, by the knowledge of the resin viscosity and total length to impregnate, the permeability is identified through the Darcy equation that relates linearly the resin velocity to the pressure gradient in the case of flow in porous media. This technique allows the permeability identification both in transient and saturated regime. However, the accuracy of the measurement can be compromised by 'race-tracking' effects. In fact, due to the larger flow along the mould edges, the permeability estimation could be greater than the real permeability of the preform. To overcome this issue, radial or three dimensional infusion experiments are performed for the in-plane or the three permeability components identification respectively. However, in the case of 3D infusion, complex three dimensional numerical simulations are generally required to evaluate the through thickness permeability. Therefore, due to the computation issues and the difficulty in following the flow front, unidirectional flow tests in saturated regime [30] are generally preferred to measure the through thickness permeability.

Alternatively, the use of discretely distributed sensors through the fiber reinforcement [31] can help the processing designer to determine the transient through thickness permeability. Ballata *et al*. [32] developed an electrical sensing grid for the *in-situ* flow monitoring during VARTM and determine the transverse transient permeability of glass random mats by a specific inverse method based on the mass conservation. Furthermore, Drapier *et al*. [30] designed a specific apparatus based on the use of optical-fibre sensors to detect the unidirectional resin flow trough a multiaxial fabric and identify the transient transverse permeability that resulted to be around a factor 10 larger than the saturated permeability.

In this study, the transient in-plane and through thickness permeability of eight stitched carbon fiber preforms have been identified during vacuum infusion tests using an aeronautical commercial epoxy resin. In particular, the resin advancement during the preform impregnation has been measured by using optical fibers that have been stitched preliminary together with the dry carbon tow during the preform manufacturing. In this way, the vacuum bag assembly procedures were simplified by limiting integration issues and the sensors position was fixed during the reinforcement impregnation. In addition, the in-plane and through thickness embedding of the optical sensors within the carbon preforms enabled to estimate the flow resistance of the preforms during a real vacuum infusion experiment by avoiding complex set-up. In fact, the permeability of the analysed fiber preforms has been identified by the best fitting of the experimental infusion times, evaluated by the sensor signals, and computation data, obtained by a three dimensional FE numerical processing simulation code.

2. Experimental

2.1. Preform characteristics

The in-plane and through thickness flow resistance of eight unidirectional stitched carbon fiber preforms (150 mm×150 mm) with different stitching characteristics has been investigated. In particular, two different carbon fibers (HTS 12k from Toho Tenax Europe GmbH, Heinsberg Germany, T800 12k from Toray Carbon fibers America, Flower Mound, USA) have been used to manufacture the fiber preforms that have been obtained by stitching eight unidirectional plies along the thickness direction. Each ply is made of dry carbon tows placed with the same orientation and stitched together by a zig-zag pattern with a stitching pitch of 5 mm for the lower and upper ply and a different stitching pitch for the other plies according with Table 1. Table 1 reports the characteristics of the stitched preforms in terms of fiber areal weight (FAW) and stitching pitch (SD) representing the superficial fiber density and the distance between two adjacent stitching points along the longitudinal direction of tow respectively (see Figure 1).

During the preform manufacturing, in accordance with the scheme shown in Figure 2, eight optical fibers were stitched in each fiber preform along the middle plane of the laminate and perpendicular to the carbon fibers. The sensors were used to monitor the resin advancement through the preform during the infusion. In addition, a reference optical fiber has been placed as very near as possible to the infusion tube in order to estimate the entry time of the resin as reference time for the eight sensor signals. Figure 3 shows a picture of a dry fiber preform with the optical fibers that exit from the reinforcement.

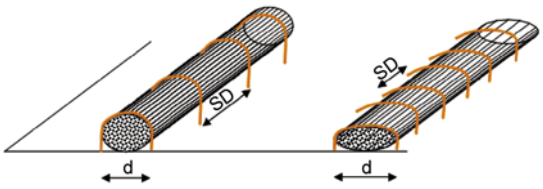

Figure 1. Stitching schematic

Table 1. Preforms stitching characteristics

Id. preformm	Carbon fiber	FAW [g/m^2]	Stitching pitch [mm]
1	HTS	270	5
2	HTS	270	30
3	HTS	270	50
4	HTS	340	5
5	HTS	400	5
6	T 800	230	5
7	T 800	230	30
8	T 800	230	50

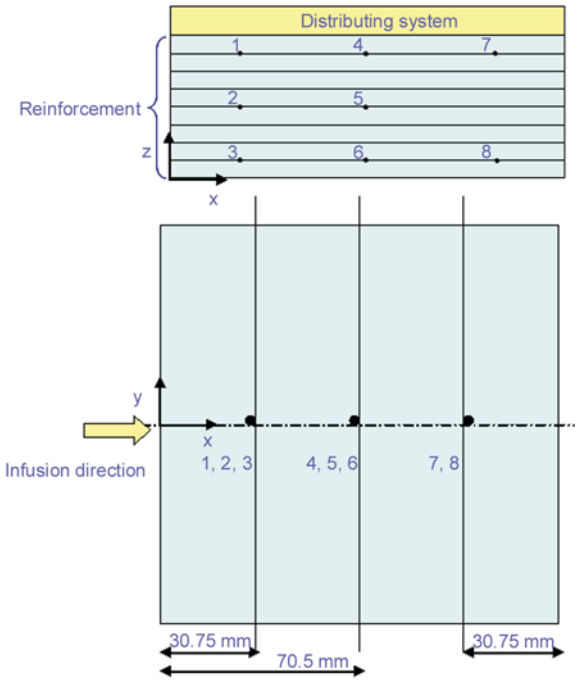

Figure 2. Schematic of optical fiber position

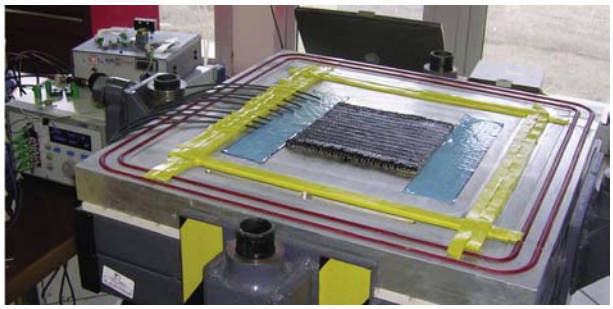

Figure 3. Dry perform with optical fibers

2.2. Sensor system

The fiber optic sensor is a powerful tool to perform remote, on-line, *in-situ* monitoring of composite manufacturing processes being free from electromagnetic interference and having high chemical and high temperature resistance. Furthermore, the fiber optical sensors can be multiplexed in several independent channels and embedded into the composite structure with minimally intrusive action due to the small size.

The hardware sensor apparatus consists of a personal computer, a data acquisition N.I. USB9215-A, an optical switch with eight channels (PRO800 from Thorlabs, Dachau, Germany), an home made

refractometer. This apparatus allows to monitor the reflectivity at the interface between the end of the optical fiber and the surrounding environment.
In particular, in this case, the resin flow front positions have been measured by using the fiber optic sensor based on the principle Fresnel reflection [32] and, thus, recording the refractive index. In fact, as a light beam is introduced into the fiber optic test segment, the optical signal is transmitted to the interface between the end of the optical fiber and the material, where the measurement is carried out. At the interface, part of the light beam is transmitted and part is reflected, depending on the refractive index mismatch between the fiber and the embedding material. The reflected signal is then back directed, by means of a fiber coupler to a photodetector. If a monomode fiber is employed, the intensity reflection coefficient R is given by Equation (1):

$$R = \left(\frac{n_f - n_m}{n_f + n_m}\right)^2 \quad (1)$$

where n_f and n_m are respectively the effective refractive index of the fiber and the sample refractive index.
The flow front position can be detected by recording the refractive index. In fact, as the optical fibers are embedded through the dry carbon reinforcement, a relatively large light signal is transmitted in absence of resin, in particular the 5% of the incident light is reflected back at the fiber-end/air interface. However, as the resin reaches the fiber/end interface, a significant dropping of the reflected signal is recorded. In this case, the mismatch between the refractive index of the resin and the fiber optical is very low being the refractive index of the epoxy resin (around 1.5) very close to the that one of the optical fiber. By placing several optical fibers in different locations, the resin advancement can be determined as it reaches each optical fiber.

2.3. Infusion tests

The composite panels have been manufactured by impregnating the carbon fiber preforms with the mono-component epoxy resin HexFlow® RTM 6 by Hexcel (Montluel, France). The infusion experiments have been designed to identify 3 orthogonal permeability components of eight unidirectional stitched preforms. The characteristics of the analysed performs are reported in Table 1. Therefore, to ensure the repeatability of the experimental measurements, 6 unidirectional preforms with the same stitching characteristics (Table 1) have been infiltrated: 3 of them have been impregnated by injecting the resin at 0° to measure the in-plane longitudinal permeability and 3 of them have been turned at 90° in order to inject the resin at 90° respect to the fiber reinforcement direction and measure the in-plane transverse permeability. In addition, the through thickness permeability has been identified by the measurement of the through thickness infiltration times and considering that the through thickness flow resistance of the 6 unidirectional preforms is the same.
The Vacuum Infusion process has been adopted according with the scheme of Figure 4, where it is possible to observe that three layers were stacked on the carbon reinforcement: the peel ply, the breather (Compoflex 150 of Fibertex Nonwovens, Aalborg, Denmark) and the flow distributing net (Green Flow – Airtech Europe Sarl, Differdange, Luxembourg) having different length to ensure different functions: the demolding, the vacuum distribution and the complete reinforcement wetting respectively. The resin injection and the vacuum were performed by two spiral pipes, connected respectively to the resin tank and to the vacuum pump. The whole system was sealed by the vacuum bag. A partial vacuum has been applied also to the resin container to reduce the local pressure variations and, hence, to minimize the thickness changes during the resin flow according with the study of Niggemann *et al*. [34] that have demonstrated the positive effect of this procedure for un-debulked preforms.
Figure 5 shows two pictures of the beginning and the end of the infusion tests.
In all tests, the resin injection temperature was settled at 80°C, while the mold temperature at 100°C. The vacuum pressure was set to 0.75 bar. Hence,

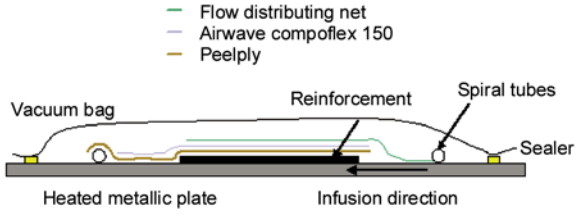

Figure 4. Schematic of infusion assembly system

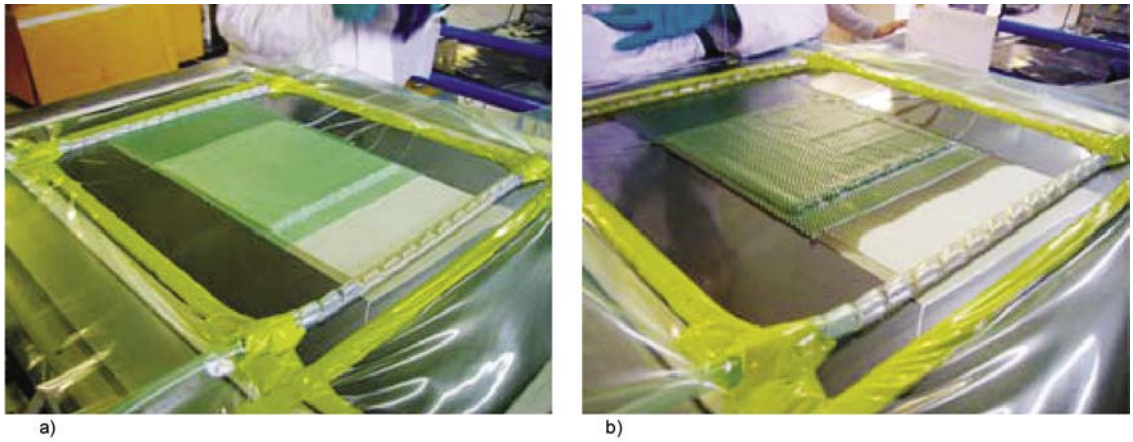

Figure 5. Beginning (a) and end of infusion (b) tests

Table 2. Composite characteristics

Id. preform	Average fibre volume fraction [%]	Average thickness [mm]
1	37.4	3.52±0,03
2	50.0	3.24±0.06
3	46.6	2.72±0.12
4	45.6	3.60±0.05
5	39.5	5.07±0,12
6	32.8	2.34±0.11
7	32.2	3.36±0.08
8	35.4	2.80±0.06

the experimental measurements and the permeability identification were performed just for the resulting unique fibre volume fraction. At the end of the fiber impregnation, the laminates have been consolidated by a cure cycle of 75 min at 160°C, followed by a plateau of 120 min at 180°C. The manufactured composite panels showed different characteristics in terms of final fiber volume fraction and thickness. Table 2 reports the averaged values of the fiber volume fraction and of thickness ± standard deviations for each perform.

3. FE processing simulation

The infusion process has been numerically simulated by the commercial finite element code PAM-RTM (ESI-GROUP, Italy) that adopts the Darcy law to describe the reinforcement impregnation [29, 31].

Since this software does not allow to create any type of geometry or mesh, the geometry and the mesh have been realized with an external code. Figure 6 shows the adopted FE model of the simulated test case. It should be noted that the model is two dimensional. In fact, just the cross section view of the distribution and reinforcement system has been considered for the numerical simulation. This assumption is based on the experimental observation that the resin generally exit from the infusion tube only after reaching the end of tube. Hence the resin flows simultaneously from all openings of the spiral infusion tube. This behaviour leads to an almost parallel resin front giving the possibility to neglect the influence of the flow along the direction parallel to the infusion tube.

Consequently, the elements for the FE model are two-dimensional (PLANE) and have a triangular shape (see Figure 6). The mesh size was selected with the objective to ensure an high level of accuracy for the individuation of the through-thickness permeability and considering that the thickness range was 3–5 mm. In particular, with reference to preform id. 5 a more refined mesh characterized by a lower longitudinal element size and aspect ratio about equal to one was also adopted finding filling times differences below 3%. According to Figure 6, the real experimental configuration of the vacuum bag assembly, consisting of the ancillary materials and dry preform, have been considered in the computational analysis. The different layers have been modelled and discretized. The first yellow layer

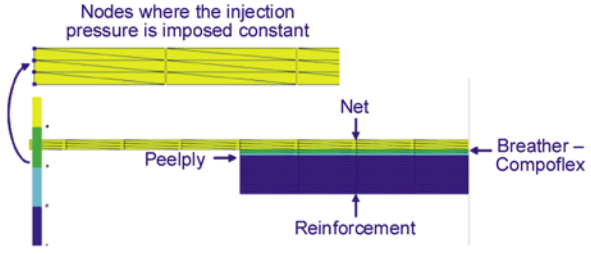

Figure 6. FE model: 1) reinforcement (blue); 2) peelply (cyan); 3) breather (green); 4) distributing net (yellow)

from the top is representative of the distribution network, then the green layer describes the breather material and, finally, the blue layer is for the peel ply. These layers are characterized by different permeability and length. In particular, the permeability characteristics have been determined preliminary by suitable experimental tests and assumed constant for all performed infusion tests. The values of the longitudinal/through thickness permeability of the different layers above the dry reinforcement were set to $2.05\cdot10^{-8}$ m^2/$2.537\cdot10^{-8}$ m^2, $2.042\cdot10^{-10}$ m^2/$1.6\cdot10^{-11}$ m^2, $1.62\cdot10^{-10}$ m^2/$3.5\cdot10^{-11}$ m^2, for distribution network, the breather and the peel ply respectively. Furthermore, it is possible to notice that the yellow top layer is longer than the others that have the same length of the fiber reinforcement. In fact, since the distributing net has the function to uniform and ease the resin flow, in the experimental tests it is placed close to the infusion tube and at a proper distance from the fiber reinforcement. This distance has been considered in the numerical simulations in order to take into account its influence on the pressure distribution and on the resin advancement. Otherwise, due to higher pressure gradients in the entry zone, the resin flow could result too fast and deviate from the real experimental data. Hence, the resin injection line has been fixed at the end of distribution net as shown in Figure 6, where the injection nodes are represented in blue. The injection pressure has been imposed constant and equal to 0.75 bar.

The resin flow has been considered isothermal. The resin viscosity and density have been assumed constant and equal to 0.7 Pa·s and 1140 kg/m^3 respectively.

4. Permeability data

The permeability values have been identified by the best fitting of the experimental impregnation times, defined as the time period needed to the resin front to reach the fiber optic sensor positions. As example, Table 3 shows the measured experimental times and the respective standard deviations for preform 5 for both infusion tests at 0 and 90° that resulted less than 20%. The sensor experimental measurements have been analysed by a proper developed numerical procedure that enables to run the commercial processing code PAMRTM in batch way. The processing simulations have been carried out simultaneously for the sixteen analysed infusion tests by changing the reinforcement permeability values and taking into account the different porosity and thickness values (Table 2) of final composites. In particular, it should be noticed that the fiber preform thickness and, hence, the permeability components for each preform have been assumed constant due to the observed low thickness gradient in the final composite (less than 1.5%).

Table 3. Experimental infusion times and the respective standard deviations for the preform 5

Sensor	0° infusion times [s]	90° infusion times [s]
1	5.91±1.18	9.52±0.09
2	9.27±2.39	9.85±1.21
3	9.78±3.33	11.43±0.09
4	17.57±2.39	18.18±1.27
5	19.62±2.15	19.33±1.33
6	19.49±2.41	20.34±0.85
7	25.22±3.33	26.33±1.33
8	29.09±4.98	28.68±0.15

After the evaluation of the numerical impregnation times, the Root Mean Square Error (RMSE) of the numerical results respect to the experimental sensor times have been evaluated as shown in Equation (2):

$$\mathrm{RMSE_{ik}} = \sqrt{\frac{\sum_{j=1}^{8}(t_{ijk} - T_{ij})^2}{8}} \tag{2}$$

where

– $\mathrm{RMSE_{ik}}$ is the error for the generic i test, with i ranging between 1 and 16 and k the permeability values assigned to the reinforcement for the i test;

– t_{ijk} is the numerical time that the resin employs to reach the j sensor (j ranges between 1 and 8, being 8 the number of the optical fibers) for the i test k the permeability values couple;

– T_{ij} is the objective experimental time that the resin employs to reach the j sensor (j ranges between 1 and 8) for the i test.

To establish the optimal permeability components, two concurrent criteria have been adopted:

– $\mathrm{RMSE_{ik}}$ has to be the minimum possible value;

– since the same reinforcement is impregnated with a 0 and 90° vacuum infusion test, its through thickness flow resistance and, consequently, the through thickness permeability has to be the same for both tests.

Table 4. Minimum error between experimental and numerical times

Id. preform	RMSE 0° infusion [s]	RMSE 90° infusion [s]
1	2.24	3.45
2	3.28	1.41
3	3.71	2.21
4	1.87	1.41
5	1.46	1.58
6	2.65	2.72
7	2.50	3.62
8	2.55	1.87

By the application of these criteria, the in-plane and through thickness permeability have been identified for each preform.

Tables 4 and 5 report the minimum RMSE and the corresponding identified permeability values for each test. As calculated, the RMSE values resulted less than 4 sec. In general, greater time differences have been found for the impregnation times relative to positions closer to the injection tube. As example, Figures 7a and 7b show the experimental and numerical infusion times for the preform '5', where it is possible to observe a good agreement between the two kinds of data. In addition, for this preform the effect of the standard deviations of the experimental times on the permeability values has been calculated. Starting from the average experimental time obtained for the i sensor, three levels of times have been considered: t_i–σ_{t_i} t_i, and t_i+σ_{t_i}, where σ_{t_i} is the standard deviation of the experimental times obtained for the *i* sensor, to evaluate the full factorial time table. Figures 8a–c report the resulting distribution of the permeability components K_x, K_y, K_z that show standard deviations equal to $4.57 \cdot 10^{-11}$, $2.77 \cdot 10^{-11}$, $7.792 \cdot 10^{-11}$ m^2 respectively.

From Table 5, it is possible to notice no large differences between the in-plane and the through thickness permeability components and a different dependence of the three permeability components on the preform stitching characteristics. In fact, the in plane permeability components don't show any dependence on FAW and SD being their values quite similar for the different preforms. This result come from the use of the distributing system that has low flow resistance and promote strongly the in-plane resin flow that so is uniformly distributed and is not affected by the in-plane flow resistance properties of the fiber reinforcement.

Otherwise, as expected, the through thickness permeability resulted lower than the in-plane permeability and is affected by the stitching characteristics. For similar FAW values, the through thickness permeability is an increasing function of the stitching pitch especially for SD variation from 5 to 30.

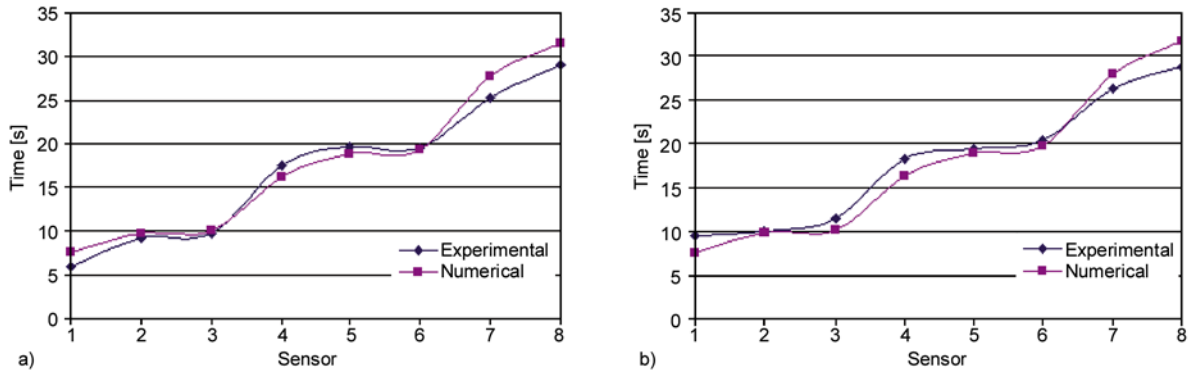

Figure 7. Experimental and numerical impregnation times for preform '5' a) 0° infusion; b) 90° infusion

Table 5. Permeability values

Id. preform	In plane longitudinal permeability [m^2]	In plane transverse permeability 90° fiber direction [m^2]	Through thickness permeability [m^2]
1	$5.93 \cdot 10^{-10}$	$1.66 \cdot 10^{-10}$	$0.75 \cdot 10^{-10}$
2	$9.42 \cdot 10^{-10}$	$8.25 \cdot 10^{-10}$	$4.40 \cdot 10^{-10}$
3	$8.25 \cdot 10^{-10}$	$6.70 \cdot 10^{-10}$	$5.00 \cdot 10^{-10}$
4	$9.61 \cdot 10^{-10}$	$4.95 \cdot 10^{-10}$	$2.35 \cdot 10^{-10}$
5	$8.64 \cdot 10^{-10}$	$7.67 \cdot 10^{-10}$	$4.80 \cdot 10^{-10}$
6	$3.99 \cdot 10^{-10}$	$2.83 \cdot 10^{-10}$	$0.95 \cdot 10^{-10}$
7	$10.0 \cdot 10^{-10}$	$0.69 \cdot 10^{-10}$	$3.00 \cdot 10^{-10}$
8	$9.42 \cdot 10^{-10}$	$9.03 \cdot 10^{-10}$	$4.20 \cdot 10^{-10}$

Furthermore, for the HTS based preforms, having the same SD (id. 1, 4, 5), the through thickness permeability depends powerfully on FAW.

In general, these results can be interpreted by considering that the permeability of stitched preforms is affected in a complex manner by the specific reinforcement architecture, microstructure and fibre areal weight. In particular, some literature papers [17, 22] have shown that the stitching enhances the flow resistance by providing additional flow paths for the resin. Drapier *et al*. [17] demonstrated that the through thickness permeability is not controlled by the stacking sequence and by the stitching patterns, but it seems to be determined by the stitching density.

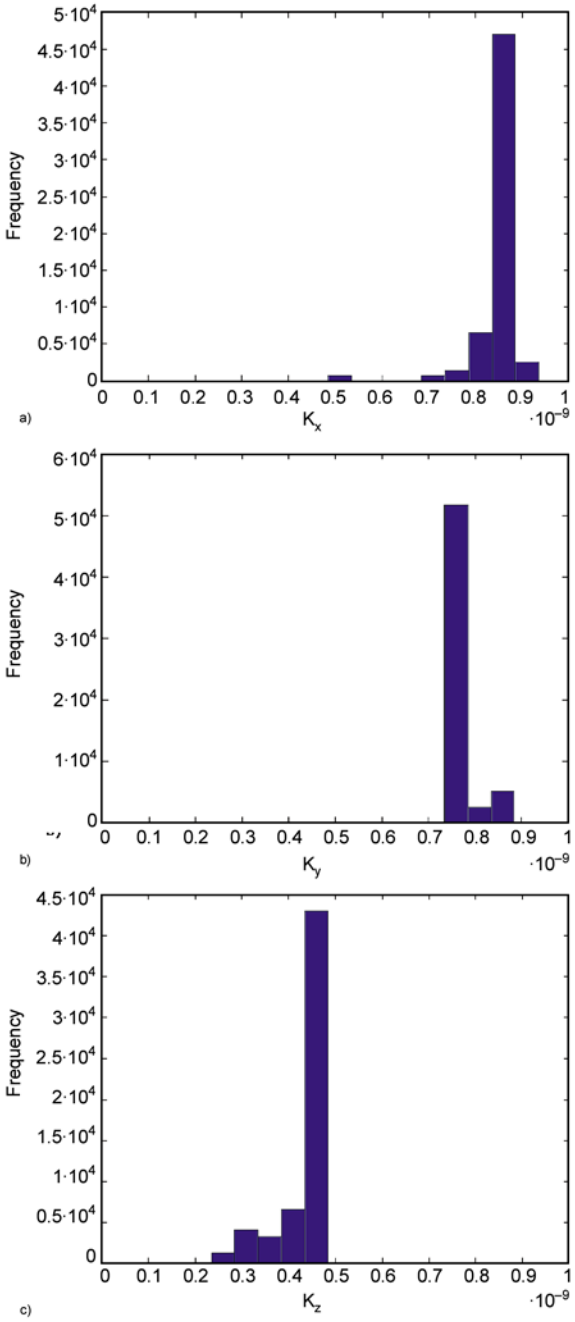

Figure 8. Permeability distributions for perform '5' a) In-plane longitudinal permeability K_x; b) In-plane transverse permeability K_y; c) Through thickness permeability K_z

The permeability results of this work seem to confirm that the investigated stitched preforms are characterized by low flow resistance and, hence, high permeability values along the three main directions. However, since it has been observed that the through thickness permeability is as increasing function of the stitching pitch parameter, it is possible to conclude that the though thickness flow resistance is influenced more by the void area left by adjacent stitching points than by the stitching density.

5. Conclusions

Vacuum infusion tests have been carried out to manufacture composite panel based on an aeronautical commercial resin and carbon fiber reinforcements. In particular, the carbon preforms have been realized by stitching, starting from two different carbon dry tows. In addition, in each investigated carbon preform eight optical fibers have been stitched along the middle plane of the lay-up in eight different positions in order to avoid undesired movements during the resin infusion. The optical fibers allowed to monitor the resin flow advancement during the vacuum infusion tests. The experimental impregnation times, obtained by the sensor signals, have been fitted by a numerical procedure based on the use of the commercial PAMRTM processing simulation code. In this way, the transient in-plane and through thickness permeability components have been identified for each fiber preform. The in-plane permeability resulted unaffected by the stitching characteristics of the preforms. On the other hand, the through thickness permeability has been found an increasing function of both the fiber areal weight and the stitching pitch of the preform. Thus, these results evidence that the distributing system has a great effect on the planar flow, having higher permeability than the reinforcement and the function to promote and homogenise the resin infiltration on the first laminate plies. Therefore, for the VARTM process and similar technologies the through-thickness permeability is the most important parameter to control the fiber impregnation and the processing time especially in the case of large

structures. Finally, the developed methodology can be a useful tool to measure the effective transient through thickness flow resistance of the reinforcements during the real process.

References

[1] Correia N. C., Robitaille F., Long A. C., Rudd C. D., Šimáček R. P., Advani S. G.: Use of resin transfer molding simulation to predict flow, saturation, and compaction in the VARTM process. Journal of Fluids Engineering, **126**, 210–215 (2004). DOI: 10.1115/1.1669032

[2] Hammami A., Gebart B. R.: Analysis of the vacuum infusion molding process. Polymer Composites, **21**, 28–40 (2000). DOI: 10.1002/pc.10162

[3] Kang M. K., Lee W. I., Hahn H. T.: Analysis of vacuum bag resin transfer molding process. Composites Part A: Applied Science and Manufacturing, **32**, 1553–1560 (2001). DOI: 10.1016/S1359-835X(01)00012-4

[4] Han K., Jiang S., Zhang C., Wang B.: Flow modeling and simulation of SCRIMP for composites manufacturing. Composites Part A: Applied Science and Manufacturing, **31**, 79–86 (2000). DOI: 10.1016/S1359-835X(99)00053-6

[5] Acheson J. A., Šimáček P., Advani S. G.: The implications of fiber compaction and saturation on fully coupled VARTM simulation. Composites Part A: Applied Science and Manufacturing, **35**, 159–169 (2004). DOI: 10.1016/j.compositesa.2003.02.001

[6] Šimáček P., Advani S. G.: Desirable features in mold filling simulations for liquid composite molding processes. Polymer Composites, **25**, 355–367 (2004). DOI: 10.1002/pc.20029

[7] Song Y. S., Youn J. R.: Modeling of resin infusion in vacuum assisted resin transfer molding. Polymer Composites, **29**, 390–395 (2008). DOI: 10.1002/pc.20326

[8] Hsiao K-T., Mathur R., Advani S. G., Gillespie J. W., Fink B. K.: A closed form solution for flow during the vacuum assisted resin transfer molding process. Journal of Manufacturing Science and Engineering, **122**, 463–476 (2000). DOI: 10.1115/1.1285907

[9] Li J., Zhang C., Liang R., Wang B., Walsh S.: Modeling and analysis of thickness gradient and variations in vacuum-assisted resin transfer molding process. Polymer Composites, **29**, 473–482 (2008). DOI: 10.1002/pc.20439

[10] Modi D., Correia N., Johnson M., Long A., Rudd C., Robitaille F.: Active control of the vacuum infusion process. Composites Part A: Applied Science and Manufacturing, **38**, 1271–1287 (2007). DOI: 10.1016/j.compositesa.2006.11.012

[11] Johnson R. J., Pitchumani R.: Simulation of active flow control based on localized preform heating in a VARTM process. Composites Part A: Applied Science and Manufacturing, **37**, 1815–1830 (2006). DOI: 10.1016/j.compositesa.2005.09.007

[12] Luce T. L., Advani S. G., Howard J. G., Parnas R. S.: Permeability characterization. Part 2: Flow behavior in multiple-layer preforms. Polymer Composites, **16**, 446–458 (1995). DOI: 10.1002/pc.750160603

[13] Lekakou C., Johari M. A. K., Norman D., Bader M. G.: Measurement techniques and effects on in-plane permeability of woven cloths in resin transfer moulding. Composites Part A: Applied Science and Manufacturing, **27**, 401–408 (1996). DOI: 10.1016/1359-835X(95)00028-Z

[14] Lundström T. S., Gebart B. R., Sandlund E.: In-plane permeability measurements on fiber reinforcements by the multi-cavity parallel flow technique. Polymer Composites, **20**, 146–154 (1999). DOI: 10.1002/pc.10342

[15] Demaría C., Ruiz E., Trochu F.: In-plane anisotropic permeability characterization of deformed woven fabrics by unidirectional injection. Part I: Experimental results. Polymer Composites, **28**, 797–811 (2007). DOI: 10.1002/pc.20107

[16] Buntain M. J., Bickerton S.: Compression flow permeability measurement: A continuous technique. Composites Part A: Applied Science and Manufacturing, **34**, 445–457 (2003). DOI: 10.1016/S1359-835X(03)00090-3

[17] Drapier S., Pagot A., Vautrin A., Henrat P.: Influence of the stitching density on the transverse permeability of non-crimped new concept (NC2) multiaxial reinforcements: Measurements and predictions. Composites Science and Technology, **62**, 1979–1991 (2002). DOI: 10.1016/S0266-3538(02)00127-6

[18] Mehri D., Michaud V., Kämpfer L., Vuilliomenet P., Månson J-A. E.: Transverse permeability of chopped fibre bundle beds. Composites Part A: Applied Science and Manufacturing, **38**, 739–746 (2007). DOI: 10.1016/j.compositesa.2006.09.006

[19] Elbouazzaoui O., Drapier S., Henrat P.: An experimental assessment of the saturated transverse permeability of non-crimped new concept (NC2) multiaxial fabrics. Journal of Composite Materials, **39**, 1169–1193 (2005). DOI: 10.1177/0021998305048746

[20] Scholz S., Gillespie J. W., Heider D.: Measurement of transverse permeability using gaseous and liquid flow. Composites Part A: Applied Science and Manufacturing, **38**, 2034–2040 (2007). DOI: 10.1016/j.compositesa.2007.05.002

[21] Ouagne P., Bréard J.: Continuous transverse permeability of fibrous media. Composites Part A: Applied Science and Manufacturing, **41**, 22–28 (2010). DOI: 10.1016/j.compositesa.2009.07.008

[22] Han N. L., Suh S. S., Yang J-M., Hahn H. T.: Resin film infusion of stitched stiffened composite panels. Composites Part A: Applied Science and Manufacturing, **34**, 227–236 (2003).
DOI: 10.1016/S1359-835X(03)00002-2

[23] Mathuw R., Advani S. G., Heider D., Hoffmann C., Gillespie J. W., Fink B. K.: Flow front measurements and model validation in the vacuum assisted resin transfer molding process. Polymer Composites, **22**, 477–490 (2001).
DOI: 10.1002/pc.10553

[24] Loos A. C., Rattazzi D., Batra R. C.: A three-dimensional model of the resin film infusion process. Journal of Composite Materials, **36**, 1255–1273 (2002).
DOI: 10.1177/0021998302036010168

[25] Yenilmez B., Senan M., Murat Sozer E.: Variation of part thickness and compaction pressure in vacuum infusion process. Composites Science and Technology, **69**, 1710–1719 (2009).
DOI: 10.1016/j.compscitech.2008.05.009

[26] Correia N. C., Robitaille F., Long A. C., Rudd C. D., Šimáček P., Advani S. G.: Analysis of the vacuum infusion moulding process: I. Analytical formulation. Composites Part A: Applied Science and Manufacturing, **36**, 1645–1656 (2005).
DOI: 10.1016/j.compositesa.2005.03.019

[27] Li J., Zhang C., Liang R., Wang B., Walsh S.: Modeling and analysis of thickness gradient and variations in vacuum-assisted resin transfer molding process. Polymer Composites, **29**, 473–482 (2008).
DOI: 10.1002/pc.20439

[28] Govignon Q., Bickerton S., Kelly P. A.: Simulation of the reinforcement compaction and resin flow during the complete resin infusion process. Composites Part A: Applied Science and Manufacturing, **41**, 45–47 (2010).
DOI: 10.1016/j.compositesa.2009.07.007

[29] Antonucci V., Giordano M., Nicolais L.: Liquid moulding processes. in 'Handbook of polymer blends and composites' (eds.: Kulshreshtha A. K., Vasile C.) Vol 2, 53–83, Rapra, Shrewsbury (2002).

[30] Drapier S., Monatte J., Elbouazzaoui O., Henrat P.: Characterization of transient through-thickness permeabilities of non crimp new concept (*NC*2) multiaxial fabrics. Composites Part A: Applied Science and Manufacturing, **36**, 877–892 (2005).
DOI: 10.1016/j.compositesa.2005.01.002

[31] Antonucci V., Giordano M., Nicolais L., Calabrò A., Cusano A., Cutolo A., Inserra S.: Resin flow monitoring in resin film infusion process. Journal of Materials Processing Technology, **143–144**, 687–692 (2003).
DOI: 10.1016/S0924-0136(03)00338-8

[32] Ballata W. O., Walsh S. M., Advani S.: Determination of the transverse permeability of a fiber preform. Journal of Reinforced Plastics and Composites, **18**, 1450–1464 (1999).
DOI: 10.1177/073168449901801601

[33] Giordano M., Nicolais L., Calabrò A. M., Cantoni S., Cusano A., Breglio G., Cutolo A.: A fiber optic thermoset cure monitoring sensor. Polymer Composites, **21**, 523–530 (2000).
DOI: 10.1002/pc.10207

[34] Niggemann C., Song Y. S., Gillespie J. W., Heider D.: Experimental investigation of the controlled atmospheric pressure resin infusion (CAPRI) process. Journal of Composite Materials, **42**, 1049–1061 (2008).
DOI: 10.1177/0021998308090650

eXPRESS Polymer Letters Vol.5, No.12 (2011) 1085–1101
Available online at www.expresspolymlett.com
DOI: 10.3144/expresspolymlett.2011.106

Efficient one-step melt-compounding of copolyetheramide/pristine clay nanocomposites using water-injection as intercalating/exfoliating aid

F. Touchaleaume[1,2,3], J. Soulestin[1,2], M. Sclavons[3], J. Devaux[3], F. Cordenier[3], P. Van Velthem[3], J. J. Flat[4], M. F. Lacrampe[1,2], P. Krawczak[1,2]*

[1]Univ. Lille Nord de France, F-59000 Lille, France
[2]Ecole des Mines de Douai, Department of Polymers and Composites Technology & Mechanical Engineering, 941 Rue Charles Bourseul, BP 10838, F-59508, Douai, France
[3]Institute of Condensed Matter and Nanoscience (Bio- and Soft-Matter) & Ecole Polytechnique de Louvain, Université Catholique de Louvain, Croix du Sud, 1 1348 Louvain-la-Neuve, Belgium
[4]Arkema – Cerdato, F-27470 Serquigny, France

Received 13 April 2011; accepted in revised form 4 July 2011

Abstract. Polyether-block-amide (PEBA) /clay nanocomposites were prepared water-assisted by twin-screw extrusion. Both organomodified and pristine (i.e. purified but non-modified) montmorillonite clays were used. A high-pressure differential scanning calorimetry analysis carried out in the processing conditions demonstrated that PEBA/water blend exhibits some miscibility and that amide blocks and water behave as a single phase. In addition to a significant decrease of the melting temperature, water injected into the melt plays a key role among the filler dispersion and prevents the matrix from degradation during melt-extrusion. This process enables the compounding of pristine clay-based nanocomposites whose dispersion state is high enough for the resulting mechanical performances in tension to be at least equivalent to what is reached with organomodified clay. Effects of the nanofiller dispersion onto the macromolecules' mobility are detailed and fracture mechanisms are identified for the various structures.

Keywords: *nanocomposites, poly(ether-block-amide), pristine clay, water injection*

1. Introduction

Polyamide/clay 'hybrids' were seen as pioneer materials 20 years ago among the polymer nanomaterials community [1]. Henceforth, different kind of polyamides (PA) or polyamide copolymers have been identified as suitable matrices for the elaboration of polymer/clay nanocomposites [2–5], bearing favorable polar amide functions along the backbone. Most of the studies dealing with PA/clay nanocomposites recourse to organically modified clay to successfully disperse the nanoplatelets. However, polyamide shows better thermodynamical interactions with pristine clay than with modified clay as calculated by molecular simulation [6, 7] and illustrated by reported successful (i.e. dispersed and exfoliated) PA6/pristine clay nanocomposites elaboration by *in situ* polymerization [8]. An interaction mechanism has been proposed by Shelley *et al*. [2] who mention the complexation of the polyamide chains (precisely by the carbonyl oxygen atoms) with the negatively charged layers. This complex distorts the conformation of the backbone at the vicinity of the mineral, explaining the widely reported crystalline phase modification in PA6/montmoril-

*Corresponding author, e-mail: jeremie.soulestin@mines-douai.fr

lonite (MMT) nanocomposites [9]. The emergence of gamma phase is representative of the favorable polar/polar interactions existing between polyamide 6 and clay. Nevertheless, a substantive role played by alkylammonium ions during melt blending is the layers preexfoliation, the platelets needing to be initially intercalated for the macromolecules to enter the galleries and to exfoliate the mineral sheets. However at the processing temperatures of polymers such as polyamides, those surfactants suffer thermal degradation [10] leading silicate layers to collapse which limits the clay dispersion. Alternative ways to preexfoliate the clay layers (generally montmorillonite) have been investigated but induce also an extra cost. The interlayer distance can be increased either before melt blending the filler into the matrix by exchanging the initial Na^+ counterion with a larger inorganic cation (K^+, Ca^{2+}, Mg^{2+}, Ba^{2+} …) [11, 12], ionic liquids [13, 14], by treating the mineral with a cold-plasma in order to graft hydrocarbon compounds on its surface [15] or by supercritical CO_2-assisted process [16, 17]. In the latter process, CO_2 molecules are claimed to penetrate the interlayer spacing in the supercritical state, a further depressurization makes the fluid expand and clay layers separate from each other.

Furthermore, due to their highly polar amide functions, polyamides are hydrophilic materials. PA – water solubility under temperature and pressure conditions has widely been reported in the literature [18–24]. Considering this peculiar behavior of polyamides and that montmorillonite platelets are separated from each other in water (constituting a colloidal dispersion), attempts have been made to elaborate PA/pristine clay nanocomposites by melt extrusion with the aid of water. Two different approaches have been proposed: injection of a slurry (clay dispersed into water) into the melt [25] or water injection into the clay/molten polymer blend [26–28]. In both cases successful dispersions of the layered silicate were achieved. A similar approach was proposed by Siengchin *et al*. to obtain toughened POM nanocomposites [29].

Besides, polyethers are reported to favor the untreated clay layers intercalation. Polyether/clay interactions have been studied for years [30]. Particularly, polyethylene oxide (PEO) is even used to quantify the clay surface area [31] as its adsorption is fast and precisely quantified. Concerning general polyethers and clay, the mechanism involves hydrogen bonds between the ether oxygen Lewis base of the polymer chain and the isolated silanols (SiOH) which are strong Brönsted acid sites on the silicate surface [32]. A mechanism involving interactions between hydrophobic siloxanes (Si–O–Si) and $(CH_2)_n$– segments along polyether backbone [33] has also been suggested. Interlayer's ions are mentioned in the mechanism because of their ability to be complexed by polyethers which then adopt a crown-ether conformation, forming cryptates due to strong Na^+-ether coordinations [34]. Even though the exact mechanism is still in debate, it is clear that there are driving forces for polyethers to enter layered pristine silicates galleries. Indeed, various polyethers were used to successfully prepare nanocomposites filled with pristine montmorillonite (NaMMT) [35, 36] and the efficiency of PEO as intercalant for the preparation of apolar polymers/ NaMMT has been demonstrated [37, 38].

Because of the above mentioned affinities for montmorillonite offered by polyethers and polyamides, trials have been successfully undertaken to prepare polyether-block-amide (PEBA)/clay nanocomposites, varying polyamide and polyether blocks [39–41]. However, only organically modified clay has been used and compounding of PEBA/pristine clay nanocomposites has never been reported so far to our knowledge.

Therefore, the present study aims at preparing nanocomposites based on a polyether-block-amide (PEBA) matrix and pristine montmorillonite (NaMMT) by melt-blending with water injection during extrusion as processing aid. Nanostructures are studied by X-ray diffraction (XRD) and transmission electron microscopy (TEM). Platelets dispersion is also evaluated by dynamic rheology. Mechanical and thermomechanical properties are studied as well as clay dispersion – material property relationship. Influence of water onto the clay dispersion and onto the polymer structure is evaluated. Organically modified clay and raw unpurified clay are used for a comparison purpose.

2. Experimental

2.1. Materials

The polyether-block-amide (PEBA) used was a PA12-block-Polytetramethyleneglycol (PTMG) (Pebax 7033 SA 01, Arkema, France). Its molar

composition is 24.8% PTMG, 73.0% PA12 and 2.2% adipic acid as a linkage [42]. Three kinds of clay were used: an organically modified montmorillonite (Cloisite 30B, Southern Clay Products, USA) further referred to as OMMT, a purified one (Cloisite Na^+, Southern Clay Products, USA), referred to as NaMMT and a raw one referred to as RawMMT (Süd Chemie, Germany). RawMMT is a non-purified bentonite, mainly made of NaMMT but also containing non smectic by-products such as quartz, mica, feldspar etc. [43]. Contrary to pristine NaMMT which only contains smectic clay after chemical treatment, the latter silicate is not washed. 'Pristine' refers to NaMMT, whose purification step from bentonite includes the use of surfactants [private communication, Süd Chemie] but is not considered as a modification. Water from lab tap was used during materials preparation. Materials were used as received.

2.2. Polymer – water solubility characterization

A high pressure differential scanning calorimeter (Mettler Toledo HPDSC 827^e, Zurich, Switzerland, maximum pressure: 100 bar) was used in order to study the phase separation or miscibility of PEBA and water at high pressure and high temperature. Its measuring chamber is connected to a pressure controlling valve (Brooks P.C. 5866 series) regulated by a Brooks valve controller (ReadOut & Control Electronics 0152). Pressure and temperature can be independently set in the DSC oven and the heating/cooling curves measured at constant pressure, allowing the simulation of the processing conditions. In order to reproduce the conditions within the extruder, PEBA powder and water were blended at a weight ratio of 70/30, the full sample weighing around 10 mg. PEBA pellets were freeze-ground in a grinding device (Pulverisette14, Fritsch/Idar-Oberstein, Germany/) at 14 000 rpm.

2.3. Nanocomposites processing and molding conditions

PEBA was used as received (vacuum packed) and clays were not dried before extrusion (stored at room conditions: 25°C, relative humidity 50%). Nanocomposites were prepared in a corotating twin screw extruder (Coperion Megacompounder length = 1000 mm, L/D = 40, screw diam: 25 mm, Coperion, Stuttgart, Germany) equipped with a water injection pump and two degassing apertures [44]. The screws are designed so that the melt pressure (70–100 bar) at the water injection point stays higher than water vapor pressure curve. Processing temperature was set at 190°C all along the screw (actual barrel temperature was 20°C lower than the setting value at the water injection point) and rotation speed was 200 rpm. Material throughput (polymer + clay) was set at 7 kg/h and water input at 3 l/h.

Preliminary thermal analysis of the modified clay indicated that organomodifiers stand for 30 wt% of OMMT, confirming values reported in the literature [45]. Therefore this organic extra content was taken into account for the final inorganic content to be comparable with other clays. As later displayed (see §4, Table 1), clays were proportioned so that inorganic contents varied from 0 to 10 wt% for NaMMT, and set at 5 wt% for OMMT and RawMMT. Material temperature was measured at the die: 190–195°C when water is injected in the melt and 210–215°C for the dry process. Extruded materials were cooled into a water bath and pelletized. The extruded nanocomposites were then vacuum-dried (90°C, 16 h) and injection-molded using an electric machine (Krauss Maffei 80-160E, Munich, Germany) as dumbbell tensile samples according to standard ISO 527-2 (sample type 1A). Injection-molding temperatures were set from 190°C (feeding zone) to 230°C (nozzle), mold temperature at 20°C, backpressure at 75 bar; injection screw speed was 80 mm/s and holding pressure was kept at 400 bar for 29 s.

Table 1. Composition of the nanocomposites

	Clay	Water	Inorganic content checked by TGA [wt%]
unprocessed PEBA	–	–	0
extruded PEBA	–	No	0
	–	Yes	0
PEBA + pristine clay	NaMMT	Yes	2.3
	NaMMT	Yes	3.9
	NaMMT	No	4.1
	NaMMT	Yes	6.4
	NaMMT	Yes	8.9
PEBA + modified clay	OMMT	Yes	5.4
	OMMT	No	5.5
PEBA + raw clay	RawMMT	Yes	4.7
	RawMMT	No	4.1

2.4. Samples structure and properties characterization

Inorganic content was checked by thermogravimetric analysis (TGA, Mettler Toledo TGA/SDTA851e Zurich, Switzerland) under nitrogen (to prevent the formation of oxidized species that could alter the final weight) from 200 to 500°C with a heating rate of 5°C per minute, with a stabilization period of 2 minutes at 200°C. Samples weighing from 7 to 10 mg were die-cut in 1 mm-thick hot-pressed films so as to keep constant dimensions and contact surface.

Molecular weight of the unloaded materials was evaluated by gel permeation chromatography (GPC, Waters Alliance 2695, Waters, Milford, MA, USA) using hexafluoroisopropanol as a solvent at 40°C. Samples were dissolved during 24 h at the concentration of 1 g/l. UV refractometer detector was set at 228 nm and calibration was performed with polymethyl methacrylate standards. Molecular weights (number average mass M_n and weight average mass M_w) are thus reported in 'PMMA-equivalents'.

Structure of the nanocomposites was evaluated using three complementary techniques; transmission electron microscopy (TEM) enables to check the local dispersion and possible exfoliation of the fillers; X-ray diffraction (XRD) analysis quantifies the intercalation in the bulk by indicating the platelets interlayer distance; and rotational dynamic rheology gives an indication of MMT dispersion in the bulk. TEM pictures were taken on the extruded pellets and on injection-molded samples. Ultrathin sections were cut at ambient temperature with a microtome (Leica Reichert FCS) and collected on a 300 mesh copper grid and observed with a TEM microscope (Leo 922 TEM).

The XRD experimental setup was a 2-circles goniometer (Siemens D5000) of 30 cm radius and 0.002° positioning accuracy. The incident beam (Cu K_α radiation, $\lambda = 0.15418$ nm) was obtained from a Rigaku rotating anode operated at 40 kV and 300 mA, fitted with a graphite secondary monochromator and a scintillation counter. Measurements were held on injection-molded samples.

Rheological analyses were performed using an advanced rheometrics expansion system (ARES, Rheometric Scientific, USA) rotational rheometer. As a block copolymer, PEBA keeps some crystalline structure till its order-disorder transition temperature which is reported to be 184°C [46]. The experiments were then held at 200°C to avoid any ordered state of the matrix and parallel plates were used (25 mm diameter, 2 mm gap). Linear domains of the different materials were identified from strain sweeps and a common strain of 15% was then selected for the different samples. Frequency sweeps were run from 0.1 to 100 rad·s^{-1}. Measurements were run three times for repeatability, using new dry samples before each analysis. Storage moduli of the molten nanocomposites are sensitive to nanocomposites structural changes [47]; slopes at low frequency (where the response of the nanocomposites are rather dominated by the polymer/filler interactions) were therefore determined. The latter is considered as a semi-quantitative measure of the degree of exfoliation of the mineral filler [48].

Mechanical properties were evaluated in dynamic and static modes. Rectangular samples (4 mm×9 mm) were die cut in 1 mm-thick hot-pressed films for dynamic mechanical analysis (DMA, Mettler Toledo DMA/SDTA 861^e, Zurich, Switzerland) in tensile mode. Oscillating frequency was set at 1 Hz, maximum force at 2 N and maximum displacement at 8 μm. Samples were dried in a vacuum oven at 80°C for 12 h before testing. Tests were run from –125°C till 180°C at a heating rate of 3°C per minute.

Tensile tests were performed on a tensile machine (Lloyd LR50K, UK) using a 5 kN force sensor and an extensometer for strain measurement. Tests were conducted according to ISO 527-1 standard at 50 mm/s crosshead speed for the yield strength measurement and at 5 mm/s for Young's modulus measurement. Samples were stored during 15 days at 23°C, 50% relative humidity before testing.

2.5. Analysis of PEBA-water solubility

Water injection into the melt can be an efficient way to disperse pristine clay into a matrix by extrusion providing that the polymer exhibits a miscibility with water [22–24]. HPDSC results are reported on Figure 1. For the PEBA/water blend studied at atmospheric pressure, two peaks can be detected for the first heat curve. The first and main one occurs just above 100°C and corresponds to water evaporation. The second one occurs at 171°C and corresponds to the PA12 block melting. This melting temperature

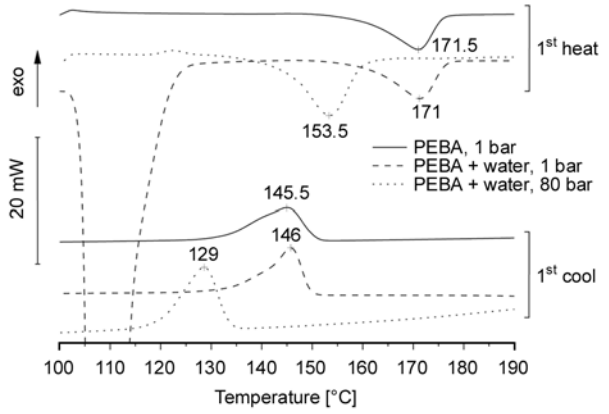

Figure 1. HPDSC of PEBA and PEBA/water blends at P = 1 bar and P = 80 bar

is not modified compared with pure PEBA since water previously evaporates from the pan. Cooling curves are similar, exhibiting a single crystallization peak at 146°C corresponding to PA12 blocks.

At high pressure (80 bar) a single peak at 153.5°C is observed. As expected, water boiling peak disappeared (at 80 bar pressure, water boiling point is 294.98°C [49]) and the remaining peak refers to the PA12 block melting. This peak shifted down by 17.5°C due to cryoscopy corresponding to the melting of a single phase made of water and PA12 blocks. In the latter phase, H-bonds make it possible for water to solvate the polyamide blocks [18].

HPDSC measurements were also performed at different pressures (20, 40, 60 and 80 bar, not reported here). Whatever the pressure, the melting point of the PEBA/water phase appears at the same temperature (153.5°C). This is in good agreement with what has been reported for other polyamides [18, 22–24]. Indeed, the cryoscopic effect played by water onto PA melting is reported when actual pressure stays higher than water vapor pressure curve (for a 20 bar pressure, water boiling point is 214.93°C [49]). The cryoscopic effect was also evidenced for the crystallization (17°C decrease). The temperature lags were not as high as the ones reported for PA6 [22, 23] (till 60°C) on the one hand because the matrix is a copolymer (PA12 blocks are reported to stand for 88 wt% [46] or for 73 mol% [40] of the copolymer) and on the other hand because of the lower H-bonding concentration among PA12 compared with PA6. Nevertheless, the HPDSC results confirm that water and the polyamide part of PEBA behave as a single molten phase in the extrusion conditions.

Consequently, PEBA fits the requirements for its diffusion and adsorption onto the clay surface, according to the mechanism described by Fedullo *et al*. [44] in the case of PA6/NaMMT nanocomposites. Indeed, the PEBA/water miscibility improves the polymer ability to diffuse into the clay by increasing its polarity and decreasing its viscosity. Then the macromolecules can adsorb on the mineral and concomitantly desorb the H_2O molecules previously adsorbed on the surface, which would not be possible if PEBA and water were immiscible.

3. Analysis of PEBA/clay nanocomposites structure

3.1. Inorganic content

Inorganic content of the compounded materials is reported in Table 1. Mineral contents referred to later correspond to the values measured by TGA under nitrogen flow.

3.2. Molecular mass

Melt processing of polycondensates, such as polyamides, usually requires cautious water removal from the resin in order to avoid backbone hydrolysis (amide links are broken into carboxy and amine ends). Even low moisture contents lead to hydrolytic chain scission and strong reduction of the molecular mass [50].

In the present work, injected water represents 30wt% of the total extrusion throughput. The backbone degradation state was therefore checked by GPC. Table 2 presents molecular masses of the PEBA matrix (in PMMA equivalents) as received and after extrusion with or without water.

A decrease of the molecular mass is observed for PEBA extruded without water injection in comparison with the initial sample (M_n: –7.4% and M_w: –11.6%). This decrease is mainly attributed to the thermal decomposition of the polymer blocks [51]. For PEBA extruded with water, molecular masses are similar to the unprocessed material (M_n: +1.3% and M_w: –4.8%). Expected decreases of the chain

Table 2. Number (M_n) and weight (M_w) average mass of PEBA before and after extrusion step. Results are given as PMMA equivalents.

	M_n [g·mol^{-1}]	Mw [g·mol^{-1}]
unprocessed PEBA	39 100	82 800
PEBA extruded with water	39 600	78 800
PEBA extruded without water	36 200	73 200

length originating from the thermal decomposition and the hydrolysis are hardly observed when water is injected during extrusion. On the contrary, water prevents the matrix from any thermal degradation in the barrel by plasticizing and lubricating the processing medium. This observation has already been reported even though the mechanism is still unclear [52].

Injecting water during extrusion prevents PEBA from thermal degradation and does not lead to the hydrolysis of the polyamide blocks, due to rather slow kinetics and short residence time (less than 30 seconds in contact with water).

3.3. Transmission electron microscopy

TEM pictures of materials prepared with OMMT are reported in Figure 2 at low and high magnification. Dispersion is homogeneous as visible at low magnification and, in addition to the intercalated layers, some part of the mineral exhibit an exfoliated state at high magnification. Samples prepared with (not shown) and without water present similar structures.

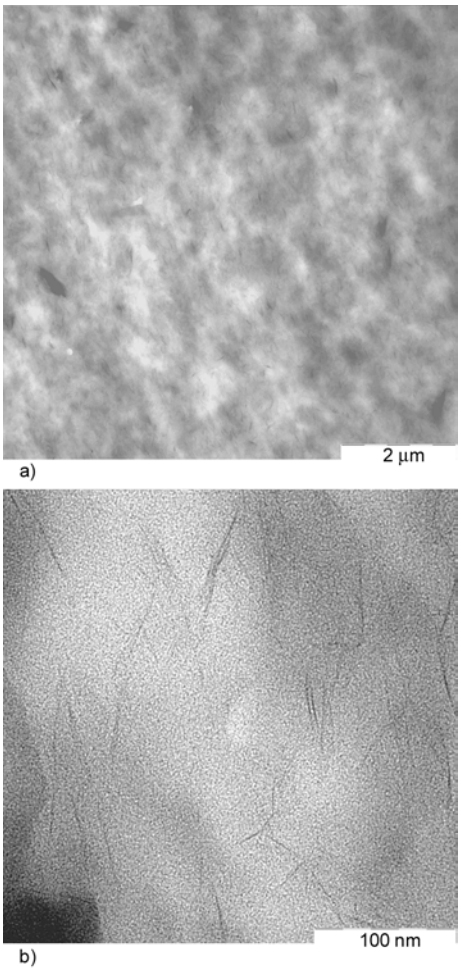

Figure 2. TEM observation of injection-molded 5.5 wt% OMMT/PEBA nanocomposite prepared without water injection at low (a) and high magnification (b)

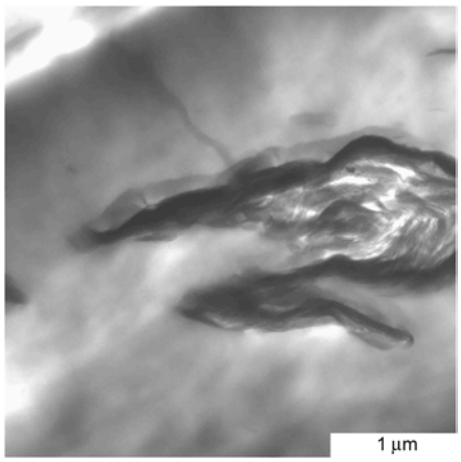

Figure 3. TEM observation of injection-molded 4.1 wt% NaMMT/PEBA nanocomposite prepared without water injection

Figures 3 and 4 show TEM images of nanocomposites prepared with 4.1 and 3.9wt% pristine clay, respectively without and with water injection. At low magnification, the images reveal the presence of micrometric tactoids for the dry processed materials (Figure 3), while the dispersion is almost homogeneous for PEBANaMMT prepared with water injection (Figure 4). This composite exhibits tactoids of reduced dimensions and single exfoliated layers are detectable at high magnification.

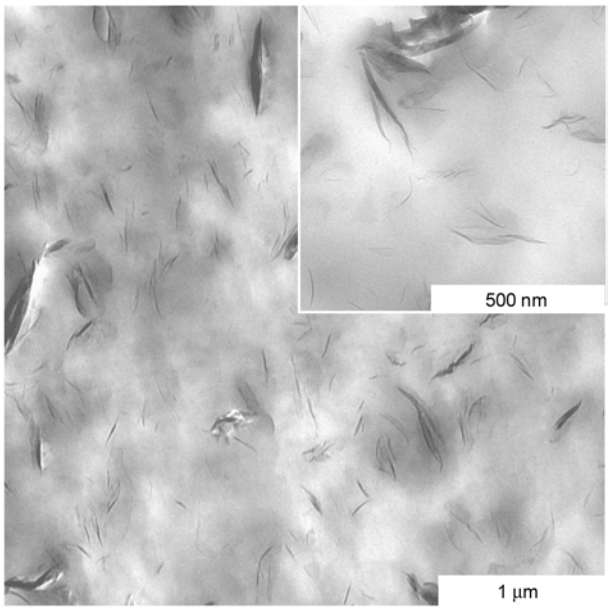

Figure 4. TEM observations of injection-molded 3.9 wt% NaMMT/PEBA nanocomposites prepared with water injection

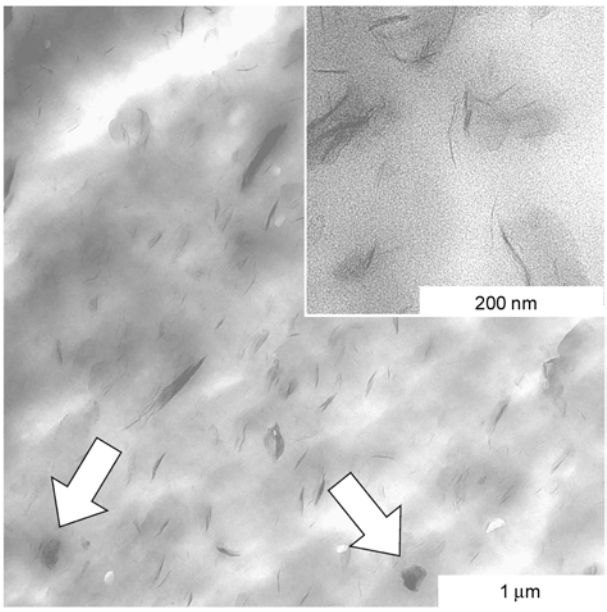

Figure 5. TEM observation of 4.7 wt% RawMMT/ PEBA nanocomposites (extruded pellet) prepared with water injection. Non smectic minerals are indicated by arrows.

The low magnification TEM pictures of the materials prepared with RawMMT when water is injected during extrusion show a structure (Figure 5) close to the one of PEBA/NaMMT with water. Moreover, the presence of black spots which are non smectic minerals (quartz etc.) is also visible in Figure 5 as indicated by arrows. Intercalated and exfoliated layers can be detected at high magnification. Samples prepared with RawMMT without water injection exhibit a structure close to that of PEBA/ NaMMT extruded in the same conditions.

According to these microscopy observations, water actually improves NaMMT and RawMMT dispersions in the PEBA matrix, both for the homogeneity and the exfoliation of the mineral, even if the materials prepared with OMMT exhibit a better dispersion degree. On the basis of TEM observations, water injection has only a limited effect, if any, on the PEBA/OMMT nanocomposites.

3.4. X-Ray diffraction

Intercalation of the mineral by the PEBA chains can be quantified by X-ray diffraction (XRD) measurement. It provides the interlayer distance (corresponding to d_{001}, distance between two consecutives clay layers) according to Bragg's law. Figure 6 shows XRD patterns corresponding to the nanocomposites constitutive components in the 2θ range:

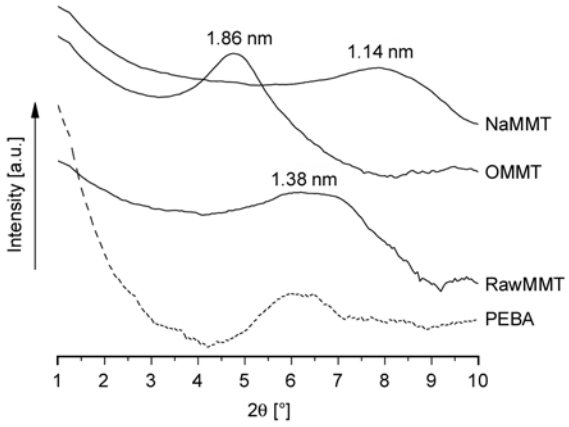

Figure 6. XRD patterns of the constitutive components

[1–10°]. OMMT exhibits a peak corresponding to an interlayer spacing of 1.86 nm which is higher than that of NaMMT and RawMMT (1.14 and 1.38 nm respectively). This result is confirmed in the literature [3, 5] and explained by the fact that minerals are modified by exchanging initial sodium ions with bigger alkylammoniums in order to change the clay polarity and pre-exfoliate the layers. The difference between the two non-modified clays may be explained by the different origins of the minerals and by the moisture content (due to the structural difference of RawMMT). For instance, the basal spacing is known to highly depend on the moisture content of the mineral (the higher the latter, the more distant the platelets) [53] and on the counterion type [12].

PEBA exhibits a diffraction peak around 6°, which corresponds to a crystalline phase of the PA12 block (corresponding to the (200) plane of pseudo-hexagonal γ–form crystal whose reflection peak should appear at $2\theta = 5.5°$ [54]). This may complicate the interpretation of the XRD patterns of the nanocomposites, as this peak position is precisely in the angle range where clay d_{001} peaks may shift.

The XRD patterns of the nanocomposites containing OMMT (Figure 7) exhibit two peaks located at 5.5° and around 2.5°, whatever the processing conditions (with or without water). The former peak refers to PEBA diffraction and the latter to the mineral d_{001} peak. The corresponding basal distance (around 3.5–4.0 nm) is increased compared with the neat OMMT (1.86 nm) indicating an intercalation by the polymer. Both nanocomposites present identical interlayer distances. Consequently, water injection during extrusion does not seem to have any

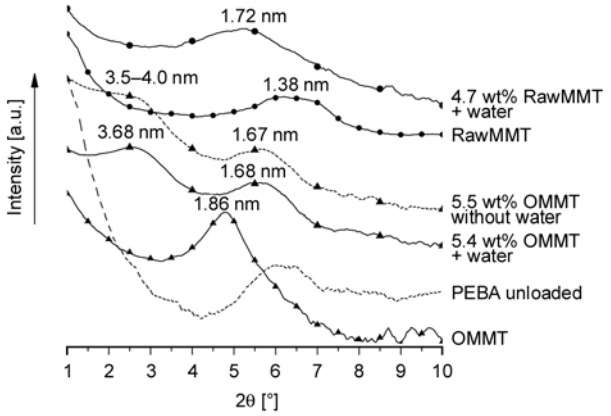

Figure 7. XRD patterns of PEBA/OMMT nanocomposites

effect in the case of PEBA/OMMT nanocomposites, as far as intercalation is concerned.

XRD patterns of PEBA/NaMMT nanocomposites are shown on Figure 8. In the case of materials prepared with water injection, XRD patterns are almost identical whatever the clay content. The neat NaMMT peak located at $2\theta = 7.7°$ is no more visible. Curves present a single broad peak around 5.4° (d_{001} = 1.65 nm) which is analogous to the diffraction peak exhibited by pure PEBA. However, no other peak is detected for PEBA/NaMMT compositions and TEM observations did not allow to consider that clay layers are fully exfoliated. Therefore, the peak located around 5.4° should be assigned to a combination of the matrix diffraction peak and the clay d_{001} peak which has shifted towards lower angles.

The nanocomposite prepared with 4.1 wt% NaMMT without any water injection exhibits two diffraction peaks (5.4° and around 9°). The first one corresponds to the matrix as detailed previously and the second one may be ascribed to the clay d_{001} diffraction peak. The corresponding interlayer distance

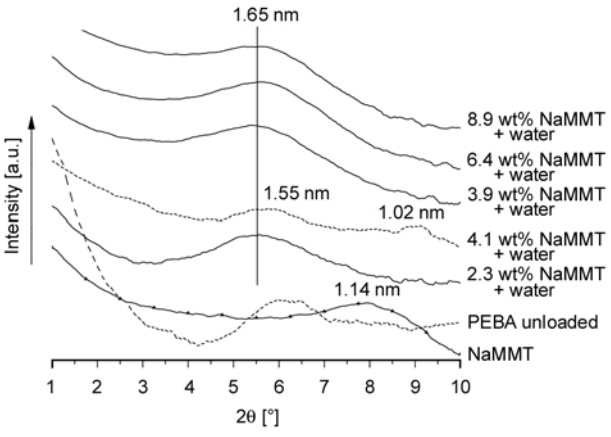

Figure 8. XRD patterns of PEBA/NaMMT nanocomposites

(1.02 nm) is lower than the neat clay (interlayer distance: 1.14 nm) and this reduction can be explained by a drying of the clay during extrusion procedure.

For PEBA/RawMMT nanocomposites, clay is intercalated and basal spacing increased by 0.34 nm in case of water injection (results not reported here), while platelets are compacted by 0.35 nm compared with the neat RawMMT when no water is injected. These compactions can be explained by the fact that neat clays were analyzed by XRD without being previously dried. During the extrusion process without water injection, the added mineral undergoes an in situ drying step; initial water molecules are removed from the clay surface and d_{001} decreases.

According to XRD analysis water injection leads to the intercalation of NaMMT and RawMMT by PEBA (otherwise clays should remain in a tactoid state), whereas it hardly modifies the intercalation state of OMMT.

3.5. Rheology

Rheology is one of the easiest and best way to quantify the filler dispersion into polymer nanocomposites, loaded with carbon nanotubes [55, 56] or with clay platelets [57]. Effects are more noticeable on the storage modulus (G') than on the loss modulus. In particular slopes and absolute values of G' at low frequencies are indicators of the dispersion state of the nanocomposite [47, 58]. In the high frequency range, the signal stands for the segmental motion of the macromolecules, which is directly linked to the molecular mass.

Storage moduli versus rotational frequency are reported in Figure 9. The Figure 9a presents curves corresponding to materials prepared with water injection and the corresponding ones prepared without. For pure PEBA, water injection increases G' at high frequency (from 1900 Pa to 6900 Pa at 19.3 rad·s^{-1}). This G' improvement at high frequency is noticeable for loaded PEBA/clay nanocomposites as well. According to the previously presented GPC results, this improvement can be attributed to a difference in molecular weights. The phenomenon of lower degradation due to the use of water, already evidenced for the neat (unfilled) PEBA, also occurs for the PEBA matrix of the various nanocomposites.

The Figure 9b shows storage moduli of the PEBA/clay nanocomposites of various clay contents. G'

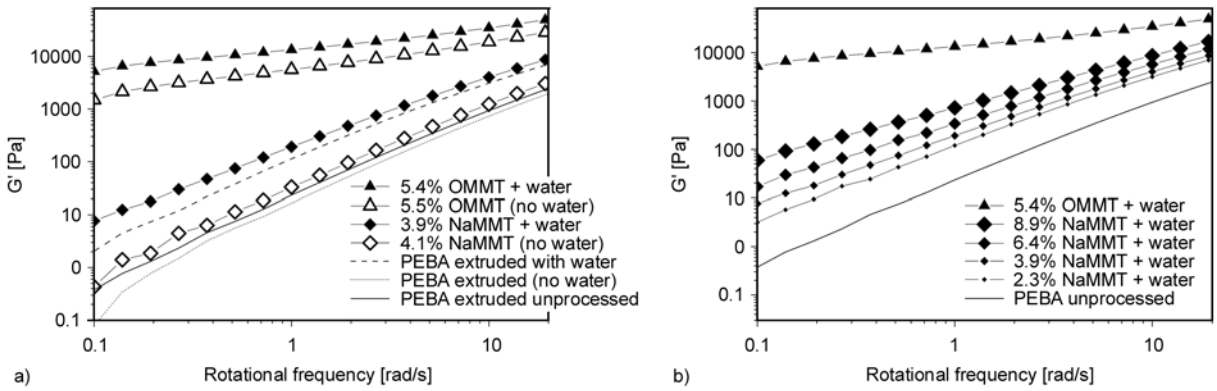

Figure 9. Storage modulus of PEBA/Clay nanocomposites with/without water injection (a) and for different clay contents (b)

Table 3. G' slopes at low rotational frequencies for PEBA/clay nanocomposites

	***G′* slope at low rotational frequency**
PEBA non extruded	1.81
PEBA + 2,3% NaMMT + water	1.56
PEBA + 3,9% NaMMT + water	1.38
PEBA + 4,1% NaMMT without water	1.89
PEBA + 6,4% NaMMT + water	1.31
PEBA + 8,9% NaMMT + water	1.09
PEBA + 5,4% OMMT + water	0.42
PEBA + 5,5% OMMT without water	0.61

slopes at low frequency are presented in Table 3 (calculated using an exponential fitting between 0.1 and 0.5 rad·s^{-1}). For PEBA/NaMMT nanocomposites the storage modulus is all the higher as the mineral content increases and differences between curves expand at low frequencies. Moreover, slopes at low frequency decrease concomitantly. For the neat PEBA, the slope is equal to 1.81 which deviates slightly from the normal terminal slope for homopolymer melts (a value of 2 is theoretically expected). When 8.9 wt% NaMMT is added to PEBA, this value falls down to 1.09. Such a G' increase is frequently reported and has been detailed as $G' = G'_{matrix} + G'_{confine} + G'_{inter}$ [59, 60]. The latter part comes from filler-filler frictional interactions and $G'_{confine}$ stands for macromolecules intercalated in between clay layers. G'_{inter} mainly contributes to the increase at low frequency of G'_{nano}, particularly when clay content is above the percolation threshold [60–62]. Similar results were reported in the literature for PA12/NaMMT prepared by solvent intercalation. G' slope at low frequency was 1.6 for the neat polymer and lowered to 1.4 and 1.2 for 2 and 4 wt% NaMMT loading, respectively [58].

For the two PEBA/NaMMT samples prepared at similar mineral contents (3.9 and 4.1 wt% NaMMT with and without water injection respectively) the modulus at low frequency increases drastically (more than one decade) and slope decreases (from 1.89 to 1.38) when the dispersion shifts from tactoid to intercalated/exfoliated (when water is used). Those two materials exhibit deeply different structures as evidenced by XRD and TEM. These results clearly emphasize that G' value and its concomitant slope are more sensitive to the quality of the clay dispersion than to the clay content. Clusters are much more numerous in the case of an intercalated and exfoliated nanocomposite than for a microcomposite such as PEBA/NaMMT prepared without water. Macromolecules of restricted mobility are less numerous for this material compared with the corresponding water-processed one.

Values of G' obtained with modified clays nanocomposites are the highest and even higher when water is used. The slope is 0.42 for PEBA/5.4 wt% OMMT nanocomposite. This plateau reached by G' at low frequency for PEBA/OMMT nanocomposites is the typical rheological signature of a high clay dispersion [63]. In the case of PEBA/OMMT prepared with or without water, clay platelets and tethered macromolecules have formed a three-dimensional superstructure. Clusters are uniformly dispersed all among the bulk. The slight difference in rheological response induced by water injection probably comes from the matrix degradation, which is limited when water is injected. Nevertheless, the clay dispersion

states are better than in the case of PEBA/NaMMT nanocomposites.

Results obtained by rheological analysis confirm and supplement the structural analysis obtained by XRD and TEM. The water injection reduces PEBA degradation during extrusion and is required in order to get NaMMT dispersion (close to OMMT), intercalation and partial exfoliation.

4. Analysis of PEBA/clay nanocomposites properties

In order to establish the nanostructure-property relationship of the PEBA/clay nanocomposites, mechanical properties were measured.

4.1. Dynamic mechanical properties

Figure 10a shows storage moduli (relative to PEBA, which was measured at 707 MPa) at 25°C of the prepared nanocomposites versus mineral content. The relative modulus increases linearly as a function of the NaMMT content when water is used. For a given NaMMT content, water injection improves the material modulus by 28%. The modulus of PEBA/NaMMT prepared without water is close to the one of pure PEBA. Such an improvement of the storage modulus either by increasing the clay content or by improving the dispersion state using water injection is directly linked to the improved interactions between the matrix and the filler, and not only to the volume fraction of the high modulus clay [2].

Nanocomposites prepared with modified clay (OMMT) exhibit a modulus slightly higher than the one filled with NaMMT. This is probably due to the better dispersion state and subsequent larger polymer/platelets interphase. When water is used, the corresponding PEBA/organoclay nanocomposite exhibits a slightly higher E' compared with the one prepared without water. This modulus difference may be inherent to the composition of the matrices as the dispersion states are similar.

It is also worth noting that the results obtained with PEBA/NaMMT are even better than the ones reported in the literature for PA6 filled with OMMT. Indeed, at 5 wt% clay loading, the normalized E' is 1.33 [2] or 1.34 [64] while it has been found to be 1.44 in the present study.

Figure 10b shows the glass transition temperature (T_g) of the PEBA matrix versus mineral content, which corresponds to PA12 blocks. Indeed, glass transition corresponding to PTMG blocks is hardly detectable because, on the one hand the soft block content is low, and on the other hand a PA12 β-transition appears in this temperature range [65]. In the case of NaMMT clay, T_g increases when the mineral content increases, from 29 to 35°C. The T_g of the PEBA/4,1 wt% NaMMT compound prepared without water injection is the same as the pure PEBA matrix. When water is injected, the T_g increases by 3°C (PEBA + 3.9 wt% NaMMT + water). This increment can be assigned to a reduced mobility of the macromolecular chains adsorbed on the mineral platelets [66]. The more exfoliated the mineral is, the less mobile the chains and consequently the higher the T_g are.

In the case of PEBA/OMMT nanocomposites prepared with or without water, T_g is increased compared with the pure polymer. It must be considered that for these modified-clay compounds, the macromolecules mobility is highly reduced by the homogeneous platelets dispersion. Such a dispersion leads to high T_g in spite of an eventual plasticizing effect provided by alkylammoniums. Indeed, some authors reported that T_g of PA12/OMMT nanocomposites is

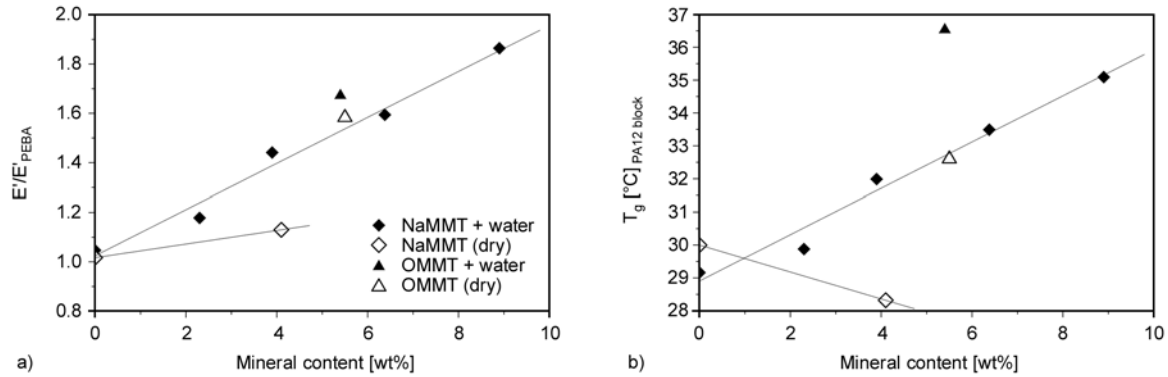

Figure 10. Relative storage modulus (a) and glass transition temperatures (b) of PA12 blocks of PEBA/Clay nanocomposites measured by DMA in tensile mode

independent of the clay content [5] because the mobility restriction is notably counterbalanced by the water plasticization. Moreover, a decrease of the nanocomposite glass transition, justified by a plasticizing effect attributed to the alkylammonium ions modifying the clay, is also reported when the mineral content increases [3]. Besides, mechanism of polyamide nanocomposites plasticization is the same as for the unfilled polyamide [66, 67]. PEBA/OMMT nanocomposite prepared with water injection exhibits a T_g higher than that of the one prepared without water. In combination with the slight structural dissimilarity detected by rheology, a plasticization phenomenon may explain this neat glass transition difference. The water-prepared PEBA/OMMT nanocomposites are less plasticized by alkylammonium because of a steam stripping of the surfactant moieties throughout the degassing apertures. Detailed results of odours and volatile organic compounds (VOC) emission analyses performed on the processed materials are reported elsewhere [67]. One of the key points is that PEBA/ OMMT prepared without water injection emits much more odours and VOCs (coming from the alkylammonium or its decomposition products) than the corresponding nanocomposite prepared with water injection. The latter emits as few VOCs as the neat PEBA. This result confirms the flushing of the plasticizing surfactant from the OMMT-filled nanocomposite when water is injected [68]. A similar phenomenon is reported in the literature for polymer/cellulose composites prepared with water injection into the melt. Cellulose degradation products responsible for the coloration of the material were steam-extracted and resulting material exhibited a limited coloration [52]. Finally, it is worth noticing that materials exhibiting similar structures detected by XRD and TEM (and limited differences in rheological responses) present different thermomechanical behaviors because of slight changes in the chemical composition (organo-modifiers account for less than 2 wt% of the PEBA/OMMT nanocomposites).

At last, the glass transition increment (ΔT_g) presented by the material containing 5.5 wt% OMMT prepared without water is comparable with the one measured for water-prepared and NaMMT-filled nanocomposite at similar (4.1 wt%) clay loading. When water is injected, PEBA/OMMT exhibits the highest improvement of glass transition (+7°C) of the series. The organomodifications and use of water enabled the fine dispersion of the clay layers and water clears the nanocomposite from the chemicals coming from the clay grafting treatment. The role played by water is different in the case of PEBA/NaMMT nanocomposites. Water allows the intercalation of pristine platelets by macromolecules whose mobility is then reduced as evidenced by T_g measurements.

4.2. Tensile properties

Results of tensile tests are reported in Figure 11. Figure 11a shows the Young modulus, defined as and Figure 11b the yield stress. Young modulus is a measure of the stiffness and is the tangent modulus of the initial, linear portion of a stress-strain curve. Yield stress is defined as the stress that can undergo the material before plastic flow. Modulus of neat PEBA extruded with water injection is slightly higher (+7%) than that of PEBA extruded without water, probably because of a limited degradation as evidenced previously by GPC and rheological analysis. The higher modulus values observed for nano-

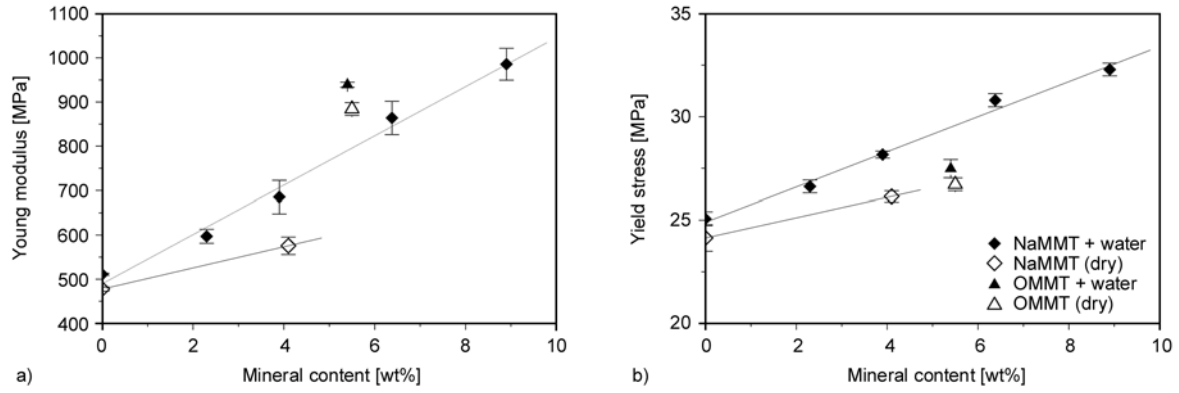

Figure 11. Tensile mechanical properties of PEBA/Clay nanocomposites (a: Young modulus; b: Yield stress). Error bars represent the standard deviation.

composites prepared with water injection also result from the higher matrix molecular weights, as a minor contribution.

In the case of NaMMT-filled materials prepared with water injection, Young modulus increases linearly with the mineral content; it is almost doubled at 8.9 wt% clay loading. However, for a given NaMMT content (around 4 wt%), the modulus is decreased by 16% if water is not injected during extrusion and is close to the unloaded PEBA modulus. As demonstrated previously the dispersion remains at 'intercalated and partially exfoliated' state for all PEBA/NaMMT nanocomposites prepared with water injection. Consequently the volume of polymer/clay interphase increases along with NaMMT content. The interphase is not only made of the adsorbed chains but also includes macromolecules entangled with the former ones. A characteristic structure of limited conformation is then created at the vicinity of the filler. Mechanical properties of this interphase strongly differ from the bulk polymer [67]. Increasing the NaMMT content improves the interphase volume and its contribution to the mechanical behavior of the whole material, as usually reported for intercalated/exfoliated nanocomposites [2, 3, 5, 70]. Injected water improves the dispersion state and the volume of polymer/clay interphase increases as evidenced by the structural analysis. The resulting modulus is thus enhanced, although the clay loading is unchanged.

Compared to the materials filled with pristine clay, the OMMT-filled nanocomposites exhibit a slightly higher Young modulus, due to the better clay dispersion. Moreover, improvement of modulus of PEBA/OMMT owing to water injection is limited (+6%). It can be attributed, on the one hand to the higher molecular mass obtained, and on the other hand to the absence of plasticization by alkylammoniums when water is used, as previously discussed for glass transition results.

Finally, as previously highlighted by rheological measurements, the interphase volume among PEBA/NaMMT nanocomposites increases with the mineral loading and water injection. For PEBA/OMMT nanocomposites, the little difference induced by water injection, previously revealed by rheological analysis, remains detectable when Young modulus is considered. Results obtained in static and dynamic modes are similar and confirm each other.

Figure 11b shows the yield stresses of the studied nanocomposites. In the case of nanocomposites filled with NaMMT, when water is injected during the melt processing, the yield stress increases with the pristine mineral content (up to +30% for 8.9 wt% clay). The nanocomposites based on NaMMT prepared without water injection have a lower yield stress. This may be attributed to the lower dispersion and also eased plastic deformation due to the presence of aggregates which induce decohesion leading to microcrazing. Both PEBA/OMMT nanocomposites exhibit slight yield stress improvements, clearly inferior to what is observed with NaMMT. Water injection has little effect onto PEBA/OMMT nanocomposites. In spite of the higher rigidity (high Young modulus) of these nanocomposites and a good dispersion as attested by rheology and TEM, the decrease of the yield stress means that the plastic deformation is eased. One can suppose that the increase of the interface proportion increases the number of crazing sites which in turn help the initiation of plastic deformation.

Elongations at break are reported on Figure 12. PEBA/NaMMT nanocomposites prepared with water injection break at lower elongation rates than neat PEBA. This ductility reduction is amplified when the mineral content increases. When no water is injected during extrusion of PEBA/4 w% NaMMT compound the elongation at break is higher than when water is injected, and unchanged in comparison with pure PEBA. The corresponding microcomposite exhibits the highest elongation at break of the filled materials' series. This result can be explained by the fact that microcomposites and

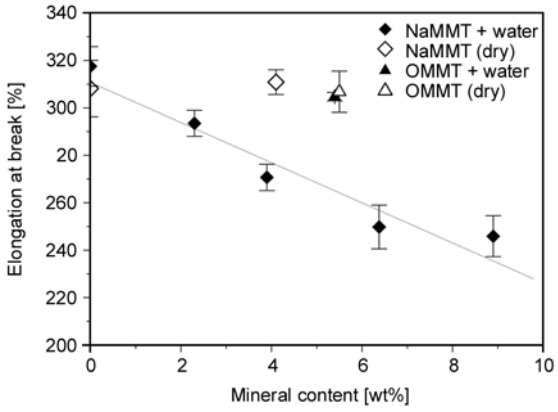

Figure 12. Relative elongation at break of PEBA/clay nanocomposites. Error bars represent the standard deviation.

nanocomposites undergo different fracture behaviors, as reviewed by Cotterell *et al*. [71]. According to the authors, semicrystalline polymer nanocomposites are toughened through to two mechanisms: particles' delamination and matrix deformation. For the latter, energy is mainly absorbed because of the formation of multiple craze-like bands while shear yielding is reported to be negligible. Moreover, particles' delamination prevails upon matrix deformation when particles are large [71]. In the case of clay nanoplatelets poorly dispersed into PA12, Kim *et al*. [72] report that the deformation process is governed by the formation of microvoids inside the filler tactoids, which toughens the material. The mechanism is illustrated in Figure 13. Such a tactoid delamination process may take place in PEBA/NaMMT prepared without water injection, whose dispersion state is poor, as evidenced previously. On the contrary, for the best dispersed nanocomposites (PEBA/OMMT, with or without water injection), the energy absorbing mechanism cannot be particles' delamination as most of the clay is dispersed as single layers. These exfoliated nanocomposites exhibit higher elongations at break owing to energy absorbing matrix deformation. Crazes are initiated at the vicinity of the platelets. These fibrillated microvoids act as energy dissipaters if the platelets are well dispersed. Otherwise crazes may cause the failure of the material [73]. The homogeneous clay dispersion observed in PEBA/OMMT leads to the uniform creation of crazes among the bulk. Once nucleated, crazes grow and concomitantly disperse the energy provided by the strain (Figure 13). Transformation of those safe and scattered microvoids into disastrous cracks requires a high density of crazes or their coalescence, and consequently appears at high elongation rates [70]. Decohesion of the filler from the matrix is not considered here because of the strong interactions between PEBA and clay platelets in the exfoliated and intercalated structures.

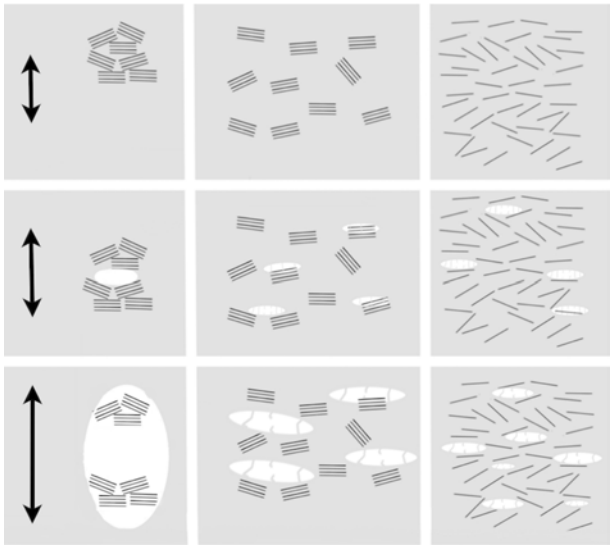

Figure 13. Deformation mechanisms of PEBA/clay microcomposite (left), intercalated nanocomposite (center) and exfoliated nanocomposite (right). Arrows indicate the loading direction and amplitude

Concerning intercalated nanocomposites, Cotterell *et al*. [71] report numerous and contradictory interpretations. However, in the case of PEBA/NaMMT nanocomposites prepared with water injection, whose morphologies are mainly intercalated but also exhibit small tactoids, it is clear that the toughening mechanism is hardly influenced by particles' delamination. Moreover, the craze formation does not toughen the materials as for exfoliated nanocomposites, even if the crazes are located close to the layers as well. For intercalated nanocomposites, stress fields created around the crazes may overlap as the platelets are not homogeneously dispersed [69, 72]. Then, adjacent microvoids may coalesce and favor the development of cracks which lead to the material breakdown as illustrated in Figure 13. Intercalated PEBA/NaMMT hardly dissipate energy under tension because of their structure. On the one hand it does not reveal the presence of large aggregates required for delamination to take place; and on the other hand it is not exfoliated enough for crazes to safely toughen the material. Such an intermediate dispersion state consequently embrittles the material. The embrittlement is all the higher as the clay content increases, acting as crack initiators. Finally, the tensile performances obtained with NaMMT are comparable with the ones reported in the literature [4]. Wilkinson *et al*. [4] report that tensile modulus and yield stress are improved by 73% and 28% respectively when 5 wt% OMMT is incorporated in a PA6 matrix. For PEBA + 6.4wt% NaMMT prepared with water injection, these improvements reach 89 and 30% respectively. Concerning elongation at break, Wilkinson reports a 93% decrease whereas the present PEBA/NaMMT nanocomposites exhibits a 43% decrease only. Moreover, tensile performances reached by PA/NaMMT prepared with in the same conditions [28]

are clearly lower than what is reported here for PEBA/NaMMT.

5. Conclusion

The aim of the present study was to elaborate nanocomposites based on a polyether-block-amide (PEBA) matrix and pristine montmorillonite using water injection during extrusion as processing aid. PEBA nanocomposites based on organo-modified montmorillonite were used as a reference. High pressure differential calorimetry evidenced that the miscibility of water and PA12 blocks in the extrusion conditions (high pressure and high temperature) makes the dispersion of clay platelets easier, as confirmed by transmission electron microscopy, X-ray diffraction and dynamic rheology. Moreover matrix degradation during extrusion, characterized by gel permeation chromatography, is reduced that way.

Injection of water into the extruder led to exfoliation and intercalation whatever the type of montmorillonite (pristine, i.e. unmodified, or organo-modified). Interestingly, water-assisted compounding is however clearly more efficient in the case of unmodified montmorillonite as the counterpart material obtained without water injection is a microcomposite (presence of micrometric aggregates).

Dynamic mechanical analysis in tension and tensile tests further confirmed the efficiency of water injection. Actually, the modulus of unmodified montmorillonite filled PEBA is higher when compounded with the aid of water and close to the one of organo-modified montmorillonite filled PEBA. Furthermore, the dispersion degree has a strong effect on the deformation mechanism and thus on the ductility of the nanocomposites. Indeed, crazes act as energy dissipaters in the case of exfoliated structure but as crack initiators for intercalated nanocomposites. Surprisingly, the ductility of the microcomposite is improved due to the formation of microvoids inside the tactoids, which toughens the material.

To conclude, water-assisted extrusion appears to be an efficient method to elaborate partially exfoliated PEBA/montmorillonite nanocomposites. Particularly, this method allows achieving partial exfoliation of unmodified montmorillonite leading to a significant improvement of the resulting mechanical properties. Thereby, water-assisted melt compounding is a convenient alternative to the classical method having recourse to expensive clay organo-modification to fabricate nanocomposites based on cheaper unmodified clay such as pristine montmorillonite.

Acknowledgements

Authors are indebted to the Nord Pas de Calais regional council for facilitating the exchanges between the two collaborating laboratories under international mobility grant # 2008_09396.

References

[1] Okada A., Fukushima Y., Kawasumi M., Inagaki S., Usuki A., Sugiyama S., Kurauchi T., Kamigaito O.: Composite material and process for manufacturing same. U.S. Patent 4739007, USA (1988).

[2] Shelley J. S., Mather P. T., DeVries K. L.: Reinforcement and environmental degradation of nylon-6/clay nanocomposites. Polymer, **42**, 5849–5858 (2001). DOI: 10.1016/S0032-3861(00)00900-9

[3] Liu T., Lim K. P., Tjiu W. C., Pramoda K. P., Chen Z-K.: Preparation and characterization of nylon 11/organoclay nanocomposites. Polymer, **44**, 3529–3535 (2003). DOI: 10.1016/S0032-3861(03)00252-0

[4] Wilkinson A. N., Man Z., Stanford J. L., Matikainen P., Clemens M. L., Lees G. C., Liauw C. M.: Tensile properties of melt intercalated polyamide 6 – Montmorillonite nanocomposite. Composites Science and Technology, **67**, 3360–3368 (2007). DOI: 10.1016/j.compscitech.2007.03.024

[5] Alexandre B., Langevin D., Médéric P., Aubry T., Couderc H., Nguyen Q. T., Saiter A., Marais S.: Water barrier properties of polyamide 12/montmorillonite nanocomposite membranes: Structure and volume fraction effects. Journal of Membrane Science, **328**, 186–204 (2009). DOI: 10.1016/j.memsci.2008.12.004

[6] Fermeglia M., Ferrone M., Pricl S.: Computer simulation of nylon-6/organoclay nanocomposites: Prediction of the binding energy. Fluid Phase Equilibria, **212**, 315–329 (2003). DOI: 10.1016/S0378-3812(03)00273-5

[7] Tanaka G., Goettler L. A.: Predicting the binding energy for nylon 6,6/clay nanocomposites by molecular modeling. Polymer, **43**, 541–553 (2002). DOI: 10.1016/S1089-3156(01)00014-9

[8] Liu A., Xie T., Yang G.: Synthesis of exfoliated monomer casting polyamide 6/Na^+-montmorillonite nanocomposites by anionic ring opening polymerization. Macromolecular Chemistry and Physics, **207**, 701–707 (2006). DOI: 10.1002/macp.200500556

[9] Maiti P., Okamoto M.: Crystallization controlled by silicate surfaces in nylon 6-clay nanocomposites. Macromolecular Materials and Engineering, **288**, 440–445 (2003).
DOI: 10.1002/mame.200390040

[10] Monticelli O., Musina Z., Frache A., Bellucci F., Camino G., Russo S.: Influence of compatibilizer degradation on formation and properties of PA6/organoclay nanocomposites. Polymer Degradation and Stability, **92**, 370–378 (2007).
DOI: 10.1016/j.polymdegradstab.2006.12.010

[11] Zhang F., Low P. F., Roth C. B.: Effects of monovalent, exchangeable cations and electrolytes on the relation between swelling pressure and interlayer distance in montmorillonite. Journal of Colloid and Interface Science, **173**, 34–41 (1995).
DOI: 10.1006/jcis.1995.1293

[12] Kadlecová Z., Puffr R., Baldrian J., Schmidt P., Roda J., Brožek J.: Homoionic inorganic montmorillonites as fillers for polyamide 6 nanocomposites. European Polymer Journal, **44**, 2798–2806 (2008).
DOI: 10.1016/j.eurpolymj.2008.06.036

[13] Kim N. H., Malhotra S. V, Xanthos M.: Modification of cationic nanoclays with ionic liquids. Microporous and Mesoporous Materials, **96**, 29–35 (2006).
DOI: 10.1016/j.micromeso.2006.06.017

[14] Gilman J. W., Awad W. H., Davis R. D., Shields J., Harris R. H., Davis C., Morgan A. B., Sutto T. E., Callahan J., Trulove P. C., DeLong H. C.: Polymer/layered silicate nanocomposites from thermally stable trialkylimidazolium-treated montmorillonite. Chemistry of Materials, **14**, 3776–3785 (2002).
DOI: 10.1021/cm011532x

[15] Célini N., Bergaya F., Poncin-Epaillard F.: Grafting of hydrocarbon moieties on smectites by cold acetylene plasma and characterization of plasma-treated clay mineral polyethylene nanocomposites. Polymer, **48**, 58–67 (2007).
DOI: 10.1016/j.polymer.2006.11.018

[16] Manke C. W., Gulari E., Mielewski D. F., Lee E. C.: System and method of delaminating a layered silicate material by supercritical fluid treatment. U.S. Patent 6469073, USA (2002).

[17] Tomasko D. L., Han X., Liu D., Gao W.: Supercritical fluid applications in polymer nanocomposites. Current Opinion in Solid State and Materials Science, **7**, 407–412 (2003).
DOI: 10.1016/j.cossms.2003.10.005

[18] Rastogi S., Terry A. E., Vinken E.: Dissolution of hydrogen-bonded polymers in water: A study of nylon-4,6. Macromolecules, **37**, 8825–8828 (2004).
DOI: 10.1021/ma0483423

[19] Vinken E., Terry A. E., Hoffmann S., Vanhaecht B., Koning C. E., Rastogi S.: Influence of hydrogen bonding on the conformational changes, the brill transition, and lamellae thickening in (co)polyamides. Macromolecules, **39**, 2546–2552 (2006).
DOI: 10.1021/ma0526903

[20] Vinken E., Terryt A. E., van Asselen O., Spoelstra A. B., Graf R., Rastogi S.: Role of superheated water in the dissolution and perturbation of hydrogen bonding in the crystalline lattice of polyamide 4,6. Langmuir, **24**, 6313–6326 (2008).
DOI: 10.1021/la800378c

[21] Vinken E., Terry A. E., Spoelstra A. B., Koning C. E., Rastogi S.: Influence of superheated water on the hydrogen bonding and crystallography of piperazine-based (co)polyamides. Langmuir, **25**, 5294–5303 (2009).
DOI: 10.1021/la804046r

[22] Wevers M. G. M., Mathot V. B. F., Pijpers T. F. J., Goderis B., Groeninckx G.: Full dissolution and crystallization of PA6 and polyamide 4.6 in water and ethanol. in 'Lecture notes in physis' (eds.: Reiter G., Strobl G.) Springer, Berlin, Vol 714, 151–168 (2007).

[23] Wevers M. G. M., Pijpers T. F. J., Mathot V. B. F.: The way to measure quantitatively full dissolution and crystallization of polyamides in water up to 200°C and above by DSC. Thermochimica Acta, **453**, 67–71 (2007).
DOI: 10.1016/j.tca.2006.10.020

[24] Charlet K., Mathot V., Devaux J.: Crystallization and dissolution behaviour of polyamide 6–water systems under pressure. Polymer International, **60**, 119–125 (2011).
DOI: 10.1002/pi.2920

[25] Hasegawa N., Okamoto H., Kato M., Usuki A., Sato N.: Nylon 6/Na–montmorillonite nanocomposites prepared by compounding nylon 6 with Na–montmorillonite slurry. Polymer, **44**, 2933–2937 (2003).
DOI: 10.1016/S0032-3861(03)00215-5

[26] Fedullo N., Sorlier E., Sclavons M., Bailly C., Lefebvre J-M., Devaux J.: Polymer-based nanocomposites: Overview, applications and perspectives. Progress in Organic Coatings, **58**, 87–95 (2007).
DOI: 10.1016/j.porgcoat.2006.09.028

[27] Korbee R. A., Van Geenen A. A.: Process for the preparation of a polyamide nanocomposite composition. U.S. Patent 6350805, USA (1999).

[28] Yu Z-Z., Hu G-H., Varlet J., Dasari A., Ma Y-W.: Water-assisted melt compounding of nylon-6/pristine montmorillonite nanocomposites. Journal of Polymer Science Part B: Polymer Physics, **43**, 1100–1112 (2005).
DOI: 10.1002/polb.20397

[29] Siengchin S., Karger-Kocsis J., Thomann R.: Nanofilled and/or toughened POM composites produced by water-mediated melt compounding: Structure and mechanical properties. Express Polymer Letter, **2**, 746–756 (2008).
DOI: 10.3144/expresspolymlett.2008.88

[30] Rubio J., Kitchener J. A.: The mechanism of adsorption of poly(ethylene oxide) flocculant on silica. Journal of Colloid and Interface Science, **57**, 132–142 (1976).
DOI: 10.1016/0021-9797(76)90182-X

[31] Yuang P-C., Shen Y-H.: Determination of the surface area of smectite in water by ethylene oxide chain adsorption. Journal of Colloid and Interface Science, **285**, 443–447 (2005).
DOI: 10.1016/j.jcis.2004.12.056

[32] Mathur S., Moudgil B. M.: Adsorption mechanism(s) of poly(ethylene oxide) on oxide surfaces. Journal of Colloid and Interface Science, **196**, 92–98 (1997).
DOI: 10.1006/jcis.1997.5192

[33] Su C-C., Shen Y-H.: Adsorption of poly(ethylene oxide) on smectite: Effect of layer charge. Journal of Colloid and Interface Science, **332**, 11–15 (2009).
DOI: 10.1016/j.jcis.2008.12.024

[34] Strawhecker K. E., Manias E.: Crystallization behavior of poly(ethylene oxide) in the presence of Na^+ montmorillonite fillers. Chemistry of Materials, **15**, 844–849 (2003).
DOI: 10.1021/cm0212865

[35] Lu Y., Kong S-T., Deiseroth H-J., Mormann W.: Structural requirements for the intercalation of polyether polyols into sodium-montmorillonite: The role of oxyethylene sequences. Macromolecular Materials and Engineering, **293**, 900–906 (2008).
DOI: 10.1002/mame.200800155

[36] Soulestin J.: Elaboration and mechanical behavior of PMMA nanocomposites (in French). PhD thesis. Université des Sciences et Technologies de Lille (2004).

[37] Moad G., Dean K., Edmond L., Kukaleva N., Li G., Mayadunne R. T. A., Pfaendner R., Schneider A., Simon G. P., Wermter H.: Non-ionic, poly(ethylene oxide)-based surfactants as intercalants/dispersants/exfoliants for poly(propylene)-clay nanocomposites. Macromolecular Materials and Engineering, **291**, 37–52 (2006).
DOI: 10.1002/mame.200500294

[38] Carretero-González J., Valentín J. L., Arroyo M., Saalwächter K., Lopez-Manchado M. A.: Natural rubber/clay nanocomposites: Influence of poly(ethylene glycol) on the silicate dispersion and local chain order of rubber network. European Polymer Journal, **44**, 3493–3500 (2008).
DOI: 10.1016/j.eurpolymj.2008.08.046

[39] Majumdar D., Dontula N., Blanton T. N., Freedman G. S.: Smectite clay intercalated with polyether block polyamide copolymer. U.S. Patent 7166656, USA (2007).

[40] Yang I-K., Tsai P-H.: Intercalation and viscoelasticity of poly(ether-block-amide) copolymer/montmorillonite nanocomposites: Effect of surfactant. Polymer, **47**, 5131–5140 (2006).
DOI: 10.1016/j.polymer.2006.04.065

[41] Yang I-K., Tsai P-H.: Preparation and characterization of polyether-*block*-amide copolymer/clay nanocomposites. Polymer Engineering and Science, **47**, 235–243 (2007).
DOI: 10.1002/pen.20670

[42] Sheth J. P., Xu J., Wilkes G. L.: Solid state structure–property behavior of semicrystalline poly(ether-*block*-amide) PEBAX® thermoplastic elastomers. Polymer, **44**, 743–756 (2003).
DOI: 10.1016/S0032-3861(02)00798-X

[43] Kaufhold S., Dohrmann R., Ufer K., Meyer F. M.: Comparison of methods for the quantification of montmorillonite in bentonites. Applied Clay Science, **22**, 145–151 (2002).
DOI: 10.1016/S0169-1317(02)00131-X

[44] Fedullo N., Sclavons M., Bailly C., Lefebvre J-M., Devaux J.: Nanocomposites from untreated clay: A myth? Macromolecular Symposia, **233**, 235–245 (2006).
DOI: 10.1002/masy.200690023

[45] Borse N. K., Kamal M. R.: Melt processing effects on the structure and mechanical properties of PA-6/clay nanocomposites. Polymer Engineering and Science, **46**, 1094–1103 (2006).
DOI: 10.1002/pen.20578

[46] Tavernier B., Mewis J., Van Puyvelde P., Takenaka M., Ernst B., Hashimoto T.: Effect of thermomechanical history on the crystallization of poly(ether-*block*-amide). Polymer Engineering and Science, **48**, 2418–2425 (2008).
DOI: 10.1002/pen.21197

[47] Durmus A., Kasgoz A., Macosko C. W.: Linear low density polyethylene (LLDPE)/clay nanocomposites. Part I: Structural characterization and quantifying clay dispersion by melt rheology. Polymer, **48**, 4492–4502 (2007).
DOI: 10.1016/j.polymer.2007.05.074

[48] Wagener R., Reisinger T. J. G.: A rheological method to compare the degree of exfoliation of nanocomposites. Polymer, **44**, 7513–7518 (2003).
DOI: 10.1016/j.polymer.2003.01.001

[49] Wagner W., Cooper J. R., Dittmann A., Kijima J., Kretzschmar H-J., Kruse A., Mareš R., Oguchi K., Sato H., Stöcker I., Šifner O., Takaishi Y., Tanishita I., Trübenbach J., Willkommen T.: The IAPWS industrial formulation 1997 for the thermodynamic properties of water and steam. Journal of Engineering for Gas Turbines and Power, **122**, 150–182 (2000).
DOI: 10.1115/1.483186

[50] La Mantia F. P., Scaffaro R.: Melt stabilization of wet polyamide 6. Polymer Degradation and Stability, **75**, 473–477 (2002).
DOI: 10.1016/S0141-3910(01)00250-6

[51] Levchik S. V., Weil E. D., Lewin M.: Thermal decomposition of aliphatic nylons. Polymer International, **48**, 532–557 (1999).
DOI: 10.1002/(SICI)1097-0126(199907)48:7<532::AID-PI214>3.0.CO;2-R

[52] Soulestin J., Quiévy N., Sclavons M., Devaux J.: Polyolefins–biofibre composites: A new way for an industrial production. Polymer Engineering and Science, **47**, 467–476 (2007).
DOI: 10.1002/pen.20706

[53] Devineau K., Bihannic I., Michot L., Villiéras F., Masrouri F., Cuisinier O., Fragneto G., Michau N.: In situ neutron diffraction analysis of the influence of geometric confinement on crystalline swelling of montmorillonite. Applied Clay Science, **31**, 76–84 (2006). DOI: 10.1016/j.clay.2005.08.006

[54] Wan C., Zhao F., Bao X., Kandasuramanian B., Duggan M.: Effect of POSS on crystalline transitions and physical properties of polyamide 12. Journal of Polymer Science Part B: Polymer Physics, **47**, 121–129 (2009). DOI: 10.1002/polb.21620

[55] Abdalla M., Dean D., Adibempe D., Nyairo E., Robinson P., Thompson G.: The effect of interfacial chemistry on molecular mobility and morphology of multiwalled carbon nanotubes epoxy nanocomposite. Polymer, **48**, 5662–5670 (2007). DOI: 10.1016/j.polymer.2007.06.073

[56] Prashantha K., Soulestin J., Lacrampe M. F., Krawczak P., Dupin G., Claes M.: Masterbatch-based multiwalled carbon nanotube filled polypropylene nanocomposites: Assessment of rheological and mechanical properties. Composites Science and Technology, **69**, 1756–1763 (2009). DOI: 10.1016/j.compscitech.2008.10.005

[57] Cassagnau P.: Melt rheology of organoclay and fumed silica nanocomposites. Polymer, **49**, 2183–2196 (2008). DOI: 10.1016/j.polymer.2007.12.035

[58] Hoffmann B., Kressler J., Stöppelmann G., Friedrich C., Kim G-M.: Rheology of nanocomposites based on layered silicates and polyamide-12. Colloid and Polymer Science, **278**, 629–636 (2000). DOI: 10.1007/s003960000294

[59] Li J., Zhou C., Wang G., Zhao D.: Study on rheological behavior of polypropylene/clay nanocomposites. Journal of Applied Polymer Science, **89**, 3609–3617 (2003). DOI: 10.1002/app.12643

[60] Wu D., Zhou C., Zhang M.: Rheology of isothermally crystallized poly(butylene terephthalate) nanocomposites with clay loadings under the percolation threshold. Journal of Polymer Science Part B: Polymer Physics, **45**, 229–238 (2007). DOI: 10.1002/polb.21044

[61] Gagali G., Ramesh C., Lele A.: A rheological study on the kinetics of hybrid formation in polypropylene nanocomposites. Macromolecules, **34**, 852–858 (2001). DOI: 10.1021/ma000565f

[62] Dorigato A., Pegoretti A., Penati A.: Linear low-density polyethylene/silica micro- and nanocomposites: Dynamic rheological measurements and modelling. Express Polymer Letters, **4**, 115–129 (2010). DOI: 10.3144/expresspolymlett.2010.16

[63] Krishnamoorti R., Yurekli K.: Rheology of polymer layered silicate nanocomposites. Current Opinion in Colloid and Interface Science, **6**, 464–470 (2001). DOI: 10.1016/S1359-0294(01)00121-2

[64] Wilkinson A. N., Man Z., Stanford J. L., Matikainen P., Clemens M. L., Lees G. C., Liauw C. M.: Structure and dynamic mechanical properties of melt intercalated polyamide 6–montmorillonite nanocomposites. Macromolecular Materials and Engineering, **291**, 917–928 (2006). DOI: 10.1002/mame.200600150

[65] Varlet J., Cavaillé J. Y., Perez J., Johari G. P.: Dynamic mechanical spectrometry of nylon-12. Journal of Polymer Science Part B: Polymer Physics, **28**, 2691–2705 (1990). DOI: 10.1002/polb.1990.090281315

[66] Huang J-C., Zhu Z-K., Yin J., Qian X-F., Sun Y-Y.: Poly(etherimide)/montmorillonite nanocomposites prepared by melt intercalation: Morphology, solvent resistance properties and thermal properties. Polymer, **42**, 873–877 (2001). DOI: 10.1016/S0032-3861(00)00411-0

[67] Vlasveld D. P. N., Groenewold J., Bersee H. E. N., Picken S. J.: Moisture absorption in polyamide-6 silicate nanocomposites and its influence on the mechanical properties. Polymer, **46**, 12567–12576 (2005). DOI: 10.1016/j.polymer.2005.10.096

[68] Thouzeau C.: Emissions during processing and use of organoclays based nanocomposites. MSc thesis, Université Catholique de Louvain (2009).

[69] Ciprari D., Jacob K., Tannenbaum R.: Characterization of polymer nanocomposite interphase and its impact on mechanical properties. Macromolecules, **39**, 6565–6573 (2006). DOI: 10.1021/ma0602270

[70] Kim G-M., Goerlitz S., Michler G. H.: Deformation mechanism of nylon 6/layered silicate nanocomposites: Role of the layered silicate. Journal of Applied Polymer Science, **105**, 38–48 (2007). DOI: 10.1002/app.26067

[71] Cotterell B., Chia J. Y. H., Hbaieb K.: Fracture mechanisms and fracture toughness in semicrystalline polymer nanocomposites. Engineering Fracture Mechanics, **74**, 1054–1078 (2007). DOI: 10.1016/j.engfracmech.2006.12.023

[72] Kim G-M., Lee D-H., Hoffmann B., Kressler J., Stöppelmann G.: Influence of nanofillers on the deformation process in layered silicate/polyamide-12 nanocomposites. Polymer, **42**, 1095–1100 (2001). DOI: 10.1016/S0032-3861(00)00468-7

[73] He C., Liu T., Tjiu W. C., Sue H-J., Yee A. F.: Microdeformation and fracture mechanisms in polyamide-6/organoclay nanocomposites. Macromolecules, **41**, 193–202 (2008). DOI: 10.1021/ma071781s

eXPRESS Polymer Letters Vol.5, No.12 (2011) 1102–1112
Available online at www.expresspolymlett.com
DOI: 10.3144/expresspolymlett.2011.107

Remarkable crystallization morphologies of poly(4-vinylpyridine) on single-walled carbon nanotubes in CO_2-expanded liquids

M. Su[1], *Y. N. Wei*[2], *L. Y. Qi*[1], *Y. C. Pang*[1], *Y. Z. Guo*[1], *P. Li*[1], *J. Li*[1], *H. P. Li*[1*]

[1]Department of Chemistry, Zhengzhou University, Zhengzhou, Henan 450001, China
[2]Physical Engineering College, Zhengzhou University, Henan 450001, China

Received 19 April 2011; accepted in revised form 4 July 2011

Abstract. Poly(4-vinylpyridine) (P4VP) is a widely studied polymer for applications in catalysis, humidity sensitive and antimicrobial materials due to its pyridine group exhibiting coordinative reactivity with transition metals. In this work, the non-covalent functionalization of single-walled carbon nanotubes (SWCNTs) with P4VP in CO_2-expanded liquids (CXLs) is reported. It is found that P4VP stabilized SWCNTs show good dispersion in both organic solvent and aqueous solution (pH = 2). The ability to manipulate the dispersion state of CNTs in water with P4VP will likely benefit many biological applications, such as drug delivery and optical sensors. Furthermore, the structure and morphology of P4VP/SWCNTs composite are examined, with the focus on molecular weight of P4VP (MW-P4VP), the pressure of CXLs and the concentration of P4VP. It is amazing that the $P4VP_{15470}$ wrapping patterns undergo a notable morphological evolution from dot-like crystals to bottle brush-like, then to compact kebab-like, and then to widely-spaced dotted kebab patterns by facile pressure tuning in the higher polymer concentration series. In other words, the CXLs method enables superior control of the P4VP crystallization patterns on SWCNTs. Meanwhile, the CXL-assisted P4VP crystal growth mechanism on SWCNT is investigated, and the dominating growth mechanism is attributed to 'size dependent soft epitaxy' in $P4VP_{15470}$/SWCNTs composites. We believe these studies would reveal great potential for P4VP in building up functional structures in CXLs that are responsive to environmental stimuli.

Keywords: *polymer composites, single-walled carbon nanotubes, CO_2-expanded liquids, non-covalent functionalization, poly(4-vinylpyridine)*

1. Introduction

Polymer/CNT nanocomposites (PCN) belong to the most promising fields for carbon nanotubes (CNTs) [1, 2]. The potential applications of PCNs include conductivity enhancement, electrostatic dissipation and aerospace structural materials, and a variety of polymers have been studied to form nanocomposites with CNTs depending on the targeted properties [3]. Meanwhile, wrapping CNTs with crystalline polymers is regarded as an ideal functionalization method considering the excellent mechanical properties of crystalline polymers as well as the potential specific chain registry of different polymers upon CNTs. This method can retain the structural integrity of CNTs and simultaneously overcome the disability of the non-covalent modification method [4]. Poly(4-vinylpyridine) is chosen because it is a widely studied polymer for applications in catalysis [5–8], humidity sensitive [9] and antimicrobial materials [10] due to its pyridine group exhibting coordinative reactivity with transition metals. Being a hydrophobic polymer in apolar solvents and a cation polyelectrolyte in water at low pH [11, 12], the pH-sensitive P4VP can be readily quaternized by alky-

*Corresponding author, e-mail: lihongping@zzu.edu.cn

logen and then form positively charged polyelectrolytes as sensors and actuators [13, 14]. Thus, the P4VP/CNT nanocomposite is expected to play a vital role in exploring and developing the potential applications of the corresponding PCNs. In this work, the non-covalent attempts to wrapping crystalline P4VP on single-walled carbon nanotubes surface using CO_2-expanded liquids (CXLs) method is introduced. It should be mentioned that CXLs are the most commonly used class of gas expanded liquids (GXLs) due to the safety and economic advantages of CO_2. The ability of GXLs to readily pressure tune the mole fraction of the gaseous component, and thereby alter the solvating power, fluidity, and many other properties of these solvents proves advantageous in materials processing [15, 16], analytical separations [17] and organic reactions [18–20] presents a great advantage. Polymer processing in CXLs taking advantage of the melting-point lowering and viscosity-lowering effects has been used to adjust particle size and morphology of polymers, and to facilitate foaming, impregnation, and comolding of polymers [21]. Moreover, GXLs/CXLs combine the beneficial properties of compressed gases and of conventional solvents, leading to a new class of tunable solvents that are often the ideal type of solvents for a given application while simultaneously reducing the environmental burden through substantial replacement of organic solvents with environmentally benign CO_2 [21]. The challenging task is to achieve the controlled functionalization of SWCNTs by regulating the P4VP crystallization patterns. Accordingly, the influence of molecular weight of P4VP (MW-P4VP), polymer concentration, and the pressure of CXLs on the morphology change are examined in this work. Meanwhile, the mechanism of CXLs-assisted P4VP crystal growth on SWCNT is investigated. We believe that this work reports a new wrapping approach in CXLs to noncovalent engineering of SWCNTs surfaces, which leads to an enhancement of solubility of SWCNTs and enables superior control of the relative placement of functionalities on the nanotube surface. Moreover, the material processing in CXLs also benefits from the milder operating conditions in contrast with the well-known supercritical antisolvent (SAS) processes [22].

2. Experimental section

2.1. Materials

SWCNTs (purity >90 wt%, outside diameter (OD) 1–2 nm, inside diameter (ID) 0.8–1.6 nm, length 5–30 μm) were from Chengdu Organic Chemicals Co. Ltd., Chinese Academy of Sciences (Chengdu, China). Dimethyl sulphoxide (DMSO) and acetic anhydride $(CH_3CO)_2O$ were supplied by the Damao Chemical Reagent Co., Ltd. (Tianjin, China). The monomer 4-vinyl pyridine (4VP) and Benzoyl Peroxide (BPO) were from Alfa Aesar (Beijing, China), and 2,2,6,6,-tetramethylpiperidine-N-oxyl (TEMPO) was supplied by Dengfeng Chemical Reagent Co., Ltd. (Tianjin, China). CO_2 with a purity of 99.95% was provided by Zhengzhou Shuangyang Gas Co. (Zhengzhou, China). 4VP was purified prior to use by fractionated distillation. BPO was purified by reprecipitation of a saturated dried chloroform solution by methanol. TEMPO and $(CH_3CO)_2O$ were used as received. $P4VP_{9615}$ (M_n = 9615 g·mol^{-1}) and $P4VP_{15470}$ (M_n = 15470 g·mol^{-1}) used in this work were prepared in our lab. SWCNTs were dried in a vacuum oven at 308.2 K for 24 h before use.

2.2. Preparation of P4VP

$P4VP_{9615}$ was prepared by a method described by Fischer *et al.* [23], and $P4VP_{15470}$ prepared according to the literature [24]. In a typical polymerization procedure, a two-necked round-bottom flask was loaded with an appropriate amount of TEMPO, 4VP, BPO, and/or $(CH_3CO)_2O$; degassed by an argon gas purge; and sealed off under vacuum. The temperature of the polymerization and the duration was varied. P4VP formed, end-capped with TEMPO, was precipitated in hexane, and dried under vacuum. The detailed treatment conditions

Table 1. Polymerization of 4-vinyl pyridine at different reaction conditions

Sample	Time [h]	Accelerator	Temperature [K]	TEMPO/BPO molar ratio	M_n[a]	M_w/M_n[a]
1	10.5	–	398.2–408.2	0.65:1	9615	1.76
2	16.0	$(CH_3CO)_2O$[b]	368.2–408.2	1.30:1	15470	1.71

[a]Number-average molecular weight (M_n) and polydispersity index (M_w/M_n) were determined by Gel Permeation Chromatography (GPC) in DMF at 313.2 K, flow rate 1 ml/min

[b]1% (w/w)

for the preparation of P4VP, the number-average molecular weight (M_n) and polydispersity index (M_w/M_n) of P4VP determined by Gel Permeation Chromatography (GPC) are provided in Table 1.

2.3. The functionalization of SWCNTs by P4VP

The experimental apparatus was described in our previous work [22]. Typically, appropriate amount of P4VP were dissolved in DMSO at a suitable temperature. 0.1 mg of SWCNTs was dispersed in DMSO solution, the mixture was then ultrasonicated for 2–4 h at the temperature between 298.2–318.2 K in order to disperse the SWCNTs homogeneously in the solution. The dispersion was then added into P4VP/DMSO solution in a tube. After equilibration, the tube containing the mixture was quickly transferred into a stainless-steel autoclave at the temperature of 338.2 K. CO_2 was then charged into the autoclave to achieve the desired pressure within a short time. After 3 h treatment in CO_2-expanded DMSO, the system was slowly depressurized and the sample was collected and labeled. Comparative experiments of $P4VP_{9615}$ or $P4VP_{15470}$ decorated SWCNTs under the same experimental conditions free of CO_2 were also performed.

To understand the polymer concentration dependence on CNTs modification, the reaction system are examined with the mass ratio of P4VP to SWCNTs selected to be 3:1 (i.e., 0.006 wt% P4VP to 0.002 wt% SWCNTs, the low polymer concentration series) and 5:1 (i.e., 0.010 wt% P4VP to 0.002 wt% SWCNTs, the higher polymer concentration series), respectively.

2.4. Characterization methods

The number-average molecular weight (M_n) and polydispersity index (M_w/M_n) of P4VP were determined by GPC (Waters 515 HPLC pump, Waters 2414 Refractive index detector; Waters Corporation, Milford, MA, USA), and are tabulated in Table 1. The morphology of P4VP functionalized SWCNTs was characterized by transmission electron microscopy (TEM). Samples were collected on a TEM grid and conducted using a JEOL JEM-2100 microscope with an accelerating voltage of 200 kV (JEOL Ltd, Tokyo, Japan).

3. Results and discussion

3.1. The enhancement of SWCNTs dispersibility using the CXLs method

Figure 1 shows the organic and aqueous suspensions of SWCNTs stabilized with and without P4VP, here the modified SWCNTs are prepared at the reaction conditions of $P4VP_{15470}$ (0.05 wt%) and SWCNTs (0.01 wt%) in CO_2-DMSO at 8.30 MPa (x_{CO_2} = 0.425) and 338.2 K for 3 h. It is shown that P4VP stabilized suspensions are homogeneous in either DMSO (Figure 1c) or aqueous hydrochloric acid solution (pH = 2, Figure 1d) with no perceptible precipitation 24 h after ultrasonication. As expected, the suspensions of SWCNTs are close to complete sedimentation in DMSO (Figure 1a) or aqueous hydrochloric acid solution (Figure 1b) after 24 h. The superior stability of suspensions stabilized with P4VP is attributed to increased non-covalent interactions between nanotubes and the P4VP. This results in an adsorbed layer of P4VP on the CNTs sidewalls, which brings about steric hindrance, preventing re-aggregation and subsequent precipitation of CNTs. We believe that the conformation of the adsorbed P4VP on CNTs would determine the dispersive behavior of as-prepared composites and their potential applications in many field. And what are the challenging factors in CXLs method to control the conformational transitions of P4VP wrap-

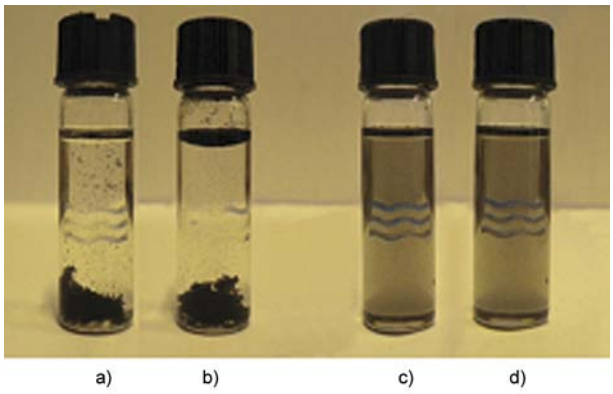

Figure 1. Organic and aqueous suspensions containing 0.010 wt% SWCNTs 24 h after ultrasonication (a) in DMSO; (b) in aqueous hydrochloric acid solution (pH = 2); (c) the modified SWCNTs in DMSO; (d) the modified SWCNTs in aqueous hydrochloric acid solution (pH = 2). The modified SWCNTs were prepared at the reaction conditions of $P4VP_{15470}$ (0.050 wt%) and SWCNTs (0.010 wt%) in DMSO at 8.30 MPa (x_{CO_2} = 0.425) and 338.2 K for 3 h.

ping styles on CNTs? Accordingly, MW-P4VP, the mass ratio of P4VP to SWCNT, and the pressure of CXLs on the morphology change are examined.

3.2. Effect of CXLs pressure and P4VP concentration on the modification of SWCNTs with $P4VP_{15470}$ – remarkable pressure dependence of morphological evolution

In this section, the pressure and polymer concentration effect on the CNTs modification with $P4VP_{15470}$ are examined with the mass ratio of P4VP to SWCNT selected to be 3:1 and 5:1, respectively. First of all, in an effort to investigate the pressure dependence, the reaction system are examined with the mass ratio of P4VP to SWCNTs as 3:1, and the pressures are chosen to be 7.99 MPa (x_{CO_2} = 0.409), 9.29 MPa (x_{CO_2} = 0.476), 11.32 MPa (x_{CO_2} = 0.587) and 12.00 MPa (x_{CO_2} = 0.626), respectively, along the bubble-point curve at 338.2 K in CO_2-expanded DMSO [25]. The corresponding structures of $P4VP_{15470}$ decorated SWCNTs are shown in the TEM image (Figure 2a–2e). It is found that multiple P4VP periodic structures are formed with increasing pressure, i.e., the P4VP decoration on SWCNTs undergoes a wrapping pattern transition first from dots (Figure 2a) to compact kebabs (Figure 2b), then to less compact kebabs (Figure 2c) and next to sparsely dotted kebabs (Figure 2d–2e) as the pressure increases from 7.99 to 9.29, 11.32 and then to 12.00 MPa, respectively. A nanohybrid shish-kebab (NHSK) like structure is observed from Figure 2b–2e: the central shish is SWCNTs, with kebab-like P4VP crystals being regarded as periodically perpendicular to the CNTs axis. Typical NHSK structures have been reported previously [4, 26, 27]. The variation trend for the size and periodicity of the kebabs is indicated in Table 2: it is found that the periodicity of the kebab increases with increasing pressure whereas the size of the kebab is less pressure dependent.

The images from Figure 2a (7.99 MPa) indicate that at relatively low pressure, P4VP starts heterogeneous crystallization on SWCNTs as dot-like crystals. The mechanism is suggested as follows. In CXLs, CO_2 cannot dissolve P4VP but is miscible with DMSO at suitable conditions, so CO_2 is used as the antisolvent for P4VP/DMSO system. The volume of the DMSO-rich phase is expanded owing to the dissolution of CO_2 and the solvent power on P4VP is getting poorer, therefore P4VP molecules precipitate out of the supersaturated solution and start to be adsorbed on the surface of SWCNTs. So at relatively low pressure as 7.99 MPa, P4VP molecules with folded-chains begin to align along SWCNTs as dots crystal so as to decrease the polymer surface energy, and consequently the CNTs surface is covered with small size of heteronucleus P4VP dots everywhere. The small dots crystal is formed due to the limited supply of P4VP in the vicinity of the CNTs during the crystal growth under lower CO_2 solubility, and they could be regarded as a steady intermediate state, which could further form ordered patterns of nanohybrid structure under higher pressure. Generally, the solvent strength of the CXLs would further decrease due to more CO_2 dissolved in DMSO, and therefore more P4VP can be deposited with increasing pressure. And what is the upcoming pressure dependent polymer crystal growth mechanism? We know that two possible factors could affect the nanohybrid conformation of P4VP crystal growth: the epitaxial growth of P4VP on CNTs and geometric confinement [3]. Here, the size of pristine SWCNTs (OD 1–2 nm) is smaller than that of $P4VP_{15470}$ (R_g, radius of gyration, about 10 nm [28]). As a polymer with such a size diffuses

Table 2. Size and periodicity of the kebabs in the $P4VP_{15470}$/SWCNTs NHSK-like stucture produced in CO_2-expanded DMSO at 338.2 K

Sample	Pressure [MPa]	x_{CO_2}	Lateral size of the kebabs [nm]	Thickness of the kebabs [nm]	Periodicity of the kebabs [nm][a]
Reaction mixture with $P4VP_{15470}$ (0.006 wt%) and SWCNTs (0.002 wt%)					
2b	9.29	0.476	35–40	35	–
2c	11.32	0.587	35–40	25–35	25–40
2d	12.00	0.626	30–35	25–35	40–75
Reaction mixture with $P4VP_{15470}$ (0.010 wt%) and SWCNTs (0.002 wt%)					
3b	8.30	0.425	25	–	–
3c	8.63	0.442	20–40	10–25	–
3d	10.53	0.543	40–60	40–60	50–80

[a]Periodicity is defined as the distance between the adjacent kekab centers

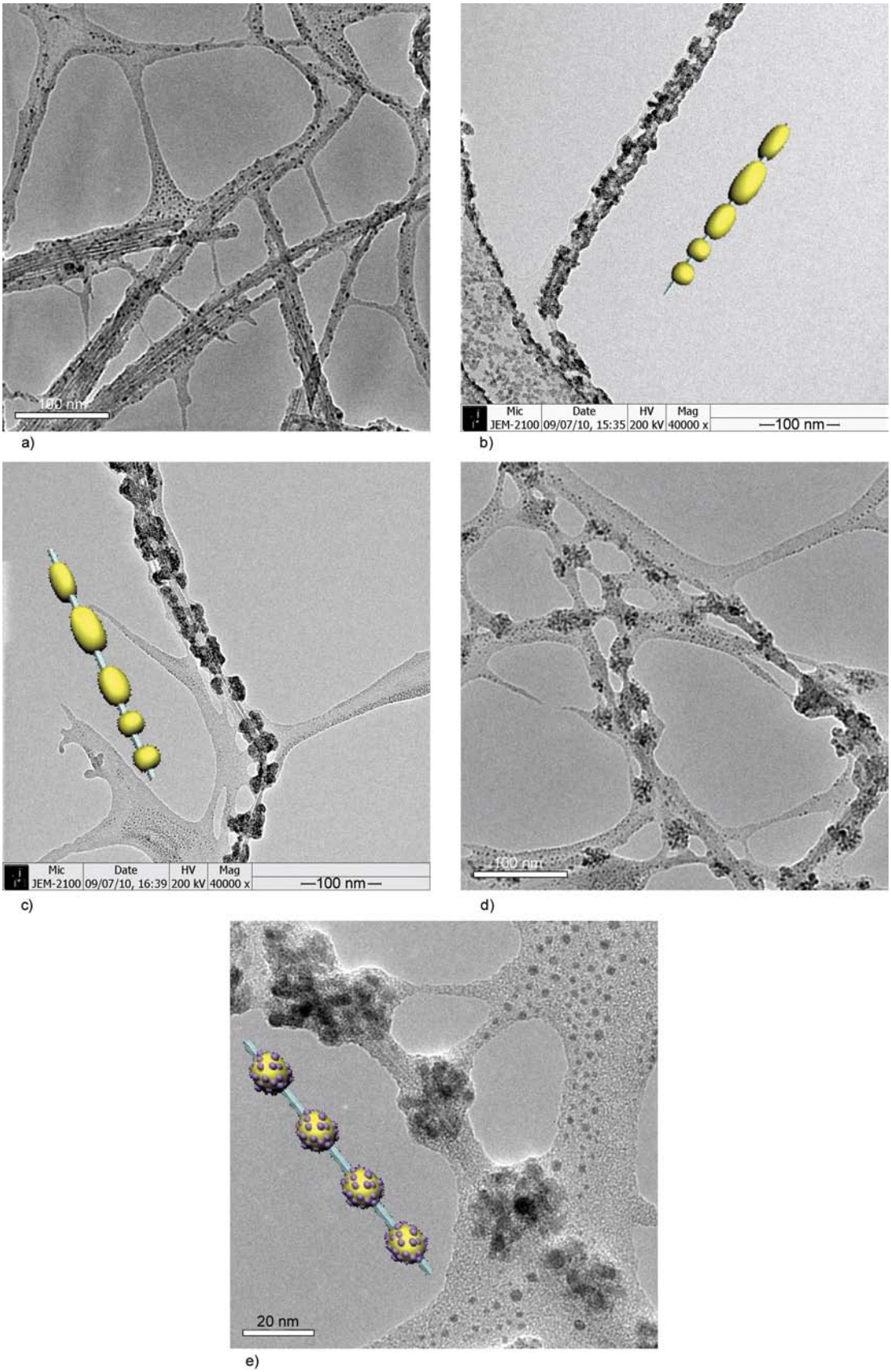

Figure 2. TEM images of $P4VP_{15470}$-decorated SWCNTs obtained in CO_2-expanded DMSO (338.2 K/varied pressure for 3 h), with 0.006 wt% $P4VP_{15470}$ and 0.002 wt% SWCNTs in DMSO: (a) 7.99 MPa (x_{CO_2} = 0.409); (b) 9.29 MPa (x_{CO_2} = 0.476); (c) 11.32 MPa (x_{CO_2} = 0.587); (d)/(e) 12.00 MPa (x_{CO_2} = 0.626). The schematic representations of the NHSK-like structure of the P4VP/SWCNTs composite are shown on image (b), (c) and (e), respectively. $P4VP_{15470}$ form kebab-like crystals on SWCNTs surface with polymer chains parallel to the SWCNT axis.

to the SWCNT surface and crystallizes, the diameter of the SWCNT plays a critical role in the formation of the crystal. Because of their small diameters, SWCNTs themselves can be considered as rigid macromolecules. Therefore, as $P4VP_{15470}$ starts to crystallize onto this surface with further pressure increasing, geometric confinement is the major factor, and thus polymer chains are exclusively parallel to the CNT axis disregarding the CNT chirality. Consequently, the polymer crystal kebabs should be perpendicular to the CNT axis, and then a NHSK-like conformation is formed in $P4VP_{15470}$/SWCNTs composite owing to the dominance of the 'size-dependent soft epitaxy' or geometric confinement factor [3]. Further morphological evolution with CXLs-pressure from compact kebabs (Figure 2b, 9.29 MPa) till dotted kebabs (Figure 2d–2e, 12.00 MPa) may be explained as follows. The precipitated P4VP can crystallize in two forms: (1) the homogeneous nucleation of P4VP itself and (2) the heterogeneous nucleation of P4VP on SWCNTs. Although the viscosity and surface tension of the CXLs will decrease with more CO_2 dissolution in DMSO, which favors the adsorption of P4VP on CNTs, the heteronucleus P4VP on CNTs may become less prevailing with increasing pressure whereas the homogeneous P4VP nucleation may consume the excessive increase in P4VP concentration. There may exist an threshold pressure around 10.00 MPa (x_{CO_2} = 0.514) in our CXLs system, and the number of heterogeneous nucleation is supposed to be predominating over the homogeneous one below the threshold pressure, whereas the homogeneous nucleation is advantageous or preferential above the threshold pressure. The observation of compact kebabs at 9.29 MPa (Figure 1b) conforms to the predominance of heteronucleus P4VP on CNTs at a pressure below the threshold pressure. The consequent less compact kebabs at 11.32 MPa (Figure 1c, periodicity 25–40 nm) and the sparsely distributed dotted kebabs (Figure 2d–2e, periodicity 40–75 nm) at 12.00 MPa can be attributed to the preference of the competitive homogeneous nucleation of P4VP above the threshold pressure. And the higher the pressure above the threshold value, the less the number of heteronucleus P4VP on CNT. In brief, this pressure tuning of competition or preference between homogeneous and heterogeneous nucleation would impede both the size and number increase of the 'hybrid kebabs' with increasing pressure, which supports the observed structural transition in this low polymer concentration series. Therefore, we can conclude that CXLs pressure offers superior control over the period and structure of polymer crystallization patterns on SWCNTs.

In an effort to better understand the polymer concentration dependence, the modifications are performed in a higher polymer concentration series with the mass ratio of $P4VP_{15470}$ to SWCNTs as 5:1, and the pressures are chosen to be 7.79 MPa (x_{CO_2} = 0.399), 8.30 MPa (x_{CO_2} = 0.425), 8.63 MPa (x_{CO_2} = 0.442) and 10.53 MPa (x_{CO_2} = 0.543), respectively, along the bubble-point curve at 338.2 K in CO_2-expanded DMSO [25]. The corresponding P4VP conformations in $P4VP_{15470}$-SWCNTs composites are reflected in Figure 3a–3d. Under higher mass ratio as 5:1, the corresponding morphology evolve from dots (Figure 3a) into bottle brush (Figure 3b), then to compact kebabs (Figure 3c), and next into dotted kebabs (Figure 3d) as the pressure increases from 7.79 to 8.30, 8.63 and then to 10.53 MPa, respectively. Surprisingly, an exceptional bottle-brush pattern of P4VP is observed at 8.30 MPa (Figure 3b). Herein, if the bottle-brush shaped $P4VP_{15470}$/SWCNTs composites could be imagined as a type of NHSK structure, with the SWCNTs the shish, and the ultrathin P4VP lamellae perpendicular to the CNTs axis, then a NHSK-like structure is again found for the higher polymer concentration series (Figure 3b–3d).

The variation trend of the kebabs is reported in Table 2 as well: it is found that both the size and periodicity of the kebabs increase with increasing pressure for the higher polymer concentration series whereas the kebabs size is less pressure dependent in the low polymer concentration series. The morphological evolution for the higher polymer concentration series is suggested as follows. Similarly, the small dots crystal at 7.79 MPa is due to the sparse supply of P4VP in the vicinity of the CNTs under weaker CO_2 antisolvent effect. Followed by a successive pressure increase within the threshold pressure value, the heterogeneous nucleation is supposed to be predominant owing to the following two reasons: (1) the viscosity and surface tension of the CXLs will decrease with increasing CO_2 solubility in DMSO, which favors the P4VP adsorption on CNTs, and (2) the crystallization theory also

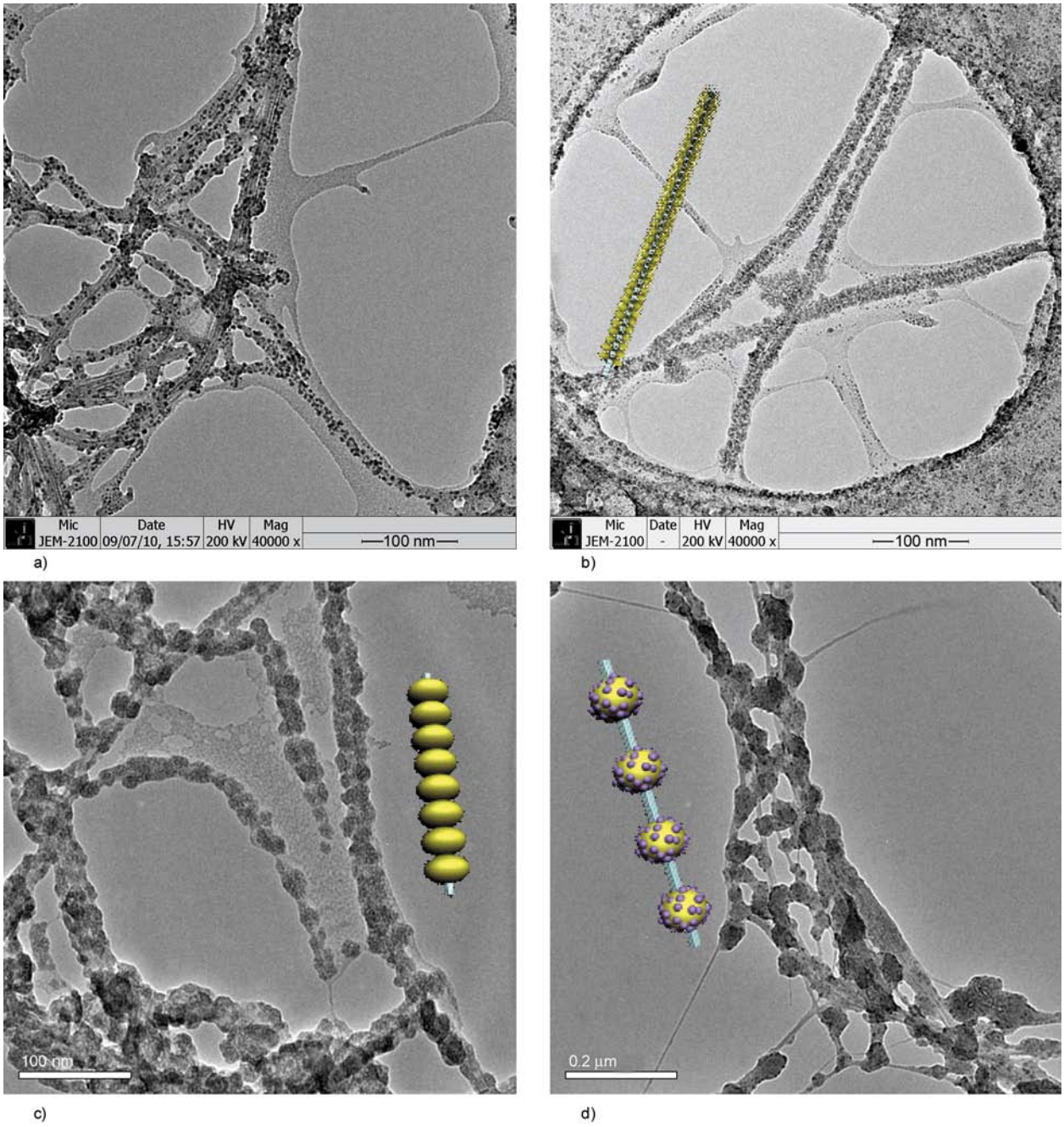

Figure 3. TEM images of $P4VP_{15470}$/SWCNTs composites obtained in CO_2-expanded DMSO (338.2 K/varied pressure for 3 h), with 0.010 wt% $P4VP_{15470}$ and 0.002 wt% SWCNTs in DMSO: (a) 7.79 MPa (x_{CO_2} = 0.399); (b) 8.30 MPa (x_{CO_2} = 0.425); (c) 8.63 MPa (x_{CO_2} = 0.442); (d) 10.53 MPa (x_{CO_2} = 0.543). There are schematic representations of the $P4VP_{15470}$/SWCNTs NHSK-like structure on image (b), (c) and (d), respectively.

supports the heterogeneous nucleation. Therefore, the preferential heterogeneous nucleation would promote the growth of the kebabs with more P4VP accumulated on CNTs surface due to pressure increase, which leads to a lateral size enhancement of kebabs with increasing pressure from 8.3 MPa (brush diameter 25 nm, Figure 3b) to 8.63 MPa (lateral size 20–40 nm, Figure 3c). However, if the pressure is above the threshold pressure, the competitive consumption of P4VP by homogeneous nucleation will dramatically slow down the heterogeneous lamellae thickening process so that less heteronucleus crystals are thickened, leading to a widely-spaced dotted kebabs conformation in the nanocomposites as shown in Figure 3d (10.53 MPa, periodicity 50–80 nm). A similar phenomenon is also found in the low polymer concentration series in Figure 2d–2e. Moreover, the TEM image reveals

some difference between the 2D NHSK reflected in Figure 2c and the 2D NHSK in Figure 3c. The rounded kebabs in Figure 3c are shorter in length and their aspect ratio is smaller as opposite to the kebabs in Figure 2c, which might be due to a much larger P4VP concentration and more heterogeneous numbers on CNTs surface in the higher polymer concentration series during the heterogeneous crystal growth process. In short, there exists notable pressure dependence of morphological evolution in $P4VP_{15470}$/SWCNTs composites at the selective conditions. Moreover, both the P4VP decoration style and the degree on SWCNTs are more sensitive to pressure tuning for the higher $P4VP_{15470}$ concentration series.

3.3. Effect of molecular weight of P4VP on the modification of SWCNTs

To reveal the MW-P4VP effect on the CNTs modification, $P4VP_{9615}$ and $P4VP_{15470}$ are selected, respectively. The P4VP (0.006 wt%) and SWCNTs (0.002 wt%) in DMSO were treated at 338.2 K and 9.30 MPa (x_{CO_2} = 0.476) for 3 h. Contrast experiments are conducted at a higher pressure around 11.30 MPa (x_{CO_2} = 0.586). The corresponding TEM images are shown in Figure 4. It is seen that the conformation of $P4VP_{9615}$ on SWCNTs are dots crystal with average diameter around 5–10 nm at 9.30 MPa (Figure 4a), and evenly distributed smaller dots crystal with diameter about 5 nm at 11.30 MPa (Figure 4b).

In contrast, the $P4VP_{15470}$/SWCNTs composites are NHSK-like structure with compact kebabs at 9.29 MPa (Figure 2b), and less compact kebabs at 11.32 MPa (Figure 2c). Herein, even if the pressure increase from 9.30 to 11.30 MPa, the conformations of $P4VP_{9615}$ on SWCNTs always adopt a dot-like pattern. It might be that the solubility of $P4VP_{9615}$ in DMSO is better than that of $P4VP_{15470}$ at the same conditions, there is limited amount of $P4VP_{9615}$ precipitated out disregarding the increase in CXLs pressure. Therefore, the dot-like crystals of $P4VP_{9615}$ are formed on SWCNTs owing to the insufficient supply of P4VP on CNTs surface. However, the size of dots crystal in $P4VP_{9615}$/SWCNTs becomes smaller with increasing pressure. Smaller size of $P4VP_{9615}$ crystal at 11.30 MPa means the growth of the heteronucleus P4VP dots is not rapid enough as opposed to that of the nearby homogeneous nucleation of P4VP when pressure is higher than the threshold pressure. Provided that the polymer concentration is the same, the modification results show analogous molecular weight tuning of structural transition from dots in $P4VP_{9615}$/SWCNTs to kebabs in $P4VP_{15470}$/SWCNTs at the selected pressures. And it seems that the CXLs method offers better morphology control over the $P4VP_{15470}$/SWCNTs systems. To summarize, $P4VP_{9615}$ forms dot-like crystals on SWCNTs while $P4VP_{15470}$ forms kebab-like crystals instead at the same polymer concentration and CXLs pressure, which suggests that the P4VP crystal conformation on CNTs surface could be also regulated by the variation in the molecular weight of P4VP. It is found that only polymers with specific molecular weight (e.g. $P4VP_{15470}$) can form the NHSK structure on SWCNTs.

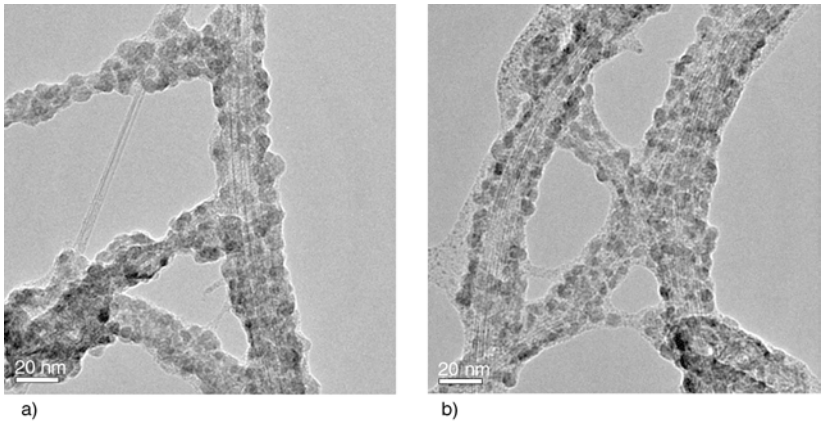

Figure 4. TEM images of $P4VP_{9615}$/SWCNTs composites obtained in CO_2-expanded DMSO (338.2 K/varied pressure for 3 h), with 0.006 wt% $P4VP_{9615}$ and 0.002 wt% SWCNTs in DMSO: (a) 9.30 MPa (x_{CO_2} = 0.476); (b) 11.30 MPa (x_{CO_2} = 0.586).

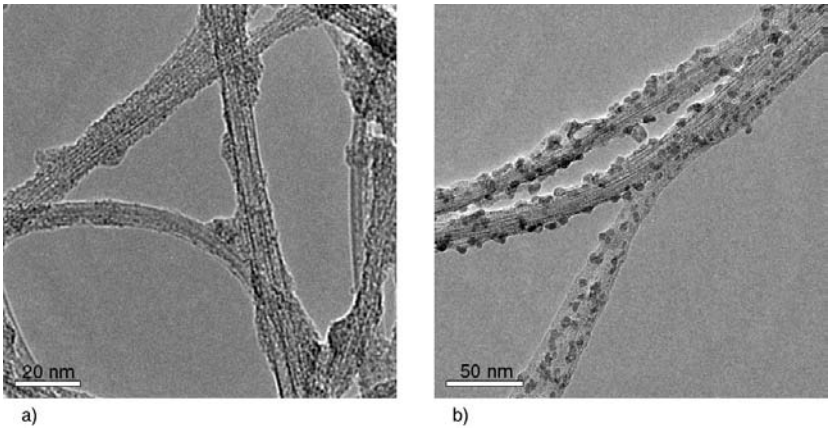

Figure 5. TEM images of P4VP-decorated SWCNTs obtained in DMSO at 338.2 K for 3 h. (a) 0.006 wt% $P4VP_{9615}$ and 0.002 wt% SWCNT (b) 0.010 wt% $P4VP_{15470}$ and 0.002 wt% SWCNT.

3.4. TEM image of $P4VP_{9615}$/ SWCNTs and $P4VP_{15470}$/ SWCNTs composites by conventional method without CO_2

The TEM images of $P4VP_{9615}$ and $P4VP_{15470}$ decorated SWCNTs under the same experimental conditions free of CO_2 are shown in Figure 5, respectively. From Figure 5, the wrapping pattern of $P4VP_{9615}$ on SWCNTs (in DMSO without CO_2) is found to be a sparsely coating structure, instead, evenly distributed dots crystal of $P4VP_{15470}$ is formed on SWCNTs surface. In contrast, the pressure dependent SWCNTs microstruture observed in $P4VP_{15470}$/SWCNTs composites (Figure 2 and Figure 3) or $P4VP_{9615}$/SWCNTs composites (Figure 4) by CXLs method suggests that nanotube microstructure in composites can be tailored as a function of CXLs pressure. Therefore, it is undoubtedly that the CXLs method offers superior control of the P4VP crystallization patterns on SWCNTs in contrast with the conventional way.

4. Conclusions

In summary, CXLs method is a facile process for preparing P4VP/SWCNT composites with controlled polymer-crystal morphology. The MW- P4VP as well as the pressure in CXLs are the effective approaches to control the polymer crystallization structures on SWCNTs, and the crystallization behavior of $P4VP_{15470}$ is dramatically affected by CXLs pressure. A threshold pressure around 10.00 MPa ($x_{CO_2} = 0.514$) is assumed to exist in our CXLs system, and the amount and number of heterogeneous polymer nucleation is supposed to be predominating over the homogeneous one below the threshold pressure, whereas the homogeneous nucleation of polymer is advantageous or preferential above the threshold pressure. The combination of desired pressure of CO_2 and MW-P4VP helps to modify the SWCNTs in a controllable way at suitable polymer concentration and temperature, which could serve as a model process to achieve ideal polymer crystals for structural and morphological study. Moreover, the P4VP crystal formation mechanism is different for SWCNTs and MWCNTs modification. The NHSK conformation of the $P4VP_{15470}$/SWCNTs in this work is attributed to 'size-dependent soft epitaxy growth' mechanism because geometric confinement of the small diameter SWCNTs (OD 1–2 nm) is the predominant factor, which dictates the polymer chain orientation in the kebabs. Instead, 'normal epitaxy growth' mechanism was supposed to play a major role, therefore P4VP helical wrapping crystals were observed on MWCNTs (OD 25–30 nm) using the CXLs method at the same polymer concentration and comparable pressures [22]. In other words, the diameter of the CNTs also plays a critical role in the morphology control of P4VP crystals on CNTs surface. This work offers an environmentally benign polymer wrapping approach in CXLs to noncovalent engineering of SWCNTs surfaces that leads to an enhancement of solubility or dispersibility of CNTs and enables superior control of the relative placement of functionalities on the CNT surface. We believe that the pressure tuning of the unique nanoscale architecture of P4VP/SWCNT composites in CXLs could find a variety of applications ranging from nanoelectronics, sensing to catalyst supports.

Acknowledgements

This work was supported by funds from the National Natural Science Foundation of China (No.21073167), and the Scientific Research Foundation for the Returned Overseas Chinese Scholars, State Education Ministry of China (No.2008890).

References

[1] Moniruzzaman M., Winey K. I.: Polymer nanocomposites containing carbon nanotubes. Macromolecules, **39**, 5194–5205 (2006).
DOI: 10.1021/ma060733p

[2] Winey K. I., Vaia R. A.: Polymer nanocomposites. Materials Research Society Bulletin, **32**, 314–319 (2007).

[3] Li L., Li B., Hood M. A., Li C. Y.: Carbon nanotube induced polymer crystallization: The formation of nanohybrid shish–kebabs. Polymer, **50**, 953–965 (2009).
DOI: 10.1016/j.polymer.2008.12.031

[4] Zhang Z. W., Xu Q., Chen Z. M., Yue J.: Nanohybrid shish-kebabs: Supercritical CO_2-induced PE epitaxy on carbon nanotubes. Macromolecules, **41**, 2868–2873 (2008).
DOI: 10.1021/ma702739n

[5] Wen F., Zhang W., Wei G., Wang Y., Zhang J., Zhang M., Shi L.: Synthesis of noble metal nanoparticles embedded in the shell layer of core−shell poly(styrene-*co*-4-vinylpyridine) micospheres and their application in catalysis. Chemistry of Materials, **20**, 2144–2150 (2008).
DOI: 10.1021/cm703378c

[6] Yarapathi R. V., Kurva S., Tammishetti S.: Synthesis of 3,4-dihydropyrimidin-2(1H)ones using reusable poly(4-vinylpyridine–co-divinylbenzene)–Cu(II)complex. Catalysis Communications, **5**, 511–513 (2004).
DOI: 10.1016/j.catcom.2004.06.007

[7] Friedrich H. B., Singh N.: The very efficient oxidation of alcohols by poly(4-vinylpyridine)-supported sodium ruthenate. Tetrahedron Letters, **41**, 3971–3974 (2000).
DOI: 10.1016/S0040-4039(00)00531-1

[8] Jackson J. A., Newsham M. D., Worsham C., Nocera D. G.: Efficient singlet oxygen generation from polymers derivatized with hexanuclear molybdenum clusters. Chemistry of Materials, **8**, 558–564 (1996).
DOI: 10.1021/cm950443f

[9] Chen Y. S., Li Y., Yang M. J.: A fast response resistive thin film humidity sensor based on poly(4-vinylpyridine) and poly(glycidyl methacrylate). Journal of Applied Polymer Science, **105**, 3470–3475 (2007).
DOI: 10.1002/app.26401

[10] Tiller J. C., Lee S. B., Lewis K., Klibanov A. M.: Polymer surfaces derivatized with poly(vinyl-N-hexylpyridinium) kill airborne and waterborne bacteria. Biotechnology and Bioengineering, **79**, 465–471 (2002).
DOI: 10.1002/bit.10299

[11] Minko S., Kiriy A., Gorodyska G., Stamm M.: Single flexible hydrophobic polyelectrolyte molecules adsorbed on solid substrate: Transition between a stretched chain, necklace-like conformation and a globule. Journal of the American Chemical Society, **124**, 3218–3219 (2002).
DOI: 10.1021/ja017767r

[12] Kiriy A., Gorodyska G., Minko S., Jaeger W., Štěpánek P., Stamm M.: Cascade of coil-globule conformational transitions of single flexible polyelectrolyte molecules in poor solvent. Journal of the American Chemical Society, **124**, 13454–13462 (2002).
DOI: 10.1021/ja0261168

[13] Li Y., Yang M. J., She Y.: Humidity sensitive properties of crosslinked and quaternized poly(4-vinylpyridine-co-butyl methacrylate). Sensors and Actuators B: Chemical, **107**, 252–257 (2005).
DOI: 10.1016/j.snb.2004.10.008

[14] Aydogdu Y., Erol I., Yakuphanoğlu F., Aydogdu A., Ahmedzade M.: Electrical conductivity and optical properties of copolymers based on 4-vinylpyridine and tetralincyclobutylhydroxyethylmethacrylate. Synthetic Metals, **139**, 327–334 (2003).
DOI: 10.1016/S0379-6779(03)00183-8

[15] Anand M., You S-S., Hurst K. M., Saunders S. R., Kitchens C. L., Ashurst W. R., Roberts C. B.: Thermodynamic analysis of nanoparticle size selective fractionation using gas-expanded liquids. Industrial and Engineering Chemistry Research, **47**, 553–559 (2008).
DOI: 10.1021/ie070981p

[16] Dehghani F., Foster N. R.: Dense gas anti-solvent processes for pharmaceutical formulation. Current Opinion in Solid State and Materials Science, **7**, 363–369 (2003).
DOI: 10.1016/j.cossms.2003.11.001

[17] Olesik S. V.: Physicochemical properties of enhanced-fluidity liquid solvents. Journal of Chromatography A, **1037**, 405–410 (2004).
DOI: 10.1016/j.chroma.2004.04.001

[18] Eckert C. A., Liotta C. L., Bush D., Brown J. S., Hallett J. P.: Sustainable reactions in tunable solvents. Journal of Physical Chemistry B, **108**, 18108–18118 (2004).
DOI: 10.1021/jp0487612

[19] Wei M., Musie G. T., Busch D. H., Subramaniam B.: Autoxidation of 2,6-di-*tert*-butylphenol with cobalt Schiff base catalysts by oxygen in CO_2-expanded liquids. Green Chemistry, **6**, 387–393 (2004).
DOI: 10.1039/B310523G

[20] Lyon C. J., Sarsani V. R., Subramaniam B.: 1-Butene + isobutane reactions on solid acid catalysts in dense CO_2-based reaction media: Experiments and modeling. Industrial and Engineering Chemistry Research, **43**, 4809–4814 (2004).
DOI: 10.1021/ie0498145

[21] Jessop P. G., Subramaniam B.: Gas-expanded liquids. Chemical Reviews, **107**, 2666–2694 (2007). DOI: 10.1021/cr040199o

[22] Liu Y., Wei Y. N., Qin R. H., Zhang L. Y., Yang L. T., Li H. P., Li X. J.: Crystalline polymer decoration on multiwalled carbon nanotubes: MWCNT-induced P4VP periodic crystallization in CO_2-expanded liquids. Express Polymer Letters, **5**, 60–72 (2011). DOI: 10.3144/expresspolymlett.2011.7

[23] Fischer A., Brembilla A., Lochon P.: Nitroxide-mediated radical polymerization of 4-vinylpyridine: Study of the pseudo-living character of the reaction and influence of temperature and nitroxide concentration. Macromolecules, **32**, 6069–6072 (1999). DOI: 10.1021/ma990116j

[24] Chalari I., Pispas S., Hadjichristidis N.: Controlled free-radical polymerization of 2-vinylpyridine in the presence of nitroxides. Journal of Polymer Science Part A: Polymer Chemistry, **39**, 2889–2895 (2001). DOI: 10.1002/pola.1268

[25] Chiu H-Y., Jung R-F., Lee M-J., Lin H-M.: Vapor–liquid phase equilibrium behavior of mixtures containing supercritical carbon dioxide near critical region. The Journal of Supercritical Fluids, **44**, 273–278 (2008). DOI: 10.1016/j.supflu.2007.09.026

[26] Zhang F., Zhang H., Zhang Z., Chen Z., Xu Q.: Modification of carbon nanotubes: Water-soluble polymers nanocrystal wrapping to periodic patterning with assistance of supercritical CO_2. Macromolecules, **41**, 4519–4523 (2008). DOI: 10.1021/ma800514a

[27] Zhang L., Tao T., Li C.: Formation of polymer/carbon nanotubes nano-hybrid shish–kebab via non-isothermal crystallization. Polymer, **50**, 3835–3840 (2009). DOI: 10.1016/j.polymer.2009.05.051

[28] Flory P. J.: Principles of polymer chemistry. Cornell University Press, Ithaca (1953).

eXPRESS Polymer Letters Vol.5, No.12 (2011) 1113–1122
Available online at www.expresspolymlett.com
DOI: 10.3144/expresspolymlett.2011.108

Curing reaction of bisphenol-A based benzoxazine with cyanate ester resin and the properties of the cured thermosetting resin

H. Kimura[*], *K. Ohtsuka, A. Matsumoto*

Thermosetting Resin Lab., Organic Materials Research Division, Osaka Municipal Technical Research Institute, 1-6-50, Morinomiya, Joto-ku, Osaka, 536-8553 Japan

Received 9 May 2011; accepted in revised form 4 July 2011

Abstract. Curing reaction of bisphenol-A based benzoxazine with cyanate ester resin and the properties of the cured thermosetting resin were investigated. The cure behavior of benzoxazine with cyanate ester resin was monitored by model reaction using nuclear magnetic resonance (NMR). As a result of the model reaction, the ring opening reaction of benzoxazine ring and thermal self-cyclotrimerization of cyanate ester group occurred, and then the phenolic hydoroxyl group generated by the ring opening reaction of benzoxazine ring co-reacted with cyanate ester group. The properties of the cured thermosetting resin were estimated by mechanical properties, electrical resistivity, water resistance and heat resistance. The cured thermosetting resin from benzoxazine and cyanate ester resin showed good heat resistance, high electrical resistivity and high water resistance, compared with the cured thermosetting resin from benzoxazine and epoxy resin.

Keywords: *thermosetting resins, benzoxazine, cyanate ester resin*

1. Introduction

Phenolic resin is used widely as an industrial material because of its good heat resistance, electrical insulation, dimensional stability, and chemical resistance. However, there are a number of shortcomings associated with those traditional phenolic resins. For example, hexamethylenetetramine (hexamine) is used as a curing agent. In the curing process of novolac-hexamine, volatiles such as water or ammonia compounds etc. are released due to the condensation reaction. These volatiles sometimes reduce the properties of cured phenolic resin because of the formation of microvoids. Moreover acid or base compounds as catalysts must be used to synthesize novolac or resole precursors of cured phenolic resin, which result in corrosion of the processing equipment. Another problem is that the cured phenolic resin is brittle.

It is well known that the benzoxazine ring is stable at low temperature, but a ring opening reaction occurs at high temperature, and novolac type oligomers having both phenolic hydroxyl group and tertiary amine group are produced [1]. Using this benzoxazine compound as a phenolic resin, it is expected to develop a new type of phenolic resin that releases no volatiles during curing reaction and needs no catalysts.

Ishida and co-workers [2–24] synthesized a lot of types of oxazines and studied their cure kinetics, molecular structures, mechanical and dynamic mechanical properties, and so on. Jang and Shin also studied the cure kinetics of a benzoxazine-based phenolic resin [25]. Jang and Seo studied the performance improvement of rubber-modified polybenzoxazine [26]. Recently, maleimide-modified [22–23, 27–28] and furan-modified [29] benzox-

[*]Corresponding author, e-mail: kimura@omtri.or.jp

azines have been synthesized, and the properties of the cured resins have been investigated. Nanocomposites using benzoxazines also recently have been reported [30–33].

We also have already investigated the curing behavior of the bisphenol-A, terpenediphenol or poly(*p*-vinylphenol) based benzoxazines with epoxy resin or bisoxazoline and the properties of the cured resins [34–41]. Consequently, the molding compound from bisphenol-A based benzoxazine and epoxy resin or bisoxazoline showed good flowability below 140°C, curing reaction proceeded above 180°C rapidly. And the cured thermosetting resins from benzoxazine compounds and epoxy resin or bisoxazoline had superior heat resistance, electrical resistivity, mechanical properties and water resistance to the cured thermosetting resins from conventional bisphenol-A type novolac and epoxy resin or bisoxazoline.

In this report, we investigated the curing behavior of benzoxazine resin with cyanate ester resin and the properties of the cured thermosetting resin.

Cyanate ester resin has drawn a great deal of attention as one of the high-performance thermosets, comparable to epoxy resins and polyimide. The cyanate ester monomer undergoes thermal self-cyclotrimerization to form a three-dimensional network structure of polycyanurate containing triazine groups [42, 43]. Polycyanurate possesses several superior properties including high heat resistance, low moisture absorption, high electrical resistivity, low dielectric constant, and low shrinkage. Therefore it is also expected that the cured thermosetting resin from benzoxazine resin and cyanate ester resin has high heat resistance, high electrical resistivity and low moisture absorption. 2,2-bis(4-cyanatophenyl) propane (bisphenol-A based cyanate ester resin) is a widely accepted cyanate ester monomer used in wide range applications. In this study, we investigated the curing behavior of bisphenol-A based benzoxazine with bisphenol-A based cyanate ester resin and the properties of the cured thermosetting resin.

2. Experimental

2.1. Materials

2,2-bis(3,4-dihydro-3-phenyl-1,3-benzoxazine) propane (bisphenol-A based benzoxazine, Ba) and 2-(3,4-dihydro-3-phenyl-1,3-benzoxazine) butane (mono functional benzoxazine, BuPa) was supplied by Shikoku Chemicals Co., Ltd. (Kagawa, Japan). 2,2-bis(4-cyanatophenyl) propane (bisphenol-A based cyanate ester, BADCy) and 2-phenyl-2-(4-cyanatophenyl) propane (mono functional cyanate

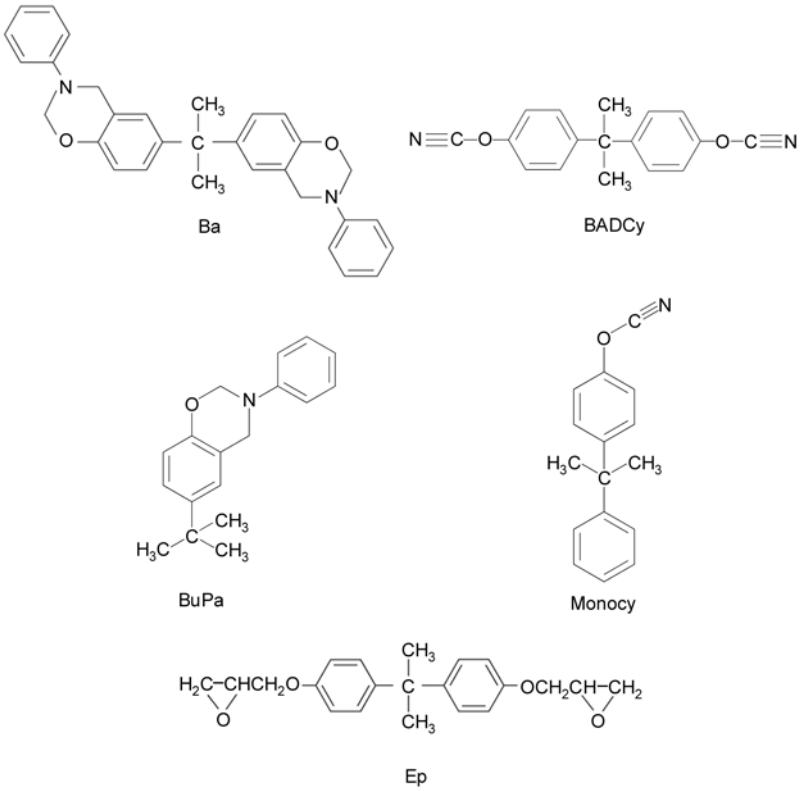

Figure 1. Chemical structures of Ba, BuPa, BADCy, Monocy and Ep

ester, Monocy) was supplied by Mitsubishi Gas Chemical Company, Inc. (Tokyo, Japan). Bisphenol A based epoxy resin (EPIKOTE 828, epoxy equivalent 186) as an epoxy resin (Ep) was supplied by Japan Epoxy Resins Co., Ltd. (Tokyo, Japan). All chemicals were used without further purification. The chemical structures of Ba, BuPa, BADCy, Monocy and Ep are shown in Figure 1.

2.2. Model reaction and characterization

It is difficult to investigate the curing reaction of Ba with BADCy in detail because both Ba and BADCy have two functionalities and gelation occurs easily, and so the compound from the reaction is partially insoluble in solvents used for the measurement of nuclear magnetic resonance (NMR) such as $CDCl_3$, acetone-D, CD_3OD and so on. In this way, BuPa and Monocy were used as each model compounds in order to investigate curing behavior of benzoxazine (Ba) with cyanate ester resin (BADCy), because both BuPa and Monocy have mono functionality and gelation does not occur, and it is easy to investigate the curing reaction. The structures of the compounds obtained by model reaction (reaction of BuPa with Monocy) were analyzed by ^{13}C-NMR measurement. ^{13}C-NMR measurement was carried out on Japan Electron Company (Tokyo, Japan) JMN-GSX-270 instrument operating at 67.8 MHz. Deuterated chloroform was used as a solvent and tetramethylsilane was used as an internal standard.

2.3. Curing condition

Samples containing 50 mol% Ba and 50 mol% BADCy were prepared and cured in a mold at a specified temperature in the oven. The curing condition of Ba with BADCy was determined as 180°C/2 h + 200°C/2 h + 220°C/2 h from the results of Fourier Transform Infrared Spectrophotometer (FT-IR). For comparison, the curing reaction of 50 mol% Ba with 50 mol% Ep was also carried out. The curing condition of Ba with Ep was determined as 170°C/2 h + 190°C/2 h + 200°C/2 h + 220°C/2 h from the results of previous paper [34].

2.4. Properties of the molding compound and the cured resin

The structure of the cured thermosetting resin was analyzed by Fourier Transform Infrared Spectrophotometer (FT-IR). FT-IR measurement was carried out on Nicolet Impact 420 instrument (Thermo Fisher Scientific K.K, Yokohama, Japan). The spectral range was 4000–400 cm^{-1}. One hundred twenty-eight scans were coadded at a resolution of 4 cm^{-1}. Samples were prepared as KBr pellets.

Differential scanning calorimetry (DSC) was applied to evaluate the cure behavior. DSC was measured with heating rate of 10°C/min under N_2 atmosphere on a Seiko Instruments Co., Ltd., (Chiba, Japan) STI EXSTAR 6000.

Thermal gravimetric analysis (TGA) was applied to evaluate the thermal stability. TGA was measured with heating rate of 10°C/min under N_2 atmosphere on a Seiko Instruments Co., Ltd. (Chiba, Japan) TGA 5200 Thermal Gravimetric Analyzer.

In order to investigate the thermal stability of the molding compound, gelation time was estimated according to JIS K6910. Namely, spatula was placed on the steel plate and the steel plate and spatula was heated to the constant temperature. Approximately 0.5 g of the sample was put on the steel plate and spread to a disc approximately 3 cm in diameter with the spatula. Then the sample was kneaded by pressing it uniformly approximately once a second, but with care to avoid spreading. The time until when the sample does not string to the spatula any more was measured. It was taken as the gelation time of the sample.

The properties of the cured thermosetting resin were characterized by heat resistance, fracture toughness, electrical insulation and water absorption.

Heat resistance was estimated by glass transition temperature (T_g) on dynamic mechanical analysis. Dynamic mechanical analysis was measured by a three points bending method at 1 Hz, with a heating rate of 2°C/min on a Seiko Instruments Co., Ltd (Chiba, Japan) DMS-110 Dynamic Mechanical Analysis Spectrometer. The peak temperature of tanδ by dynamic mechanical analysis was considered as T_g [44].

Fracture toughness was estimated by critical stress intensity factor (K_{IC}) according to ASTM D5045.

Electrical insulation was estimated by volume resistivity. Volume resistivity was measured by Yokogawa-Hewlett-Packard Co., Ltd (Tokyo, Japan) HP4339A according to JIS K6911. Namely, the disk test pieces (approximately 50 mm diameter and 3 mm thickness) were charged with electricity (500 V), and after 1 min volume resistance was

measured. Volume resistivity was calculated by the Equation (1):

$$\rho_V = \frac{\pi d^2}{4t} \cdot R_V \quad (1)$$

where ρ_V is the volume resistivity; d is the outside diameter of inner circle of face electrode, t is the thickness of test piece, and R_V is the volume resistance.

Water absorption was estimated according to JIS K7209. Namely, the disk test pieces (approximately 50mm diameter and 3 mm thickness) were weighed to the nearest 0.1 mg, and the mass was taken as M_1. Then the test pieces were put in a container containing boiling water. After 2 h, the test pieces were taken out of the boiling water and cooled down by putting them in water kept at the temperature of the testing room for 15 min. After taking the test pieces out of the water, they were weighed to the nearest 0.1 mg, and the mass was taken as M_2. Water absorption was calculated by the Equation (2):

$$\text{Water absorption}\,[\%] = \frac{M_2 - M_1}{M_1} \cdot 100 \quad (2)$$

3. Results and discussion

3.1. Model reaction

^{13}C-NMR spectrum of the product obtained by model reaction (reaction of BuPa with Monocy) at 200°C for 1 hr is shown in Figure 2. As a result, both

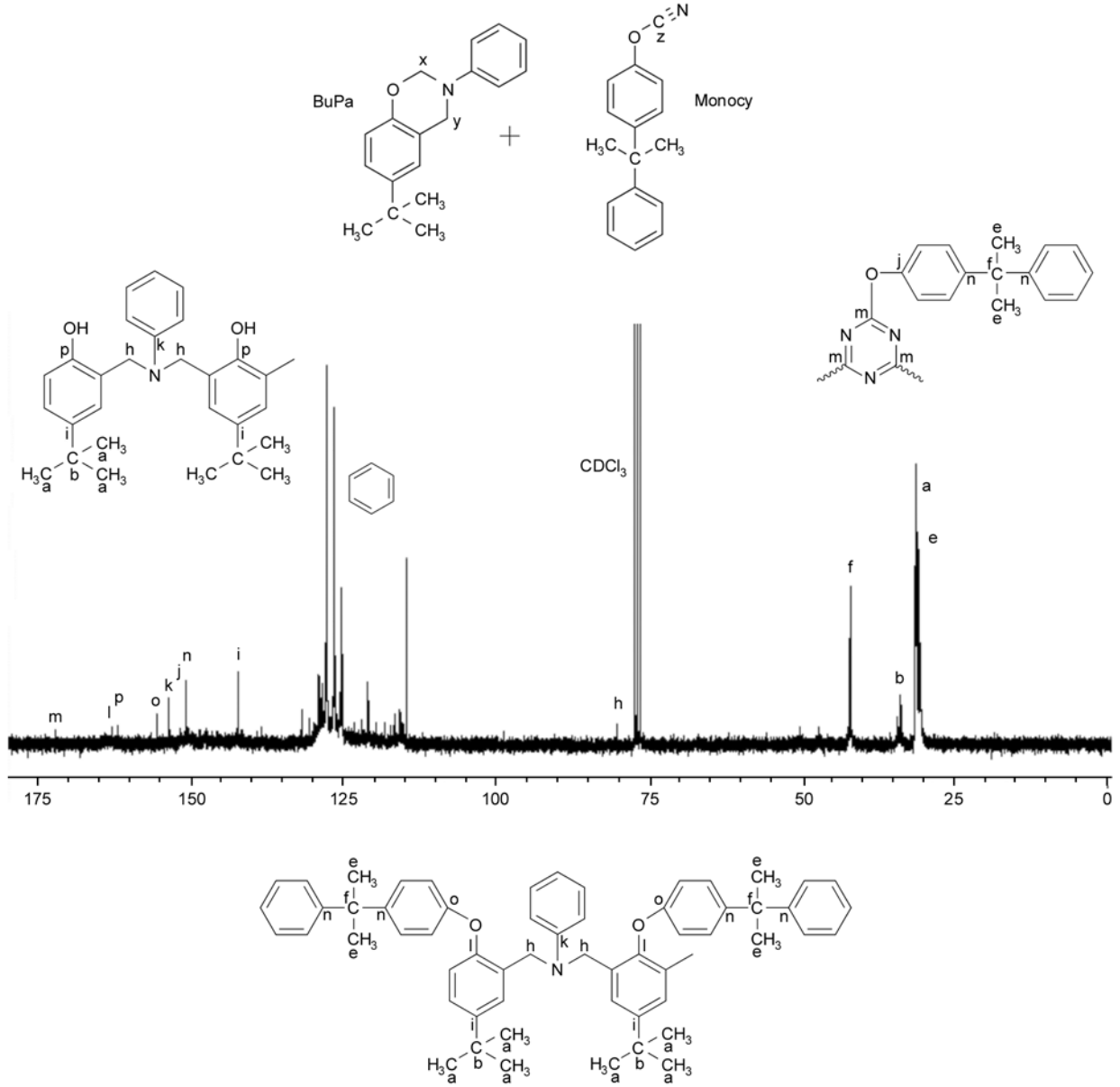

Figure 2. ^{13}C-NMR spectrum of the product obtained by model reaction at 200°C for 1 hr

two peaks (x, 79.1 ppm and y, 50.7 ppm) assigned to the carbon of benzoxazine ring and a peak (z, 108.8 ppm) assigned to the carbon of cyanate ester group were not detected. The peak (p) assigned to C1 carbon of the benzene ring adjacent to phenolic hydroxyl group generated by the ring opening reaction of benzoxazine ring was detected. The peak (h) assigned to methylene carbon of

$Ph(OH)–CH_2–N(Ph)–CH_2–Ph(OH)$,

which was produced by the ring-opening reaction of benzoxazine ring, was also detected. It was found that the ring-opening reaction of the benzoxazine ring occurred (Figure 3). And the peak (m) assigned to C1 carbon of the benzene ring adjacent to triazine group generated by the thermal self-cyclotrimerization of cyanate ester group was detected. It was found that thermal self-cyclotrimerization of cyanate ester group occurred (Figure 3). Furthermore, the peak (l) assigned to C1 carbon of the benzene ring adjacent to ether bond was detected. It was suggested that the phenolic hydroxyl group produced by the ring opening reaction of BuPa reacted with cyanate ester group of Monocy. Namely, shown in Figure 4, the phenolic hydroxyl group produced by the ring opening reaction of benzoxazine co-reacted with cyanate ester group to form the intermediate iminocarbonate, which further induce curing reaction of cyanate ester to form polycyanulate.

3.2. Curing reaction of Ba with BADCy

To investigate the curing reaction of Ba with BADCy, FT-IR measurement was carried out. FT-IR spectra of the compound before and after the curing reaction of Ba with BADCy are shown in Figure 5. As a result, the absorption at 949 cm^{-1} assigned to the tri-substituted benzene ring in the benzoxazine ring structure disappeared after 2 h at 180°C (Figure 5b). And the absorptions at 2266 and 2230 cm^{-1} assigned to cyanate ester group also disappeared after 2 h at 180°C (Figure 5b). The new absorptions at 1565 and 1370 cm^{-1} assigned to the triazine group appeared after 2 h at 220°C (Figure 5d). It was found the ring opening reaction of benzoxazine ring and thermal self-cyclotrimerization of cyanate ester group occurred, and then the phenolic hydroxyl groups generated by the ring-opening reaction of benzoxazine ring might react with cyanate ester as shown in Figure 4 from the results of model reaction.

From the results of FT-IR measurement, the curing condition was determined as follows: after the molding compound softened at 150°C to remove any bubbles containing in it sufficiently, curing reaction was carried out stepwise at 180°C/2 hr + 200°C/2 hr. Finally, at 220°C/2 hr the cured thermosetting resin was postcured so that the curing reaction could proceed completely. In this way, the curing condition of Ba with BADCy was determined as 180°C/2 hr + 200°C/2 hr + 220°C/2 hr.

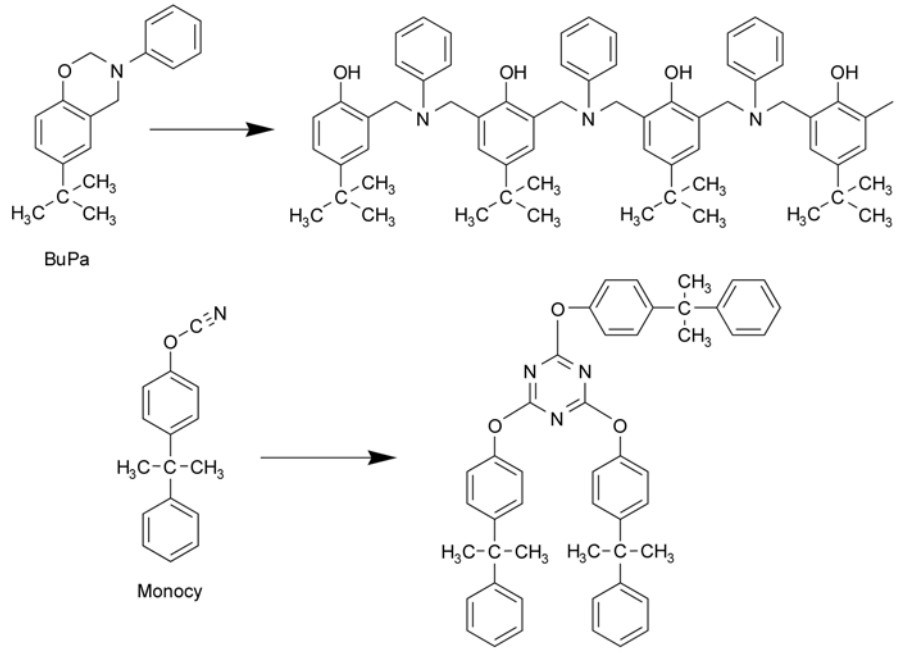

Figure 3. Ring-opening reaction of benzoxazine (BuPa) and thermal self-cyclotrimerization of cyanate ester (Monocy)

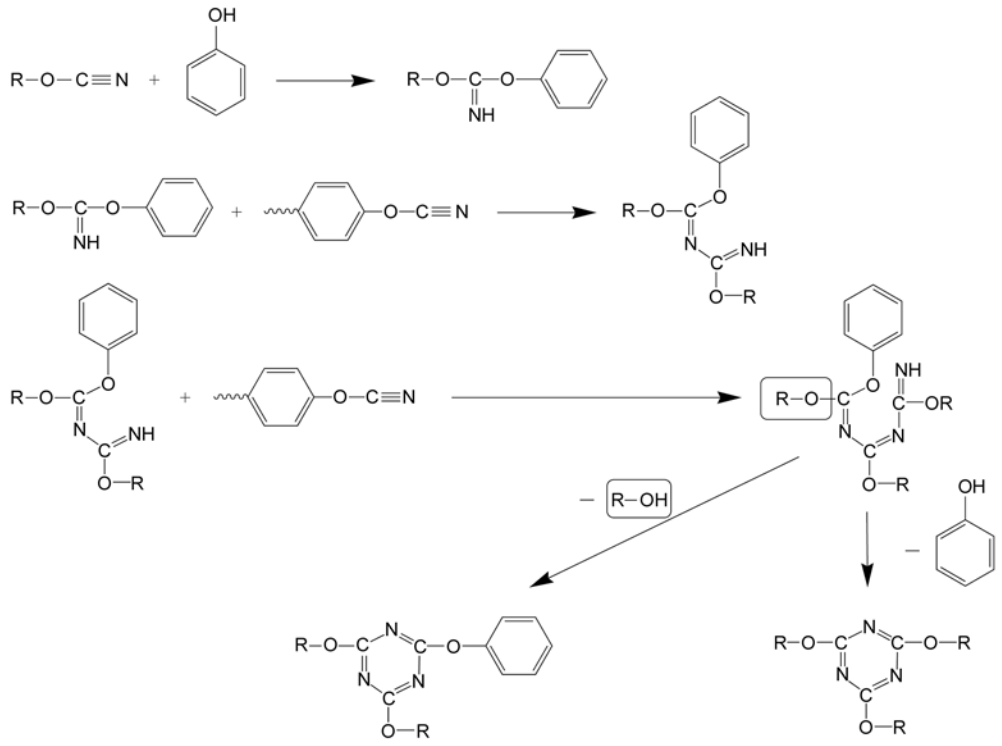

Figure 4. Co-reaction of benzoxazine (BuPa) with cyanate ester (Monocy)

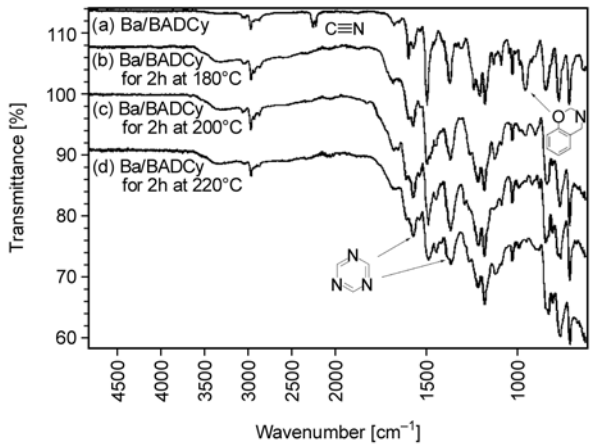

Figure 5. FT-IR spectra of the compound from curing reaction of 50 mol% Ba with 50 mol% BADCy. (a) before curing reaction, (b)after 180°C/2 hr, (c) after 180°C/2 hr + 200°C/2 hr, (d) after 180°C/2 hr + 200°C/2 hr + 220°C/2 hr.

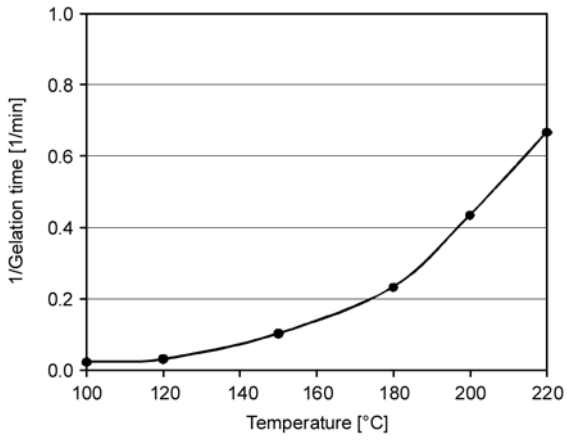

Figure 6. Reciprocal plot of gelation time as a function of temperature

3.3. Thermal stability of the molding compound from Ba and BADCy

The gelation time of the molding compounds from 50 mol% Ba and 50 mol% BADCy was measured. Furthermore, the reciprocal plot of gelation time as a function of temperature is shown in Figure 6. The molding compound was thermally stable under 120°C for about 45 min, because the curing reaction could not occur. This was because the ring opening reaction of benzoxazine ring was difficult to occur under 120°C, especially under dilution by BADCy, and the phenolic hydroxyl groups that contributed to the curing reaction were not produced. However, the gelation time was shortened with the rise of the molding temperature, because the benzoxazine ring opened and the phenolic hydroxyl groups that contributed to the curing reaction were produced easily, and thermal self-cyclotrimerization of cyanate ester group occurred.

3.4. DSC analysis of the molding compound

Figure 7 shows the DSC curves of the molding compounds from Ba and BADCy or Ep. From the

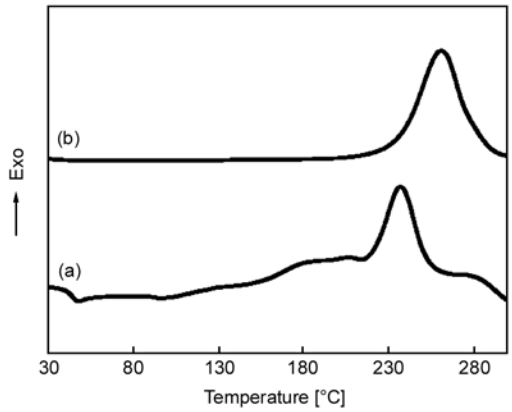

Figure 7. DSC curves of the molding compounds from Ba and BADCy or Ep. (a) Ba + BADCy, (b) Ba + Ep.

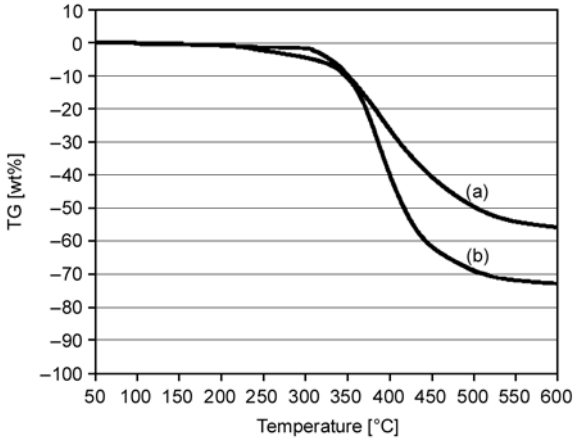

Figure 8. TGA curves of the molding compounds from Ba and BADCy or Ep. (a) Ba + BADCy, (b) Ba + Ep.

results of DSC, the maximum exotherm temperature (peak temperature) of the molding compounds from Ba and BADCy shifted to lower temperature side by about 20°C, compared with that of the molding compounds from Ba and Ep. It was found that the curing reaction of Ba with BADCy could proceed more rapidly than that of Ba with Ep. The reason might be considered that the co-reaction of the phenolic hydroxyl group produced by the ring opening reaction of benzoxazine with cyanate ester group occurred more rapidly than that of the phenolic hydroxyl group produced by the ring opening reaction of benzoxazine with epoxy group.

3.5. TGA analysis of the molding compound

Figure 8 shows the TGA curves of the molding compounds from Ba and BADCy or Ep. For the molding compounds from Ba and BADCy, the initial decomposition that was defined as 5 wt% of mass loss occurred about 330°C and the char yield at 600°C was 44 wt%. For the molding compounds from Ba and Ep, the initial decomposition that was defined as 5 wt% of mass loss occurred about 310°C and the char yield at 600°C was 27 wt%. In terms of the thermal gravimetric results, the thermal decomposition stability of the molding compounds from Ba and BADCy was superior to that of the molding compounds from Ba and Ep.

3.6. Properties of the cured thermosetting resin

The properties of the cured thermosetting resins from Ba and BADCy or Ep are shown in Table 1. And the curves of Dynamic mechanical analysis (DMA) are shown in Figure 9. As a result, glass transition temperature (T_g) of the cured thermosetting resin from Ba and BADCy was much higher than that of the cured thermosetting resins from Ba and Ep. The cured thermosetting resin from Ba and BADCy had extremely high volume resistivity of commercial resins, and volume resistivity of the cured thermosetting resin from Ba and BADCy was a little higher than that of the cured thermosetting

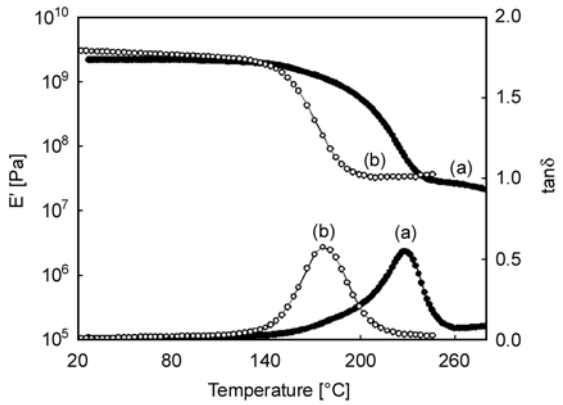

Figure 9. DMA curves of the cured thermosetting resins from Ba and BADCy or Ep. (a) Ba/BADCy, (b) Ba/Ep.

Table 1. Properties of the cured thermosetting resins

Sample	T_g[a] [°C]	K_{IC} [MPa·m$^{1/2}$]	Volume resistivity [Ω·cm]		Water absorption[b] [wt%]
			Before boiling	After 2 h boiling	
Ba/BADCy	223	0.61	$5.5 \cdot 10^{16}$	$5.2 \cdot 10^{15}$	0.26
Ba/Ep	175	0.54	$4.0 \cdot 10^{16}$	$1.2 \cdot 10^{15}$	0.46

[a]Peak temperature of tan δ by DMA.
[b]After 2 h boiling.

resins from Ba and Ep. K_{IC} of the cured thermosetting resin from Ba and BADCy was also slightly higher than that of the cured thermosetting resin from Ba and Ep. Water absorption after 2 h boiling of the cured thermosetting resin from Ba and BADCy was superior to that of the cured thermosetting resin from Ba and Ep. The reason of these results (good heat resistance, high electrical resistivity and high water resistance) might be due to the formation of rigid and hydrophobic triazine ring by thermal self-cyclotrimerization of cyanate ester group [43].

4. Conclusions

In this study, we investigated the curing reaction of bisphenol-A based benzoxazine with cyanate ester resin and the properties of the cured thermosetting resin. As a result of model reaction, it was found that the ring opening reaction of benzoxazine ring and thermal self-cyclotrimerization of cyanate ester group occurred. Furthermore, it was suggested that the phenolic hydroxyl group produced by the ring opening reaction of benzoxazine co-reacted with cyanate ester group to form the intermediate imonocarbonate, which further induce curing reaction of cyanate ester to form polycyanulate containing triazine groups. The molding compound from benzoxazine and cyanate ester resin showed good thermal stability below 120°C, but above 160°C the curing reaction of benzoxazine with cyanate ester resin proceeded more rapidly. From the thermal gravimetric results, the thermal decomposition stability of the molding compounds from benzoxazine and cyanate ester resin was superior to that of the molding compounds from benzoxazine and epoxy resin. The cured thermosetting resin from benzoxazine and cyanate ester resin had superior heat resistance, electrical resistance and water resistance to those from benzoxazine and epoxy resin. This might be because rigid and hydrophobic triazine ring structure was incorporated into the backbone of the cured thermosetting resin by thermal self-cyclotrimerization of cyanate ester group.

References

[1] Riess G., Schwob J. M., Guth G., Roche M., Lande B.: Ring opening polymerization of benzoxazines. in 'Advances in polymer synthesis' (eds.: Culbertson B. M., Mcgrath J. E.) 27–49, Plenum Press, New York (1985).

[2] Ning X., Ishida H.: Phenolic materials via ring-opening polymerization of benzoxazines: Effect of molecular structure on mechanical and dynamic mechanical properties. Journal of Polymer Science Part B: Polymer Physics, **32**, 921–927 (1994). DOI: 10.1002/polb.1994.090320515

[3] Ning X., Ishida H.: Phenolic materials via ring-opening polymerization: Synthesis and characterization of bisphenol-A based benzoxazines and their polymers. Journal of Polymer Science Part A: Polymer Chemistry, **32**, 1121–1129 (1994). DOI: 10.1002/pola.1994.080320614

[4] Ishida H., Rodriguez Y.: Catalyzing the curing reaction of a new benzoxazine-based phenolic resin. Journal of Applied Polymer Science, **58**, 1751–1760 (1995). DOI: 10.1002/app.1995.070581013

[5] Ishida H., Rodriguez Y.: Curing kinetics of a new benzoxazine-based phenolic resin by differential scanning calorimetry. Polymer, **36**, 3151–3458 (1995). DOI: 10.1016/0032-3861(95)97878-J

[6] Dungers J., Ishida H.: Vibrational assignments of N,N-bis(3,5-dimethyl-2-hydroxybenzyl)methylamine in the fingerprint region. Spectrochimica Acta Part A: Molecular and Biomolecular Spectroscopy, **51**, 855–867 (1995). DOI: 10.1016/0584-8539(94)00187-G

[7] Dungers J., Ishida H.: Vibrational assignment of 3-alkyl-3,4-dihydro-6-methyl-2H-1,3-benzoxazines in the fingerprint region. Spectrochimica Acta Part A: Molecular and Biomolecular Spectroscopy, **51**, 1061–1074 (1995). DOI: 10.1016/0584-8539(94)00114-Q

[8] Ishida H., Allen D. J.: Physical and mechanical characterization of near-zero shrinkage polybenzoxazines. Journal of Polymer Science Part B: Polymer Physics, **34**, 1019–1030 (1996). DOI: 10.1002/(SICI)1099-0488(19960430)34:6<1019::AID-POLB1>3.0.CO;2-T

[9] Shen S. B., Ishida H.: Synthesis and characterization of polyfunctional naphthoxazines and related polymers. Journal of Applied Polymer Science, **61**, 1595–1605 (1996). DOI: 10.1002/(SICI)1097-4628(19960829)61:9<1595::AID-APP19>3.0.CO;2-P

[10] Ishida H., Allen D. J.: Mechanical characterization of copolymers based on benzoxazine and epoxy. Polymer, **37**, 4487–4495 (1996). DOI: 10.1016/0032-3861(96)00303-5

[11] Shen S. B., Ishida H.: Development and characterization of high-performance polybenzoxazine composites. Polymer Composites, **17**, 710–719 (1996). DOI: 10.1002/pc.10663

[12] Dunkers J., Zarate E. A., Ishida H.: Crystal structure and hydrogen-bonding characteristics of *N*,*N*-bis(3,5-dimethyl-2-hydroxybenzyl)methylamine, a benzoxazine dimer. The Journal of Physical Chemistry B, **100**, 13514–13520 (1996). DOI: 10.1021/jp961293e

[13] Ishida H., Low H. Y.: A study on the volumetric expansion of benzoxazine-based phenolic resin. Macromolecules, **30**, 1099–1106 (1997).
DOI: 10.1021/ma960539a

[14] Russel V. M., Koenig J. L., Low H. Y., Ishida H.: Study of the characterization and curing of a phenyl benzoxazine using ^{15}N solid-state nuclear magnetic resonance spectroscopy. Journal of Applied Polymer Science, **70**, 1401–1411 (1998).
DOI: 10.1002/(SICI)1097-4628(19981114)70:7<1401::AID-APP15>3.0.CO;2-2

[15] Russel V. M., Koenig J. L., Low H. Y., Ishida H.: Study of the characterization and curing of benzoxazines using ^{13}C solid-state nuclear magnetic resonance. Journal of Applied Polymer Science, **70**, 1413–1425 (1998).
DOI: 10.1002/(SICI)1097-4628(19981114)70:7<1413::AID-APP16>3.0.CO;2-0

[16] Kim H. J., Brunovska Z., Ishida H.: Dynamic mechanical analysis on highly thermally stable polybenzoxazines with an acetylene functional group. Journal of Applied Polymer Science, **73**, 857–862 (1999).
DOI: 10.1002/(SICI)1097-4628(19990808)73:6<857::AID-APP1>3.0.CO;2-C

[17] Brunovska Z., Ishida H.: Thermal study on the copolymers of phthalonitrile and phenylnitrile-functional benzoxazines. Journal of Applied Polymer Science, **73**, 2937–2949 (1999).
DOI: 10.1002/(SICI)1097-4628(19990929)73:14<2937::AID-APP18>3.0.CO;2-E

[18] Shen S. B., Ishida H.: Dynamic mechanical and thermal characterization of high-performance polybenzoxazines. Journal of Polymer Science Part B: Polymer Physics, **37**, 3257–3268 (1999).
DOI: 10.1002/(SICI)1099-0488(19991201)37:23<3257::AID-POLB1>3.0.CO;2-0

[19] Rimdusit R., Ishida H.: Development of new class of electronic packaging materials based on ternary systems of benzoxazine, epoxy, and phenolic resins. Polymer, **41**, 7941–7949 (2000).
DOI: 10.1016/S0032-3861(00)00164-6

[20] Wang Y-X., Ishida H.: Development of low-viscosity benzoxazine resins and their polymers. Journal of Applied Polymer Science, **86**, 2953–2966 (2002).
DOI: 10.1002/app.11190

[21] Kim H-D., Ishida H.: Model compounds study on the network structure of polybenzoxazines. Macromolecules, **36**, 8320–8329 (2003).
DOI: 10.1021/ma030108+

[22] Chaisuwan T., Ishida H.: High-performance maleimide and nitrile-functionalized benzoxazines with good processibility for advanced composites applications. Journal of Applied Polymer Science, **101**, 548–558 (2006).
DOI: 10.1002/app.23509

[23] Ishida H., Ohba S.: Thermal analysis and mechanical characterization of maleimide-functionalized benzoxazine/epoxy copolymers. Journal of Applied Polymer Science, **101**, 1670–1677 (2006).
DOI: 10.1002/app.22499

[24] Allen D. J., Ishida H.: Physical and mechanical properties of flexible polybenzoxazine resins: Effect of aliphatic diamine chain length. Journal of Applied Polymer Science, **101**, 2798–2809 (2006).
DOI: 10.1002/app.22501

[25] Jang J., Shin S.: Cure studies of a benzoxazine-based phenolic resin by isothermal experiment. Polymer Journal, **27**, 601–606 (1995).
DOI: 10.1295/polymj.27.601

[26] Jang J., Seo D.: Performance improvement of rubber-modified polybenzoxazine. Journal of Applied Polymer Science, **67**, 1–10 (1998).
DOI: 10.1002/(SICI)1097-4628(19980103)67:1<1::AID-APP1>3.0.CO;2-V

[27] Agag T., Takeichi T.: Preparation, characterization, and polymerization of maleimidobenzoxazine monomers as a novel class of thermosetting resins. Journal of Polymer Science Part A: Polymer Chemistry, **44**, 1424–1435 (2006).
DOI: 10.1002/pola.21245

[28] Liu Y-L., Yu J-M.: Cocuring behaviors of benzoxazine and maleimide derivatives and the thermal properties of the cured products. Journal of Polymer Science Part A: Polymer Chemistry, **44**, 1890–1899 (2006).
DOI: 10.1002/pola.21290

[29] Liu Y-L., Chou C-I.: High performance benzoxazine monomers and polymers containing furan groups. Journal of Polymer Science Part A: Polymer Chemistry, **43**, 5267–5282 (2005).
DOI: 10.1002/pola.21023

[30] Liu Y., Zheng S.: Inorganic–organic nanocomposites of polybenzoxazine with octa(propylglycidyl ether) polyhedral oligomeric silsesquioxane. Journal of Polymer Science Part A: Polymer Chemistry, **44**, 1168–1181 (2006).
DOI: 10.1002/pola.21231

[31] Lee Y-J., Kuo S-W., Hung C-F., Chang F-C.: Synthesis and characterization of polybenzoxazine networks nanocomposites containing multifunctional polyhedral oligomeric silsesquioxane (POSS). Polymer, **47**, 4378–4386 (2006).
DOI: 10.1016/j.polymer.2006.03.111

[32] Yei D-R., Fu H-K., Chen W-Y., Chang F-C.: Synthesis of a novel benzoxazine monomer-intercalated montmorillonite and the curing kinetics of polybenzoxazine/clay hybrid nanocomposites. Journal of Polymer Science Part B: Polymer Physics, **44**, 347–358 (2006).
DOI: 10.1002/polb.20693

[33] Chen Q., Xu R., Yu D.: Multiwalled carbon nanotube/polybenzoxazine nanocomposites: Preparation, characterization and properties. Polymer, **47**, 7711–7719 (2006).
DOI: 10.1016/j.polymer.2006.08.058

[34] Kimura H., Matsumoto A., Hasegawa K., Ohtsuka K., Fukuda A.: Epoxy resin cured by bisphenol A based benzoxazine. Journal of Applied Polymer Science, **68**, 1903–1910 (1998).
DOI: 10.1002/(SICI)1097-4628(19980620)68:12<1903::AID-APP2>3.0.CO;2-P

[35] Kimura H., Matsumoto A., Hasegawa K., Fukuda A.: New thermosetting resin from bisphenol A-based benzoxazine and bisoxazoline. Journal of Applied Polymer Science, **72**, 1551–1558 (1998).
DOI: 10.1002/(SICI)1097-4628(19990620)72:12<1551::AID-APP7>3.0.CO;2-5

[36] Kimura H., Murata Y., Matsumoto A., Hasegawa K., Ohtsuka K., Fukuda A.: New thermosetting resin from terpenediphenol-based benzoxazine and epoxy resin. Journal of Applied Polymer Science, **74**, 2266–2273 (1999).
DOI: 10.1002/(SICI)1097-4628(19991128)74:9<2266::AID-APP16>3.0.CO;2-5

[37] Kimura H., Matsumoto A., Sugito H., Hasegawa K., Ohtsuka K., Fukuda A.: New thermosetting resin from poly(*p*-vinylphenol) based benzoxazine and epoxy resin. Journal of Applied Polymer Science, **79**, 555–565 (2001).
DOI: 10.1002/1097-4628(20010118)79:3<555::AID-APP190>3.0.CO;2-H

[38] Kimura H., Taguchi S., Matsumoto A.: Studies on new type of phenolic resin (IX) curing reaction of bisphenol A-based benzoxazine with bisoxazoline and the properties of the cured resin. II. Cure reactivity of benzoxazine. Journal of Applied Polymer Science, **79**, 2331–2339 (2001).
DOI: 10.1002/1097-4628(20010328)79:13<2331::AID-APP1041>3.0.CO;2-9

[39] Kimura H., Matsumoto A., Ohtsuka K.: New type of phenolic resin – The curing reaction of bisphenol A based benzoxazine with bisoxazoline and the properties of the cured resin. III. The cure reactivity of benzoxazine with a latent curing agent. Journal of Applied Polymer Science, **107**, 710–718 (2008).
DOI: 10.1002/app.26963

[40] Kimura H., Matsumoto A., Ohtsuka K.: Studies on new type of phenolic resin – Curing reaction of bisphenol-A-based benzoxazine with epoxy resin using latent curing agent and the properties of the cured resin. Journal of Applied Polymer Science, **109**, 1248–1256 (2008).
DOI: 10.1002/app.28279

[41] Kimura H., Matsumoto A., Ohtsuka K.: New type of phenolic resin: Curing reaction of phenol-novolac based benzoxazine with bisoxazoline or epoxy resin using latent curing agent and the properties of the cured resin. Journal of Applied Polymer Science, **112**, 1762–1770 (2009).
DOI: 10.1002/app.29301

[42] Reghunadhan Nair C. P., Mathew D., Ninan K. N.: Cyanate ester resins, recent developments. in 'Advances in polymer science: New polymerization techniques and synthetic methodologies' (eds.: Abe A., Albertsson A-C., Cantow H-J., Dušek K., Edwards S., Höcker H., Joanny J. F., Kausch H-H., Kobayashi T., Lee K-S., McGrath J. E., Monnerie L., Stupp S. I., Suter U. W., Wegner G., Young R. J.) Springer, Berlin, Vol. **155**, 1–99 (2001).

[43] Hamerton I.: Chemistry and technology of cyanate ester resins. Blackie Academic and Professional, New York (1994).

[44] Kwei K. T.: Viscoelasticity of crosslinked epoxy polymer in the transition region. Journal of Polymer Science Part A-2: Polymer Physics, **4**, 943–949 (1966).
DOI: 10.1002/pol.1966.160040609